Superprotonic Phase Transitions in Solid Acids: Parameters affecting the presence and stability of superprotonic transitions in the MH_nXO_4 family of compounds (X=S, Se, P, As; M=Li, Na, K, NH_4, Rb, Cs)

Thesis by

Calum Ronald Inneas Chisholm

In Partial Fulfillment of the Requirements

for the Degree of

Doctor of Philosophy

California Institute of Technology

Pasadena, California

2003

(Defended December 13th, 2002)

Acknowledgements

I must first say that I have had a truly wonderful time here at Caltech. I can only hope that the carefree lifestyle and true intellectual forum Caltech offers to its graduate students remain available to future generations. I count myself doubly blessed to have been accepted at this most distinguished institution.

I owe, of course, the greater part of my success and happiness at Caltech to my professor and mentor, Sossina Haile, without whose care and guidance I might never have discovered my love of research. I feel my critical thinking and ability to express ideas has been incalculably increased by our interactions. It has truly been a pleasure and honor to have worked with Professor Haile, and I am overjoyed to have the opportunity to collaborate with her for post-doctoral research.

Needless to say (but I certainly must), I thank my mother, who, after all, typed up my graduate applications and kept me from sending them in late. She has been a constant source of comfort and encouragement. Thanks, Momma. To my father, I am ever grateful to him for being my hero and role model, not just in the sciences, but in all of life's pursuits. His love for his work and his words of wisdom regarding a career in science convinced me long ago that my life would be fuller following the path I now tread. Cheers, Dad.

This work would not be possible without the efforts of other co-researchers. First and foremost, Dane Boysen, without whose efforts, assistance, and collaboration I might never have stepped into the lab, much less have arrived at the conclusions of this study. I must also single out Ryan Merle, who helped me immensely by doing all the "dirty work" and who has been a constant sounding board for new ideas. For the simulations work, I owe a huge debt of gratitude to Yun Hee Jang. Without her ever thoughtful assistance I could not have begun or finished that study.

There are a whole host of others that I have to thank for their time and effort, including: Sonjong Hwang, Dr. Ma Chi, Dr. Chuck Strouse, Lisa Cowen, Liz Miura, Prof. Rossman, Prof. Goddard, Lan Yang, Prof. Grubbs, and Prof. Fultz. To Dr. Chuck Witham, who was my first friend at work and always helped me both on and off campus, I wish you were here laughing at my defense, buddy. I must also thank my friends all over the states that have always supported me in my endeavors.

Financial support was provided by The National Science Foundation and various Caltech fellowships, making my life very easy here.

And finally, I must thank Erica, with whom I have shared this entire experience. You make me a better person who looks to the future while still enjoying the present.

Abstract

The present work attempted to uncover the structural and chemical parameters that favor superprotonic phase transitions over melting or decomposition in the $MHXO_4$, MH_2ZO_4, and mixed $MHXO_4$-MH_2ZO_4 classes of compounds (X=S, Se; Z=P, As; M=Li, Na, K, NH_4, Rb, Cs) and to thereby gain some ability to "engineer" the properties of solid acids for applications. Three approaches are described. First, the general observation that larger cations enable superprotonic transitions was investigated in both the isostructural $M_2(HSO_4)(H_2PO_4)$ and non-isostructural $MHSO_4$ family of compounds. The results of these studies confirmed and explained such a cation size effect, and also supplied a crystal-chemical measure for determining the likelihood of a compound undergoing a phase transition. Second, the entropic driving force behind the transitions was explored in the mixed $CsHSO_4$-CsH_2PO_4 system of compounds. From these investigations, a general set of rules for calculating the entropy change of a superprotonic transition was established and the role of entropy in the transitions illuminated. Finally, the superprotonic phase transition of $CsHSO_4$ was simulated by molecular dynamics, with which means the transition was probed in ways not possible through experimental methods. A sufficiently general approach was utilized so as to be applicable to other (as yet un-synthesized) compounds, thereby speeding up the process of discovering novel superprotonic solid acids. All three approaches increase the fundamental understanding of which chemical/structural features facilitate superprotonic transitions and should aid attempts to create new solid acids with properties ideal for application.

Contents

List of Figures

List of Tables

Chapter 1 Introduction

1.1 Overview

Solid acids, or acid salts, are a class of compounds with unique properties arising from the incorporation of "acid" protons into a crystalline structure: e.g., ½ Cs_2SO_4 + ½ H_2SO_4 → $CsHSO_4$. Initial research into these compounds focused on the ferroelectric properties that many solids acids, such as KH_2PO_4, express below room temperature due to ordering of the protons within their potential wells[1]. Near room temperatures, the structural proton leads to protonic conductivity on the order of Log(σ) ~ -6 to –9 in most solid acids. This conductivity is due to local defects in the structure and subsequent protonic hopping[2].

While most early studies focused on low temperature behavior of solid acids, in 1981 it was observed that $CsHSO_4$ had a first-order phase transformation at 141° C[3]. Not long after, it was discovered that as a result of this solid-solid phase transformation, the protonic conductivity increased by over three orders of magnitude[4]. Since then, there has been increasing interest in the high temperature properties of these compounds and their first-order phase transformations.

Most solid acids with superprotonic phase transitions have monoclinic symmetry in their room temperature phase[5]. Above the phase transition temperature, the symmetry of the compounds increases and to accommodate the higher symmetry, the oxygens become disordered. The partial occupancy of the oxygen sites gives a nearly liquid-like nature to the protons as the previously static hydrogen bonded system becomes highly

dynamic[6,7]. In this dynamic system, the XO4 groups librate at ~10^{11} Hz with inter-tetrahedra hopping of the proton occurring at ~10^{9} Hz[8]. This fast reorientation of the tetrahedra in conjunction with proton translations leads to the jump in conductivity across the phase transition and the "superprotonic conduction" many solid acids exhibit in their high temperature phases.

With the discovery of superprotonic conductivity in $CsHSO_4$, other known solid acids were investigated to reveal if they exhibited similar properties, resulting in many new superprotonic conductors being found. The three most extensively studied families of solid acids with superprotonic phase transitions have formulas $M_3H(XO4)_2$, $MHXO_4$, and MH_2YO_4 (X=S, Se; Y=P, As; M=Li, Na, K, NH4, Rb, Cs). The high temperature behavior of these compounds has been analyzed by a myriad of techniques including, but not limited to, X-ray diffraction, impedance spectroscopy, thermal calorimetry and gravimetric analysis, infrared and Raman spectroscopy, acoustic absorption, neutron diffraction and scattering, and NMR spectroscopy. There is therefore a good physical understanding of these phase transition. They are order-disorder transitions of first order that are entropically driven. Below the transition, the protonic transport is of the intrinsic type due to proton defects in the static hydrogen bonded network. Above the transition, symmetry increases and proton transport is due to fast reorientations of the XO4 tetrahedra in combination with proton translation along a "dynamically disordered network of hydrogen bonds"[9].

However, in spite of this plethora of theoretical and experimental data, there were only generalities for the question of which chemical and structural properties influence superprotonic phase transitions in solid acids. The objective of this thesis work was,

therefore, to uncover the chemical and structural parameters that favor superprotonic phase transitions over melting or decomposition in the $MHXO_4$, MH_2YO_4, as well as the new mixed $MHXO_4$-MH_2YO_4 classes of compounds and to thereby gain some ability to "engineer" the properties of solid acids for applications.

1.2 Ionic Conductivity[10-12]

In general, the total ionic conductivity of a material, under the influence of an electric field, will be the sum of the conductivities of each mobile species in the material. The conductivity of each ionic species is directly proportional to the number density of the ions, their mobility and the charge per ion. The total conductivity is then

$$\sigma_{\text{total}} = \sum_i \sigma_i = \sum_i N_i e z_i \mu_i \qquad (1\text{-}1)$$

where *i* refers to the species, N_i is the number of mobile ions per unit volume, μ_i is their mobility, and ez_i equals the ion's charge (charge per electron times valence of ion). For a pure ionic conductor in which the current is carried by only one type of ion, the total conductivity simplifies to

$$\sigma_i = N_i e z \mu_i \qquad (1\text{-}2)$$

The evaluation of the conductivity can then be reduced to calculating N_i and μ_i.

In the calculation of N_i we must consider the mechanism of ion mobility. For any crystalline material, the diffusion of atoms will be caused by the presence of defects in its

structure. These defects allow the atoms of the material to move on an otherwise fixed lattice. The intrinsic defect concentration can be evaluated as follows.

Thermodynamically, the very presence of these defects is due to the increase in entropy when some number of defects are added to the material. For an ideal solution, this increase in entropy per mole can be written

$$S_{mix} = - R[(1 - N_1)\ln(1 - N_1) + N_1 \ln(N_1)] \tag{1-3}$$

where here, N_1 is now the mole fraction of defects. The increase in entropy per mole of material, ΔS_{mix}, due to a small addition to the mole fraction of defects, ΔN_1, is then

$$\Delta S_{mix} = \frac{dS_{mix}}{dN_1}\Delta N_1 = -R\ln\left(\frac{N_1}{1-N_1}\right)\Delta N_1 \tag{1-4}$$

As this function shows, the initial increase in entropy per vacancy added is extremely large: $\Delta S_{mix} - \propto$ as $N_1 - 0$. Therefore, for a material at equilibrium there will always be a finite number of defects. To calculate this equilibrium number, we can use the fact that the change in Gibbs free energy, G, of a system in equilibrium is zero for any small displacement. The change in the Gibbs free energy, ΔG, with the addition of ΔN_1 defects to a mole of crystal already containing a concentration N_1 of defects is

$$\Delta G = H_d \frac{\Delta N_1}{N} - T\frac{\partial S}{\partial N_1}\frac{\Delta N_1}{N} \tag{1-5}$$

where N is Avagadro's number, and H_d / N and $(\partial S / \partial N_1)(1/N)$ are the increase in enthalpy and entropy, respectively, in the crystal per defect added. The enthalpy increase is due to local distortions to the atomic and electronic configuration resulting from the incorporation of a defect into the crystal structure. The entropy term includes the ideal entropy of mixing given in Eq. (1-3) plus another term due to the change in vibrations of the atoms when a defect is included, S_d / N. Substituting these entropy terms into Eq. (1-5) gives

$$\Delta G = \left[H_d - TS_d + RT \ln \frac{N_1}{1 - N_1} \right] \frac{\Delta N_1}{N} \tag{1-6}$$

Now, if the concentration of defects is very low, they are unlikely to interact and H_d and S_d should be independent of N_1. This equation then is most appropriate when $N_1 << 1$. This is certainly true for most metals and ionic solids, where $N_1 < 10^{-4}$ (Shewman, p70, 160). Using $N_1 << 1$, Eq. (1-6) becomes

$$\Delta G = \left[H_d - TS_d + RT \ln N_1 \right] \frac{\Delta N_1}{N} \tag{1-7}$$

Since $\Delta G = 0$ for any small displacement, ΔN_1, from equilibrium, we can write the equilibrium concentration of N_1 as

$$N_1^{equil} = \exp(S_d / R) \exp(-H_d / RT) \tag{1-8}$$

or,

$$N_1^{equil} = \exp(-G_d / RT) \tag{1-9}$$

where $G_d = H_d - TS_d$ is the free energy change to the crystal per one mole of defects added, on top of the entropy of mixing.

For ionic solids, the dominant defect will be a vacancy or interstitial[10]. Also, defects must leave the material charge neutral. These two facts lead to two types of disorder in ionic solids: Schottky and Frenkel. For Schottky disorder, an equal number of anion and cation vacancies are formed. It is found in materials where the energies of formation of a defect on either lattice are similar and the motion of both defects can be measured. However, experimentally it is observed that the mobility of cation vacancies is often much greater than that of anion vacancies, due mostly to the fact that cation vacancies are usually smaller than their companion anion vacancies. Cation vacancies are therefore responsible for most ionic conductivity by the Schottky defect mechanism. Using the results from Eq. (1-9), we find that at equilibrium in an ideal solution where defects do not interact,

$$(N_{va}^{equil})(N_{vc}^{equil}) = \exp[-(G_{va} + G_{vc}) / RT] \tag{1-10}$$

where $G_{va} = H_{va} - TS_{va}$ and $G_{vc} = H_{vc} - TS_{vc}$ are the molar free energy of formation of an anion and cation vacancy, respectively. Now, $N_{va}^{equil} = N_{vc}^{equil}$, so we can write Eq. (1-10) as

$$N_{va}^{equil} = \exp[-(G_{va} + G_{vc}) / 2RT] = \exp[-G_S / 2RT] \tag{1-11}$$

where G_S is the molar free energy to form the pair of vacancies. Schottky defects are found in alkali halides, e.g., NaCl and CsCl.

If the Frenkel type of disorder is dominant, the molar free energy to form a cation interstitial, G_{ic}, is much less than that to form an anion vacancy, G_{va}. Cation vacacies will then be charged balanced by cations jumping to interstitial sites rather than anion vacancies. Hence, the equilibrium concentration of cation interstitials, N_{ic}^{equil}, and cation vacancies, N_{vc}^{equil}, will be equal. As opposed to the Schottky mechanism where only the cation vacancies were significantly mobile, for Frenkel defects, cation mobility is due to both the vacancy and interstitial mechanism. If these defects are randomly located (i.e., do not interact), we can again use Eq. (1-9) to get

$$(N_{ic}^{equil})(N_{vc}^{equil}) = \exp[-(G_{ic} + G_{vc})/RT] = \exp(-G_F/RT) \tag{1-12}$$

or, since $N_{ic}^{equil} = N_{vc}^{equil}$,

$$N_{ic}^{equil} = \exp[-(G_{ic} + G_{vc})/2RT] = \exp(-G_F/2RT) \tag{1-13}$$

where G_F is the molar free energy of formation for the cation interstitial-vacancy pair. This type of disorder is found in AgCl and AgBr.

We will now look at the other unknown in Eq. (1-2), the mobility of the charge carrier, μ_i. Because the movement of an ion under the influence of an electric field is governed by the same atomistic mechanisms as diffusion of atoms due to a concentration

gradient, the ionic mobility can be directly related to the ion's diffusivity. This is expressed by the Nernst-Einstein equation:

$$\frac{\mu_{ion}}{ez} = \frac{D}{k_B T} \tag{1-14}$$

where k_B is Boltzmann's constant (8.62x10^{-5} eV/K), T is the temperature in degrees Kelvin and D is the diffusion coefficient. Regardless of the method of transport, if we assume that the jumps of the ion are uncorrelated and random, then the diffusion coefficient is equal to

$$D = \gamma a_o^2 \Gamma \tag{1-15}$$

where γ is a geometric constant derived from the structure, a_o is the jump distance and Γ is the jump frequency. As the jumping of the atom necessarily involves some amount of energy, we can give the jump frequency an Arrhenius-type temperature dependence:

$$\Gamma = \nu_o \exp(-G^o_{jump} / k_b T) \tag{1-16}$$

where ν_o is the attempt frequency, and $G^o_{jump} = H^o_{jump} - TS^o_{jump}$ is the jump activation energy per ion. The exact value of ν_o is difficult to determine from theory. It is comparable to a phonon frequency and is often approximated by the Debye frequency. The attempt frequency can be measured directly by experiments; usually by neutron scattering, nuclear magnetic resonance, or light scattering techniques. The exponential in (1-16) represents the probability that any given oscillation will cause a jump. Replacing Γ in Eq. (1-15) with the right side of Eq. (1-16) gives

$$D = \gamma a_o^2 \nu_o \exp(-G^o_{jump} / k_b T) \tag{1-17}$$

If we set $D_o = \gamma a_o^2 \nu_o$, then Eq. (1-17) becomes

$$D = D_o \exp(-G^o_{jump} / k_b T) \tag{1-18}$$

Using Eqs. (1-18) and (1-14) we can now express the conductivity as

$$\sigma_i = \frac{N_i (ez)^2 D}{k_b T} \tag{1-19}$$

$$\sigma_i = \frac{N_i (ez)^2 D_o}{k_b T} \exp\left(\frac{-G^o_{jump}}{k_b T}\right) \tag{1-20}$$

or

$$\sigma_i = \frac{N_i (ez)^2 \gamma a_o^2 \nu_o}{k_b T} \exp\left(\frac{-G^o_{jump}}{k_b T}\right) \tag{1-21}$$

with $D_o = \gamma a_o^2 \nu_o$.

From Eq. (1-9), we can solve for N_i since

$$N_i = N_1^{equil} N_o = N_o \exp(-G_d / RT) \tag{1-22}$$

where N_o is the number of lattice sites of the mobile ion per molar volume of the crystal. We can convert the exponential in Eq. (1-22) to the same units as the exponential of Eq. (1-21) by substituting

$$R = k_b N_A \tag{1-23}$$

where N_A is Avagadro's number = 6.023×10^{23}. Eq. (1-22) then becomes

$$N_i = N_o \exp\left(\frac{-G_d}{k_b N_A T}\right) = N_o \exp\left(\frac{-G_d / N_A}{k_b T}\right) = N_o \exp\left(\frac{-G^o_{defect}}{k_b T}\right) \tag{1-24}$$

The term G^o_{defect} represents the free energy of formation for one defect. So, Eq. (1-24) simply states that the equilibrium concentration of defects will equal the number of possible defects sites per unit volume times the probability (Boltzman) that a defect will exist. Substituting the right side of Eq. (1-24) into Eq. (1-21) for N_i gives

$$\sigma_i = \frac{(ez)^2 \gamma a_o^2 \nu_o}{k_b T} N_o \exp\left(\frac{-G^o_{defect}}{k_b T}\right)\exp\left(\frac{-G^o_{jump}}{k_b T}\right) \tag{1-25}$$

$$\sigma_i = \frac{N_o (ez)^2 \gamma a_o^2 \nu_o}{k_b T}\exp\left(\frac{S^o_{defect}+S^o_{jump}}{k_b}\right)\exp\left(\frac{-(H^o_{defect}+H^o_{jump})}{k_b T}\right) \tag{1-26}$$

using the fact that $G^o_{jump} = H^o_{jump} - TS^o_{jump}$ and $G^o_{defect} = H^o_{defect} - TS^o_{defect}$.

Eq. (1-26) can be further simplified to:

$$\sigma_i = \frac{A}{T}\exp\left(\frac{-Q}{k_b T}\right) \tag{1-27}$$

where

$$A = \frac{N_o (ez)^2 \gamma a_o^2 \nu_o}{k_b}\exp\left(\frac{S^o_{defect} + S^o_{jump}}{k_b}\right) \tag{1-28}$$

and

$$Q = H^o_{defect} + H^o_{jump} \tag{1-29}$$

The parameters A and Q will vary from material to material, but are independent of temperature. Eq. (1-27) then relates the underlying structural and thermodynamic properties of an ionic solid to its conduction. Experimentally, we find A and Q from an Arrhenius plot of Eq. (1-27) in the form of $\ln(\sigma_i T)$ versus 1/T. Q is often called the

activation energy for migration: the energy required to both form (H^o_{defect}) and move (H^o_{jump}) a defect to an adjacent lattice site. These two terms can be resolved by either calculations of the electronic energy change due to defect formation/migration or by experimentation.

For ionic solids, these experiments usually involve doping of the sample. If a material is heavily doped, then there will exist some low temperature range where the number of defects due to doping (N_{dp}), which is fixed, will be greater than the number of intrinsic defects (N^{equil}_{va} , N^{equil}_{ic} , and N^{equil}_{vc}), which increases/decreases exponentially with increasing/decreasing temperature. In this low temperature region, then, the concentration of defects is independent of temperature and a plot of $\ln(\sigma_i T)$ versus 1/T will give a slope proportional to $Q = H^o_{jump}$. The conductivity of the material in this region is called "extrinsic" as it depends on the dopant concentration and not the inherent properties of the crystal.

For sufficiently high temperatures, the number of intrinsic defects will be much greater than the number of defects due to doping. For this high temperature range, the concentration of defects will vary with temperature according to Eqs. (1-10) and (1-12), for Schottky and Frenkel defect mechanisms, respectively. The slope of $\ln(\sigma_i T)$ versus 1/T in this region will be proportional to $Q = H^o_{defect} + H^o_{jump}$, as the conductivity will be due to both defect formation and migration. Not surprisingly, the conductivity of this region is labeled "intrinsic." The change in slope going from the extrinsic to intrinsic regions should then be equal to H^o_{defect} .

The only variable not yet evaluated in Eq. (1-27) is then $S^o_{total} = S^o_{defect} + S^o_{jump}$. A direct measurement of the entropy of ionic conduction is difficult and since it is independent of temperature, it is often simply lumped into c_o and forgotten. However, it can be estimated from theory. Both S^o_{defect} and S^o_{jump} are due to changes in the vibrational spectrum when a defect is created or an ion jumps, respectively. We can calculate this change by using the harmonic oscillator approximation of the vibrational partition function[13]:

$$Z_{vib} = \sum_i e^{-(\varepsilon_i / k_b T)} = \sum_i e^{-[(i+1/2)\hbar\nu / k_b T]} = \frac{e^{-1/2(\hbar\nu / k_b T)}}{1 - e^{-h\nu / k_b T}} \tag{1-32}$$

where the partition function is over all possible states of one harmonic oscillator. We can then use the definition of the Helmholtz free energy, relative to that at absolute zero, to get

$$F = -k_b T \ln Z_{vib} = -k_b T \sum_i \ln\left(\frac{1}{1 - e^{-h\nu_i / k_b T}}\right) \tag{1-33}$$

where the summation is now over all frequencies of the crystal (i.e., system of harmonic oscillators). We can substitute Eq. (1-33) into the thermodynamic equation

$$S = -(\partial F / \partial T)_V \tag{1-34}$$

and get

$$S = -k_b \sum_i \left\{ \ln\left(\frac{1}{1 - e^{-h\nu_i / k_b T}}\right) - \frac{h\nu_i}{k_b T}\left(\frac{1}{e^{-h\nu_i / k_b T} - 1}\right) \right\} \tag{1-35}$$

or for temperatures well above the Debye temperature, where $k_b T >> h\nu_i$,

$$S = -k_b \sum_i \ln\left(h\nu_i / k_b T\right) \tag{1-36}$$

The entropy change as the crystal is perturbed from its ideal structure is then:

$$S = -k_b \sum_i \ln\left(\nu_i^i / \nu_i^p\right) \tag{1-37}$$

where ν_i^i and ν_i^p are the vibrational modes of the ideal and perturbed crystal, and the summation is over all vibrational modes of the crystal lattice. This summation is not easily done, but by dividing the crystal into nearest neighbors, elastically stressed neighbors, and the rest of the lattice, one can arrive at a good approximation.

It is possible then, at least in theory, to completely describe the ionic conductivity in terms of the structural and thermodynamic properties of a material. This is done experimentally most often by measuring not only the ionic conductivity of a material, but also its diffusion coefficient or attempt frequency, so that the other parameters in Eq. (1-27) can be resolved. More generally, Eq. (1-27) is used to calculate the activation energy of ion transport and the overall structural parameter. These are then compared to like compounds and the method of ionic transport is inferred from known conduction mechanisms.

1.3 Structural Features of Solid Acids

Before describing the mechanisms of proton transport, which differs quite significantly from that of other ions, it is necessary to describe the structural features of solid acids which influence proton conduction. Very generally, the structures of solid acids are similar to that of other ionic solids in that the compounds are made up of two lattices, one for cations and one for anions. However, the incorporation of the acid proton leads to the fundamental structural difference between solid acids and their analogous salts: the presence of hydrogen bonds. These hydrogen bonds link the anions together and the conduction of protons will be greatly effected by both the types of and particular arrangement of the hydrogen bonds found in a solid acid. Therefore, to properly explain protonic conduction in solid acids, it is necessary to first describe the types of hydrogen bonds and hydrogen-bonded networks that are found in them.

1.3.1 Characterization of Hydrogen Bonds

A hydrogen bond is said to exist if two electronegative species X and Y are connected to each other through bonds to a hydrogen atom, H. Usually, one bond will be stronger, written X—H, and is called the normal X—H bond while the weaker bond, written H···Y, is termed the hydrogen bond. The X and Y atoms are termed the donor and acceptor atoms, respectively. The dissociation energy of the X—H···Y complex is equal to the strength of the H···Y bond or the hydrogen bond strength[14]. Hydrogen bond strengths run in the range of 2 to 15 kcal/mole, which is significantly greater than other intermolecular forces (e.g., van der Waals forces with energies in the range of 0.1 to 2

kcal/mole for smaller molecules), but much less than intra-molecular covalent bonds (30 to 230 kcal/mole)[15].

This bond energy is not entirely due to the electrostatic attraction between the electronegative atoms and the hydrogen, but also involves a certain amount of covalent character arising from the overlap of lone pair electrons from the Y acceptor atom with those of X—H bond. As the hydrogen-acceptor distance decreases, the amount of covalency increases and so does the hydrogen bond strength[16]. This correlation between bond strengths and bond distances leads to hydrogen bonds being *very generally* labeled as strong, medium, or weak depending upon their donor-acceptor and donor-hydrogen lengths. As shown in Table 1.1 for X,Y = O, the hydrogens of strong hydrogen bonds are more equally shared between the donor and acceptor oxygens (O_d and O_a, respectively), resulting in smaller $O_d \cdots O_a$ and bigger O_d—H distances when compared to weak bonds[17,18].

Table 1.1 Correlation between hydrogen bond strength, $O_d \cdots O_a$, and O_d—H distances[14,17,18]

Bond Strength	$d_{Od \cdots Oa}$(Å)	$d_{Od—H}$(Å)
Strong	2.4 to 2.6	1.3 to 1.0
Medium	2.6 to 2.7	1.02 to 0.97
Weak	2.7 to ~3	Below 1.0

Which strength hydrogen bond favors protonic conductivity depends on a material's mechanism of proton transport. If protons are transported on a mobile species, then strong hydrogen bonds would decrease the mobility of the carrier. Hence, weak

hydrogen bonds are preferable for such a mechanism. However, if the mechanism of proton transport requires both the translation of protons along hydrogen bonds and the breaking of hydrogen bonds, then medium strength hydrogen bonds are preferable. This is due to the trade-off between the energy required for proton translation, which decreases with increasing hydrogen bond strength (decreasing $O_d \cdots O_a$ distance), and the energy required to break the bond, which by definition decreases with decreasing hydrogen bond strength (increasing $O_d \cdots O_a$ distance)[19].

The local crystallographic symmetry also effects proton conduction as the geometry of a hydrogen bond is partially determined by its site symmetry. This can be seen in Figure 1.1 for an O—H···O bond. For two oxygen atoms related by a center of symmetry and bound by a strong hydrogen bond, the potential energy of the proton will have a single minimum exactly between the two oxygens; the dual nature of each oxygen is signified by the label $O_{a/d}$. If the oxygen atoms are not related by symmetry, the hydrogen will reside slightly closer to one oxygen, but the hydrogen will be strongly bound near the center of the $O_d \cdots O_a$ complex.

In hydrogen bonds with medium $O_d \cdots O_a$ distances, two minima exist in the proton potential and the presence or absence of local symmetry influences the relative population of each minima by the proton. For the symmetric case, the proton will be found with equal probability in either minima and therefore can be considered "locally disordered" as the proton will hop between the two sites[17]. When the potential well of the proton is asymmetric, the proton will preferentially occupy one minimum over the other. However, the proton will still occasionally hop to the second minimum, thus dramatically increasing its intra-hydrogen bond mobility.

bond type	strong	medium	weak
symmetric	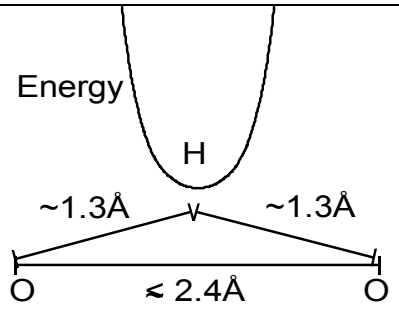	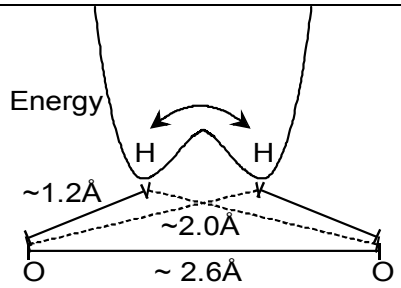	not generally observed
asymmetric	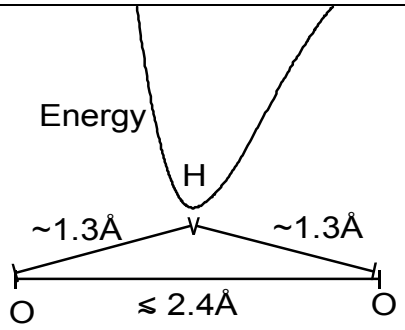	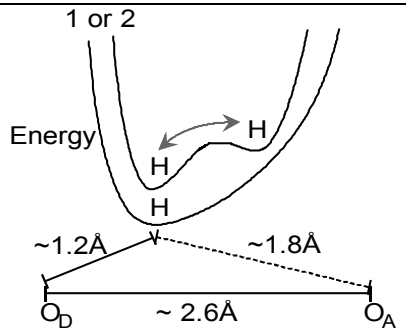	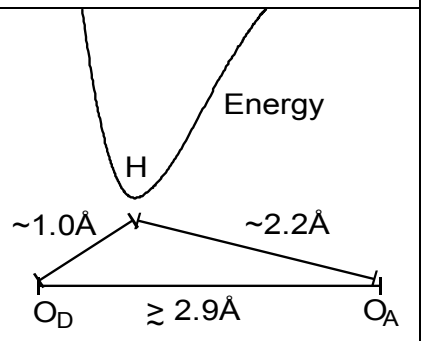

Figure 1.1 Effects of symmetry on strong, medium and weak hydrogen bonds[18].

Weak hydrogen bonds are almost always asymmetric, with only one minimum in potential energy of the proton. Moreover, as stated earlier, a weak hydrogen bond requires large energies to transfer the proton to the other side of the potential well (~2 to 10 times that of medium and strong hydrogen bonds, respectively)[19]. Consequently, the local symmetry of the hydrogen bond has a much greater effect on the proton transport properties of medium strength hydrogen bonds than it does on those of weak or very strong hydrogen bonds. The hydrogen bonds found in solid acids are ~2.5 to 2.7 Å[20] and are thus, for both symmetric and asymmetric examples, of the moderately strong to medium strength type of hydrogen bonds. Hydrogen bond energies associated with O···O distances of 2.5 to 2.7 Å are ~14 to 6 kcal/mole, respectively[21].

1.3.2 Hydrogen-Bonded Networks in Solid Acids

Very generally, hydrogen bonds can link together molecules into structures of 0, 1, 2, 3 dimensions. Some simple hydrogen-bonded networks found in solid acids are shown in Figure1.2. More complicated networks involve tetrahedra linking in such a way as to give three-dimensional structures (e.g., branched chains or layers) or true 3-D networks that run through out the crystal. To a certain degree, the type of hydrogen-bonded network found in a solid acid is predetermined by the average number of hydrogen-bonded oxygens per XO_4 tetrahedra. This number is itself a function of the compound's $H:XO_4$ ratio. Table 1.2 shows the hydrogen-bonded structures for an average of 1, 2, 3, and 4 bonded oxygens per XO_4 group. The example structures in this table were selected from solid acids of interest to this work.

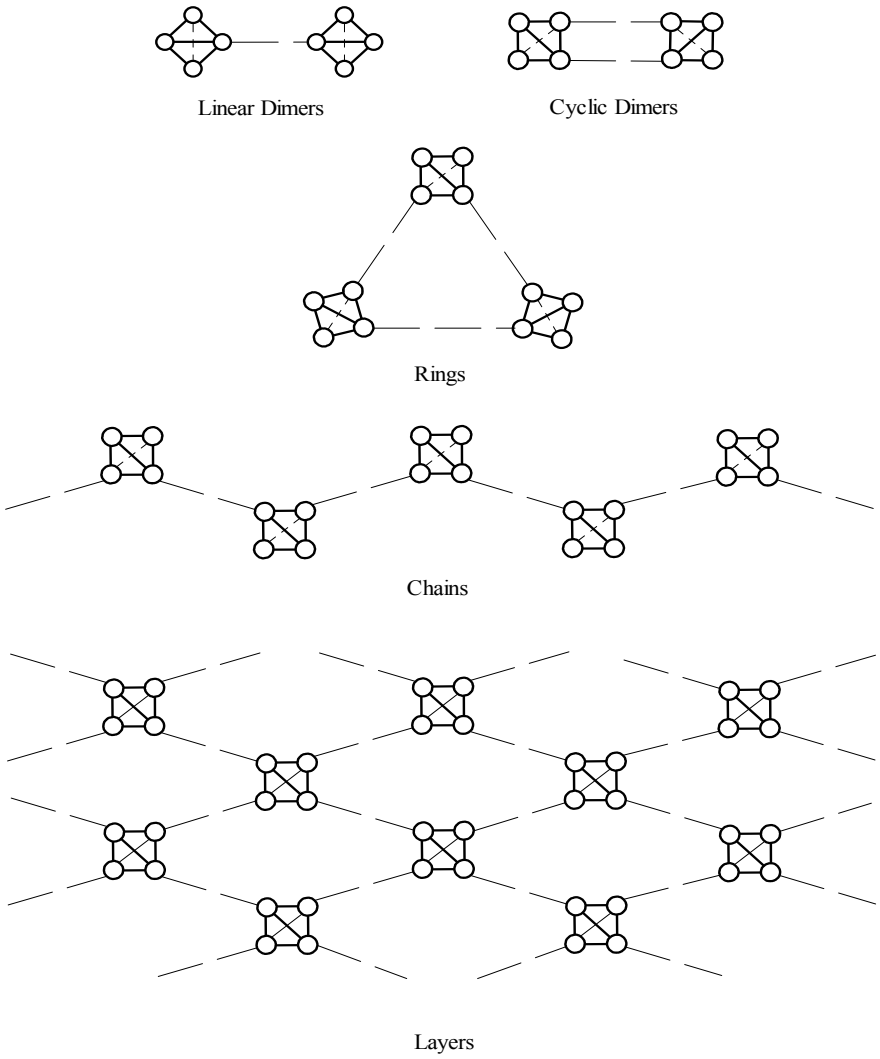

Figure 1.2 Simple hydrogen-bonded networks found in solid acids. Hydrogen Bonds are indicated by —— —— lines.

Table 1.2. Hydrogen-bonded networks in solid acids by their H:XO_4 ratio[22]

H:XO_4 ratio	Number of oxygens involved in hydrogen bonds per XO_4	Type of hydrogen-bonded network	Examples from MH_xXO_4 and $M_3H(XO_4)_2$ compounds - {ref}
1:2	1	Dimer	$K_3H(SO_4)_2$ - [23]
1:1	2	Cyclic dimer Rings Chains	$KHSO_4$ [2] - [24] $Cs_2Na(HSO4)_3$ - [25] $CsHSO_4$ - [26]
3:2	3	Layers	$Cs_2HSO_4H_2PO_4$ - [27]
2:1	4	Layers 3-dimensional	CsH_2PO_4 - [28] KH_2PO_4 - [29]

1.3.3 Common Structures Found in the Low Temperature Phases of Solid Acids

The zigzag chains of Figure 1.2 are a very common feature in solid acids. Straight chains are also observed, but more often than not a chain of tetrahedra will zig and zag as will the surrounding cations to a give a "checker-board" appearance to the arrangement of anions and cations[30]. This arrangement of atoms is shown in Figure 1.3 for the stable room temperature structure of CsHSO4 (phase II)[26].

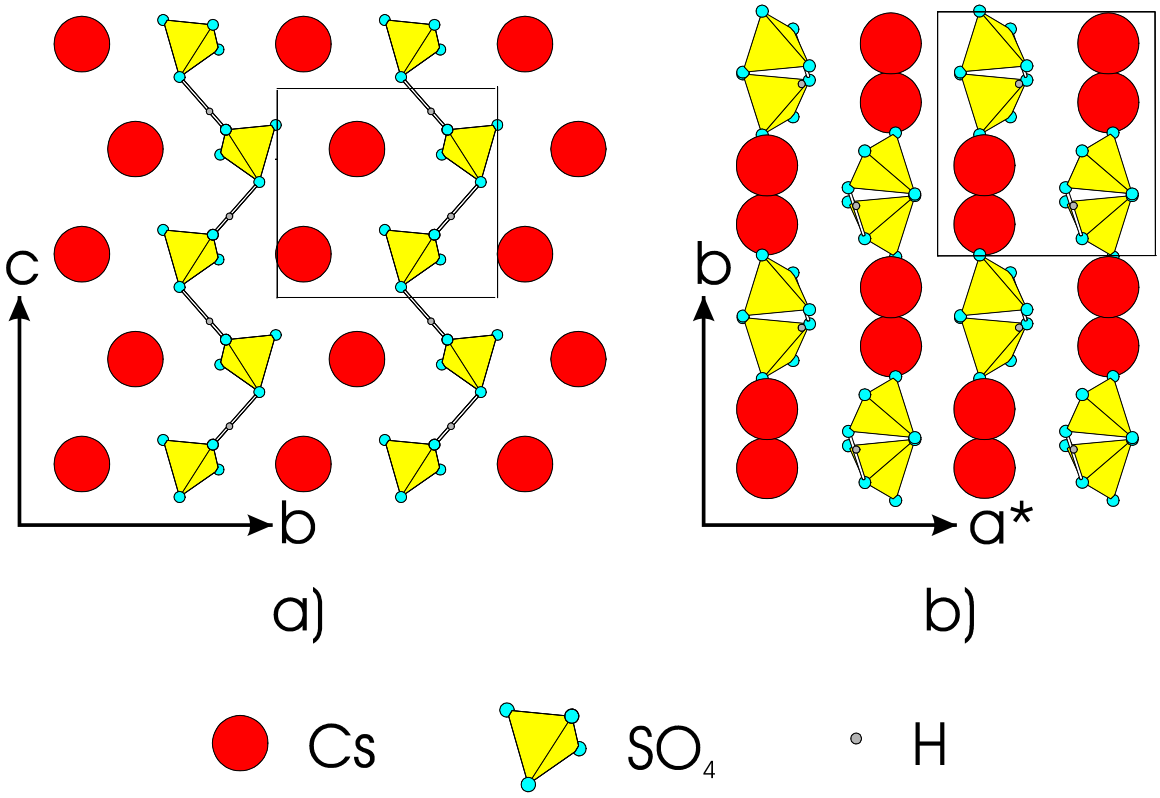

Figure 1.3 Room temperature structures for $CsHSO_4$ and CsH_2PO_4: a) the $\vec{b}\,x\,\vec{c}$ plane of $CsHSO_4$ showing zigzag chains of sulfate tetrahedra parallel to $\vec{c}$ and b) view down the c-axis revealing the checkerboard arrangement of cation and anion chains The rectangles represent unit cells.

These zigzag chains are often found in solid acids with higher dimensional networks where they are cross-linked by other hydrogen bonds to form planes and three-dimensional hydrogen-bonded networks [31,31,32]. The zigzag chains found in CsH_2PO_4 are cross-linked to form planes of hydrogen-bonded tetrahedra perpendicular to the [001] direction[32]. In KH_2PO_4, each tetrahedron is connected to two zigzag chains at right angles to each other to form a hydrogen-bonded network of tetrahedra that runs throughout the structure, Figure1.4.

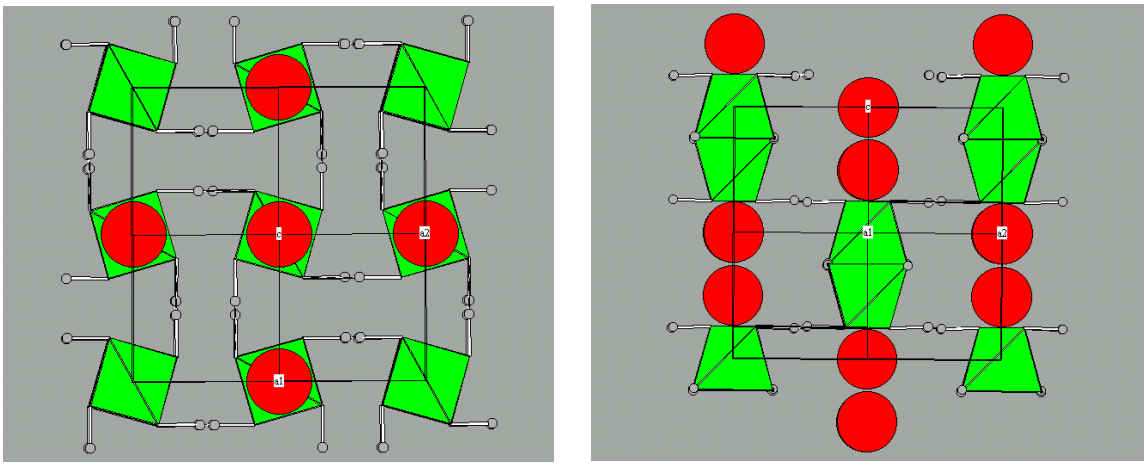

a) b)

Figure 1.4 Tetragonal structure of KH_2PO_4 projected down a) the [001] and b) the [100] directions. Chains of hydrogen-bonded PO_4 tetrahedra extend along the [100] and [010] directions in a) and the zigzag nature of these chains can be seen in b). Circles represent K atoms and tetrahedra PO_4 groups.

Another common structural type is found in solid acids belonging to the $M_3H(XO_4)_2$ family of compounds (M=Cs, Rb, NH_4, K, Na; X=S, Se). In the ordered (room temperature) phases of these compounds, the tetrahedra are hydrogen-bonded together into dimers. These dimers and their companion cations are arranged in such a way as to form planes with almost trigonal symmetry perpendicular to the [001]

direction, the true symmetry being monoclinic, space group A2/a. For the compound $K_3H(SO_4)_2$, this arrangement of sulfate dimers and K^+ ions is shown in Figure 1.5[32].

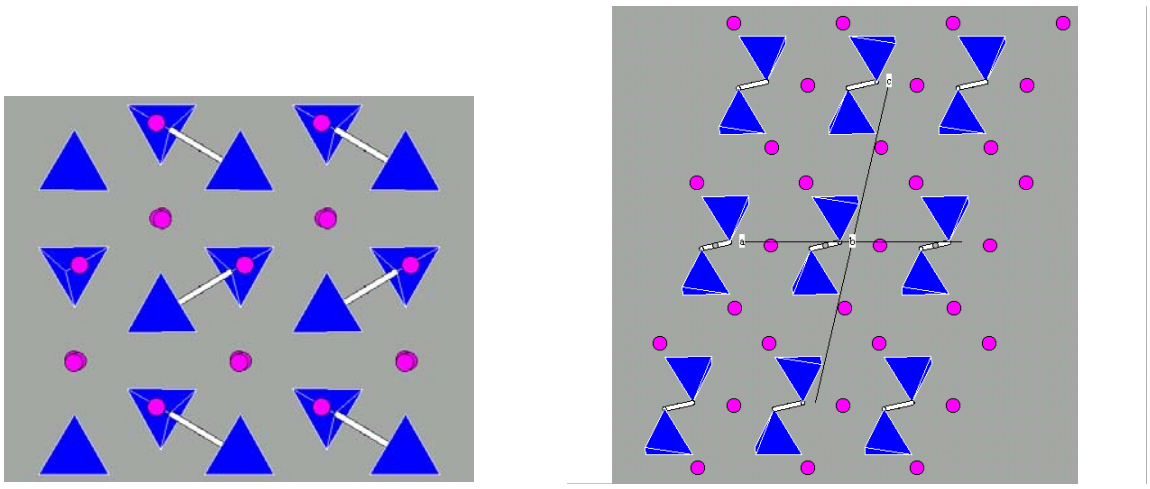

a) b)

Figure 1.5 Structure of monoclinic $K_3H(SO_4)_2$ projected down a) the c*-axis and b) down the b-axis.

1.4 Protonic Conduction

1.4.1 Mechanisms of Proton Transport

Although the general concepts of ionic conduction apply to protonic conduction, there is a fundamental difference between the two due to the fact that H^+ is the only ion with no core shell of electrons. It must therefore be solvated by the electrons of another atom or atoms[33,34]. For nonmetallic materials, and in particular ionic solids, the proton will be coordinated by only one or two atoms[35]. Due to the positive charge on the proton, the coordinating atom is usually the most electronegative atom around: F,O, N and sometimes Cl and S[15,34].

For most protonic conductors, the coordinating atom(s) is an oxygen. If the oxygen is well separated from other oxygen atoms, the proton-oxygen pair forms an O-H bond ~ 1 Å in length. As the distance to other electronegative species lessens, a hydrogen bond, O-H···O, will be formed, with O···O distances in the range of 2.4-3 Å long[20]. As the proton can never be free from the electron density of its neighbors, it must move by a method where it is bonded to at least one atom during the entire process[36]. This restraint leads directly to the two main methods of proton conduction: the vehicle and Grotthus mechanisms[2,37].

In the vehicle mechanism, the proton is attached to a mobile species (e.g., $H_2O+H^+ \rightleftharpoons H_3O^+$). Protonic conductivity is then achieved by the diffusion of the vehicle and counter-diffusion of unprotonated vehicles (here, H_2O), as shown in Figure 1.6. Clearly, in this mechanism the diffusion rate of the vehicle will determine the overall conductivity of the proton[38]. This mechanism is responsible for the protonic conductivity in oxonium β-alumina, hydrogen uranyl phosphate, and hydrated acidic polymers (e.g., NAFION)[37,39].

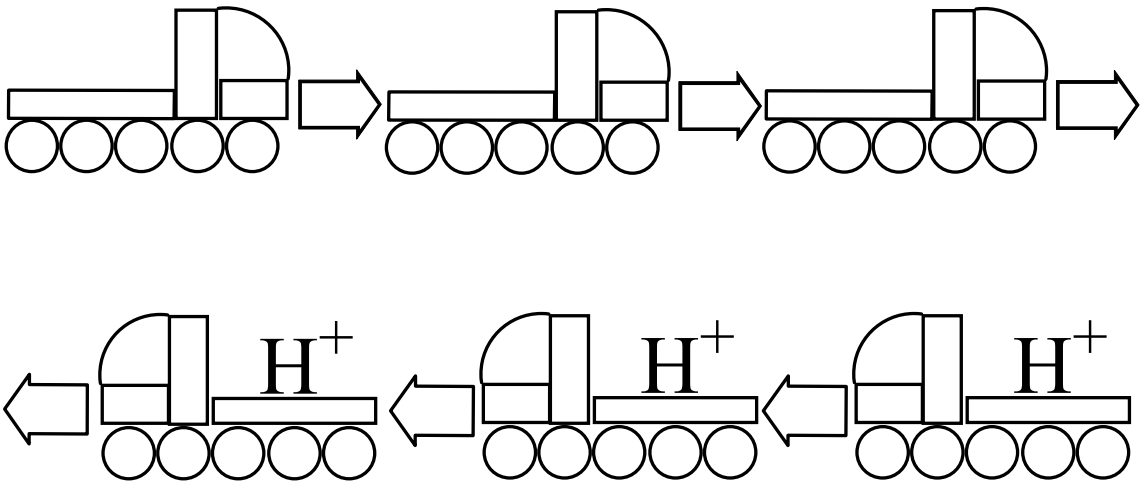

Figure 1.6 Vehicle mechanism of proton transport. Protons are carried to the left while empty vehicles travel to the right[37].

In contrast, the Grotthuss mechanism has the chemical species to which the proton is attached remain translationally stationary on the timescale of proton transport. By transfer of the proton within a hydrogen bond and subsequent structural relaxation (i.e., a structural or dipole reorientation of the new carrier), the proton can diffuse through the material[40]. This process requires that the protonic carriers have significant local dynamics. The relevant rates for this mechanism are then that of proton transfer and structural relaxation. Some materials that conduct protons by the Grotthuss process are ice[37], concentrated aqueous solutions and hydrates of acids (e.g., H_3PO_4, H_2SO_4, HCl, etc.) [41,42 43], fused phosphoric acid[44], the solid proton conductor $HClO_4$[45], and solid acids in both their low and high temperature phases [35,46,47]. A schematic description of the Grotthuss mechanism for ice is shown in Figure 1.7.

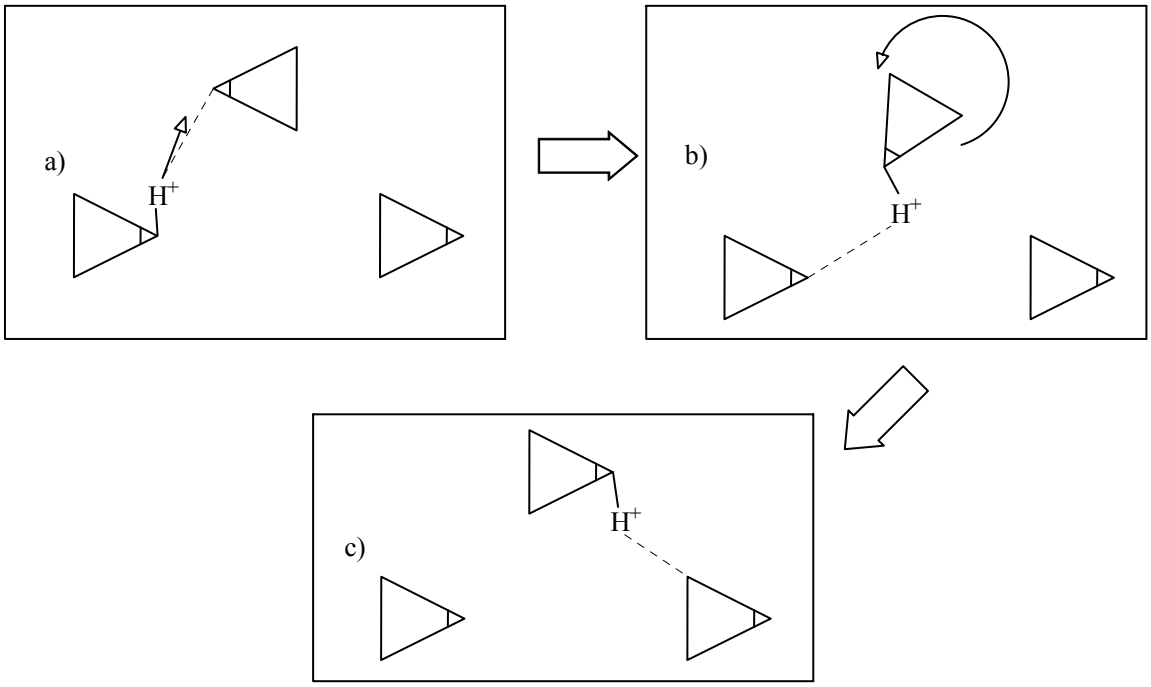

Figure 1.7 Grothhuss mechanism of proton transport. Proton jumps to an adjacent vehicle, a), which then reorients, b), to form a new hydrogen bond, c).

The ideal structure of normal (hexagonal) ice, first described by Bernal and Fowler, has each oxygen atom tetrahedrally coordinated by four other oxygens at a distance of 2.76 Å. Associated with each oxygen will be exactly two protons. Each proton will form a hydrogen bond with O—H and OH···O distances of 0.95 and 1.81 Å, respectively, resulting in each oxygen being involved in four hydrogen bonds[48]. According to the prevailing theory, there are two pairs of defects responsible for protonic conduction in ice. The first pair is created by reorientation of the water molecule, which causes doubly occupied and empty hydrogen bond sites: D and L defects, respectively[49]. This reorientation cannot be definitively labeled as a structural reorientation (with the molecule rotating around an axis of symmetry) or a dipole orientation (with the proton hopping from one site to another). Thermodynamically, both mechanisms must be present to some degree, but which one dominates the structural relaxation involved in

ice's protonic conduction is difficult to determine. Intra-hydrogen bond translation of the proton results in the formation of the second defect pair: the hydroxyl (OH^-) and hydronium ions (H_3O^+)[50]. Note that both steps require the protons to move from one to another crystallographic proton site.

It is necessary for both types of defect pairs to exist for true translation of a proton as each pair, alone, moves the protons in only a coordinated way, leaving the hydrogen-bonded system "polarized" in the direction of proton transport. By traveling along the same hydrogen-bonded system, the alternative pair can "unpolarize" this chain of hydrogen bonds. In particular, a D defect traveling in the same direction as a hydronium ion (and vice versa) will "unpolarize" the hydrogen-bonded system, as shown in Figure 1.8 c, d, and e. Similarly, an L defect following a hydroxyl ion (and vice versa) will allow for a continuation of proton migration in the same direction[37]. Proton conduction in ice then requires both proton transfer along hydrogen bonds and a reorientation of the proton carriers, and hence occurs by the Grotthuss mechanism.

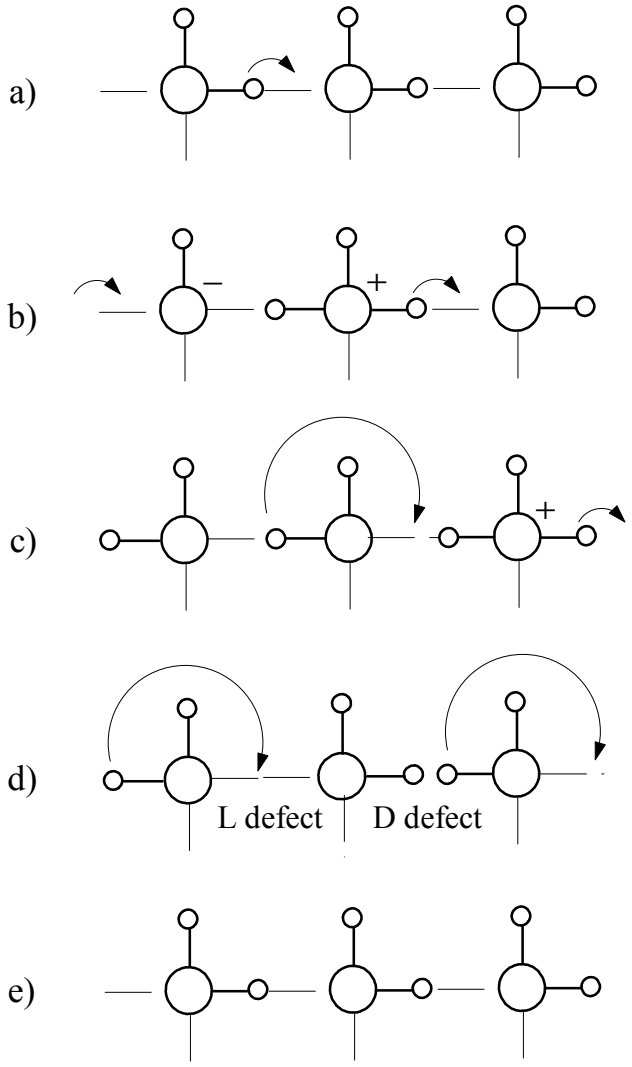

Figure 1.8 Representation of the Grotthuss mechanism in ice. Intra-hydrogen bond transfer of the proton, a), leads to the formation of hydroxyl (OH-) and hydronium (H3O+) ions, b). Reorientation of a water molecule, c), results in an L/D defect pair, d), with further reorientations removing the defects and leaving the chain able to continue proton conduction to the right, e).

For completeness, it should be mentioned that some materials exhibit mixed vehicle and Grotthuss mechanisms of proton transport. This occurs when there is both a high mobility for the proton carriers and a significant amount of proton transference between carriers. Dilute aqueous solutions of acids and bases and solid acid hydrates with high water content have mixed mechanisms of proton transport[39]. However, in general,

these two mechanisms operate exclusively of each other. The presence of continuous hydrogen-bonded pathways is essential to proton conduction via the Grotthuss mechanism, but an extensive hydrogen-bonded network hinders the translation of mobile species necessary to the vehicle mechanism[51].

1.4.2 Room Temperature Proton Conduction in Solid Acids

Proton conduction in solid acids is similar to that in ice for the low temperature, low symmetry, and (for the most part) ordered phases of solid acids that exist near room temperatures. Migration of protons again requires both transfer of the protons along hydrogen bonds and reorientations of the tetrahedral anions. As with ice, it is unclear as to whether the necessary structural reorientations occur by a physical rotation of the tetrahedra or by proton hopping leading to dipole reorientations. The transfer of protons along hydrogen bonds will result in the formation of tetrahedra that are negatively and positively charged when compared to average charge on the tetrahedra (e.g., $2(HSO_4^-) \rightarrow SO_4^{-2} + H_2SO_4$).

For solid acids with all tetrahedral oxygen atoms involved in hydrogen bonds, the formation of D and L defects would seem essential for proton conduction and the mechanism of proton conduction to be nearly identical to that found in ice. Indeed, models proposed by Murphy[52], O'Keeffe[53] and Pollock[54] relate the intrinsic conductivity to the formation of D and L defects in KH_2PO_4 type solid acids. In KH_2PO_4, all oxygens are involved in crystallographically symmetric hydrogen bonds (with O···O distances of 2.491 Å), and the proton resides in a symmetric double minimum potential well[55].

Evidence of this symmetric double minimum over a single minimum is found in KH_2PO_4's low temperature ferroelectric properties[56]. The distance between the minima is ~ 0.37 Å, a distance much shorter than the van der Waals radius for hydrogen (r = 1.2 Å)[15]. D defects will therefore have a large electrostatic repulsive energy associated with them[1]. To avoid the formation of such high energy defects, a model put forth by Sharon[57] involves the synchronous reorientations of multiple tetrahedra. Disadvantages to this model are that it requires the breaking of multiple hydrogen bonds as well as the coordinated rotation of multiple tetrahedra[57].

All the above models require the proton to move from one normal (crystallographic) site to another normal site; similar to the mechanism proposed for ice. In contrast, Baranov suggests a mechanism of proton conduction where the protons hop between normal and interstitial (i.e., non-crystallographic) sites, similar to a Frenkel defect mechanism[2]. This mechanism requires neither the formation of D defects nor rotations of the tetrahedra, since the protons jump between the normal and interstitial sites without aid of tetrahedral reorientations [2]. The necessary structural relaxation for a Grotthuss proton conduction mechanism is accomplished by dipole reorientations in this model. Intra-hydrogen bond transfer of the protons will still lead to tetrahedral equivalents of hydroxyl and hydronium ions, but the equivalent of the D, L defect pair for this model is a proton vacancy (L defect) and interstitial pair. The free energy of formation of the proton vacancy/interstitial pair will be lowest for interstitial sites that reform a hydrogen bond. Proton conduction is then possible by the migration of protons within and between the normal hydrogen-bonded network and the instantaneous network of interstitial hydrogen bonds.

In KH_2PO_4, Baranov suggests probable interstitial sites with O(1)···O(2') distances of 3.16 Å, which could form a weak to medium strength hydrogen bond after structural relaxation [46]. A representation of this interstitial site is shown in Figure 1.9 a. An equivalent interstitial site in ice is not found as the next-nearest neighbor oxygens for each oxygen atom are ~ 4.5 Å distant, too far away to form a hydrogen bond[58]. Baranov states this mechanism of proton conduction seems even more likely for solid acids with oxygens that are not structurally involved in hydrogen bonds, such oxygens acting as "built-in" interstitial sites. The direction(s) of the interstitial hydrogen bond(s) are then determined by finding the nearest oxygen atoms. In the $M_3H(XO_4)_2$ compounds, the pseudo-trigonal symmetry of the room temperature phases results in two interstitial sites per tetrahedron and is schematically depicted in Figure 1.9 b[46]. For a solid acid containing infinite chains of hydrogen-bonded tetrahedra similar to those found in $CsHSO_4$[26], a vacancy/interstitial proton conduction mechanism is shown in Figure 1.10. The ideal structure of $CsHSO_4$-II has O(3) and O(4) atoms not involved in hydrogen bonds. An interstitial hydrogen bond between these two oxygens is proposed by Baranov as the O(3)·· O(4) distance is only 3.2 Å[46].

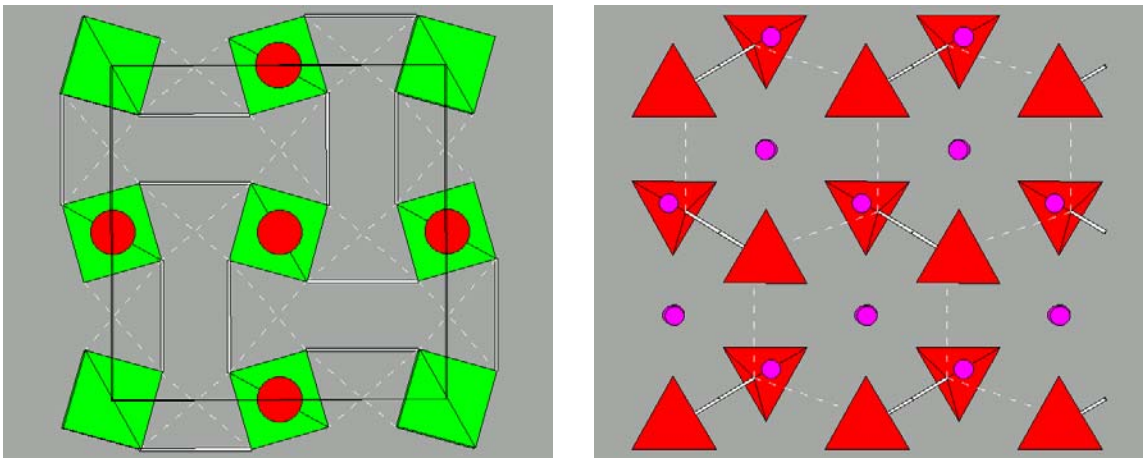

Figure 1.9 Normal and interstitial hydrogen bonds proposed for room temperature phases of a) KH_2PO_4 and b) the $M_3H(XO_4)_2$ class of compounds. Solid and dashed lines denote normal and interstitial hydrogen bonds, respectively.

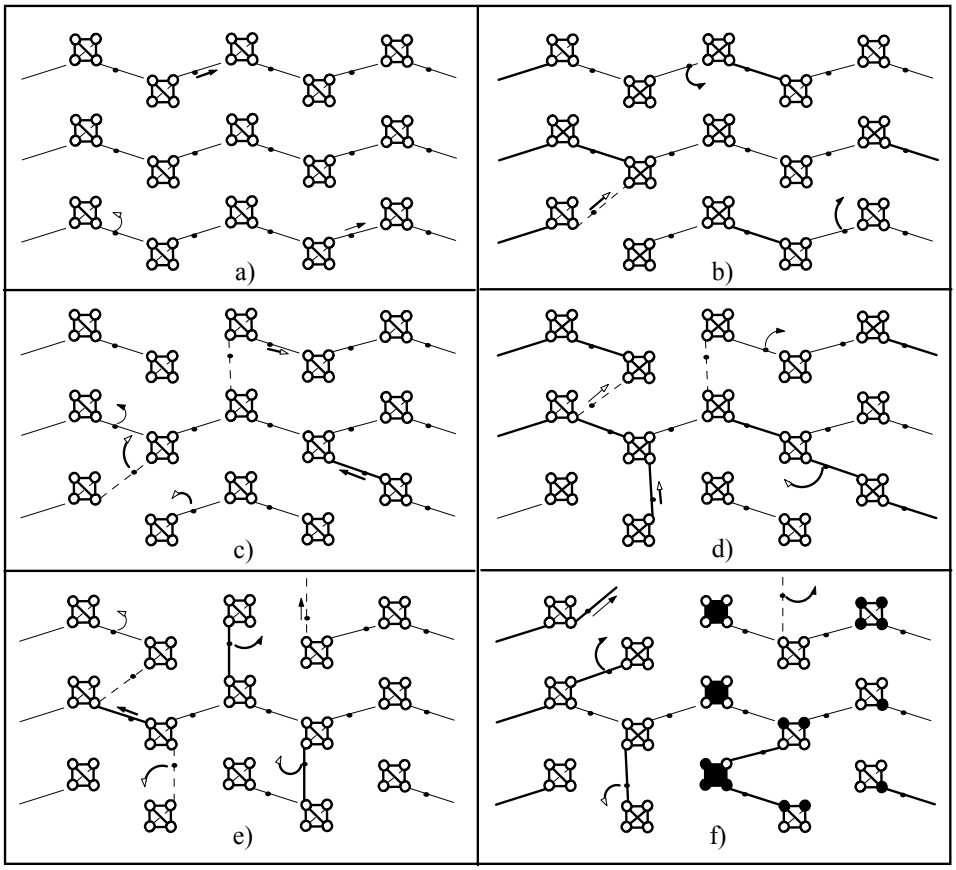

Figure 1.10 Possible conduction paths for proton vacancy/interstitial defects along and in between hydrogen-bonded zigzag chains of anion tetrahedra. Notice the formation of potential water molecules (i.e., an oxygen with two hydrogen bonds) is not a necessity for proton transport.

Although there is agreement in the literature that proton conduction occurs by the Grotthuss mechanism in the low temperature phases of solid acids, in the end there is no definitive proof of the particulars of the mechanism. Hence, there is a question as to which pair is formed: D and L or vacancy/interstitial defect pairs. Similarly, it has not been determined if the structural relaxation necessary for protonic conduction in these low temperature phases occurs by actual rotations of the tetrahedra or simply by dipole reorientations resulting from proton jumps.

1.4.3 High Temperature Proton Conduction in Solid Acids

For the high temperature superprotonic phases of solid acids, the mechanism of proton conduction is not in dispute. A highly disordered state leads to fast local dynamics of the anion tetrahedra and subsequent proton translation via the Grothhuss mechanism[35]. It has been determined that the tetrahedra are librating much faster (10^{11} Hz) than protons are being transferred (10^{9} Hz) which indicates that the structural relaxation essential to the Grotthuss mechanism is due to the physical reorientations of the tetrahedra in these phases[59,60]. The increase in symmetry across the phase transition (typically monoclinic $\rightarrow$ rhombohedral, tetragonal, or cubic) results in disorder on the oxygen sites, which are then free to vibrate and librate between crystallographically identical positions. This nearly free rotation of the tetrahedra creates many more crystallographically equivalent proton sites than there are protons, resulting in a "dynamically" disordered hydrogen-bonded network[9].

In contrast to protonic conduction in the room temperature phases of solid acids, it is then possible for proton conduction through only "normal," crystallographic proton sites. The combination of fast tetrahedral dynamics and proton translations along hydrogen bonds of a disordered network results in high protonic conductivity. Superprotonic conduction is therefore a result of the ideal structure rather than intrinsic defects[60]. In terms of Equation 1-1, this superprotonic conductivity is a product of the increase in the proton's mobility and the increase in the number of mobile protons (all of them).

The structure proposed by Jirak for $CsHSO_4$ in its superprotonic phase is given in Figure 1.11[61]. It should be mentioned that there is some disagreement in the literature over the exact position of the oxygen atoms, and hence the protons. This structure was chosen as it gives the most realistic arrangement and length to the hydrogen bonds, as well as its overall fit to experimental data (to be discussed in Section 4.6.1).

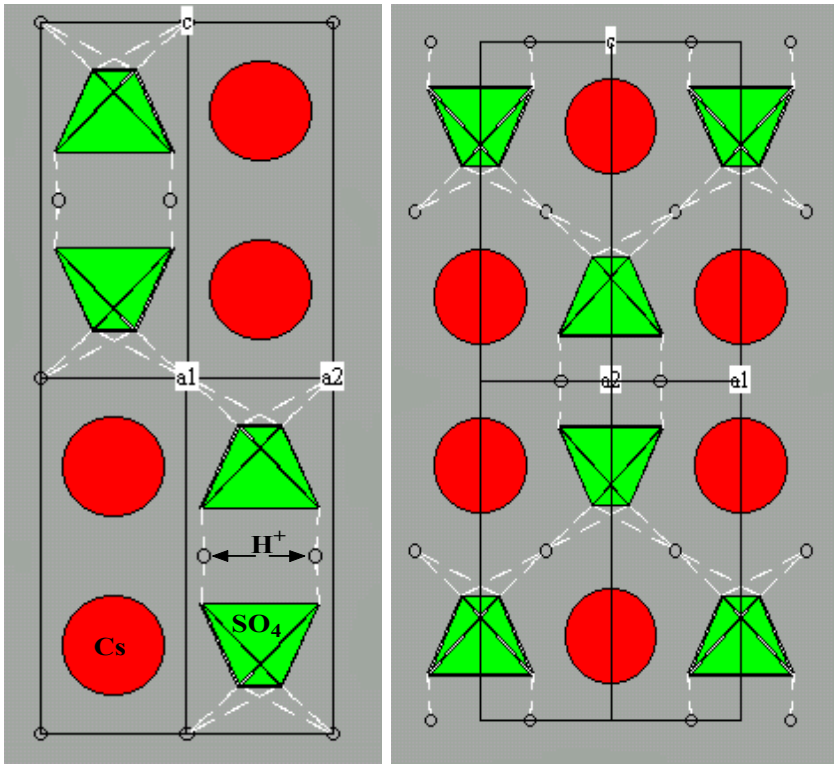

a) b)

Figure 1.11 Tetragonal structure of $CsHSO_4$ above its superprotonic phase transition projected along the [100], c), and [010], d), directions. Two orientations of the tetrahedra result in partially occupied proton sites and a disordered network of hydrogen bonds (dashed lines).

The room temperature phase of $CsHSO_4$-II is monoclinic, space group $P2_1/c$, comprising zigzag chains of hydrogen bonded SO_4 tetrahedra alternating with zigzag rows of cesium atoms (Figure1.3). There are four crystallographically distinct oxygens, two of which are involved in asymetric hydrogen bonds with O(1)···O(2) distances of 2.63 Å[26]. On the contrary, after transforming to the superprotonic tetragonal phase (space group $I4_1/amd$), the oxygens become crystallographically identical and all oxygens participate in hydrogen bonds. There are two possible orientations of the tetrahedra, resulting in ½ and ¼ occupancy of the oxygen and proton sites, respectively. Hydrogen bonds of average length 2.78 Å connect the oxygens[61]. Other proposed structures have a

different number of tetrahedral orientations, hydrogen bond lengths and hydrogen bond orientations. However, regardless of the exact configuration of oxygens and protons in the superprotonic phase of $CsHSO_4$, the method of proton conduction remains the same: rapid reorientations of the SO_4 group forming a dynamically disordered network of hydrogen bonds through which protons can jump from one tetrahedron to the next.

This mechanism of proton transport is responsible for the high conductivity in all superprotonic phases of solid acids, with any differences between their conductive processes attributed largely to the relative symmetry of the specific material. For example, $CsHSO_4$, being tetragonal, shows a small anisotropy in its conductivity parallel and perpendicular to its 4-fold axis[62]. In contrast, the compound $Cs_2(HSO_4)(H2PO_4)$, which transforms to a cubic structure (space group $Pm\bar{3}m$) exhibits isotropic conductivity in the superprotonic phase[63]. Nevertheless, on a very local scale, the process of proton transfer and reorientation is considered to be very similar in all superprontic phases and conclusions reached for one compound should apply at least to structurally related compounds, if not to the whole class of solid acids.

Chapter 2. Experimental Methods

2.1 Synthesis

The solid acids analyzed in these studies were all grown by slow evaporation of an aqueous solution containing high purity metal carbonates and the appropriate mineral acids:

$$M_2CO_3 + H_nXO_4 + H_2O \xrightarrow{-H_2O} \text{single crystals}$$

where M = Cs, Rb, NH_4, K, Na, Li and X = S, P. Most crystals were grown at room temperatures, but some compounds were found to grow only at elevated/lowered temperatures. The compounds discussed in this work are primarily mixed cation sulfates (Chapter 3) and cation sulfate-phosphates (Chapter 4). First attempts at their synthesis were carried out in solutions with total metal to anion ($M:XO_4$) ratios of 1:1. Therefore, unless otherwise noted, it is safe to assume a compound was synthesized at ~25°C with a solution $M:XO_4$ ratio of 1:1.

After the formation of crystal samples, they were collected by either removing individual crystals directly from solution, or by filtration over a porous ceramic (since the solutions are still quite acidic and would eat through normal filters). If necessary, the samples were washed with acetone or isopropanol to remove any excess solution clinging to the crystals. Deliquescent compounds were placed in desiccated containers, while most other samples were stored in ambient conditions.

For large quantities of a desired phase or to force the synthesis of a compound not found to grow by the above method, organic solvents were used to precipitate powder samples. The most common solvents used were acetone, methanol, and isopropanol. The

powders were filtered from solution and washed with the precipitating liquid on ceramic filters. Powder samples were stored in sealed containers to limit surface water absorption.

2.2 X-ray Diffraction

X-ray diffraction methods were almost exclusively used to identify the phases of crystals grown as above. For the most part, the diffraction measurements were performed on single crystal samples so as to provide very accurate phase determinations, single crystal samples for other measurements, and the possibility of orienting the samples. If it was necessary to analyze the abundance of different phases grown from the same solution, a random sampling of crystals was finely ground together and a powder X-ray diffraction (PXD) measurement taken.

Single crystal X-ray diffraction (SCXD) measurements also provided the data for determining the structures of any novel compounds. SCXD samples were cut from single crystals and shaped into rough cubes, on average ~ 0.15 mm a side. The small crystallites were then attached to the top of a thin glass fiber by a common two-part epoxy and the glass fiber mounted in a cylindrical brass holder. The brass holder was then placed in a goniometer and the cube aligned in the center of the X-ray beam. Diffraction intensity data for the aligned samples were obtained on a Syntex four-circle diffractometer using Mo Kα radiation ($\lambda = 0.71073$ Å). Decay and absorption corrections were applied as necessary and structural refinements performed on the resulting F^2 data for the collected reflections. The SHELXS86 and SHELXL93 (or SHELXL97) programs were used for structure solution and refinement, respectively[64,65]. Visual inspection and depiction of the structures were accomplished with the ATOMS program[66].

Unfortunately, the relatively large (~ 1 to 2 %) volume changes typical of superprotonic transitions causes single crystal samples to turn polycrystalline and become useless in SCXD measurements. Hence, the high temperature structures were determined from PXD measurements taken above the phase transition temperature. Also, from Reitveld refinements of PXD patterns taken at elevated temperatures the thermal expansion coeffiecients for both low and high temperature phases were measured allowing for accurate calculations of the transition volume changes. The program Rietica was used in such refinements[67]. PXD measurements were also used to confirm the phase purity of solvent precipitated samples. Calculated patterns were generated from published data using the Micro-Powd program and then compared to the measured PXD patterns with the program JADE[68,69]. Unless otherwise stated, the PXD measurements reported in this work were taken on a Siemens D500 diffractometer with Cu Kα radiation (λ = 1.5418 Å).

2.3 Neutron Diffraction

Neutron diffraction on both single crystal and powder samples was performed to take advantage of its sensitivity to light elements and atoms with similar atomic numbers. Due to the difficulty in taking such measurements, a nuclear reactor or scintillation source being required, neutron diffraction measurements were only taken when analysis of the X-ray diffraction data failed to definitively resolve a crystal's structure. For compounds in this work, any ambiguity in their structures usually resulted from the inability to accurately locate H/D atoms or to differentiate between sulfate and phosphate groups. Both problems are a direct result of the fact that the scattering lengths for X-rays

increases monotonically with atomic number. Hence, H/D atoms are fairly transparent to X-rays, while SO_4 and PO_4 groups will scatter X-rays almost identically[70].

Conversely, in neutron diffraction H and D atoms are easy to discern as their coherent scattering lengths are -3.739 and 6.671 fm, respectively, making both atoms strong neutron scatterers[71]. Also, the scattering lengths for S and P are quite different for neutrons (5.13 and 2.847 fm, respectively), and it is usually straightforward to distinguish between the two atoms or even determine their individual occupancies on a mixed S/P site[72]. In particular, neutron diffraction was used in this work to resolve the H/D and O positions for atoms involved in disordered hydrogen bonds in the otherwise ordered room temperature phases. For the superprotonic phases, the H/D and O positions resulting from the fast reorientations of the tetrahedra were also investigated, along with the possible existence of superstructures do to potential ordering of the tetrahedra in mixed sulfate-phosphate compounds. Measurements used thermal neutrons with wavelengths ~ 1 Å generated from both reactor and spallation sources.

2.4 Thermal Analysis

The behavior of compounds with increasing temperature was probed by two main techniques: differential scanning calorimetry (DSC) and thermal gravimetric analysis (TGA). The presence and characterization of phase transitions both above and below room temperature were accomplished by DSC measurements. A compound's response to heating was examined with a Perkin-Elmer DSC 7 calorimeter in a flowing nitrogen environment. The most common heating rates were 5, 10, and 20°C/min. For low temperature measurements, an in house apparatus was used which essentially consisted of a Perkin-Elmer DSC 7 calorimeter immersed in a helium environment that had been cool

by liquid nitrogen. A sample was therefore cooled to ~ -150°C (the limit for LN_2) and heated, at rates varying from 1-5°C, in 30°C intervals to limit instrument drift.

The onset of decomposition in a sample was probed by a Perkin-Elmer TGA 7 or Neztsch STA 449 analyzer under flowing nitrogen and argon, respectively. Again, the most common heating rates were 5, 10, or 20°C/min. The Neztsch system can simultaneously take DSC and TGA data, but for consistency's sake all DSC measurements were taken on the Perkin-Elmer machines.

2.5 Chemical Analysis

The compositions of any new compounds were measured using a JEOL JXA-733 electron microprobe. Single crystal samples were mounted in an epoxy resin, polished and then coated in carbon by evaporation. The polishing of single crystal samples was not trivial as the compounds are water soluble. For some compounds, even best attempts at polishing still resulted in poor quality surfaces for microprobe measurements. Hence, pressed powder pellet samples (from ground up single crystals) were also analyzed, with the advantage that the surfaces of the pellets were already flat and needed only to be carbon coated. Microprobe data were taken at a minimum of seven points on a sample for statistical averaging. High quality samples (single crystals or pellets) of compounds with a like, but known, nature were used as standards. Measured X-ray peak intensities were converted to elemental weight percentages using the CITZAF program[73]. For most compounds (new/known solid acids and single crystal/pellet samples alike), visible beam damage was observed during data collection. This damage is most likely the dehydration of the surface when excited by the electrons in the beam. For this reason, larger rather than smaller areas were scanned in the measurements.

2.6 Optical Spectroscopy/Microscopy

Superprotonic phase transitions of some compounds were further investigated by infrared (IR) spectroscopy and polarized light microscopy. The vibrational spectrum of compounds pressed into optically transparent KBr pellets (sample:KBr mass ratio of 1:300) were measured on a Nicolet Magna 860 FTIR spectrometer in flowing nitrogen. An in house heating stage was employed to heat the pellets and observe the changes in their spectrums with temperature. Most attention was given to the changes with temperature in the bending and stretching modes of the tetrahedrons (in the range of 450 to 1100 cm^{-1}) as well as the OH stretching modes within the O-H···O bonds. These modes show up as three broad peaks ~ 1700, 2400, and 2800 cm^{-1} and are often referred to as the "ABC bands" of hydrogen bonds[14]. From the behavior of the tetrahedral modes, the increase in symmetry associated with almost all superprotonic transitions could be observed, hopefully validating the assigned symmetry taken from PXD data. Observations of the ABC bands not only confirmed the presence of hydrogen bonds, but also revealed the general effect of a phase transition on these bonds.

Polarized light microscopy was most often used to judge the quality of single crystal samples. This was accomplished by observing the sample under extension conditions on a transmission Leica DMLB microscope. For a single domain crystal without inclusions or attached crystallites the perceived image should be homogeneous. By attaching a single crystal sample to a heating stage, high temperature transitions could be observed. In most cases, single crystal samples would become completely opaque above a superprotonic transition due to the high symmetry of the phases. This technique

was also an easy way to determine if single crystal samples would turn polycrystalline or not when undergoing a transition, which influenced other measurements.

2.7 NMR Spectroscopy

Pulsed Fourier transform H^+ NMR measurements were performed on a finely ground sample to characterize the proton environment of the compound. Specifically, the number of crystallographically distinct hydrogen atoms and their relative amounts were investigated. Also, the percent deuteration of a compound was accurately measured by taking the ratio of the integrated intensities of deuterated and fully protonated samples. All measurements were taken on either a Bruker DSX 500 MHz or a Bruker AM 300 MHz NMR spectrometer. The chemical shifts of the samples were referenced to tetramethylsilane (TMS). Magic angle spinning (MAS) was employed to reduce the proton-proton dipole broaden of the signal lines resulting from the local interactions of a proton's magnetic moment with the dipole fields generated its neighbors.

For most measurements, a 12 kHz spinning rate was used in conjunction with a 4 μs, 90° pulse. The spin-lattice relaxation time, T_1, was on the order of 1000 s for all compounds measured, revealing that the excited H^+ nuclei in these solid acids interact weakly with their surrounding lattices. The observed chemical shifts for the crystallographic protons were ~ 10-12 ppm, typical values for protons residing in medium strength hydrogen bonds[74]. There was often a very sharp peak seen at ~ 6 ppm that was attributed to absorbed water based on its disappearance with heating and a comparison to measurements on calcium phosphates, where similar peaks were observed and assigned to surface water[75].

2.8 Impedance Spectroscopy

The conductivity of a compound was measured by a.c. impedance spectroscopy using a 4284 LCR (inductance-capacitance-resistance) meter. Conductivity measurements were taken on cut and polished single crystal samples along known crystallographic directions (as determined by SCXD methods), while polycrystalline samples were made from finely ground single crystals that had been uni-axially pressed into pellets. Silver paint (Ted Pella cat. no. 16032) served as the electrode material. Samples were prepared so as to have a large area to length ratio (A/L) with respect to the direction of the applied field. Such a geometric ratio is desirable as it decreases a sample's effective resistance and gives better signal resolution. Measurements were made over the frequency range of 20 Hz to 1 MHz with an applied voltage of 1 V under either inert (dry argon or nitrogen) or ambient atmospheres. Heating and cooling rates were 0.5°C/min (unless otherwise noted). For most samples, the impedance spectra exhibited a single arc in the Nyquist representation. The effective d.c. resistivity, ρ, was determined by fitting such an arc to an equivalent (RQ) circuit using the least squares refinement program EQUIVCRT[76]. The effective resistivities (ρ = R) were then converted into geometry independent conductivities, $\sigma = 1/(\rho * A/L)$, and plotted in an Arrhenius form to facilitate the extraction of informative parameters from the data (see section 1.2). Since this impedance spectroscopy method is probably the least well known technique used in this work, its basic theory will be described below.

2.8.1 Complex Impedance (from ref [77-79])

The simplest model for an electrode-sample system under an applied voltage is a capacitor and resistor in parallel, Figure 2.1 a. The capacitor is a result of the sample's geometry, while the resistor represents the resistivity of the bulk. For such a circuit, the response to an applied voltage,

$$V(t) = V_o e^{i\omega t} \tag{2-1}$$

will be a current in the resistor,

$$I_R = \frac{V_o e^{i\omega t}}{R} = \frac{V(t)}{R} \tag{2-2}$$

and a current in the capacitor,

$$I_C = \frac{dQ(t)}{dt} = \frac{d(CV(t))}{dt} = C\left(\frac{dV_o e^{i\omega t}}{dt}\right) = i\omega CV_o e^{i\omega t} = i\omega CV(t) \tag{2-3}$$

The total current in the circuit is then

$$I_{total} = I_R + I_C = \frac{V(t)}{R} + i\omega CV(t) \tag{2-4}$$

Exactly like the conventional impedance, Z, the complex impedance is defined as the ratio between the voltage and current, which is here:

$$Z = \frac{V(t)}{\frac{V(t)}{R} + i\omega CV(t)} = \frac{1}{\frac{1}{R} + i\omega C} \tag{2-5}$$

The impedance can be separated into its real, Z′, and imaginary, Z″, parts to give

$$Z = \frac{\frac{1}{R}}{\left(\frac{1}{R}\right)^2 + (\omega C)^2} - i\frac{\omega C}{\left(\frac{1}{R}\right)^2 + (\omega C)^2} = Z' - iZ'' \qquad (2\text{-}6)$$

A plot of Z′ vs. -Z″ (as parametric functions of ω) will result in a semicircle of radius R/2 in the first quadrant, Figure 2.1 b. The time constant of this simple circuit is defined as

$$\tau_o = RC = \frac{1}{\omega_o} \qquad (2\text{-}7)$$

and corresponds to the characteristic (dielectric) relaxation time of the sample. Substituting ω_o from Eq. (2-7) into Eq. (2-6) gives Z′ = R/2, Z″ = R/2, so that the characteristic frequency lies at the peak of the semi-circle. A plot of Z′ vs. -Z″ is often called a Nyquist plot.

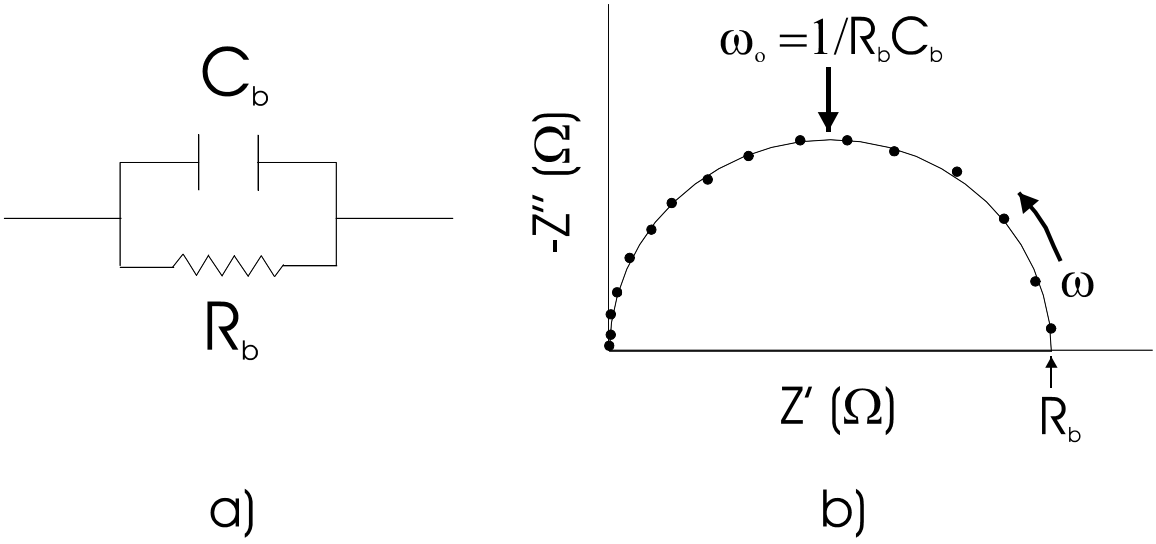

Figure 2.1 Equivalent circuit for a dielectric material between two electrodes, a): R_b and C_b represent the bulk resistance and capacitance, respectively. This circuit gives a semi-circle in the complex impedance plot of Z′ vs. -Z″. The frequency increase from right to left and the characteristic frequency of the electrode-material system lies at the peak of the semicircle.

One of the major advantages of complex impedance spectroscopy over single frequency or DC techniques is its ability to resolve the electrode, bulk, and grain boundary (for polycrystalline samples) contributions to the resistance. In an ideal sample, the impedance plot would show three semicircles and would be modeled as three (RC) circuits in series, Figure 2.2. This type of impedance plot is often seen for pure ceramics such as ZrO2, but almost never seen for the proton conducting compounds of this work. Instead, only one (single crystal samples) or two semi-circles (polycrystalline samples) were usually present at low temperatures, representing the bulk and grain boundary responses to the applied voltage. This type of impedance plot was modeled by two (RC) circuits in series, i.e., the first two circuits in Figure 2.2 a.

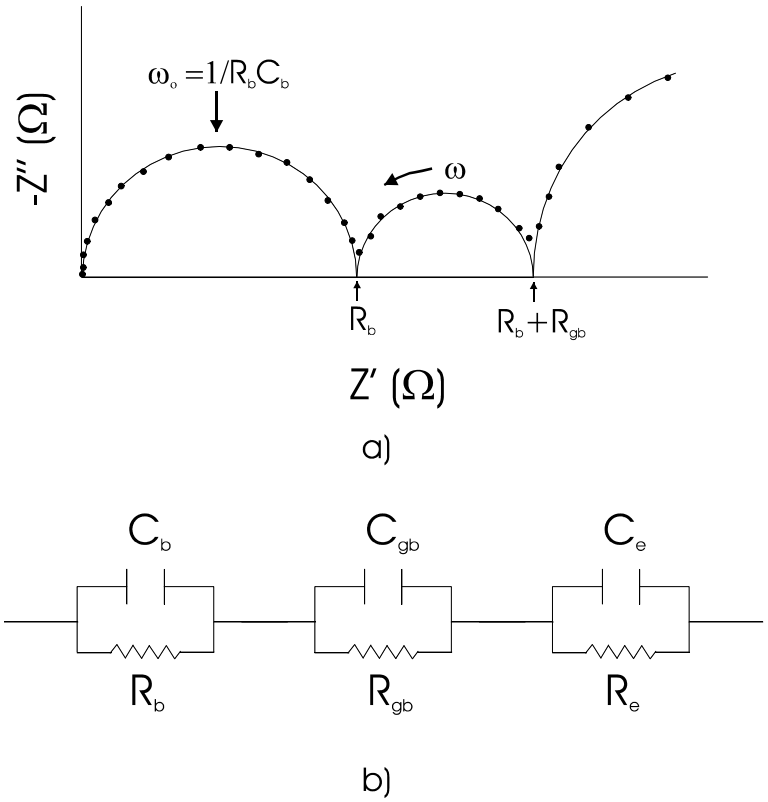

Figure 2.2 Separation of bulk, grain boundary, and electrode resistances is possible by impedance spectroscopy if a sample's complex impedance plot shows three separate semi-cirlces, a), by fitting the data to a three element RC circuit, b).

At elevated temperatures, the second arc (due to grain boundaries) virtually always disappeared, which can be attributed to the grain boundaries having a higher (than the bulk) activation energy for proton conduction. The total resistance of the grain boundaries would then decrease much faster than the bulk, represented in the Nyquist plots by an ever shrinking second arc with increasing temperature. In its place, a nearly straight line was usually seen, caused by a variation of the effective resistance and capacitance of some element(s) in the circuit with frequency, Figure 2.3 a. This variation comes from a distribution of relaxation times in the sample as a result of inhomogeneties in the material and/or when the diffusion of an uncharged (or effectively uncharged) species responding to a chemical potential becomes the rate controlling step. For solid electrolytes, the later situation typically refers to the mobile species diffusing through the electrodes, which have an effective potential gradient of zero due to the presence of majority electronic carriers. Such a process results in a straight line at 45° degrees to the Z' (real) axis as proven by Warburg and Macdonald[78,80].

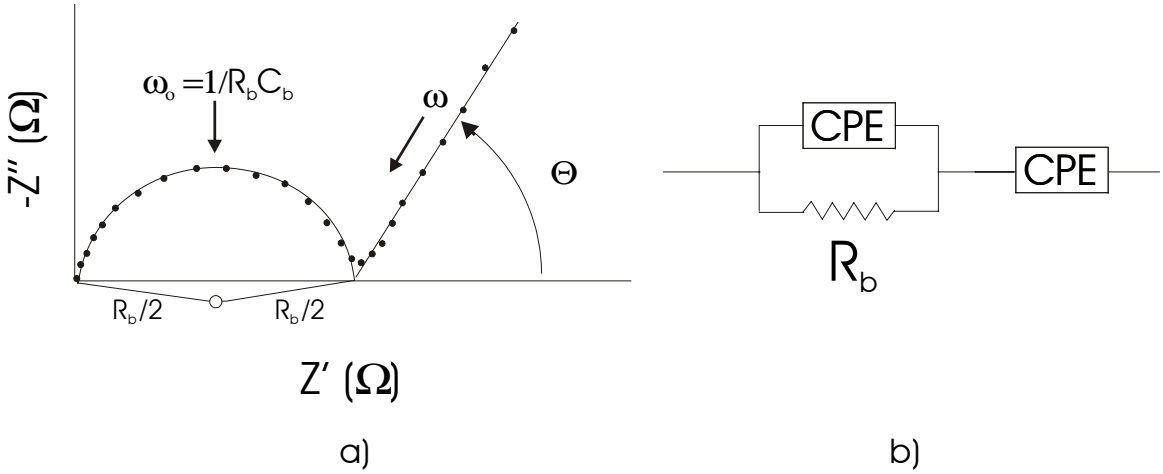

Figure 2.3 Realistic impedance plot showing a depressed semi-circle with center below the real axis and straight line at low frequencies, a). Both effects are due to the distribution of characteristic frequencies in the sample and are modeled with a constant phase element (CPE), b).

However, lines observed in this work usually deviated from 45 degrees, attesting to true physical inhomogeneities in the samples. The most common cause of such inhomogeneous behavior is rough electrode/electrolyte interfaces, which causes the microscopic resistivities and capacitances near the interface to be "distributed" around the mean macroscopic values. Distributed relaxation times are also caused by variations of local composition and/or structure. As well as the appearance of lines at low frequencies, these inhomogeneities also result in depressed semi-circles with centers below the real axis, Figure 2.3 a. Both these distributed effects are modeled by introducing a constant phase element (CPE) with impedance

$$Z_{CPE} = A(i\omega)^{-\psi} \tag{2-8}$$

The CPE equivalent of the normal RC circuit then has an impedance of

$$Z = \frac{V(t)}{\frac{V(t)}{R} + \frac{V(t)}{A(i\omega)^{-\psi}}} = \frac{1}{\frac{1}{R} + A(i\omega)^{\psi}} \tag{2-9}$$

The CPE reduces to an ideal capacitor for $\Psi = 1$ and to a resistor for $\Psi = 0$, and thus can model the distribution of microscopic capacitors and resistors in a material.

For compounds with superprotonic transitions, the conductivity increases by ~ 10^2-10^3 across the transition. Not surprisingly then, the semi-circle in Figure 2.3 a disappears, usually leaving only a straight line visible in the Nyquist plots of the superprotonic phases. The resistance of the bulk (and therefore the materials conductivity) was then estimated by the intercept with the real axis of a least squares

refinement on the line. This estimation was necessary as the frequencies associated with superprotonic conduction exceeded the upper limit of our impedance meter (1 MHz), but nevertheless gave highly reproducible values that also compared well with those in the literature, and so was deemed acceptable.

Chapter 3. Cation Size Effect on the Superprotonic Transitions of MH_nXO_4 compounds (M = Cs, Rb, NH_4; X = S, Se, P, As; n = 1-2)

3.1 Introduction

The effect of alkali ion substitution on solid to solid phase transitions in the MH_nXO_4 class of compounds has been well documented. The initial investigations of these solid acids focused on the low temperature behavior of the MH_2XO_4 (M = Cs, Rb, NH_4, K; X = P, As) compounds, looking for ferroelectric transitions similar to that discovered in KH_2PO_4 at 123K[1]. It was found that the K, Rb, and Cs phosphates and arsenates all exhibited ferroelectric transitions with the average change in the transition temperatures upon isovalent substitution being[81]:

$$K \xrightarrow{\oplus 14\,K} Rb \xrightarrow{\oplus 36\,K} Cs \qquad (3\text{-}1)$$

$$PO_4 \xrightarrow{-40\,K} AsO_4$$

From this it seems clear that larger cations inhibit the ferroelectric transitions in this class of compounds.

After the discovery of the superprotonic phase transition in $CsHSO_4$ at 142°C, the high temperature properties of the entire class of compounds began to be examined[3]. In contrast to the results of the low temperature transitions, increased cation size was found to lower the superprotonic phase transitions, which were observed only in the compounds

with the largest cations, Table 3.1. The explanation for this phenomenon was generally held to be that the increased ionic radius of the cations resulted in larger X-X distances (X = S, Se, P, As), thereby creating more room for the nearly free rotations of the tetrahedra observed in the superprotonic phases[39]. The phosphate and arsenate compounds are not listed on Table 3.1 as only the Cs compounds undergo superprotonic phase transitions at 232 and 162°C for CsH_2PO_4 and CsH_2AsO_4, respectively[46]. Also, the $TlHSO_4$ compound is reported to have a superprotonic transition at 115°C, but its room temperature structure has not yet been reported and hence the coordination of the Tl cations is not known[82]. Since the ionic radius of the Tl ions varies from 1.76 to 1.60 in going from a coordination of XII to VIII, respectively, it is not appropriate to compare the properties of $TlHSO_4$ to those of the other $MHSO_4$ compounds until its structure is known.

Table 3.1 Superprotonic phase transitions for $MHXO_4$ class of compounds. The ionic radii of the cations are based on their average coordination (superscripted Roman numerals) in these materials. For the central ion of the tetrahedra, the covalent radii are given for a four-fold coordination[83].

Radius of M/X (Å)	S^{IV} 0.26	Se^{IV} 0.43	Ref
Cs^{X} 1.81	T_{sp} = 142 °C Mono, $P2_1/c \rightarrow$ Tetra, $I4_1/amd$	T_{sp} = 128 °C Mono, $P2_1/c \rightarrow$ Tetra, $I4_1/amd$	84 85
Rb^{VIII} 1.61	T_{sp} = 227 °C at 0.31 GPa Mono, $P2_1/c \rightarrow$? At 1 atm, T_{melt} = 203 °C	T_{sp} = 174 °C Mono, B2 $\rightarrow$ Mono, C_{2h}?	86 85,87 88
NH_4^{VIII} 1.59	T_{sp} = 177 °C at 1.77 GPa Mono, $B2_1/a \rightarrow$? At 1 atm, T_{melt} = 146 °C	T_{sp} = 144 °C Mono, B2 $\rightarrow$ Mono, $P2_1/b$?	89 90 91

As was seen in the ferroelectric transitions, substitution of a larger central ion in the tetrahedra lowers the superprotonic transition temperatures. This effect is evident in

the fact that under ambient conditions the Rb and NH_4 selenate compounds have superprotonic phase transitions before melting, whereas in the analogous sulfate compounds pressure must be applied to raise T_{melt} above that of T_{sp}[86]. Also, in the Cs phosphate and arsenate compounds, the transition temperature drops 60 degrees when the PO_4 groups are replaced by the larger AsO_4 tetrahedra. These results are at odds with the statement that larger cations increase the volume in which the tetrahedra reorient since one would then expect the bigger tetrahedra to require coordination by proportionally larger cations for a superprotonic transition to be feasible. However, exactly the opposite result is measured. The underlying cause for the observed behavior was therefore not clearly understood with the limited number of data points given in Table 3.1, although the overall effect of increasing the size of the cation and/or the tetrahedral ion is clearly to promote superprotonic phase transitions in these compounds.

This work was carried out to better explain this connection between cation/tetrahedral ion size and the presence of superprotonic transitions. The approach taken was to synthesize compounds with mixed M^{+1} ions and thereby vary the average cation size. Unfortunately, attempts to grow selenate compounds categorically failed; the normal (and even abnormal) synthesis routes resulting in, almost exclusively, the M_2SeO_4 salts. Also, the phosphate and arsenate compounds were avoided due to the known instability of the superprotonic phases of the pure cesium compounds[92,93]. Hence, attention was focused on mixed cation sulfate compounds.

3.2 Mixed Cation Sulfate Systems

Attempts to deduce the correlation between a compound's average cation size and the presence/absence of a superprotonic phase transition started with investigations into

the mixed Cs/K, Cs/Na, and Cs/Li systems. The emphasis on Cs is for the obvious reason that $CsHSO_4$ has a known superprotonic transition. On the other hand, the K, Na, and Li hydrogen sulfate compounds all melt/decompose without transforming to a highly conductive phase[94-96]. Therefore, replacing some of the Cs atoms with the smaller alkali cations in $CsHSO_4$ was hoped to have quite dramatic and quantifiable effects on the superprotonic transition. Mixed Cs/Rb compounds were not explored as the Cs/Rb system had already been investigated resulting in two new compounds, $Cs_{0.9}Rb_{0.1}HSO4$ and $Cs_{0.1}Rb_{0.9}HSO4$, which can be considered as structural modifications of end members $CsHSO_4$ (phase II) and $RbHSO_4$, respectively[97,98]. The high temperature properties of these compounds are nearly unchanged from those from which they were derived, namely the cesium rich compound has a superprotonic transition ~ 142°C, while the rubidium rich compound exhibits no high temperature transition before melting ~ 177°C[99]. These compounds then confirm that a larger average cation radius encourages superprotonic transitions, but do not further illuminate the fundamental correlation between the two parameters since the structures and properties are nearly identical to those of the end-member compounds.

Mixed Cs/NH_4 compounds were avoided as the presence of the NH_4 cations is known to cause markedly different properties in solid acids. For example, the $(NH_4)_3H(SeO_4)_2$ compound has a superprotonic phase transition at 27°C, whereas the isostructural K and Rb compounds have transitions at 115° and 185°C, respectively[100,101]. Also, note that the NH_4HSeO_4 compound transforms to the superprotonic phase 30 degrees lower than the RbHSeO4 compound, Table 3.1. This anomalous behavior is attributed to the fact that the hydrogen atoms of the ammonium ions often form hydrogen

bonds to the tetrahedral oxygen atoms and that the NH_4 groups typically show some degree of disorder at room temperatures[102-104]. The bonding of the ammonium cations will therefore be highly directional and/or highly variable when compared to the purely electrostatic interactions of the spherical alkali metal cations. Analysis of any mixed Cs/NH_4 compounds would be complicated by such considerations, it being difficult to resolve the cation size effect from the ammonium ion effect on a phase transition, and therefore their synthesis was not attempted.

For the above reasons, only the mixed Cs- K/Na/Li systems were investigated. These systems also had the additional advantage in that there is a large difference between ionic radius of Cs versus K, Na, and Li. It was hoped that this difference would highlight the essential structural properties associated with large cations and superprotonic phase transitions. It should be mention here that the synthesis and characterization of all the mixed systems Cs/M^{+1} mentioned here have been reported by other researchers (primarily Mhiri et al.). The published results suggest that solid solutions of the mixed cations are possible and that often the high temperature properties gradually change from those of $CsHSO_4$ to those of the $MHSO_4$ compound in question. This is in complete disagreement with the results of the present work and seems highly implausible as none of the other $MHSO_4$ compounds are isostructural to $CsHSO_4$. Moreover, except for work on crystals whose structure had been determined (e.g., $Cs_{0.9}Rb_{0.1}HSO_4$ and $Cs_{0.1}Rb_{0.9}HSO_4$), these investigations analyzed powder samples created by grinding together crystals grown by aqueous synthesis[99,105,106 107]. It is therefore not very surprising that they found very smooth changes in properties as the percentage of substitutant M^{+1} cation in the solutions was increased. Also, the techniques

used to characterize the powders measured only the average properties of the samples: powder X-ray diffraction, Raman spectroscopy, differential scanning calorimetry, and conductivity measurements of pressed powder pellets. For these reasons, this work will not refer to these investigations.

3.2.1 Synthesis and Characterization Techniques

Crystals examined in these mixed cation systems were synthesized by mixing the appropriate amounts of the metal carbonates (Alpha Aesar puratonic, assay 99.999%) and sulfuric acid (98% aq. sol.) in an aqueous solution, followed by slow evaporation at room temperatures:

$$(1\text{-}x)*Cs_2CO_3 + (x)*M_2CO_3 + H_2SO_4 + H_2O \xrightarrow{\sim 25^\circ C} \text{single crystals}$$

where M = K, Na, or Li and the total cation to anion ratio, (Cs+M):SO_4, was held at 1:1. This process was carried out in 10% molar increments of the secondary cation, M, except where the discovery of new compounds merited a smaller increment of 5%.

The phases of the resulting single crystals were identified by single-crystal X-ray diffraction (SCXD) techniques. Differential scanning calorimetry (DSC) and thermal gravimetric analysis (TGA) were used to measure the thermal properties of the single-crystals at elevated temperatures. Finally, conductivity measurements on single crystals, or single crystals ground-up and pressed into pellets, were performed to confirm the presence/absence of a superprotonic transition and to compare with the conductivity of $CsHSO_4$. The emphasis here is that whenever possible, only single-crystal samples were grown and only single-crystal samples were analyzed.

3.2.2 Resulting Phases of the Mixed System Investigations

The above synthesis route resulted in the compounds listed in Table 3.2. At very high cesium percentages, slight modifications to $CsHSO_4$-III, the meta-stable phase of $CsHSO_4$ that grows out of aqueous solutions, were discovered for all three systems. The evidence for incorporation of the smaller cations into $CsHSO_4$-III was first seen in the SCXD measurements. The lattice constants of the modified structures were nearly identical to that of $CsHSO_4$-III, in an alternative primitive cell, but with the length of the c-axis tripled compared to the pure compound. This primitive cell is transformed into the crystallographically correct cell of undoped $CsHSO_4$-III by the transformation: a′ = a – ½*c, b′ = b, c′ = 2*c. The amount of K, Na , and Li incorporated into $CsHSO_4$-III's structure is quite small as full data collections were not able to locate the ions although they did confirm the tripling of the c-axis. It would appear that the smaller cations are substituted on the Cs sites where they are hidden by cesium's much larger scattering factor for X-rays[108]. In a similar manner, electron microprobe measurements were unable to observe the lighter cations.

For the Na compound, both Na^+ and H^+ NMR measurements were performed. A very small peak in the Na^+ NMR measurement was observed, but it was impossible to rule out small amounts of Na contaminants as the cause of this peak. The proton NMR measurements were more conclusive, in that two distinct peaks of significant magnitude were observed for the doped sample, whereas the scan of the reference, undoped, $CsHSO_4$ sample showed only one peak (see appendix A). The sodium ions then again

Table 3.2 Compounds synthesized in the mixed Cs-K/Na/Li systems. The average cation radius was calculated using both the ratio and particular coordination of the cations in a compound.

System	Solution Composition % M_2CO_3	Compound Obtained	Space Group or Symmetry	Lattice Parameters	Average Cation Radius	Phase Transitions Above RT	Comments and References
All Systems	0	$CsHSO_4$-III	$P2_1/n$	a = 8.229(2) Å, b = 5.8163(9) Å c = 9.996(3) Å, β = 106.46(2)°	1.81 Å	~ 62°C→$CsHSO_4$-II; 142 °C→supeprotonic	a [109]
$CsHSO_4$–$KHSO_4$	10-30	α-$CsHSO_4$-III	$P2_1$(?)	a = 7.311(5) Å, b = 5.818(4) Å c = 16.52(2) Å, β = 101.55(4)º	~ 1.81 Å	~ 67°C→$CsHSO_4$-II?; 140 °C→supeprotonic	New modification of $CsHSO_4$–III
	40	α-$CsHSO_4$-III & $K_3H(SO_4)_2$					
	50-100	$K_3H(SO_4)_2$	A2/a	a = 9.790(4) Å, b = 5.682(2) Å c = 14.702(4) Å, β = 103.02(5)º	1.51 Å	190 °C→supeprotonic 190 °C→supeprotonic	a; b [23,110]
$CsHSO_4$–$NaHSO_4$	5-10	β-$CsHSO_4$-III	$P2_1/m$	a = 7.329(5) Å, b = 5.829(4) Å c = 16.52(1) Å, β = 101.55(3)º	~ 1.81 Å	~73°C→$CsHSO_4$-II?; 141 °C→supeprotonic	New modification of $CsHSO_4$–III
	15-35	$Cs_2Na(HSO_4)_3$	$P6_3/m$	a = 8.572(2) Å c = 9.982(2) Å	1.55 Å	139°C→melt	**new compound** [25,111]
	40	$Cs_2Na(HSO_4)_3$ & $CsNa_2(HSO_4)_3$					
	45-55	$CsNa_2(HSO_4)_3$	$P2_13$	a = 10.568(2) Å	1.28 Å	125°C→melt	**new compound** [25,111]
	60-100	$NaHSO4{\cdot}H_2O$					a
$CsHSO_4$–$LiHSO_4$	10	γ-$CsHSO_4$-III	$P2_1$(?)	a = 7.316(10) Å, b = 5.818(7) Å c = 16.50(2) Å, β = 101.54(5)º	~ 1.81 Å	~108°C→$CsHSO_4$-II?; 141 °C→supeprotonic	New modification of $CsHSO_4$–III
	20-80	$Cs_2Li_3H(SO_4)_3 \bullet H_2O$	$Pbn2_1$	a = 12.945(3) b = 19.881(4) c = 5.111(1)	1.08 Å	105°C→slow decomposition	**new compound**
	90-100	$Li_2SO_4 \bullet H_2O$					a

a) Compound previously known.
b) High temperature properties not previously investigated.

revealed their presence indirectly through their effect on the surrounding structure, in this case, the environment of the protons.

The incorporation of the K, Na and Li ions also showed up in the DSC measurements. Upon heating the modified forms of $CsHSO_4$-III, the transition to $CsHSO_4$-II (another monoclinic form) was observed to be systematically shifted to higher temperatures as the size of the secondary cation decreased, Figure 3.1 a. Also, for the Cs/Na compound, β-$CsHSO_4$-III, two exothermic transitions instead of only one where observed upon cooling, Figure 3.1 b. For this reason, the β-$CsHSO_4$-III compound was more extensively studied than the others. Conductivity measurements along the b-axis revealed three, rather than two transitions, Figure 3.1 c. This discrepancy between the DSC and conductivity results is probably due to sample size, i.e., very small crystals and very large crystals were used in the DSC and conductivity measurements, respectively. Low temperature DSC measurements also revealed an apparently second order transition at -123.25°C not found in $CsHSO_4$, Figure 3.1d[112].

The temperature of the superprotonic phase transition, however, was not significantly effected by the small amounts of K, Na, and Li present, Figure 3.1 a, although the transition enthalpy was consistently lower for the mixed $CsHSO_4$-III compounds (see appendix A). These compounds, as was the case with $Cs_{0.9}Rb_{0.1}HSO_4$, do little to illuminate the cation size effect: their superprotonic phase transitions and structures being essentially identical to those of $CsHSO_4$. On the other hand, they do reveal how sensitive these solid acids are to the addition of a secondary cation. In fact, trace levels would appear to be the upper solubility limit for K, Na, and Li in $CsHSO_4$

(and vice versa), the rest of the crystals synthesized being either line compounds or compounds with a single type of cation, Table 3.2.

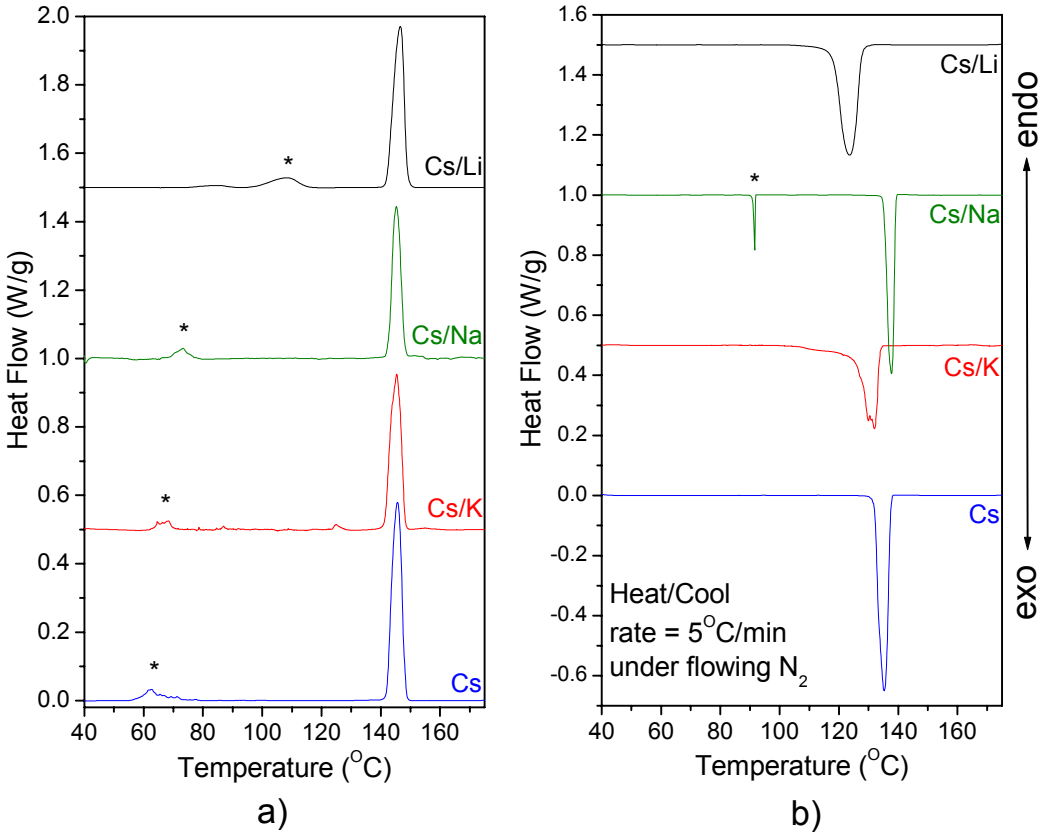

Figure 3.1 (See figure caption on next page.)

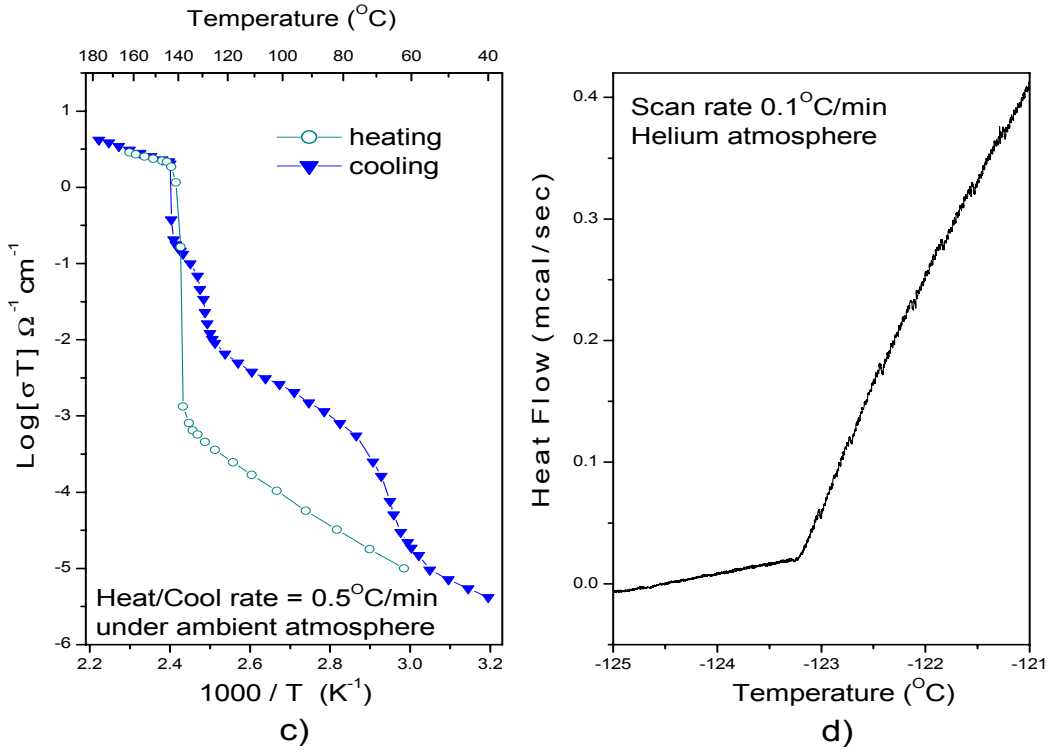

Figure 3.1 Measurements on the α, β, γ-$CsHSO_4$-III compounds. DSC curves upon heating, a), and cooling, b) for all three modified forms of $CsHSO_4$-III. Also, b-axis conductivity and low temperature DSC measurements for the Na compound, c) and d), respectively. Figure a) shows an increase in the phase III-II transition temperature with K to Na to Li substitution. The difference of the Na compound from pure $CsHSO_4$ is shown in its two and three reverse transitions visible in the DSC, b), and conductivity data, c), as well as the presence of a low temperature (apparently second order) transition, d). Experimental parameters given on graphs.

For the Cs/K system, this insolubility phenomenon is particularly easy to see in that only α-$CsHSO_4$-III and $K_3H(SO_4)_2$ crystals grew from the solutions. The $K_3H(SO_4)_2$ compound belongs to another class of superprotonic conductors with general formula $M_3H(XO_4)_2$ (M = Cs, Rb, NH_4, K, Na and X = S, Se). This compound had been previously synthesized and its structure determined, but its high temperature properties had not been sufficiently investigated[23]. Our studies revealed $K_3H(SO_4)_2$ to have two high temperature transitions before decomposition, both of which are superprotonic in nature

and neither of which are analogous to the superprotonic transitions found in the other $M_3H(XO_4)_2$ compounds[110]. Typically, these transitions involve very small structural changes from pseudo-trigonal to trigonal unit cells, with superprotonic conduction primarily in the basal planes[100]. The tetrahedra in the superprotonic phases do not undergo true rotations, but simply librate around a site with C_3 symmetry[113]. These librations primarily effect the positions of basal plane oxygen atoms, hence the anisotropic proton conduction of the phases. It is therefore not appropriate to compare the superprotonic transitions of the $M_3H(XO_4)_2$ compounds to those of the $MHXO_4$ compounds, and so the results for $K_3H(SO_4)_2$ will not be included in this work.

The Cs/Li system resulted in a new mixed compound, $Cs_2Li_3H(SO_4)_3 \cdot H_2O$. DSC, TGA and conductivity measurements show no evidence for a superprotonic transition before the start of decomposition above 105°C (see appendix A). The lack of a superprotonic transition is not surprising as the average radius for the four- and tenfold oxygen coordinated lithium and cesium ions, respectively, is 1.078 Å[83]. Also, as this compound is hydrated and has a cation to tetrahedra ratio of 5:3 (instead of the desired 1:1 ratio), any correlations between its structure and properties are not particularly pertinent to the present discussion.

Fortunately, the Cs/Na system did produce two new mixed solid acids in the $MHXO_4$ family with chemical formulas of $Cs_2Na(HSO_4)_3$ and $CsNa_2(HSO_4)_3$[25]. The unit cell of $Cs_2Na(HSO_4)_3$ is hexagonal while that of $CsNa_2(HSO_4)_3$ is cubic, both novel symmetries for the room temperature structures of the $MHXO_4$ compounds. Moreover, the single asymmetric hydrogen bond in both compounds links the SO_4 groups into unique three-membered $(HSO_4)_3$ rings. These rings are most likely due to the Na atom's

preference for a 6-fold oxygen coordination, with the resulting NaO_6 octahedra serving as a template for the $(HSO_4)_3$ units[22]. The Cs atoms in both compounds reside in irregular polyhedra with a coordination of 9 to 12 oxygens, depending on the upper limit one sets for the Cs-O bonds. The rings in $Cs_2Na(HSO_4)_3$ are linked together by NaO_6 octahedra to form infinite $Na(HSO_4)_3$ chains that extend along [001], Figure 3.2 a and b, while in $CsNa_2(HSO_4)_3$ the rings form a distorted cubic close-packed array. In this array, the Cs atoms are located within the "octahedral" sites and the Na atoms within the "tetrahedral" sites, Figure 3.2 c and d.

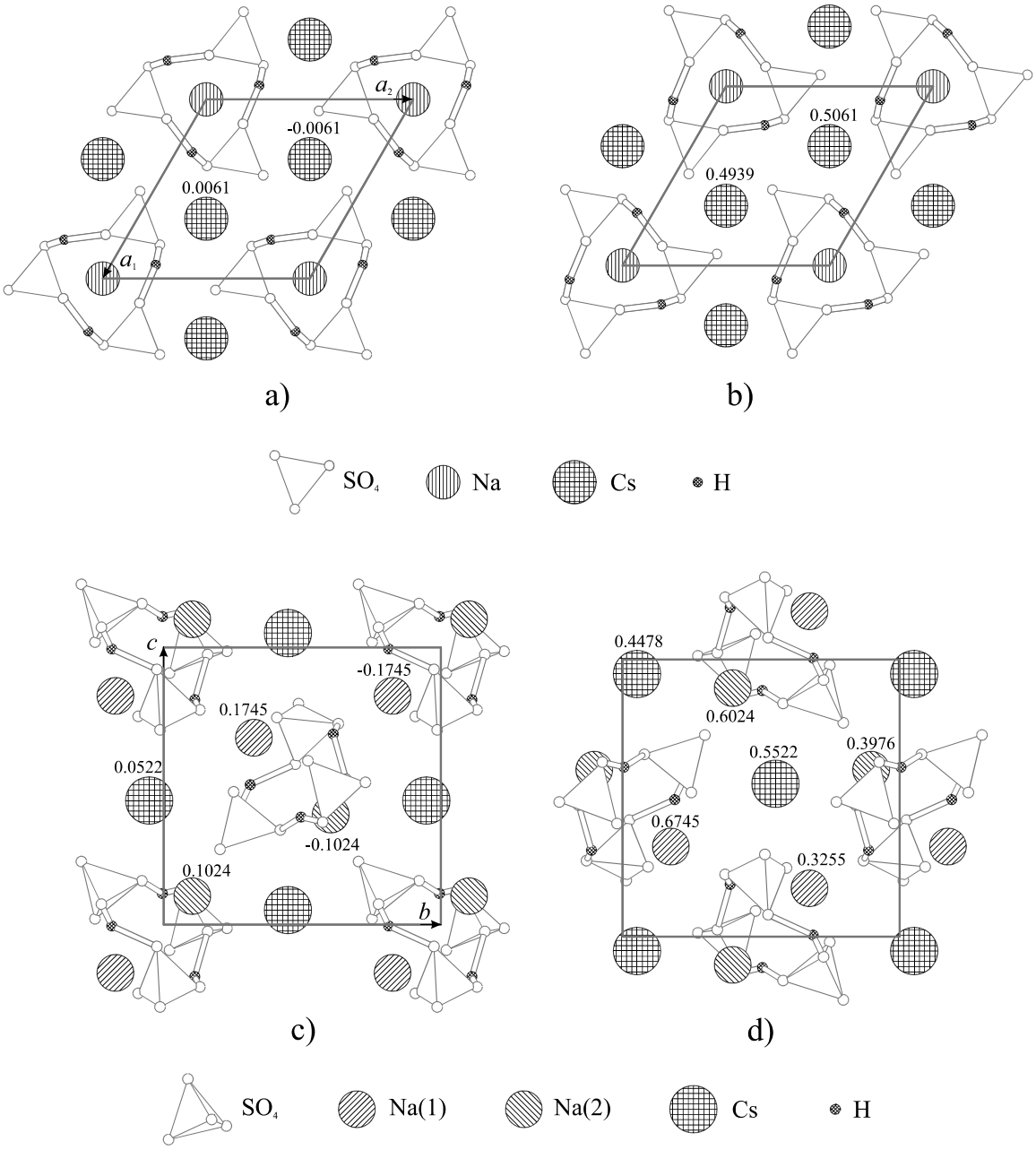

Figure 3.2 Crystal structures of the mixed Cs/Na compounds. The hexagonal structure of $Cs_2Na(HSO_4)_3$ is projected down [001]: a) unit cell contents from z = 0 to ½ and b) from z = ½ to 1. Sodium atoms have elevations of z = 0 and ½, while those of the cesiums are as indicated. Cubic structure of $CsNa_2(HSO_4)_3$ projected along [100]: c) unit cell contents from x = -¼ to +¼ and d) from x = +¼ to ¾. Elevation of cations as indicated. Some oxygen atoms have been omitted for clarity[25].

Neither of these compounds undergoes a superprotonic phase transition before melting at 139 and 125°C for $Cs_2Na(HSO_4)_3$ and $CsNa_2(HSO_4)_3$, respectively, as

established by thermal analysis and visual inspection. The DSC curves for the compounds are shown in Figure 3.3, along with conductivity measurements which show the compounds to be fairly poor protonic conductors despite their high crystalline symmetry.

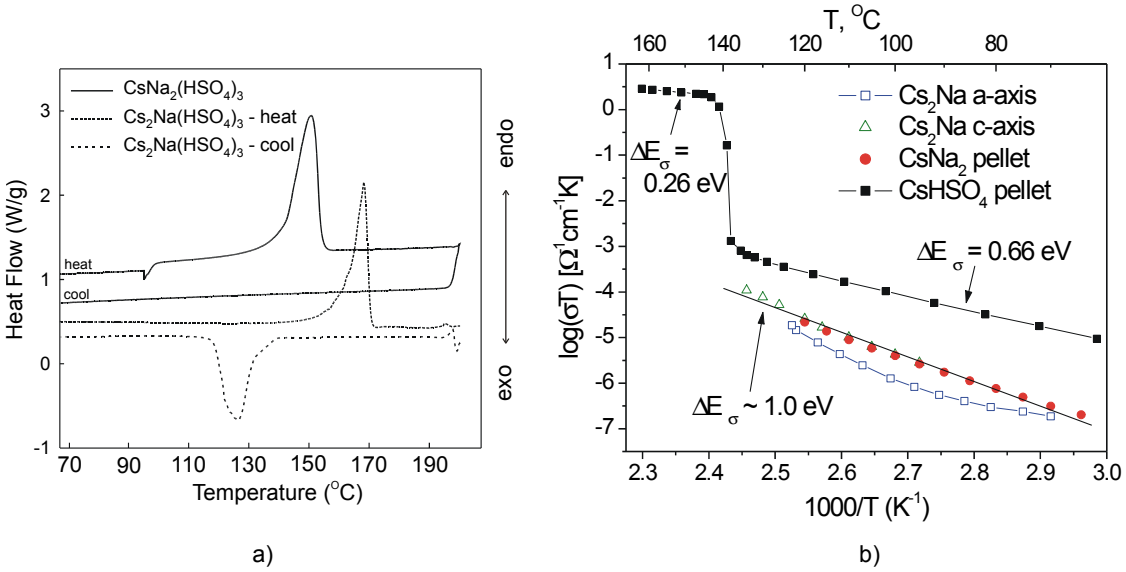

Figure 3.3 a) DSC and b) conductivity measurements on $Cs_2Na(HSO_4)_3$ and $CsNa_2(HSO_4)_3$. Figure a) shows the melting transitions of the compounds beginning at 139 and 125°C, respectively. The cooling curve for $CsNa_2(HSO_4)_3$ does not reveal a solidification peak, which is in agreement with visual observations that the compound solidifies as a glass upon cooling from the melt. Conductivity measurements revealed the compounds' protonic conductivity to be lower and activation energy higher than that of $CsHSO_4$'s room temperature phase. The observed curvature in the conductivity of $Cs_2Na(HSO_4)_3$'s a-axis is likely due to the onset of melting. DSC and conductivity measurements taken under flowing N_2 and dry argon atmospheres, respectively, with heating/cooling rates of 10°C/min and 0.5°C/min, respectively.

3.2.3 Conclusions from Mixed System Investigations

Studies into the mixed $CsHSO_4$-K/Na/$LiHSO_4$ systems have resulted in six new compounds, two of which are appropriate with the other $MHXO_4$ compounds. Three of the compounds (α, β, γ-$CsHSO_4$-III) are slight modifications of $CsHSO_4$-III, with

correspondingly small changes to the structural and superprotonic parameters of the parent compound. Analysis of these compounds with respect to the cation-size/superprotonic-transition correlation tells us little we did not already know from $CsHSO_4$ itself. On the other hand, the new solid acid discovered in the Cs/Li system, $Cs_2Li_3H(SO_4)_3 \cdot H_2O$, has a very different structure from the other $MHXO_4$ compounds. However, this compound also has a cation to anion ratio of 5:3 and is hydrated, both properties which any cation-size effect conclusions drawn from this compound unsuitable for comparision with those of the $MHXO_4$ family of compounds.

Hence, the only compounds synthesized of use to the present discussion are the mixed Cs/Na compounds, $Cs_2Na(HSO_4)_3$ and $CsNa_2(HSO_4)_3$. Using the structures of these two compounds as well as those of the other $MHSO_4$ compounds, we can create a graph that depicts the changes to the characteristic distances of the crystals as a function of the average cation radius, Figure 3.4. These distances act as crystal-chemical measures of the cations' role in the presence or absence of a superprotonic phase transition. Such distances include the mean S-S, M-S, M-M, and M-O distances and the effective length per formula unit (taken as the cube root of the volume per $MHSO_4$ unit). The trend of the mean S-S distance with cation radius is of particular interest because, as mentioned earlier, the general consensus is that large X-X distances are necessary to lower anion-anion interactions and thereby promote the rapid XO_4 reorientations of the superprotonic phases[35]. The most salient feature of Figure 3.4 is then that the average S-S distance in $Cs_2Na(HSO_4)_3$ is larger than that of $CsHSO_4$. This result suggests that either the XO_4 to XO_4 interactions are not critical to superprotonic transitions, or that the <X-X> distance

is not a useful measure of such interactions. The same can be said of the <M-M> distance as that of $Cs_2Na(HSO_4)_3$ is also larger than that found in $CsHSO_4$.

On the other hand, the average M-S, M-O and $V^{1/3}$ distances all scale with the mean cation radius. Of these three distances, the M-S distance varies much more across the no-transition/transition line than the other two. This tends to confirm the observation derived from the effects of substituting Se for S in the Cs, Rb, and NH_4HXO4 compounds (Table 3.1) that the M-X distance reflects a truly critical crystal-chemical parameter with respect to superprotonic phase transitions. Of course, these results do not exclude the possibility that the M-O and $V^{1/3}$ distances are of equal or more importance than the M-X distance.

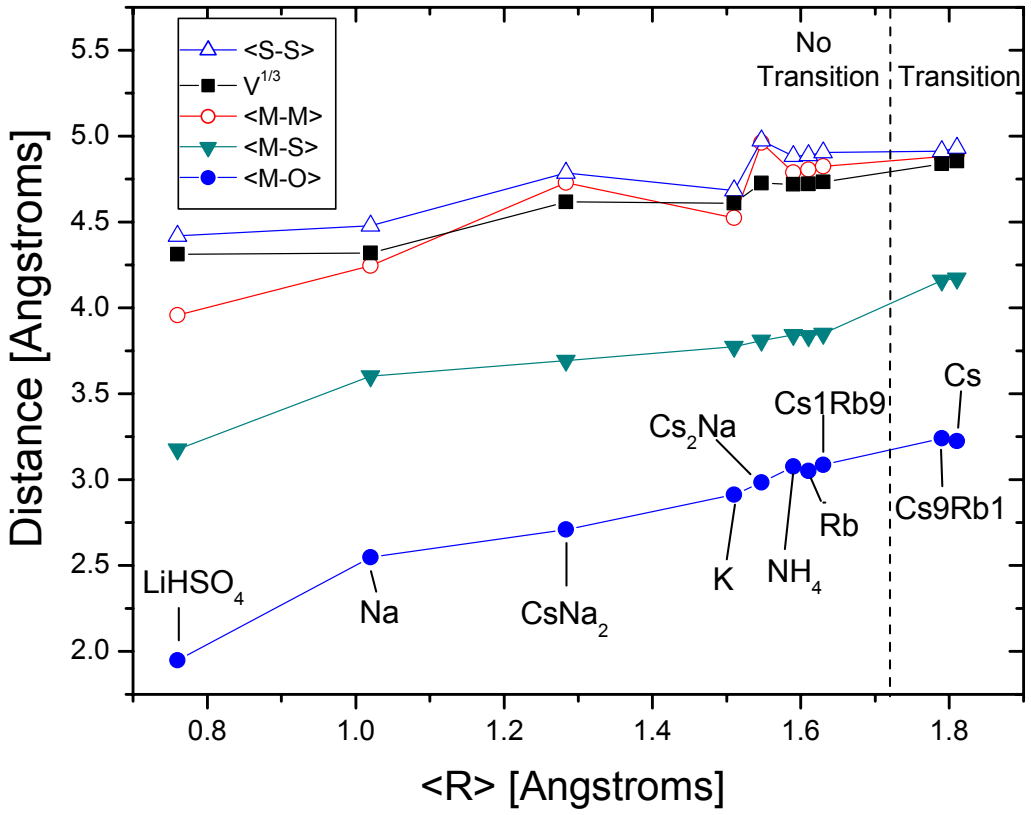

Figure 3.4 Characteristic lengths of $MHSO_4$ compounds as a function of average cation

radius. Crystallographic data taken from the following sources: $LiHSO_4$, [114]; α-$NaHSO_4$, [115]; $CsNa_2(HSO_4)_3$, [25]; $KHSO_4$, [24]; $Cs_2Na(HSO_4)_3$, [25]; NH_4HSO_4, [116], $RbHSO_4$, [117]; $Cs_{0.1}Rb_{0.9}HSO_4$, [98]; $Cs_{0.9}Rb_{0.1}HSO_4$, [97]; $CsHSO_4$-II, [26].

Another distance of possible significance is the average O-O distance of the hydrogen bonds in these solid acids. This distance is proportional to the energy associated with a compound's hydrogen bonds. As the energy of a hydrogen bond exponentially increases with decreasing O-O distance, shorter hydrogen bonds will require much more energy to break than longer bonds[21]. One would then expect that the presence of longer (weaker) hydrogen bonds would favor a compound transforming to a superprotonic phase, where these bonds will have to be continually broken and reformed as the tetrahedra reorient. Moreover, the hydrogen bonds of the superprotonic phases are nearly always longer than those below the transition[35]. Therefore, shorter bonds at room temperature should increase the required transition enthalpy to the high temperature phase. Nevertheless, in plotting the mean hydrogen bond O-O distance versus average cation radius, Figure 3.5, there is no apparent relationship between the hydrogen bond lengths and the presence of a superprotonic transition. This is concluded from the fact that $LiHSO_4$, $NaHSO_4$, $CsNa_2(HSO_4)_3$, and $Cs_2Na(HSO_4)_3$ all have longer $\langle O\text{-}O \rangle_{HBOND}$ distances than $CsHSO_4$ and $Cs_{0.9}Rb_{0.1}HSO_4$.

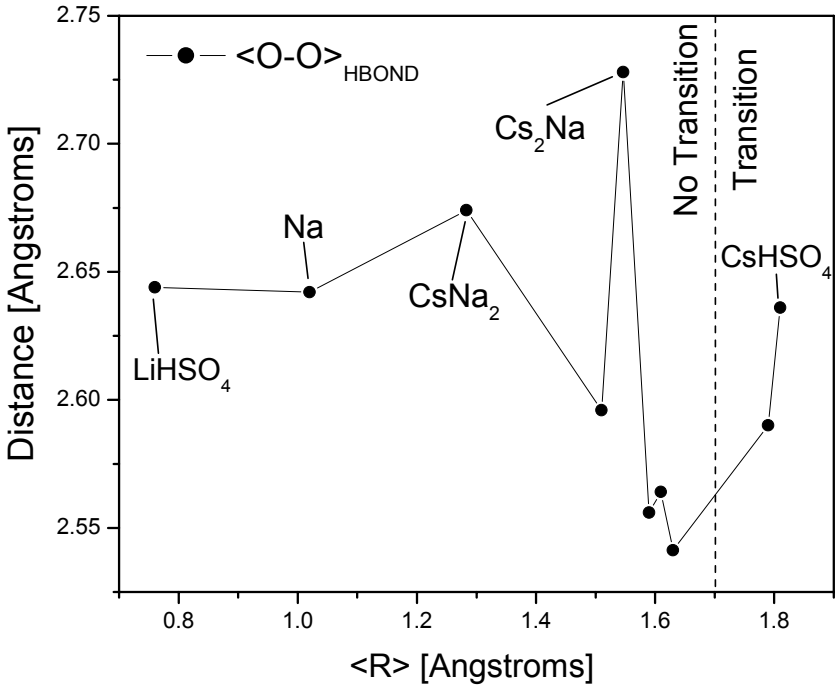

Figure 3.5 Average hydrogen bond length versus mean cation radius. The Li, Na, $CsNa_2$ and Cs_2Na compounds all have an average hydrogen bond length longer than that of $CsHSO_4$. This fact suggests it would require a smaller loss in hydrogen bond energy for these compounds to transform to a superprotonic phase compared to $CsHSO_4$.

There is, however, a problem to the above comparisons and the conclusions drawn from them, which is simply that the structures of the compounds are not the same. In particular, the mixed Cs/Na compounds are quite different from the other compounds. First, the unit cell symmetries of $CsNa_2(HSO_4)_3$ and $Cs_2Na(HSO_4)_3$ are cubic and hexagonal, respectively, versus the monoclinic or tetragonal cells found in the other $MHSO_4$ compounds. Second, the alternating rows of anions and cations almost always observed in the MHSO4 compounds are replaced with either the channels or FCC-like array of the mixed Cs/Na compounds[31]. Finally, the way in which the tetrahedra are connected by hydrogen bonds in $CsNa_2(HSO_4)_3$ and $Cs_2Na(HSO_4)_3$, into three-membered

rings, is completely unique for the $MHSO_4$ family of compounds. It is then possible that the properties of the mixed Cs/Na compounds are due to their unique structures, making a comparison with the other $MHSO_4$ compounds less than ideal.

A rigorous application of this argument also invalidates the comparison between the remaining $MHSO_4$ compounds for all but $RbHSO_4$ and NH_4HSO_4, which are isostructural to each other[118]. This fact is particularly evident when evaluating the hydrogen bond lengths, which are very much connected to the types of hydrogen bonds (single or double minimum; fully or partially occupied) and hydrogen-bonded networks (dimers, rings, or chains) present in the compounds. As seen in Table 3.3, the differing structures of the $MHSO_4$ compounds result in their having a broad distribution of hydrogen bond types and networks, possibly explaining the seemingly random trend seen in Figure 3.5.

Table 3.3 Hydrogen bond parameters for the MHSO4 compounds. Single, double and partial hydrogen bond types refer to ordered single minimum, disordered double minimum and partially occupied hydrogen bonds, respectively. Shaded cells denote isostructural compounds.

Compound	Space Group	Mean O-O distance	Types of H-bonds present	H-bonded networks present	ref
$LiHSO_4$	$P2_1/c$	2.644	Single	Chains	114
α-$NaHSO_4$	$P\bar{1}$	2.642	Single, double, partial	Branched chains	115
$CsNa_2(HSO_4)_3$	$P2_13$	2.674	Single	Rings	25
$KHSO_4$	Pbca	2.596	Single, double	Dimers, chains	24
$Cs_2Na(HSO_4)_3$	$P6_3/m$	2.728	Single, partial?	Rings	25
NH_4HSO_4	$B2_1/a$	2.556	Single, partial	chains	116
$RbHSO_4$	$P2_1/c$	2.564	Single, partial	chains	117
$Cs_{0.1}Rb_{0.9}HSO_4$	$P2_1/c$	2.541	Single, double	Chains	98
$Cs_{0.9}Rb_{0.1}HSO_4$	$P2_1$	2.59	Single	Chains	97
CsHSO4-II	$P2_1/c$	2.636	Single	Chains	26

The conclusions drawn from this work on the mixed Cs-K/Na/LiHSO$_4$ systems in conjunction with the other MHSO$_4$ compounds therefore concur with the initial observations that the <M-X> distance seems to be a critical crystal-chemical measure of whether a compound will have a superprotonic transition or not, rather than the X-X or other characteristic distances in the compounds. However, a plausible argument against this result is that the underlying structural differences in the compounds *may* have a much more important role in determining the presence/absence of a transition than either the cation or anion size effect. To deconvolute any structural effects from the cation/anion size effect, it is necessary to find a system of compounds that remained isostructural while the size of the cation/anion is changed. The results from such a system would complement those of the above mixed systems, the problem having being approach from both top and bottom, so to speak. If the same trends were observed, it would conclusively confirm the M-X distance as the critical parameter in predicting superprotonic phase transitions. Luckily, just such a system exists.

3.3 $M_2(HSO_4)(H_2PO_4)$ Compounds

The $M_2(HSO_4)(H_2PO_4)$ compounds are isostructural for M = K, NH_4, Rb, and Cs (Table 3.4), the Cs compound being discovered during the investigations of the $CsHSO_4$-CsH_2PO_4 system (Chapter 4). Characterization of $Cs_2(HSO_4)(H_2PO_4)$ showed it to have a superprotonic phase transition in the range of 61 to 110°C[63]. On the other hand, the properties of the other M_2 compounds at elevated temperatures were not known. The combination of these compounds being isostructural and having a known superprotonic transition makes this system ideal for exploring the cation size effect irrespective of structure.

3.3.1 Structures of the $M_2(HSO_4)(H_2PO_4)$ compounds

These compounds crystallize in a monoclinic unit cell, space group $P2_1/n$, with two formula units per cell. Their lattice parameters and other crystallographic data are listed in Table 3.4. Each compound has six crystallographically distinct, non-hydrogen atom sites: one for the M^{+1} cations, four for the oxygen atoms and one site on which the S and P atoms are evenly distributed. The structures consist of loosely defined MO_x polyhedra and well-defined XO_4 tetrahedra. For the K, NH_4 and Rb compounds the cations are coordinated by nine oxygens, while the Cs compound has CsO_{10} polyhedra. These coordination numbers are not particularly well defined as they depend to a great deal on the upper limit one puts on the M-O bonds. However, using the published coordination numbers, the ionic radii of the cations are 1.55, 1.61, 1.63, and 1.81 Å, for K, NH_4, Rb, and Cs, respectively[83]. Here, the radius of the ammonium cations has been scaled with those of the rubidium ions for the sake of consistency with the previous section and because it is difficult to calculate a spherical radius for these cations due to the presence of highly directional N-H-O hydrogen bonds[119]. Considering that the NH_4 compound's volume is slightly larger than the Rb's, it might be closer to the truth if the $R_{NH4} > R_{Rb}$, but as the difference between the compounds is minimal, setting $R_{NH4} < R_{Rb}$ should make little to no difference in the analysis.

Table 3.4 Crystallographic data for the $M_2(HSO_4)(H_2PO_4)$ compounds

Cation	Space Group	a (Å)	b (Å)	c (Å)	β (Å)	Vol. (Å^3)	Z	D_{calc} (g/cm^3)	Radius M_2 (Å)	ref
Cs	$P2_1/n$	7.856	7.732	7.827	99.92	468.3	2	3.261	1.81	[27]
Rb	$P2_1/n$	7.632	7.552	7.448	100.47	422.1	2	2.872	1.63	[120]
NH_4	$P2_1/n$	7.723	7.540	7.482	101.32	427.2	2	1.789	1.61	[119]
K	$P2_1/n$	7.434	7.341	7.148	99.56	384.7	2	2.350	1.55	[121]

The M-O and X-O distances in these compounds are all quite regular. For $Cs_2(HSO_4)(H_2PO_4)$, the mean Cs-O distance is 3.27 Å, with a low of 3.055(4) and high of 3.622(4) Å, giving a calculated bond sum of 1.10. The bond valence sum at the X cation site is 5.51, in good agreement with the value of 5.5 predicted from a site occupancy of 0.5 S^{6+} and 0.5 P^{5+}. The tetrahedral angles for this compound range from 107.1(2) to 112.6(3)°, as expected for PO_4 and SO_4 anions[27]. The average X-O distance varies very little with the nature of the cation: the K, NH_4, Rb, and Cs compounds having values of 1.508, 1.506, 1.505, and 1.503 Å, respectively. These values all lie between those typically encountered in PO_4 and SO_4 tetrahedra, ~1.52 and ~1.47 Å, respectively, agreeing with the assignment of a completely mixed S/P occupancy on the X site[83].

More confirmation of this mixing on the X site is evident in the fact that each XO_4 group is involved in exactly three hydrogen bonds, the mean value of the two and four bonds expected for HSO_4 and H_2PO_4 tetrahedra, respectively. Two of these hydrogen bonds connects the XO_4 tetrahedra into zigzag chains running in the [010], while the third bond cross-links the chains into sheets that lie in parallel (-101), Figure 3.6 a) for $Cs_2(HSO_4)(H_2PO_4)$. The hydrogen bonds of the chains are ordered (single minimum potential), while the cross-linking bonds are disordered (double minimum potential). The zigzag chains of hydrogen-bonded tetrahedra alternate with rows of M^{+1} cations to give a checkerboard pattern, shown for the Cs compound in Figure 3.6 b.

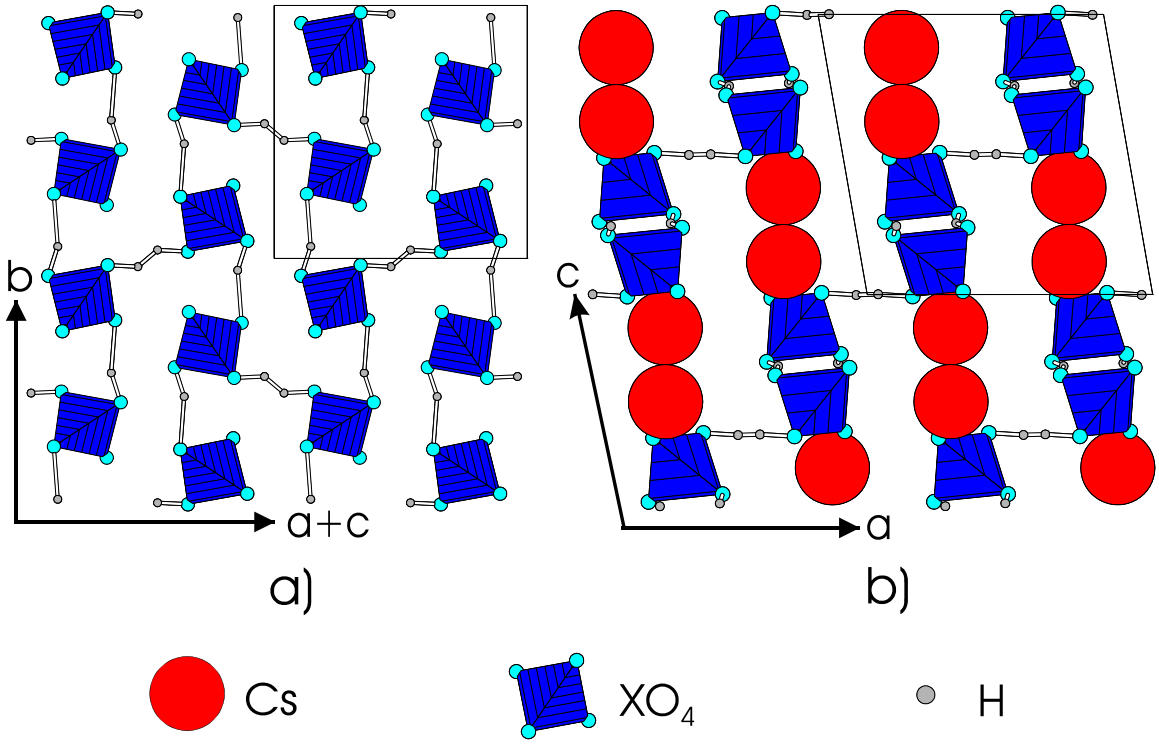

Figure 3.6 Structure of $Cs_2(HSO_4)(H_2PO_4)$: a) the sheets of hydrogen bonded tetrahedra in the (-101) plane with zigzag chains running in [010] and cross-linking hydrogen bonds connecting the chains in [100]. A projection down [010], b), shows the checkerboard arrangement of anion and cation rows as well as the sheets of tetrahedra extending along [101][27]. A unit cell is outlined in each picture.

High temperature X-ray powder diffraction and infrared spectroscopy revealed that the high temperature phase of $Cs_2(HSO_4)(H_2PO_4)$ is cubic, with $a_o = 4.926(5)$ Å. The suggested symmetry of the unit cell is $Pm\bar{3}m$, in which the compound would take on a CsCl structure, with Cs atoms at the corners of a simple cubic unit cell, and the XO_4 groups at the center, Figure 3.7[63]. The coordinates for the Cs and X atoms are therefore 0 0 0 and ½ ½ ½, respectively. The oxygen atoms were placed at ½ ¼ 0.323 based on X-O and Cs-O distance considerations. The single, crystallographic oxygen resides on a 24*l* site, resulting in 6 orientations of the XO_4 tetrahedra. Rapid librations between these orientations, facilitating proton transport between the tetrahedra, are thought to result in

the high conductivity of this phase, a nearly identical process being known to occur in the superprotonic phase of $CsHSO_4$[60].

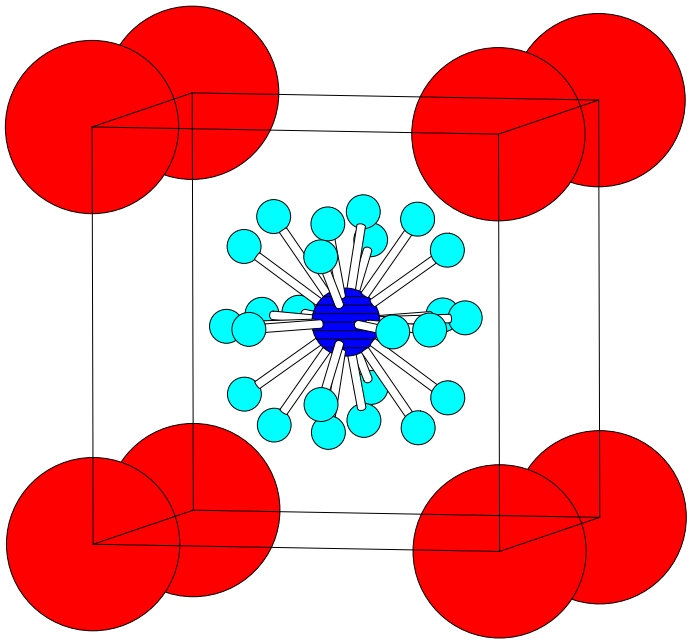

Figure 3.7 Cubic phase of $Cs_2(HSO_4)(H_2PO_4)$. Cs atoms reside at the corners and S/P atoms in the center surrounded by the partially occupied oxygen sites.

3.3.2 Synthesis of the $M_2(HSO_4)(H_2PO_4)$ compounds

These $M_2(HSO_4)(H_2PO_4)$ compounds were synthesized by slow evaporation from aqueous solutions using the following procedure:

$$M_2CO_3 + x{*}H_3PO_4 + y{*}H_2SO_4 + H_2O \xrightarrow{10-25^{\circ}C} \text{single crystals}$$

where x and y were varied from 1 as necessary to achieve the desired compound. The reagents used were the same as those for the mixed Cs/M systems with the addition of phosphoric acid (86% aq. sol.). Successful synthesis conditions varied slightly from compound to compound, Table 3.5. Copious amounts of large wedged-shaped crystals were easily grown for the K, NH_4, and Rb compounds once the synthesis route was

perfected. On the other hand, the Cs compound was very difficult to grow, with only small quantities of plate like crystals being produced after much perseverance. The phases of the crystals were confirmed using SCXD techniques, at which time the crystals were also oriented for directional conductivity measurements. All experimental results presented here were performed on single crystals so identified.

Table 3.5 Successful synthesis conditions for the $M_2(HSO_4)(H_2PO_4)$ compounds.

Cation	M_2CO_3:H_2SO_4:H_3PO_4	Temperature (°C)	Resulting Phases
Cs	1:1:1	10	$Cs_2(HSO_4)(H_2PO_4)$ & $Cs_3(HSO_4)_2(H_2PO_4)$
Rb	1:1:1	25	$Rb_2(HSO_4)(H_2PO_4)$
NH_4	1:1:1	25	$(NH_4)_2(HSO_4)(H_2PO_4)$
K	1:2:6	25	$K_2(HSO_4)(H_2PO_4)$

3.3.3 Characterization of the $M_2(HSO_4)(H_2PO_4)$ compounds

The presence and type of phase transitions present in these compounds were determined by thermal (DSC and TGA) and conductivity measurements. The results of these measurements showed that only the Cs compound undergoes a superprotonic phase transition, the other compounds melting at 110, 160, and 170°C, for the NH_4, Rb and K compounds, respectively. The melting of these compounds (instead of decomposition) was determined by comparing the DSC scans with the TGA curves, Figure 3.8, and by visual inspection of heated crystals under an optical microscope. The specifics of the high temperature transitions of these compounds are given in Table 3.6.

Table 3.6 High temperature transition parameters for the $M_2(HSO_4)(H_2PO_4)$ compounds.

Cation	Transition Type	T_{onset} (°C)	$T_{decomp.}$ (°C)
Cs	Superprotonic	60	190
Rb	Melt	160	193
NH_4	Melt	110	143
K	Melt	170	183

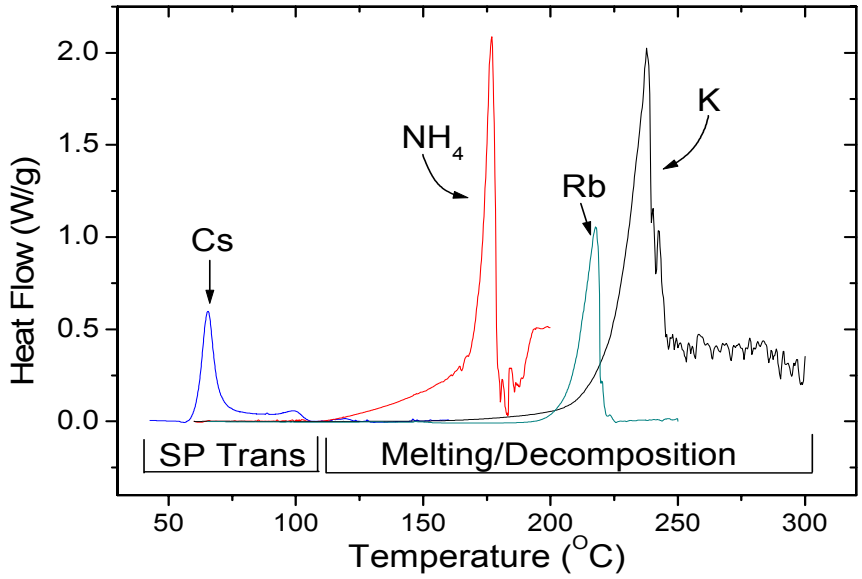

a)

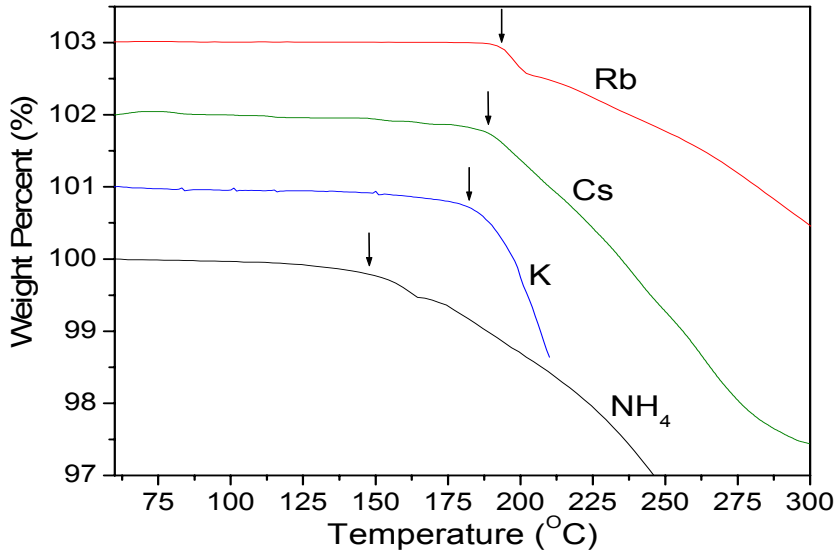

b)

Figure 3.8 Thermal analysis of the $M_2(HSO_4)(H_2PO_4)$ compounds at elevated temperatures by DSC, a), and TGA, b), measurements. The DSC scans show the superprotonic and melting transitions of the compounds, while the start of decomposition is indicated by arrows in the TGA curves. Both sets of measurements were taken at 5°C/min under flowing argon (DSC) or nitrogen (TGA) atmosphere.

From these results one can conclude that large cations are indeed necessary for superprotonic transitions without any structural qualifications. This conclusion was supported by conductivity measurements, which showed the K, NH_4, and Rb compounds to remain poor conductors up to the onset of melting, Figure 3.9.

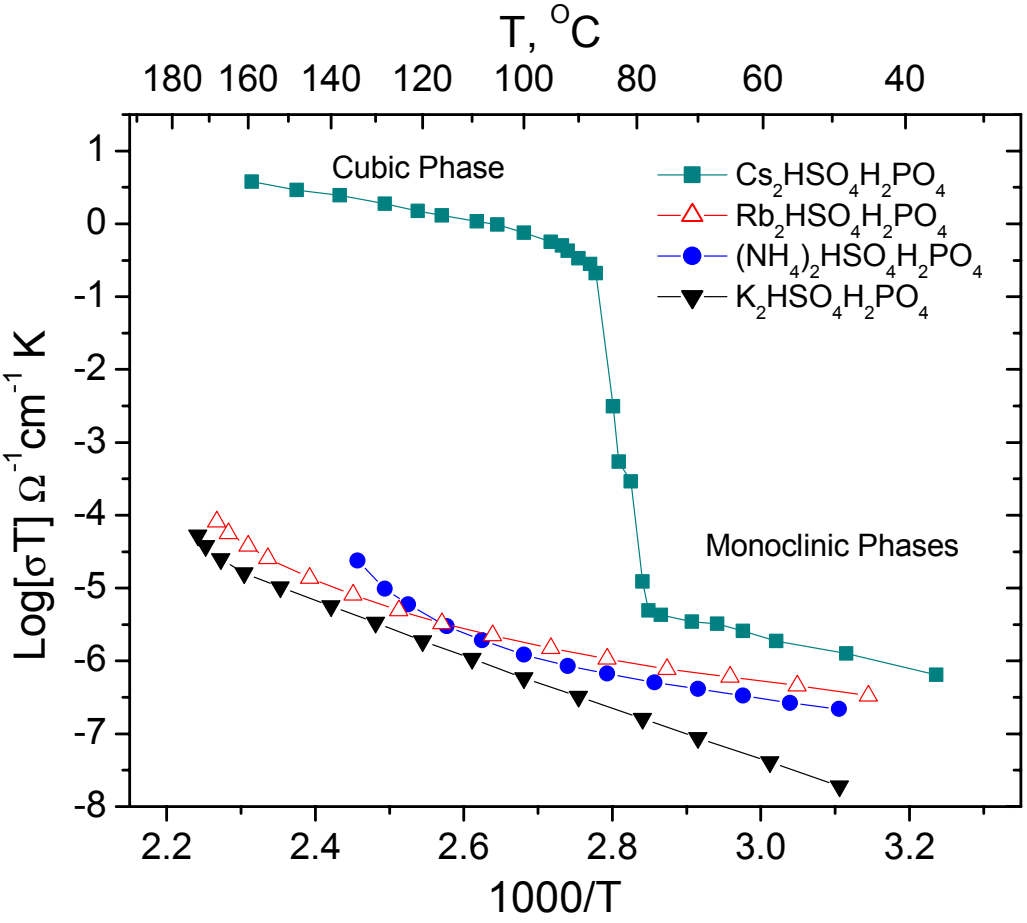

Figure 3.9 Conductivity measurements along the b-axis of the $M_2(HSO_4)(H_2PO_4)$ compounds. The measurements were taken in a dry argon atmosphere with a heating rate of 0.5°C/min.

Looking at Figure 3.9, it is quite interesting to note that a larger cation size facilitates the room temperature conductivity of a compound as well as its transition to a

superprotonic state. In fact, if one plots the logarithm of the conductivity versus cation radius for the compounds, there is a highly linear relationship that becomes more linear as the temperature approaches that of the Cs compound's superprotonic transition, Figure 3.10. This effect on the room temperature conductivities is expected if one considers the mechanisms thought to govern protonic conductivity in the room temperature phases as precursors to those known to occur in the superprotonic phases.

In the room temperature phases of solid acids, protons are thought to conduct by the formation and migration of defects such as doubly occupied and empty hydrogen bonds (D and L defects), interstitial hydrogen bonds (Frenkel-like defects), and positive/negative ion pairs (i.e., $H_2SO_4^+$ and SO_4^- in $CsHSO_4$)[2,37,46]. By either proton hops or tetrahedral rotations, these defects move through the otherwise ordered structures of the room temperature phases. Proton conduction by any of the proposed defect mechanisms will therefore result in increased hydrogen bond and orientational (dipole or tetrahedral) disorder. It is then quite logical that if larger cations favor the transition to a state in which a disordered hydrogen-bonded network and rapid tetrahedral reorientations are built into the structure, they should also facilitate the defect conduction mechanisms of the room temperature phases. Exactly why the conductivity of the compounds produces the effect seen in Figure 3.10 b is unclear, but it would seem that as the cation size effect becomes more fully realized, possibly due to increased thermal vibrations of the atoms, the possibility of transforming to the superprotonic state becomes open for compounds with large enough cations.

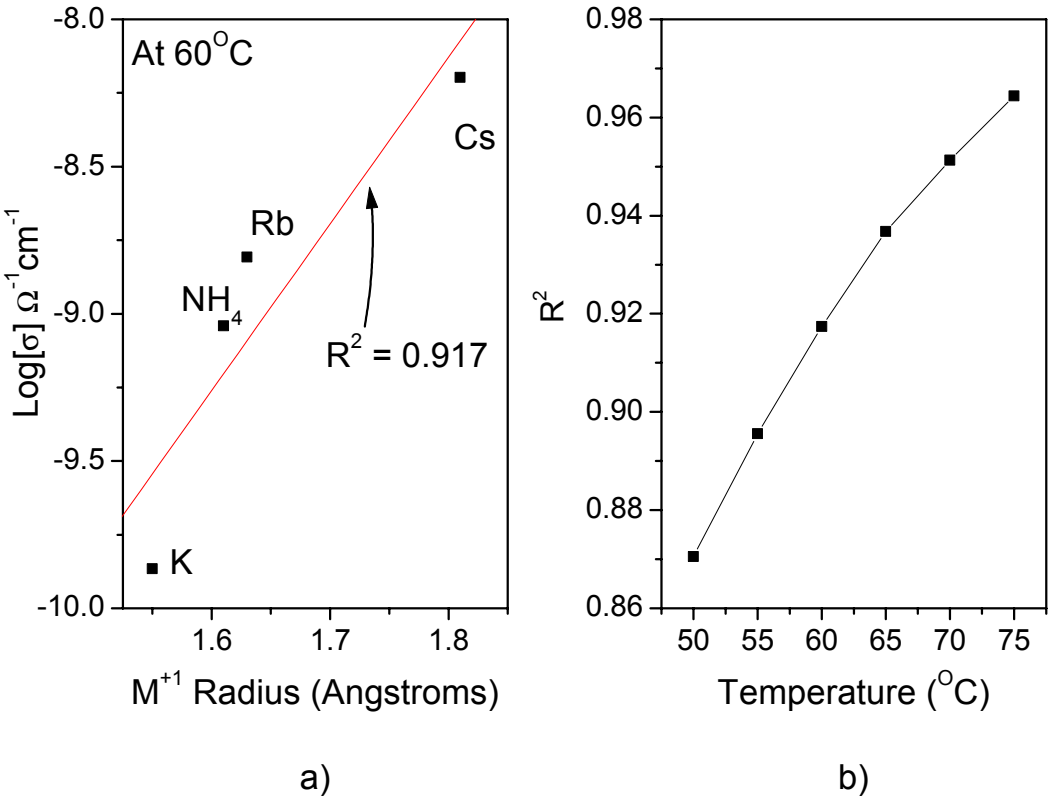

Figure 3.10 Cation size effect on the room temperature conductivities: the logarithm of conductivity versus cation radius, a), shows an almost linear relationship, which becomes more pronounced as the temperature is increased, b).

Since the overall magnitudes of the room temperature conductivities appear to scale with the size of a compound's cations, it is quite interesting that neither the activation energy nor pre-exponential function of the compounds follows such a trend. The values for these parameters are given in Table 3.7 and show the K and Cs compounds to have both higher activation energies and greater pre-exponential functions than the Rb and NH_4 crystals. The activation energy represents the energy required for a successful proton migration step, while the pre-exponential function mainly reflects the number density of proton conduction producing defects [122]. Intuitively, one might guess

that if larger cations facilitate protonic transport, this effect would show up in either smaller activation energies or larger pre-exponential terms as the cation size increased. However, neither trend is evident.

Table 3.7 Activation energy and pre-exponential term for proton conduction in the room temperature phases of the the $M_2(HSO_4)(H_2PO_4)$ compounds determined from a fit of the data to $\sigma = (A/T)\exp[E_a/k_bT]$. The conductivity of the crystals at 60°C is also given. The crystal axis refers to the direction of the applied field with respect to the crystallographic axes of the monoclinic phases.

Cation	Crystal Axis	E_a (eV)	Log[A] (Ω^{-1} cm^{-1} K)	σ(60°C) (Ω^{-1} cm^{-1})
Cs	b	0.43	0.82	6.4×10^{-9}
Rb	b	0.30	-1.80	1.6×10^{-9}
NH_4	b	0.31	-1.84	9.1×10^{-10}
K	b	0.71	3.57	1.4×10^{-10}

If, on the other hand, one compares the relationship between activation energies and pre-exponential terms (independently of cation size) one finds a strong correlation. This can be seen by plotting the two terms against each other, which gives a nearly linear relationship between the parameters, Figure 3.11 a. Such a phenomenon has been observed for thermoactivated processes in general, and in particular, for solid acids by Sinitsyn et al. who labeled it the compensation law for protonic conductors[122]. This law correlates the activation energy required for proton transport with the entropy created by the migration process. If we include the data points for the $M_2(HSO_4)(H_2PO_4)$ compounds with those of other solid acids, the R^2 value of a linear fit *increases* from the 0.84 value reported by Sinitsyn to 0.90, Figure 3.11 b. However, in spite of the improved fit to the data, the results of the $M_2(HSO_4)(H_2PO_4)$ compounds actually contradicts one of the paper's main results: that for activation energies smaller than 0.5 eV room

temperature proton transport is impossible as the entropy of the conduction process becomes negative below this value (by their estimations). As can be seen in Figure 3.11 b, this statement was supported by the data available at the time and it is possible that the estimations taken to derive this limit were correct for the other solid acids, but not for this family of crystals. In any case, this data makes it clear that activation energies as low as 0.3 eV are possible in the room temperature phases even though such values are usually associated with superprotonic conduction [122].

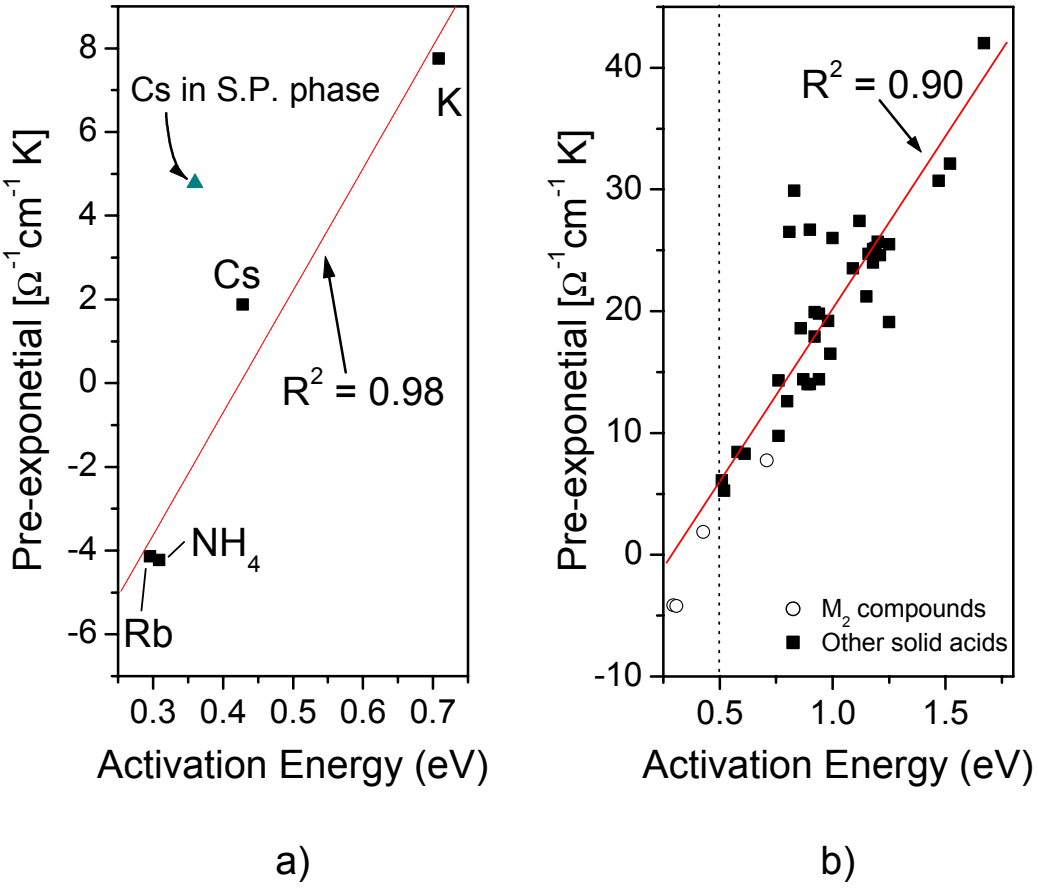

Figure 3.11 Compensation law for $M_2(HSO_4)(H_2PO_4)$ compounds, a), and the entire family of solid acids, b), both show linear relationships between the activation energies and pre-exponential terms derived from a fit of the data to $\sigma = (A/T)\exp[E_a/k_bT]$. Dotted line in b) designates the cutoff activation energy of 0.5 eV calculated by Sinitsyn[122].

To conclude, both the overall magnitude and particular parameters of these compounds' conductivities behave expectedly/understandably in the room temperature phases: a larger cation radius enhancing the protonic conductivity in a manner presumably similar to the size effect of the superprotonic transitions.

3.3.4 What exactly is the effect of cation size?

The previous section provided the evidence that large cations are essential to the presence of superprotonic transitions, but what exactly is so crucial about the size of the cations? A very simple guess might be that large cations are require to stabilize the high temperature structure. Such a guess would lead to the critical ratio between the anion (R) and cation (r) radius in the CsCl structure of the Cs compound's high temperature phase. Assuming hard spheres for the ions and using the eightfold coordination of this structure, the critical r/R value becomes 0.732, below which the anion (which usually has the larger radius) spheres will begin to overlap. This coordination is stable until the r/R value is greater than one, at which point a twelvefold coordination becomes more energetically stable[123]. Estimating the radius of the XO_4 groups is much more speculative than those of the cations, but if we use the reported values for the covalent radius of oxygen coordinated by four atoms (1.24 Å) and the average of the S and P covalent radii in tetrahedral coordination (0.26 and 0.31 Å, respectively), the average X+O radius is[83]:

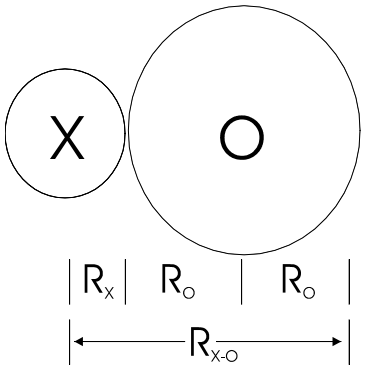

$$= \frac{0.26 + 0.31}{2} + 1.24 + 1.24 = 2.765 \text{ Å}$$

The X-O distance calculated this way is 1.525 Å, very close to the average value of ~ 1.51 Å observed in the room temperature structures. The calculated (*spherical*) anion radius of 2.765 Å would then seem to be a reasonable value for the XO_4 groups. Using this anion radius in the high temperature phase, the r/R value for the Cs (1.81 Å) compound is 0.655, significantly below the critical value of 0.732. Of course the r/R value is even farther away from the critical value for Rb, NH_4, and K in the CsCl structure, Table 3.8.

There is a major problem with this calculation, however, which arises from the basic assumption that the tetrahedra act like hard spheres. This does not seem too unreasonable for a superprotonic phase, where the tetrahedra undergo rapid reorientations, but nevertheless leads to unrealistic consequences in the high temperature CsCl-like structure of the Cs compound. In a qualitative way, making the tetrahedra into hard spheres allows for the possibility of linear configurations like X-O-O-X and X-O-Cs, which are very unlikely [63]. Quantitatively, anion spheres with a radius of 2.765 Å are incompatible with the experimental findings as they would result in a lattice constant for a CsCl cubic cell of 2*2.765 = 5.53 Å, based on the anion spheres just touching. Since the value observed for the Cs compound is 4.926 Å, it would appear that although the distance from the center of a tetrahedron to the outer edge of one of its oxygens is on the order of 2.765 Å, the effective radius of the tetrahedra must be smaller than this number.

A very straightforward way of estimating an *effective* anionic radius is to simply do the reverse of the above calculation and take the known lattice constant, 4.926 Å, and

divide it by two, giving a value of R = 2.463 Å. With such an effective radius for the XO_4 groups and the critical r/R value of 0.723, it is trivial to calculate the minimum radius required for the cations r = (r/R)*R = 0.723*2.463 = 1.803 Å. For such a cutoff, only the Cs compound would be stable in the CsCl structure (i.e. r/R > 0.732), in good agreement with the experimental findings, Table 3.8.

Taking the above estimation one step further, we note that the cesium radius is slightly larger than 1.803 Å, and therefore the tetrahedra do not actually touch in the cubic structure so that the true effective radius is even smaller than 2.463 Å. Assuming that the anion and cation radii touch along the body diagonal, this *structure* determined effective radius will simply be half the body diagonal minus the radius of a cesium ion:

$$\sqrt{3}/2 * a_O - r_{cesium} = 0.866 * 4.926 - 1.81 = 4.266 - 1.81 = 2.456 \text{ Å}$$

For this value, all the cation to anion radius ratios increase, but the Cs compound is still the only crystal with a ratio above 0.732, Table 3.8.

The CsH_2PO_4 compound is also reported to have CsCl structure and a lattice constant of 4.961 Å[92]. Calculating the different anionic radii as was done for $Cs_2(HSO_4)(H_2PO_4)$ results in ratios all below the critical value of 0.732 for Rb, NH_4, and K, Table 3.7. In the case of CsH_2PO_4, however, the r/R values evaluated using the anion radii derived from the structure are close to the critical value, which agrees with the nearly commensurate superprotonic phase transition and decomposition of the compound at 232°C[92]. It should be noted that a Cs ionic radius of 1.81 Å assumes a coordination by ten oxygen atoms (as opposed to the eight fold coordination of the Cs site), which is the case the room temperature structures of $Cs_2(HSO_4)(H_2PO_4)$ and CsH_2PO_4, but may not be the case in the superprotonic phases[27,28]. In fact, assuming an average of 1½ oxygens

from each of the eight surrounding tetrahedra, a coordination number of 12 seems quite possible, which would equate to a ionic radius of 1.88 Å for Cs^{83}. There is then some flexibility in the calculated ratios, although even with a 12-fold coordination, the Rb, NH_4, and K compounds would remain below the critical r/R ratio of 0.732 (i.e. Rb^{XII} = 1.73 Å)[83].

Table 3.8 Cation/anion radius ratios for the $M_2(HSO_4)(H_2PO_4)$ and MH_2PO_4 compounds in a CsCl structure. The cation radius is given for an eight-fold coordination while the anion radius is fixed at the three values derived in text. The stability range for eight fold coordination is $0.723 \leq r/R < 1$.

Radius (Å)	Cs-1.81	Rb-1.63	NH_4-1.61	K-1.55
XO_4-structure 2.456	0.737	0.664	0.656	0.631
XO_4-effective 2.463	0.735	0.662	0.654	0.629
XO_4-spherical 2.765	0.655	0.590	0.583	0.561
PO_4-structure 2.486	0.728	0.656	0.648	0.623
PO_4-effective 2.480	0.730	0.658	0.649	0.625
PO_4-spherical 2.790	0.649	0.585	0.577	0.556

One might now be tempted to conclude that the cation size effect on superprotonic transitions is no more than the prerequisite that the high temperature structures be energetically stable, which of necessity calls for large cations. However, just as was the case with the initial observations on the $MHXO_4$ family of compounds, this logic leads to the conclusion that larger XO_4 groups are detrimental to the presence of a superprotonic transition as proportionally larger cations would be required to meet the critical r/R value. This flies in the face of all available experimental evidence which shows larger tetrahedral groups to facilitate superprotonic transitions. The cation size

effect, although undoubtedly linked to the discussed ratio rule considerations, must therefore have more subtle effects as well.

To uncover such effects, let us look at the characteristic distances in these compounds as we did previously for the $MHSO_4$ compounds. A graph similar to Figure 3.4 reveals no critical parameters as all the distances scale with cation radius, Figure 3.12 a. Interestingly, the hydrogen bond lengths of the compounds do not show a particularly strong dependence on the size of the cations, Figure 3.12 b. This analysis does not reveal a critical crystal-chemical parameter for exactly the same reason that the results of these compounds are so conclusive, namely the compounds are isostructural.

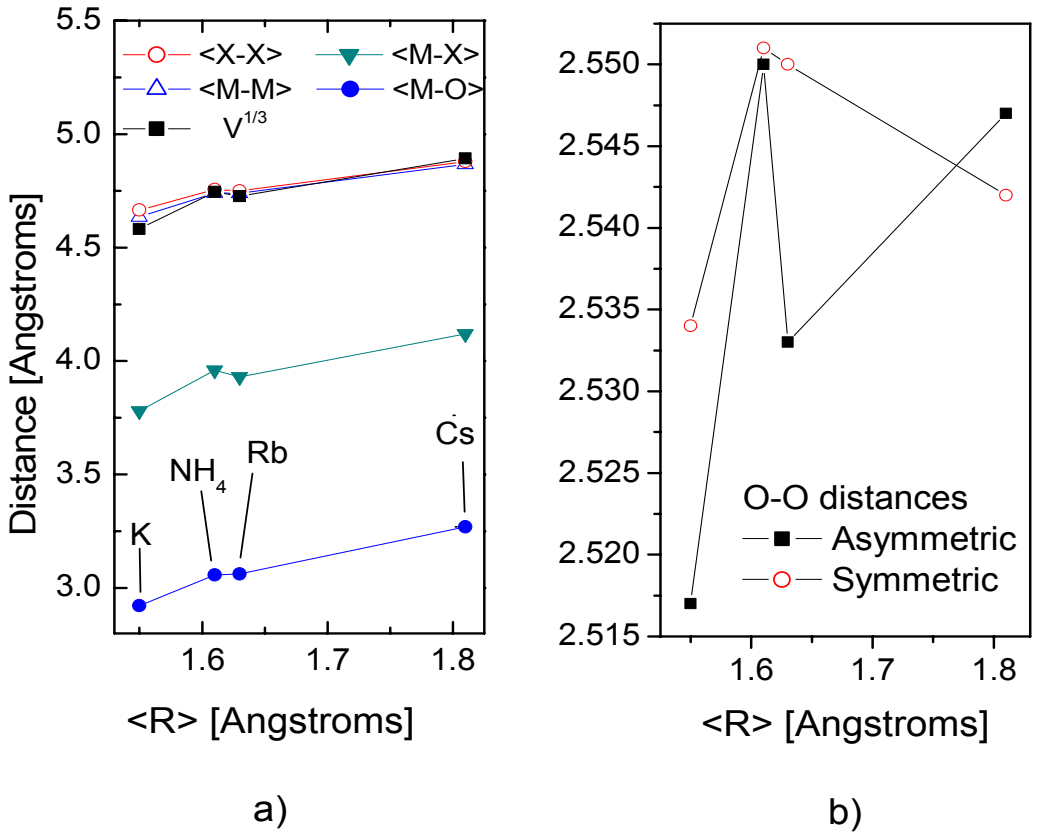

Figure 3.12 Characteristic distances for the $M_2(HSO_4)(H_2PO_4)$ compounds, a), scale with the cation radius, while the O-O lengths of the symmetric and asymmetric hydrogen

bonds found in the crystals do show a fairly random dependence with <R>, b). If the NH_4 compound is removed from consideration, however, the asymmetric bonds that link the tetrahedra might be said to lengthen as <R> increases. Crystallographic data taken from the same sources as found in Table 3.3.

For an increased understanding of the cation size effect on superprotonic transitions, it is therefore necessary to analyze the transition in which we have just determined the cation size effect to play the dominant role in its presence, i.e., the transition of $Cs_2(HSO_4)(H_2PO_4)$. If we look the changes in the characteristic distances across the transition, it is immediately clear that the Cs-X distance changes most, Figure 3.13. Furthermore, this fact appears to be true for $CsHSO_4$ and CsH_2PO_4 as well (the only other $MHXO_4$ compounds with superprotonic transitions for which both the room and high temperature structures are known), Figure 3.13. This is particularly interesting for $CsHSO_4$ as its superprotonic phase is tetragonal, space group $I4_1/amd$, and so is quite different from the CsCl structure into which CsH_2PO_4 and $Cs_2(HSO_4)(H_2PO_4)$ transform at high tempertures[61]. The <M-X> distance therefore again emerges as the single most important crystal-chemical measure of a $MHXO_4$ compound's likely-hood to undergo a superprotonic phase transition. Moreover, as the structures of $Cs_2(HSO_4)(H_2PO_4)$, $CsHSO_4$ and CsH_2PO_4 vary significantly in both the low an high temperature regimes, the <M-X> distance would appear to be predictive irrespective of a $MHXO_4$ compound's structure both below and above the transition.

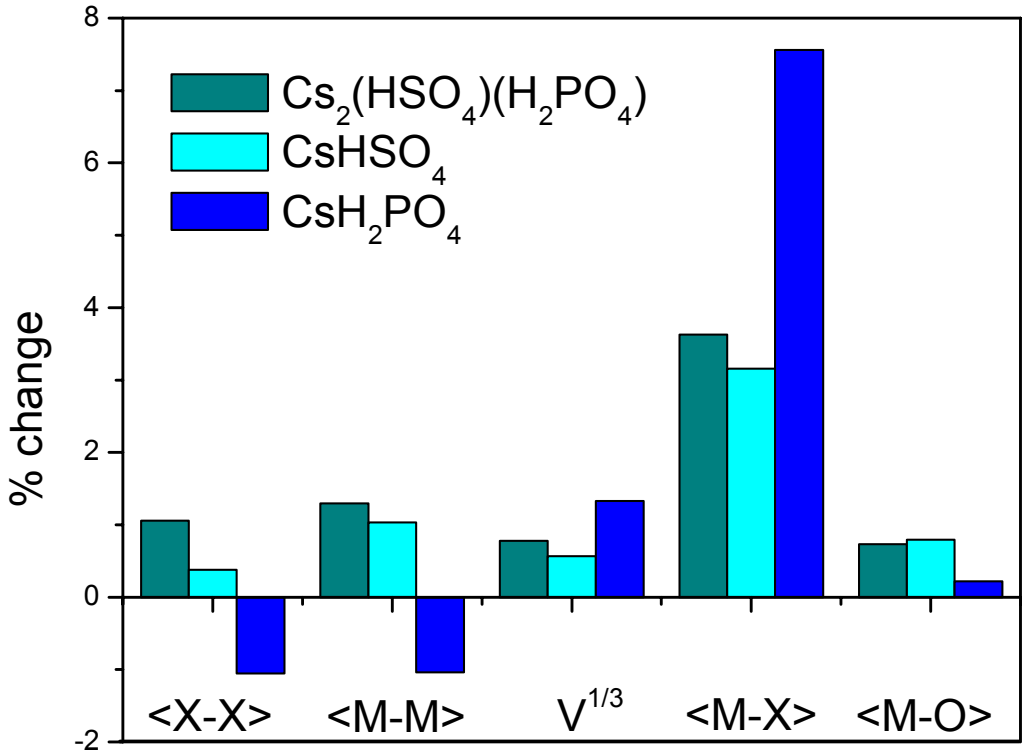

Figure 3.13 Changes in the characteristic distances of $Cs_2(HSO_4)(H_2PO_4)$, $CsHSO_4$ and CsH_2PO_4 across their superprotonic transitions. The crystallographic data comes from the following sourses: $Cs_2(HSO_4)(H_2PO_4)$[27,63]; $CsHSO_4$[26,61,124,125]; CsH_2PO_4[28,92]. For $CsHSO_4$, the position of the oxygen atoms in the superprotonic phase is in dispute, so the average of the <M-O> distances from the three different structures proposed was used in the figure.

3.3.5 Conclusions and interpretations of the cation/anion effect

This work has shown conclusively that large cations are necessary for superprotonic transitions in the $M_2(HSO_4)(H_2PO_4)$ family of compounds. From this it was established that the average cation to tetrahedral anion, <M-X>, distance surfaces as the best measure of a $MHXO_4$ compound's probability for undergoing a supeprotonic transition, agreeing with the generally observed behavior of the compounds. The <X-X>

distance was found to be much less useful as a predictive measure of a superprotonic transition, contrary to the proposed hypothesis that the main effect of increased cation size was to create larger X-X distances and thereby allow freer rotations of the tetrahedra.

Having identified M-X distances as such a critical crystal-chemical measure, the question is then what exactly does this distance do to the interactions of the atoms so as to favor the presence of superprotonic transitions. In the present study, the <M-X> distance was modified by varying the radius of the cations, but as can be seen in the $MHSO_4$/$MHSeO_4$ systems, varying the size of the tetrahedra has an equal, if not greater, effect on superprotonic transitions, Table 3.1. As stated before, this anion size effect contradicts the assumption that bigger X-X distances are the critical measure for transitions, as bigger tetrahedra in an otherwise unchanged structure should cause more steric hindrances between the oxygen atoms of the tetrahedra. Instead, increasing the size of a tetrahedron, which is equivalent to increasing the <X-O> distance, seems to decrease these inhibiting interactions. For this reason, it is sensible to assume that the increased X-O distances allow for a greater degree of freedom in the oxygen's position as a tetrahedron rotates/librates. Similarly, a larger cation radius equates to proportionally larger <M-O> distances, creating "floppier" MO_x polyhedra. An increase in the <M-X> distance therefore causes both the XO_4 tetrahedra and MO_x polyhedra to loosen up, which can be seen experimentally in the increasing thermal parameters of the oxygen atoms with increasing <M-O> distances, Figure 3.14. The good match between the two parameters is particularly pleasing since this comparison includes all the compounds presented in this work, plus all the published compounds from the MH_2XO_4 and mixed

$MHYO_4$-MH_2XO_4 family of compounds (M = alkali metals and NH_4; X = P, As; Y = S, Se).

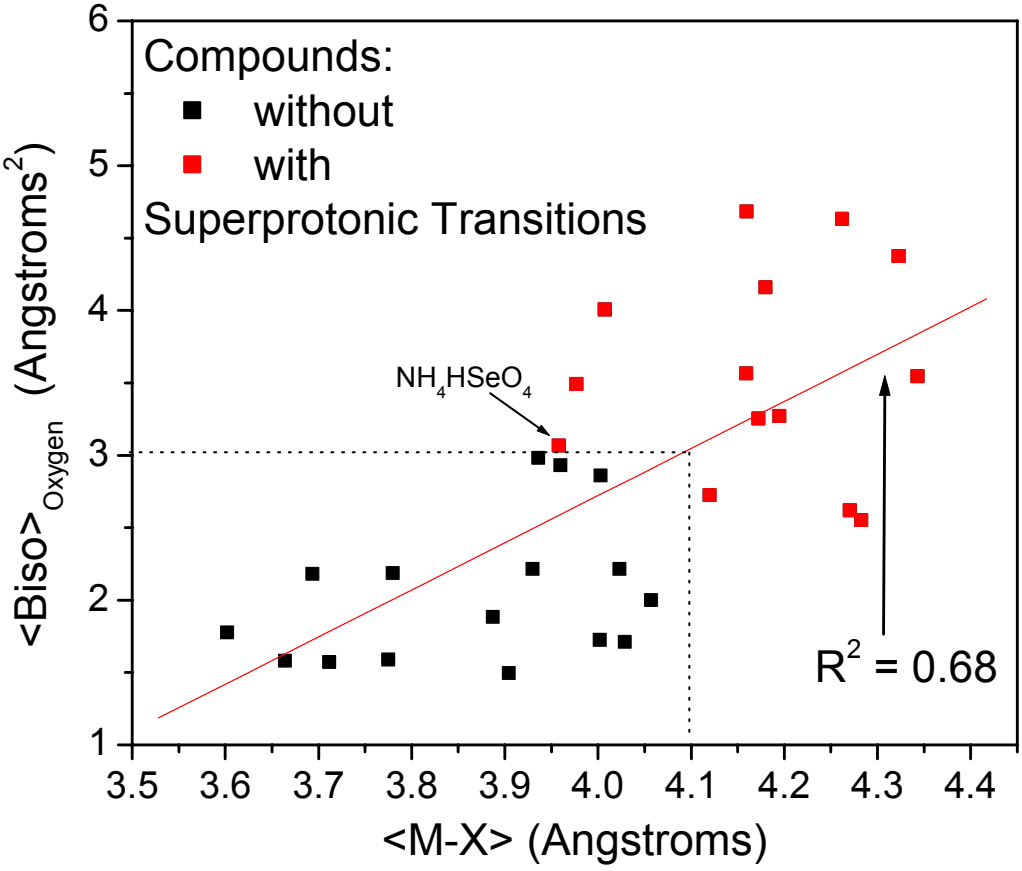

Figure 3.14 Average thermal parameters of the oxygen atoms versus <M-X> distances: the two parameters generally scale with each other. The dashed lines denotes the cutoff between the with and without transition regions of the graph. It appears that either <M-X> distances larger than ~ 4.1 Å and/or $<Biso>_{Oxygen}$ parameters greater than ~ 3.0 $Å^2$ in a room temperature compound are likely to produce a superprotonic transition. Note that one might not predict the NH_4HSeO4 compound to transform from these criterion, but its transition is probably facilitated by the presence of the highly directional ammonium ions. Crystallographic data was taken from various sources.

The <M-X> distance is then a measure of the overall mobility of the oxygen atoms, an increase in which should lower any barriers to tetrahedral reorientations.

Specifically, the oxygen atoms would have more flexibility to avoid close contact with the electrons of the cations by bending their respective M-O and X-O bonds. With respect to the cation size effect, this flexibility in the M-O bonds could be restated in terms of the higher polarizability of the cations as their radius increases, Figure 3.15. In this case, it would be the electrons of the cations that are adjusting their positions, resulting in the oxygen atoms having access to positions not available to them with smaller cations. Such a phenomenon also explains the observed increase in room temperature protonic conduction of the $M_2(HSO_4)(H_2PO_4)$ compounds as the cation radius is enlarged (section 3.3.3), bigger movements of the oxygen atoms facilitating the formation and migration of defects. Larger M-X distances then assist both room temperature conduction and superprotonic transitions by enhancing the mobility of the oxygen atoms and thereby reducing barriers to structural rearrangements.

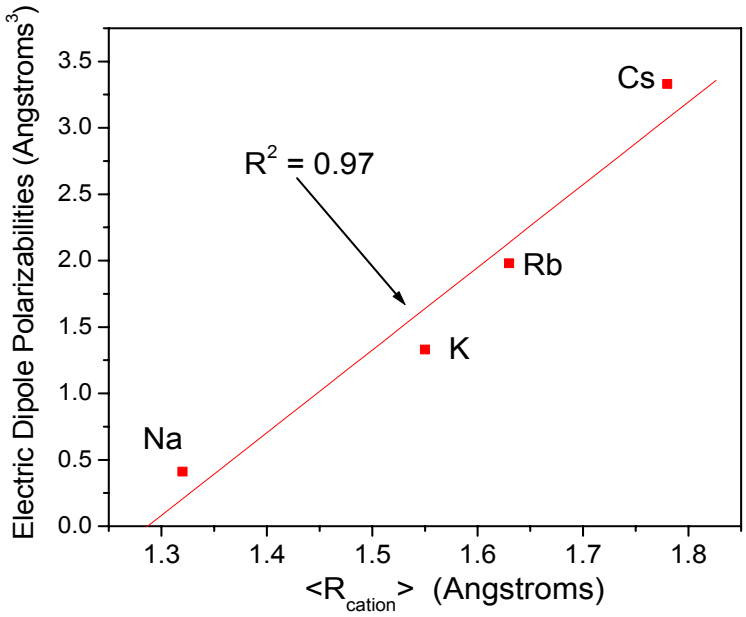

Figure 3.15 Cation radius versus polarizablity shows a nearly linear relationship between the two parameters. Larger cations therefore lead to "floppier" MO_x polyhedra. Polarization data taken from calculated electric dipole polarizabilities of M^{+1} cations[126].

This reduction of the barriers to tetrahedral reorientations can be visualized energetically by considering that longer M-X distances will lead to weaker M-O and X-O bonds. The potential wells in which the oxygen atoms reside will therefore become increasingly shallow as M-X distances are lengthened. For such potentials, oxygen atoms will have a larger range of motion and smaller transition energies when compared to the deeper potential wells associated with smaller M-X distances, Figure 3.16. The transitions under consideration here are distortions from the optimal arrangement of the oxygen atoms due to the formation of defects and/or XO_4 reorientations. This energetic explanation of the cation/anion size effect then further illuminates the correlation between the magnitude of a room temperature phase's protonic conductivity and its probability of having a superprotonic transition.

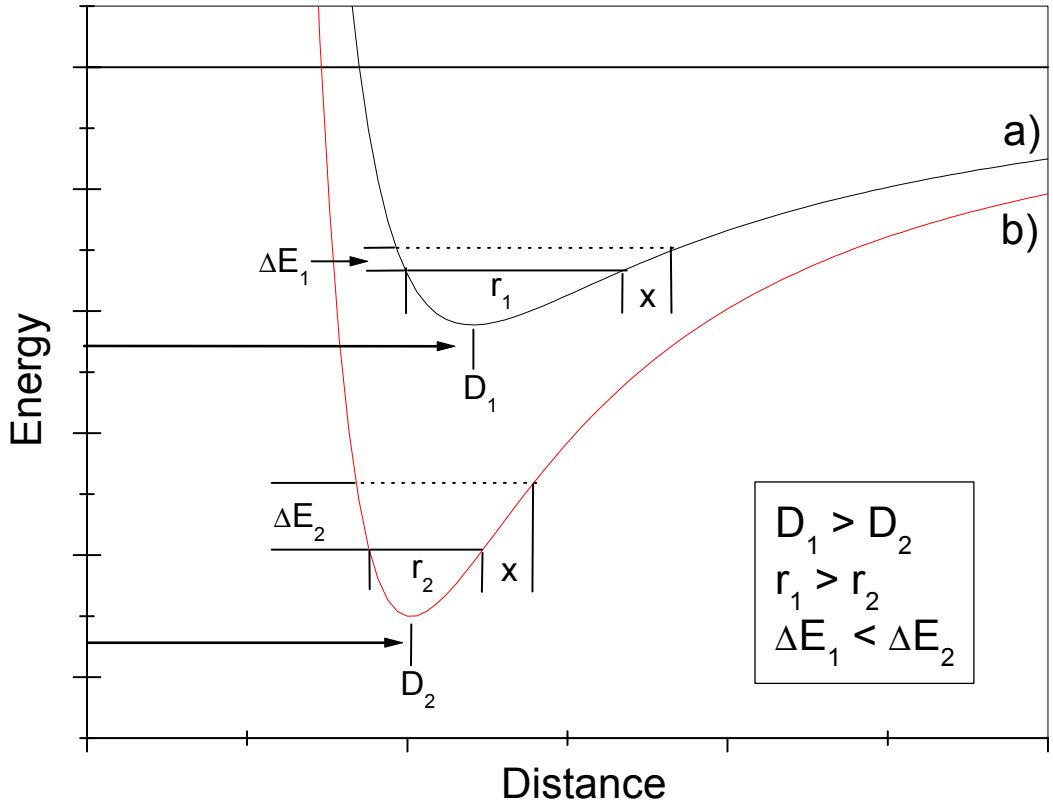

Figure 3.16 Schematic representation of the potential wells for oxygen atoms with a) longer and b) shorter M-O/X-O distances. A shallow potential well associated with a long M-X distance results in a large range of motion for an oxygen atom, but small transition energy necessary to reach a distance outside of this range. In contrast, a shorter M-X distance will result in the oxygen atom residing in a deeper well with a smaller range of motion and bigger transition energy.

As all the above interpretations of the cation/anion size effect are quite general in nature, larger M-X distances should facilitate tetrahedral reorientations, and thereby superprotonic transitions, in a similarly general manner. However, this effect will be most evident for superprotonic transitions in which almost freely rotating tetrahedra are required. For the superprotonic transitions of the $MHXO_4$ compounds, the <M-X> distance is then a good chemical-crystal measure with which to predict the presence of

superprotonic transitions, the known superprotonic phases for this family of compounds having highly disordered tetrahedra. For other compounds, the anion/cation size effect should still apply, but may not be the determining factor in the presence or absence of a transition, other structural effects having a more dominant role (i.e., the $M_3H(XO_4)$ family of compounds). Even in such compounds, the results of these studies should help reveal exactly what is the critical parameter, as any cation/anion size effects can be examined in the manner shown here and removed from consideration if they are found not to fully describe the situation. Moreover, as the stoichiometry of a compound can often be used to guess its possible superprotonic structure (which in turn governs how the tetrahedra will reorient), the search for new superprotonic conducting solid acids can be narrowed to those most likely to have a transformation using the criteria described in this chapter. This focused attention will hopefully speed up the process of synthesizing novel solid acids with properties ideal for application.

Chapter 4. Mixed Cesium Sulfate-Phosphates: Driving Force for the Superprotonic Transitions of MH_nXO_4 compounds (M = Cs, Rb, NH_4; X = S, Se, P, As)

4.1 Introduction

Preliminary investigations into the $CsHSO_4$-CsH_2PO_4 system[127] were conducted in the hope of explaining why $CsHSO_4$ exhibited a superprotonic transition at 141° C[3] while CsH_2PO_4 was reported to decompose and/or transform to a cubic phase around 230° C[46,93]. This difference in high temperature properties was in spite of the structural similarities of the compounds at room temperature with regards to the arrangement of the Cs^+ cations and tetrahedral anions [26,28]. By making solid solutions of $CsHSO_4$ and CsH_2PO_4, it was anticipated that compounds with varying S to P ratios could be created. Analysis of such compounds could help answer questions about the driving force behind superprotonic transitions similar to that of $CsHSO_4$. Questions such as what structural features are necessary for a transition to occur? Does the presence of phosphorus somehow hinder the transition? How is the transition effected by the density and distribution of hydrogen bonds?

Unfortunately, solid solutions proved impossible to achieve in the initial and all following studies into the $CsHSO_4$-CsH_2PO_4 system. Fortunately, these studies did discover many new line compounds with varying S:P ratios. And indeed, the analysis of

these compounds answered many of the initial questions: The presence of phosphorous does not prohibit superprotonic phase transitions as all the mixed cesium sulfates to date have superprotonic phases at elevated temperatures. There are no apparent structural features essential to these transitions; the mixed compounds having a very diverse set of room temperature structures. Neither the density of hydrogen atoms in the structure (varying from a $H:XO_4$ of 1:1 to 2:1), their distribution (linking the tetrahedra into 1-D, 2-D, or 3-D networks), or their local geometry(symmetric or asymmetric) are a determining factor in the presence or absence of a transition. Nevertheless, the question of what exactly was the driving force behind these transitions still remained unanswered. The most obvious answer is entropy, since the superprotonic phases of these compounds were found to have disordered oxygen atoms while the room temperature phases have fixed oxygen positions. Until very recently, however, precisely how entropy was driving the transitions was not clear. In fact, this chapter is dedicated to not only an in-depth description of the structures and properties exhibited by the mixed cesium sulphate-phosphates, but mainly to a theory that describes the change in transition entropy as the S:P ratio is varied.

4.2 Characterization of Mixed Cesium Sulfate-Phosphates

As was the case with $CsHSO_4$ and CsH_2PO_4, the basic arrangement of cations and tetrahedra is quite similar for all the mixed compounds. However, the actual structures and properties of the compounds can be quite different from each other. This section will give a general comparison of the mixed compounds, as well as $CsHSO_4$ and CsH_2PO_4, in terms of their room and high temperature structures, conductivities, and thermal

properties. Such a comparison is in preparation for the entropy calculations that will follow, in which the structures of each compound will be examined in more detail.

4.2.1 Synthesis of the Compounds

The synthesis of these compounds was not trivial. Although most of the compounds can be grown from slow water evaporation of an aqueous solution, the resulting crystals are extremely sensitive to the solution stoichiometry, synthesis method, and solution temperature. Table 4.1 shows the particulars for the compounds used in this work. The reagents for all compounds listed in consisted of high purity cesium carbonate powder (99.999%), and aqueous solutions of sulfuric (98%) and phosphoric acid (86%). It was essential to keep the solutions free from contaminants, particularly other metal cations, for the properties of the compounds to remain consistent.

Table 4.1 Synthesis of the Mixed Cesium Sulfate-Phosphates

Compound	Compound-S:P	Solution-S:P	Solution-Cs:XO_4	Method	Temp. (°C)
$CsHSO_4$	100:0	100:0	1:1	Slow H_2O evaporation	25
$Cs_3(HSO_4)_{2.50}(H_2PO_4)_{0.50}$	83:17	75:25	1:1	Slow H_2O evaporation	25
$Cs_3(HSO_4)_{2.25}(H_2PO_4)_{0.75}$	75:25	55:45	1:1.5	Methanol precipitation	25
$Cs_3(HSO_4)_2(H_2PO_4)$	67:33	70:30	1:1	Slow H_2O evaporation	25
$Cs_5(HSO_4)_3(H_2PO_4)_2$	60:40	50:50	1:1	Agitated H_2O evaporation	60
$Cs_2(HSO_4)(H_2PO_4)$	50:50	50:50	1:1	Slow H_2O evaporation	10
$Cs_6(H_2SO_4)_3(H_{1.5}PO_4)_4$	43:57	45:55	1:1	Slow H_2O evaporation	25
CsH_2PO_4	0:100	0:100	1:1	Slow H_2O evaporation	25

The primary synthesis route attempted was the room temperature evaporation of aqueous solutions with varying S:P ratios, but a fixed Cs:XO4 ratio of 1:1. High-quality single crystals were not always attained by this process, requiring further experimentation. The highlighted cells in Table 4.1 show the most significant departures from the normal route. For both the $Cs_3(HSO_4)_{2.25}(H_2PO_4)_{0.75}$ and $Cs_5(HSO_4)_3(H_2PO_4)_2$ compounds, it was not possible to acquire the quantity and quality of single crystals desired, so high quality powders were made. For all other compounds high quality, but not always high quantity, single crystals were synthesized.

4.2.2 Structural Features of Room Temperature Phases

The room temperature structures of the mixed cesium sulfate-phosphates, including $CsHSO_4$ and CsH_2PO_4, are listed in Table 4.1. These room temperature phases are comprised of isolated anion tetrahedra linked together by hydrogen bonds with the Cs^{+1} cations arranged between the anions in loosely defined CsO_{10-12} polyhedra. The polyhedra have an average Cs-O distance of 3.28 Å with a range of 3.02 to 3.72 Å, all typical values for Cs coordinated polyhedra[83]. Not surprisingly, the bond valence sums calculated using the Cs-O distances of these polyhedra give values very close to expected value of 1.0[128].

Tetrahedra found in these structures are quite regular with deviations from the ideal O-X-O angle of 109.5° and expected X-O bond distances attributed to the presence of hydrogen bonds. Hydrogen bonds are well known to cause an increase in the

Table 4.2 Structural parameters of the mixed cesium sulfate-phosphates in their room and high temperature phases.

Compound	S:P	H:XO_4	RT structure	H-bond network and type	HT (Superprotonic) structure	refs
$CsHSO_4$-II	1:0	1:1	Monoclinic, $P2_1/c$*	1-D, chains – 1 ordered	Tetragonal, $I4_1/amd$	[26,61]
$Cs_3(HSO_4)_{2.50}(H_2PO_4)_{0.50}$	5:1	1.16:1	Monoclinic, C2/c	3-D, cross-linked chains – 2 ordered & 1 disordered	Cubic, $Pm\bar{3}m$ & Tetragonal, $I4_1/amd$*	[32]
$Cs_3(HSO_4)_{2.25}(H_2PO_4)_{0.75}$	3:1	1.25:1	Monoclinic, C2/c*	3-D, cross-linked chains – 2 ordered & 1 disordered	Cubic, $Pm\bar{3}m$ & Tetragonal, $I4_1/amd$*	
$Cs_3(HSO_4)_2(H_2PO_4)$	2:1	1.33:1	Monoclinic, $P2_1/n$	3-D, cross-linked chains – 3 ordered & 2 disordered	Cubic, $Pm\bar{3}m$*	[30]
$Cs_5(HSO_4)_3(H_2PO_4)_2$	1.5:1	1.4:1	Monoclinic, C2/c	2-D, cross-linked & branched chains – 2 ordered & 3 disordered	Cubic, $Pm\bar{3}m$*	[31]
$Cs_2(HSO_4)(H_2PO_4)$	1:1	1.5:1	Monoclinic, $P2_1/n$*	2-D, cross-linked chains – 1 ordered & 1 disordered	Cubic, $Pm\bar{3}m$*	[27]
$Cs_6(H_2SO_4)_3(H_{1.5}PO_4)_4$	0.75:1	1.71:1	Cubic $I\bar{4}3d$*	3-D, inter-connected XO_4's – 1 ordered	Cubic, $Pm\bar{3}m$?*	
CsH_2PO_4	0:1	2:1	Monoclinic, $P2_1/m$	2-D, cross-linked chains – 1 ordered & 1 disordered	Cubic, $Pm\bar{3}m$	[28,92]

*this work

X-O distances of both donor and acceptor oxygen atoms while simultaneously decreasing the remaining tetrahedral X-O bond lengths[22]. This effect gives rise to the 1.43 to 1.58 Å range of X-O distances found in the room temperature phases of the compounds. However, overall these deviations do not unduly distort the tetrahedra and the average X-O distance for the whole group is 1.5 Å, in between the typical values of ~ 1.52 and ~ 1.47 Å for PO_4 and SO_4 tetrahedra, respectively[83]. Moreover, bond valence sums calculated using the P-O and S-O distances give values very close to the expected numbers of 5 and 6 for phosphate and sulfate tetrahedra, respectively, while the same calculation on tetrahedra with a mixed central cation results in intermediate values[128]. Finally, the angles of the tetrahedra are quite normal for sulfates and phosphates, ranging from a low of 102.3 to a high of 114.8°[22].

Thermal displacements for the Cs, S, and P atoms are all rather isotropic, whereas the oxygen atoms most often have the greatest thermal displacements in the direction perpendicular to the X-O bond, as expected for such compounds. Both asymmetric and symmetric hydrogen bonds are present in the room temperature phases of the mixed cesium sulfate-phosphates. These bonds have the chemical and geometric features typical of strong to medium strength hydrogen bonds with an average O···O distance of 2.54 Å and a range of 2.45 to 2.64 Å[5,17].

In some cases the symmetric hydrogen bonds have sufficiently short O···O distances (< 2.47 Å) to have a single minimum potential well; however, crystallographic data and the similarities of the compounds strongly suggest that all the symmetric hydrogen bonds in the room temperature phases have double-minima potential energy wells. For example, CsH_2PO4 is well known to have a ferroelectric transition at 159 K,

attributed to the protons ability to hop between the two minima of the paraelectric phase's symmetric hydrogen bond (O···O distance of 2.472(7) Å)[28,81]. The symmetric hydrogen bonds in these room temperature phases are hence often called "disordered" since the hydrogen resides equally on either side of the double-minima potential well. Consequently, asymmetrical hydrogen bonds are frequently termed "ordered" hydrogen bonds.

Despite the stoichiometry differences, all but the $Cs_6(H_2SO_4)_3(H_{1.5}PO_4)_4$ compound have similar anion and cation arrangements in their structures. This underlying configuration is best described as zigzag chains of hydrogen bonded tetrahedra that alternate with similarly zigging and zagging rows of cesium atoms in a checkerboard appearance. As the phosphorous content of these compounds increases, the chains of anions become increasingly more cross-linked, resulting in the diverse set of hydrogen-bonded networks found in these compounds. In Figure 4.1, it can be seen that both room temperature phases of $CsHSO_4$ and CsH_2PO_4 are comprised of zigzag rows of hydrogen bonded tetrahedra, the chains being cross-linked in CsH_2PO_4[30]. The zigzag chains of sulfates and phosphates are clearly visible in Figure 4.1 a and c, respectively, while the straight cross-linking chains in CsH_2PO_4 can be seen in Figure 4.1 d. The checkerboard pattern to the chains and rows of anions and cations are evident in Figure 4.1 b and c, for $CsHSO_4$ and CsH_2PO_4, respectively. This arrangement is aligned down the zigzag chains (c-axis) in the sulfate compound, but runs perpendicular to such chains in phosphate compound, where the pattern is observable down the straight chains (c-axis), Figure 4.1 c.

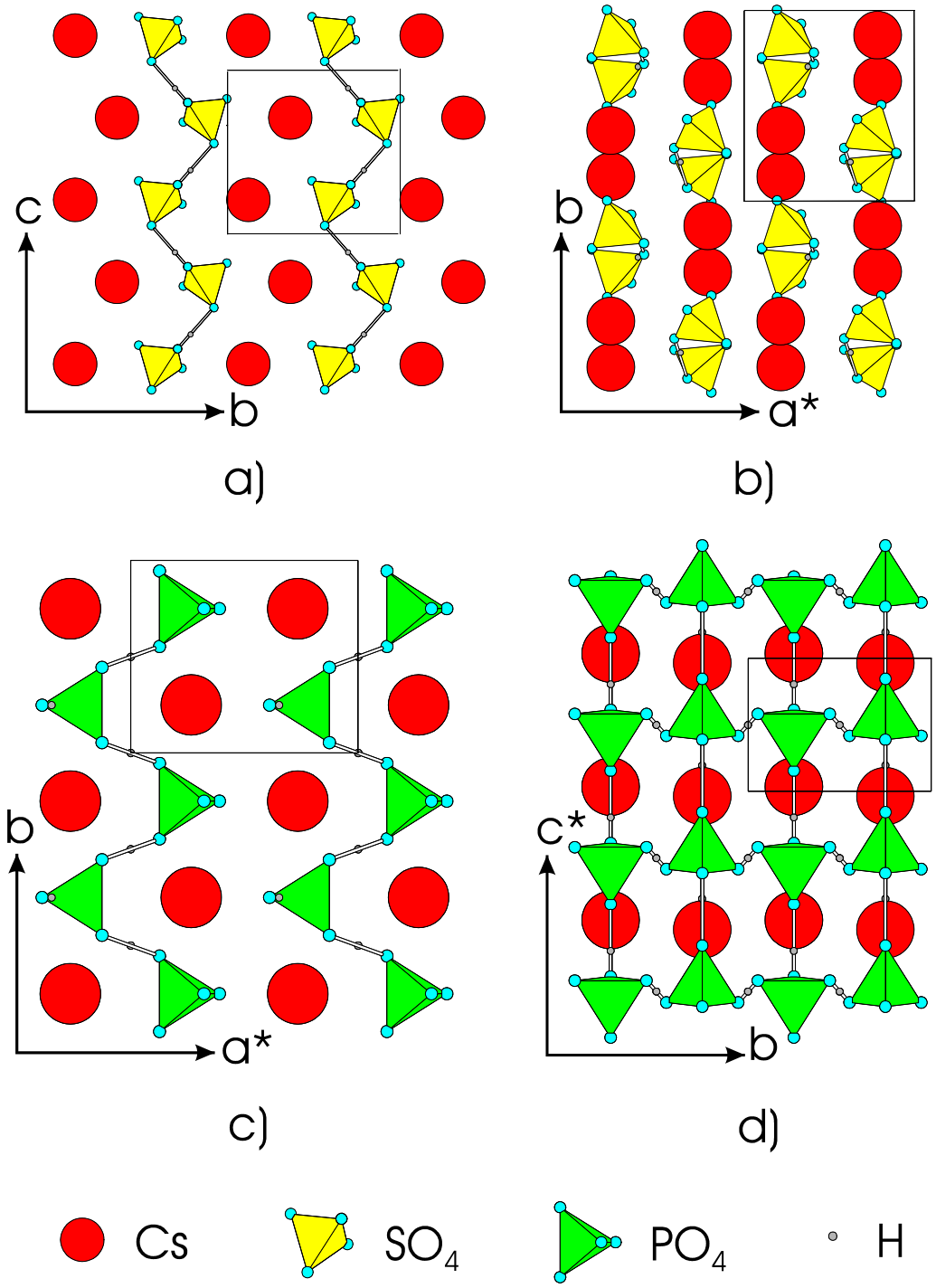

Figure 4.1 Room temperature structures for $CsHSO_4$ and CsH_2PO_4: a) the $\vec{b}\,x\,\vec{c}$ plane of $CsHSO_4$ showing zigzag chains of sulfate tetrahedra parallel to $\vec{c}$ and b) view down the c-axis revealing the checkerboard arrangement of cation and anion chains[26]; c) in CsH_2PO_4 hydrogen bonds connect the phosphate groups into zigzag chains along $\vec{b}$ and d) cross-link the tetrahedra into straight chains running parallel to the $\vec{c}$ -axis[28]. The rectangles represent the unit cells of the compounds.

The X-ray powder diffraction patterns for these compounds are shown in Figure 4.2. The structures of the first four compounds from the bottom to top are very similar, with the phosphate tetrahedra being incorporated in ever increasing amounts to every third tetrahedra down the zigzag chains of $CsHSO_4$, until in $Cs_3(HSO_4)_2(H_2PO_4)$, these sites are occupied exclusively by phosphate groups. This structural likeness results in the similarity of the low angle peaks for these four X-ray powder diffraction patterns. The variation of the top four patterns reveals that although these compounds have very similar general structural features, they can be crystallographically quite different from each other in there room temperature phases.

It should be noted here that the $Cs_6(H_2SO_4)_3(H_{1.5}PO_4)_4$ compound is quite unique for the mixed compounds in terms of both its arrangement of cations and anions and hydrogen bonded network. This difference is most apparent in the cubic symmetry of its room temperature phase instead of the otherwise universal monoclinic symmetry of the other seven room temperature phases. Its uniqueness is undoubtedly due to the fact that it is the only compound not to have a $Cs:XO_4$ ratio of 1:1 (it has 6:7), with a proton taking the place of a Cs^{+1} cation, resulting in a structure quite distinctive among these compounds.

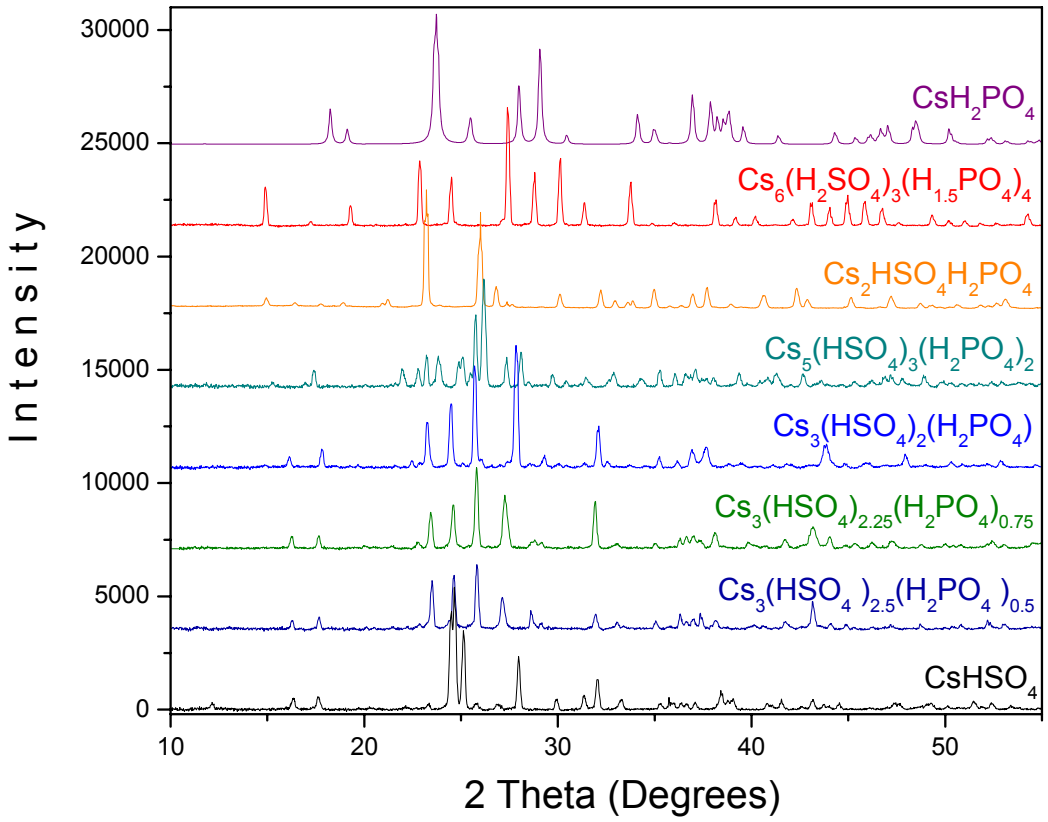

Figure 4.2 X-ray powder diffraction patterns of the mixed cesium sulfate-phosphates at room temperatures (~ 25°C).

4.2.3 Structural Features of High Temperature Phases

Although some of the compounds were previously known and their high temperature structures previously investigated, the high temperature diffraction patterns of all the compounds (with the exception of CsH_2PO_4) were collected to permit direct comparisons, Figure 4.3.

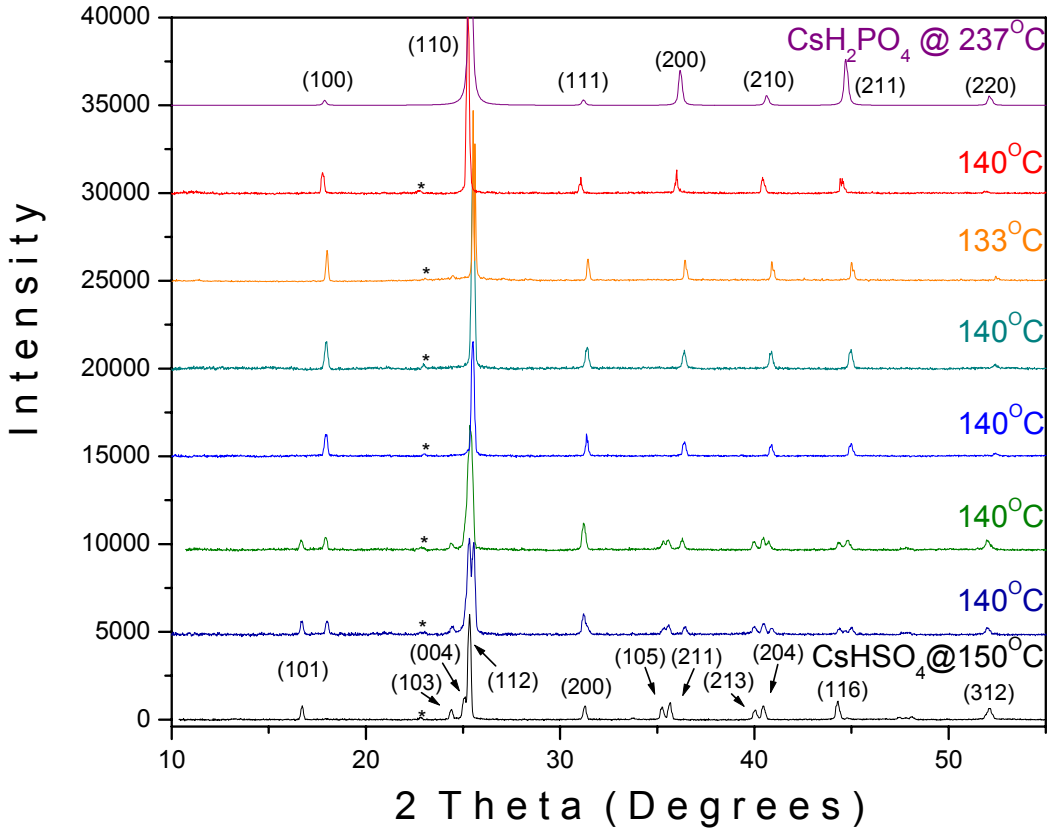

Figure 4.3 X-ray powder diffraction patterns of the mixed cesium sulfate-phosphates above their superprotonic phase transitions. The order of the patterns is the same as that shown in Figure 4.2. Peaks for the tetragonal and cubic structures of $CsHSO_4$ and CsH_2PO_4, respectively, have been indexed. The pattern for CsH_2PO_4 was calculated from the published structure[92]. The * indicates the position of K-beta peaks.

It is quite clear from Figure 4.3 that these high temperature diffraction patterns resemble that of $CsHSO_4$, CsH_2PO_4, or a combination of the two. These X-ray diffraction results, as well as that from preliminary neutron diffraction, advocate that these compounds exhibit only two structural types at elevated temperatures: a tetragonal body centered structure and a cubic structure similar to that of CsCl, Figure 4.4. The tetragonal structure has space group $I4_1/amd$ as determined by X-ray and neutron diffraction measurements on the superprotonic phase of $CsHSO_4$. High temperature X-ray powder

diffraction measurements on CsH_2PO_4 (under water saturated atmosphere) revealed that this phase's space group is most likely $Pm\bar{3}m$.

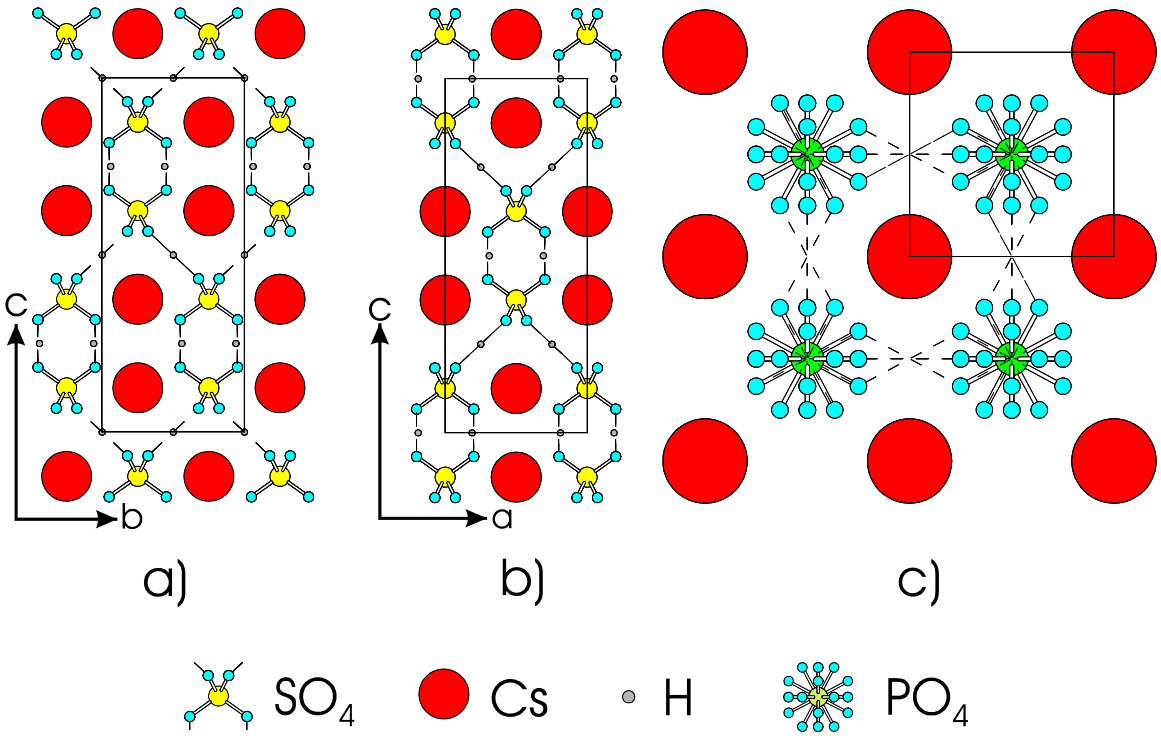

Figure 4.4 Proposed superprotonic structures for $CsHSO_4$ and CsH_2PO_4. The tetragonal phase of $CsHSO_4$ (Jirak's) is shown along its twofold axes a), b) and the cubic phase of CsH_2PO_4, c), viewed down [100]. Dashed lines represent the dynamically disordered hydrogen bonds. The two closely spaced oxygen atoms of the sulfate tetrahedra and hedgehog appearance of the phosphate groups are a result of tetrahedral disorder of the tetragonal and cubic phases (2 and 6, respectively)[61,92]. Rectangles represent the unit cells.

The tetrahedra in these structures are distributed over crystallographically identical orientations, the direction and number of which is of some debate in the literature. For the tetragonal phase of $CsHSO_4$, three distinct structures have been proposed, exemplified by those of Jirak, Merinov, and Belushkin[61,124,125]. These published structures are in agreement with respect to the lattice parameters and symmetry of the unit cell, as well as the position of the cesium and sulfur atoms, but in marked

disagreement in the position of the oxygen atoms. This disagreement is undoubtedly caused by the disorder of the oxygen atoms (i.e., tetrahedral reorientations), which make it extremely difficult to determine their exact positions. For the purpose of this paper, the disagreement boils down to there being either 2 (Jirak and Merinov) or 4 (Belushkin) orientations for the sulfate groups. Unfortunately, without further experimentation it is impossible to favor one published structure above the others. The entropy of the high temperature phases exhibiting this tetragonal structure will therefore need to be calculated with both 2 and 4 orientations of the tetrahedra. For CsH_2PO_4, and hence the other cubic phases, it is quite clear that the tetrahedral groups have six orientations[63,92].

The 2/4 versus 6 orientations of the tetrahedra is then the most relevant difference between the tetragonal and cubic structures, respectively, with regards to evaluating the configurational entropy of the high temperature phases. The X-ray diffraction peaks arising from the tetragonal and cubic structures are labeled for $CsHSO_4$ and CsH_2PO_4 in Figure 4.3. From a comparison of the patterns, it is evident that the high temperature forms of the $Cs_3(HSO_4)_{2.5}(H_2PO_4)_{0.5}$ and $Cs_3(HSO_4)_{2.25}(H_2PO_4)_{0.75}$ compounds consist of a combination of the tetragonal and cubic phases, whereas the other compounds are purely cubic. It should then be possible to calculate the entropy of these compound's high temperature forms once an entropy model for the tetragonal and cubic structures has been worked out and the amount of each structure in a phase is determined.

4.2.4 Key Features of the Superprotonic Phase Transitions

Although the X-ray diffraction patterns are quite convincing evidence that the high temperature phases are superprotonic, this assumption was not confirmed until the ionic conductivity was measured in these phases. Figure 4.5 shows conductivity for this

whole group of compounds, all of which exhibit a 2-3 order of magnitude jump in their conductivity from the low to high temperature phase. The disorder of the oxygen atoms, or alternatively, reorientations of the tetrahedra are responsible for the phenomenon of superprotonic conduction in solid acids[35]. The combination of X-ray diffraction and conductivity data then justifies assigning the disordered structures proposed for $CsHSO_4$ and CsH_2PO_4 to the rest of the high temperature phases of the mixed cesium sulfate-phosphates.

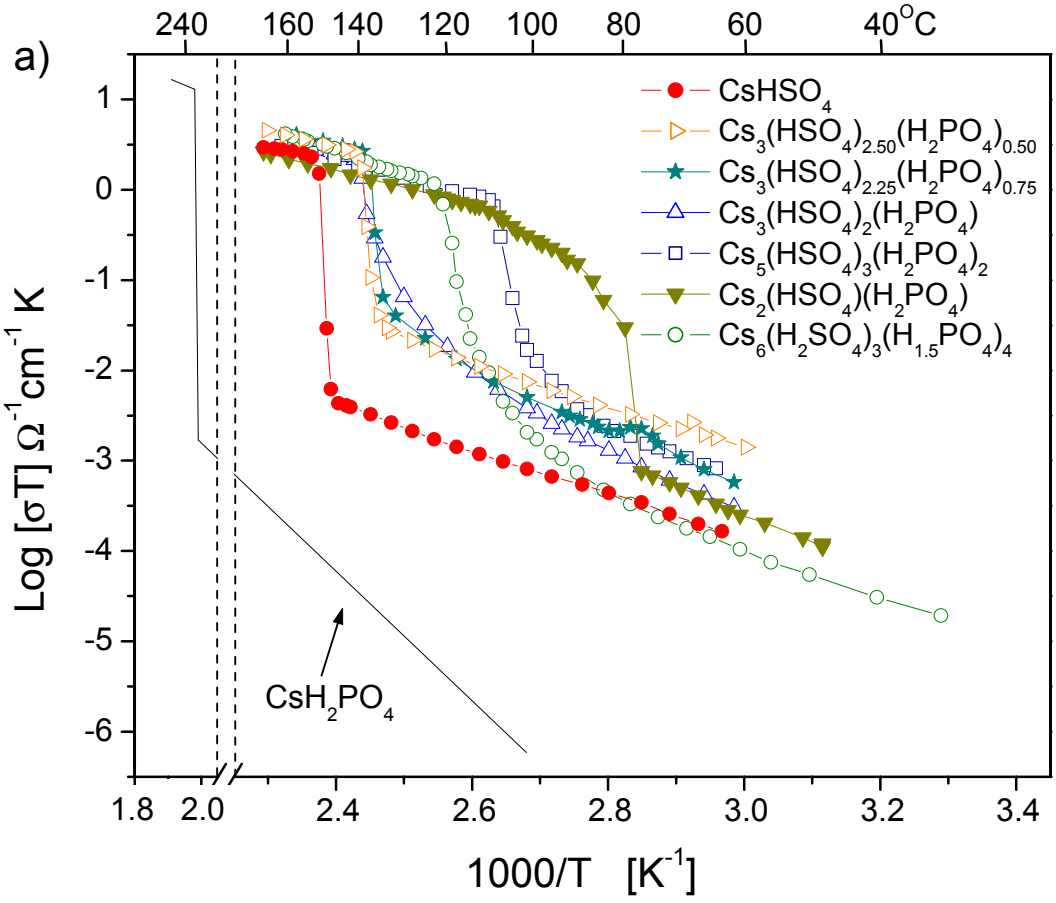

Figure 4.5 (See caption on next page.)

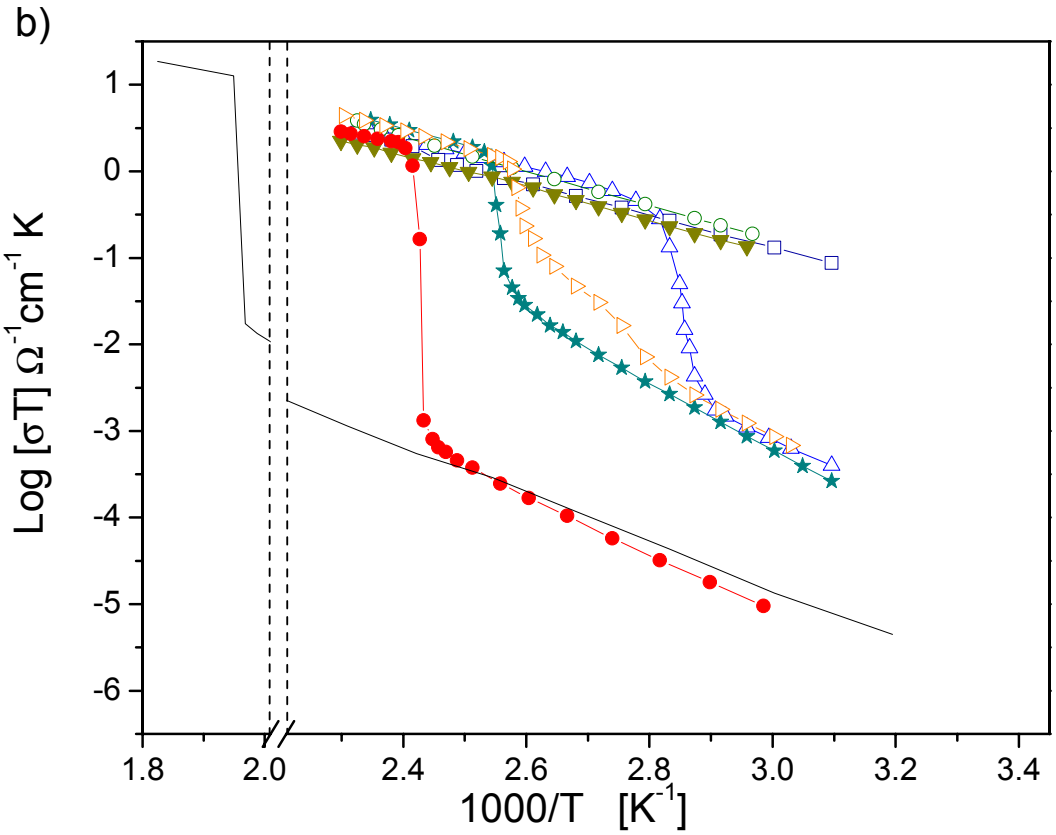

Figure 4.5 Protonic conductivity of the mixed cesium sulfate-phosphate compounds measured by a.c. impedance spectroscopy: a) upon heating of fresh (never heated) samples and b) upon cooling. All experiments were performed on pressed powder samples with heating/cooling rates of 0.5°C/min under dry argon, except for the CsH_2PO_4 compound. The heating data for CsH_2PO_4 was taken on a large single crystal sample to decrease the effect of surface dehydration[46]while the cooling data used pressure (1GPa) to inhibit decomposition of a pressed pellet sample[129]. The dashed lines represent cuts in the temperature axis and the jump in the cooling conductivity for CsH_2PO_4 in its low temperature phase is an artifact of the cut.

Before discussing the trends in these data, we note that there are moderate to large differences between the published transition enthalpies and those reported in this work (see Table 4.3). The discrepancy in the values could be due to many factors including (1) use of powder vs. single crystal samples, (2) difficulty in obtaining large quantities of

high quality crystals for many of the phases, and (3) sensitivity of material properties to very slight impurity concentrations. See appendix A for the specifics of these effects.

The greatest cause of variation between measurements is quite possibly the use of single crystal versus powdered samples. It is well documented that measurements on powdered samples of these compounds can give highly varying results due to surface interactions with water[92,130]. Powdered samples also tend to dehydrate sooner and it was likely just this effect that gave the erroneous ΔH of 7.6 J/mol for CsH_2PO_4's superprotonic transition[131]. Therefore, single crystal samples were used wherever possible and powder samples only when there was no alternative or because a measurement required it (e.g., powder X-ray diffraction experiments). Regardless of these potential sources of error, the values presented in this work should be internally consistent as they were obtained using exactly the same instruments, procedures and experimental parameters, and executed by the same individual.

Looking at Figure 4.5, it would appear that some properties correlate with phosphorous content, in particular the superprotonic transition temperature, whereas others show only a mild or even, erratic correlation. A summary of properties taken from conductivity, DSC, TGA, and PXD measurements is provided in Table 4.3, most of which are plotted versus phosphorous percentage in Figure 4.6. It can be seen in Figure 4.6 a, that from $CsHSO_4$ to $Cs_2(HSO_4)(H_2PO_4)$, the onset (σ) of the transitions drop from 144° to 78°C, respectively. This observed trend of falling transition temperatures with rising phosphorus content was the impetus behind this search for the entropic driving force of the transitions. Of course, from $Cs_2(HSO_4)(H_2PO_4)$ to CsH_2PO_4 the transition

temperature increases from 78° to 228°C, a fact that any entropic theory would also need to explain.

The transition range ($T[\sigma]_{final} - T[\sigma]_{onset}$) on heating also seems to show some dependence on phosphorous content changing from 6° to 31°C as the S:P ratio decreased from 1:0 to 1:1, respectively, and then back down to 3°C for a ratio of 0:1, Figure 4.6 b. An exception to the range-of-transition trend is found in $Cs_5(HSO_4)_3(H_2PO_4)_2$, which transforms much faster than the compounds with similar S/P ratios. This is probably due to its room temperature structure, being composed of alternating layers of $CsHSO_4$ and CsH_2PO_4 like layers, which is quite unique among the compounds (see section 4.4.5).

It is interesting to note that these increased transition ranges appear to be a thermodynamic, rather than kinetic, phenomenon. This conclusion was derived from the fact that the X-ray powder diffraction patterns measured in the transition regions showed a reproducible mixture of the room and high temperature phases. Moreover, these diffraction patterns confirmed the onset temperatures and ranges observed in the conductivity measurements even though the powders were held above the transition temperatures for ~ 2 hrs/pattern. Presumably, if the width of a transition upon heating is due to a kinetic process, the heating rate of the measurement would have a large effect on this width. However, thermal analysis on these compounds gave results data very similar to those of the conductivity and diffraction experiments. Experiments with nominal heating rates of ~ 5, .5, and 0.05°C/min (DSC, σ, PXD rates, respectively) then all gave roughly the same values and therefore, the spans of the transitions should truly be a result of the thermodynamics of the phase.

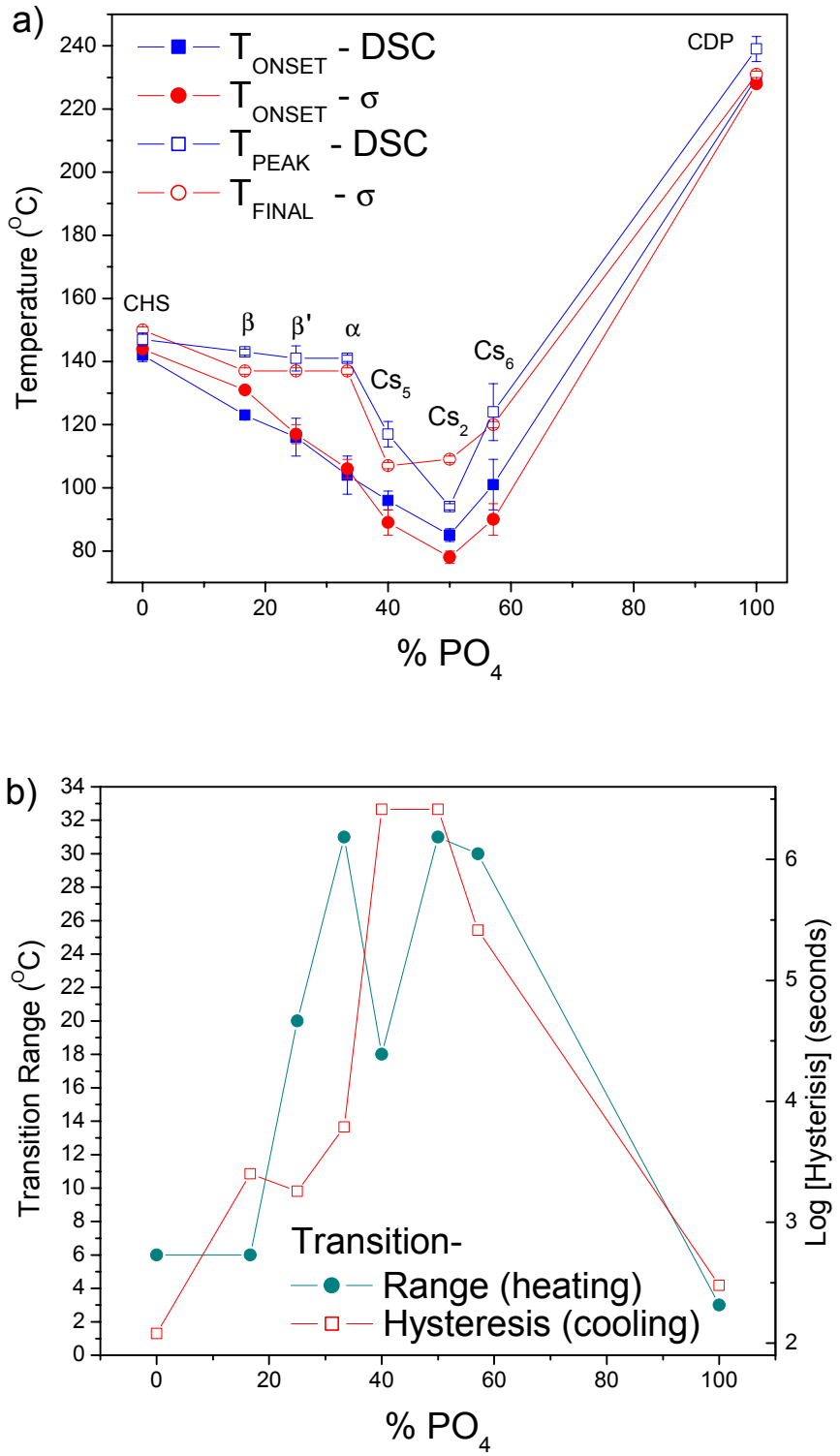

Figure 4.6 (See caption on next page.)

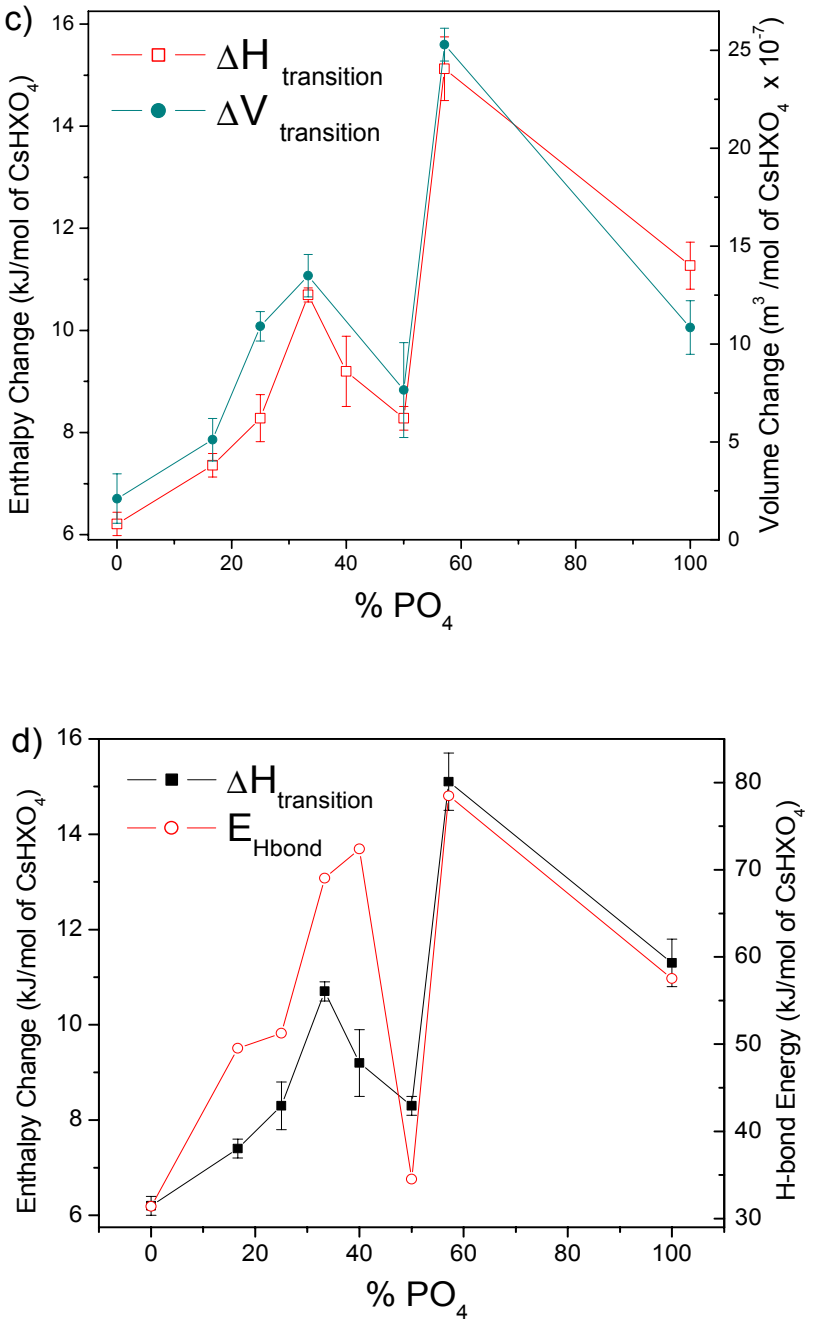

Figure 4.6 Various transition properties versus phosphate percentage: transition a) temperature upon heating by various definitions, b) range and hysteresis upon heating and cooling, respectively, c) enthalpy and volume change, and d) enthalpy compared to H-bond energy of RT structures. The range and hysteresis values taken from conductivity data collected at 0.5°C/min in ambient atmospheres. DSC data obtained at 5°C/min under flowing N_2. Transition volume changes calculated from PXD pattern refinements (see appendix A for measurement specifics). H-bond energies calculated using H-bond energy vs. O-O distance correlation[21] and RT structures (references on Table 4.2).

Upon cooling, the presence of phosphate groups has perhaps an even more dramatic effect, with some of the higher phosphorus content compounds revealing no reverse transition in both the temperature and time scale of the conductivity measurements, Figure 4.5 b. This effect has been quantified as the hysteresis, temperature difference between the end of the transition on heating and beginning of the transition on cooling, and is shown as function of PO_4 percentage in Figure 4.6 b. As measured by powder X-ray diffraction, this transition hysteresis from a high to low temperature form can last from days to months (see Appendix A). However, this trend does not directly correlate to the increasing phosphate content of the compounds going from $CsHSO_4$ to CsH_2PO_4. Even if the results of the $Cs_6(H_2SO_4)_3(H_{1.5}PO_4)_4$ compound are excluded because of its unusual $Cs:XO_4$ ratio, recent experiments on CsH_2PO_4 have definitely shown a very fast superprotonic transition to occur above 230°C with a hysteresis effect upon cooling similar to that found in $CsHSO_4$[129].

Furthermore, the behavior of the transitions for the $Cs_3(HSO_4)_{2.5}(H_2PO_4)_{0.5}$, $Cs_3(HSO_4)_{2.25}(H_2PO_4)_{0.75}$, and $Cs_3(HSO_4)_2(H_2PO_4)$ compounds on cooling seem to be reversed with the higher phosphorus content compound transforming rapidly from the high to low temperature phase, while the compound with the least amount of phosphorous transforms over a range of 38°C, Figure 4.5 b. These compounds also show a strange behavior to the onset temperature of the reverse transitions, with a hysteresis of 22, 16, and 53 degrees for the $Cs_3(HSO_4)_{2.5}(H_2PO_4)_{0.5}$, $Cs_3(HSO_4)_{2.25}(H_2PO_4)_{0.75}$, and $Cs_3(HSO_4)_2(H_2PO_4)$ compounds, respectively. Again, the phosphate content of the three compounds does not obviously relate to the observed trend. These mixed compounds

Table 4.3 Thermodynamic parameters of the superprotonic phase transitions. The sometimes large errors of the values are due to variations *between* measurements. These variations were particularly noticeable for the compounds with drawn-out transitions and did not decrease significantly with the number of measurements. Numbers in [ ] brackets are the published values.

Compound (Sample type)-abbreviation	T_{sp} – Onset, DSC (ºC)	T_{sp} – Onset, σ(ºC)	T_{sp} – Peak, DSC (ºC)	T_{sp} – Final, σ(ºC)	$T_{melt/decomp}$ (ºC)	ΔH_{sp} (kJ/mol)	ΔV_{sp} (m^3/mol)*x 10^{-7}	refs
$CsHSO_4$-II	142(2)	144(1)	147(2)	150(1)	Melt-200(3)	6.2(2)	2.1(13)	[4,59,130]
(Single crystals)-CHS	[142(2)]	[139]	[145(2)]	[141]	[205]	[5.5]	[1.7]	
$Cs_3(HSO_4)_{2.50}(H_2PO_4)_{0.50}$	123(1)	131(1)	143(1)	137(1)	Melt-175(3)	7.4(2)	5.1(11)	[132]
(Single crystals)-β	[130.8]	[119(2)]	[140.2]	[129(2)]		[6.9(2)]		
$Cs_3(HSO_4)_{2.25}(H_2PO_4)_{0.75}$	116(6)	117(3)	141(4)	137(1)	Melt-150(2)	8.3(5)	10.9(8)	
(Powder)- β′								
$Cs_3(HSO_4)_2(H_2PO_4)$	104(6)	106(3)	141(1)	137(1)	Melt-148(2)	10.7(2)	13.5(11)	[30,127]
(Single crystals)-α	[139]	[111]	[143]	[125]	[150]	[9.2]		
$Cs_5(HSO_4)_3(H_2PO_4)_2$	96(3)	89(4)	117(4)	107(1)	Decomp-180(2)	9.2(7)	N/A	[133]
(Powder)-Cs_5	[110(2)]		[116(2)]			[10.2]		
$Cs_2(HSO_4)(H_2PO_4)$	85(2)	78(2)	94(1)	109(1)	Decomp-185(2)	8.3(2)	7.6(24)	[27,63]
(Single crystals)-Cs_2	[61]	[75(2)]	[65]	[110(1)]	[187]	[10.1(5)]		
$Cs_6(H_2SO_4)_3(H_{1.5}PO_4)_4$	101(8)	90(5)	124(9)	120(1)	Decomp-200(3)	15.1(6)	25.3(8)	
(Single crystals)-Cs_6								
CsH_2PO_4	230(2)	228(1)	239(4)	231(1)	Decomp-203(3)	11.3(5)	[10.8(14)]	[46,92,93,134]
(Single crystals)-CDP	[230]	[229(1)]	[233(1)]	[232(1)]	[175]	[7.6]		

*Values are given per molar unit of $CsHXO_4$; the $Cs_6(H_2SO_4)_3(H_{1.5}PO_4)_4$ compound was assigned a value of 6.4 molar units (based on MW ratios, interatomic distances, and simple geometric considerations) when converting the ΔH and ΔV from the measured units.

then have a very complicated set of reverse transitions. Any possible overarching explanation for the behavior of these transitions with respect to the phosphorus content of the compounds is likely to be similarly complex. At this time and with the limited data available, no such model presents itself which sufficiently explains the varying behavior of these compounds upon cooling.

A look at Figure 4.6 c shows that the change in transition enthalpies with phosphate percentage is closely mimicked by the volume change of the transitions. This would suggest that the amount of energy required to transform into a high temperature phase is directly linked to the increase in volume necessary to achieve that phase's structure. However, the work required for even the substantial transition volumes of these compounds is inconsequential (at ambient atmosphere). For the $Cs_6(H_2SO_4)_3(H_{1.5}PO_4)_4$ compound, with the largest volume change, the reversible work done by the crystal would only be $P\Delta V \cong (1x10^5\ Pa)*(25.3x10^{-7}\ m^3/mol\text{-}CsHXO_4) \cong 0.25\ m^3Pa/mol = 2.5x10^{-4}$ kJ/mol, an insignificant value when compared to the transition enthalpies. It must then be the internal energies of the compounds which are changing across the transitions.

This change in the internal energy is most easily attributed to the loss of ionic and hydrogen bond energies, resulting from increased interatomic distances and the dynamic behavior of the high temperature phases. With respect to the hydrogen bond energy, this statement is supported by Figure 4.6 d, which shows a fairly good correlation between the transition enthalpies and their RT structure's mean hydrogen bond energy. This mean energy was calculated using the published O-O distances and multiplicities of the hydrogen bonds and the energy versus O-O distance function given by Lippincott et al.[21].

The observed correlation is quite logical since the more hydrogen bond energy a compound has at room temperature, the more it has to lose when transforming to a higher volume structure, which will necessarily show-up in the transition enthalpy. This statement is particularly true for compounds which have similar high temperature structures (i.e., the pure cubic phases). The $Cs_5(HSO_4)_3(H_2PO_4)_2$ compound, as with the range-of-transition trend, is the odd man out, which is again attributed to its unusual structure.

Of course there must be an energetic advantage to a transition or it will not happen. This energetic benefit is most easily modeled through a configurational entropy change across a compound's transition which we can compare to the experimental value, derived from the measured transition enthalpy and temperature via $\Delta G = 0 \Rightarrow \Delta S = \Delta H/T_c$. It is therefore the experimental entropies that these calculations will aim to duplicate.

4.3 Introductory Comments on Entropy Rules

The following two sections will set down the rules used in calculating the configurational entropy of each compound's room and high temperature structure, and thereby, the entropy change (disregarding other non-structural forms of disorder) of its superprotonic transition. That two different sets of rules are required for evaluating the entropy of the low and high temperature phases is probably not surprising. However, the fact that the entropy rules for the "static" low temperature structures are actually more complicated and subjective than those that describe the "dynamically disordered" superprotonic phases, was indeed unexpected (at least to this researcher). After all, at

room temperatures the exact positions of the compounds' atoms are known. Any configurational entropy should, as a result, be easily identified and accounted for. Unfortunately, in appraising the entropic contributions from symmetric hydrogen bonds, mixed S/P sites, and partially occupied hydrogen positions, many "best guess" estimates will have to be made based on the results of relevant literature and its implications to the particular structure in question.

In contrast, the rules applied to the highly disordered, but also highly symmetric, superprotonic phases are quite universal; applying equally well to both the cubic and tetragonal structures. The process for evaluating the entropy of these phases combines Pauling's ice rules for the calculation of the residual entropy of ice at 0 K with the orientational disorder of the tetrahedra[135]. This approach gives a much better agreement to experimental results than traditional methods which focus on only the disordering of the protons or on tetrahedral reorientations, but not both[136,137].

4.4 Entropy Rule for Room Temperature Structures

Contributions to the entropy of the room temperature structures come from two basic sources: mixed S/P sites and hydrogen bond disorder. The mixed S/P tetrahedra result in the well-known entropy of mixing for two species on one site:

$$S_{mix} = -R[(1-N_1)\ln(1-N_1) + N_1\ln(N_1)] \qquad (4\text{-}1)$$

where N_1 and $(1-N_1)$ are the mole fractions of S and P (or vice versa) on the site and R is the universal gas constant = 8.314 J/mol*K. However, in these compounds, the local density of hydrogen around a tetrahedron should (very generally) be more nearly 2 for a

phosphate and 1 for a sulfate. An alternative phrasing for this fact is that the phosphates are usually involved in four hydrogen bonds (1 per oxygen), while sulfate tetrahedron typically participate in two hydrogen bonds. This general rule is followed in all the room temperature phases of these compounds (except the $Cs_5(HSO_4)_3(H_2PO_4)_2$ and $Cs_6(H_2SO_4)_3(H_{1.5}PO_4)_4$ compounds) and agrees with the difference in p*K* values of phosphoric and sulfuric acid[138]. Therefore, one might expect that the particulars of the local structure will greatly affect the specifics of the local hydrogen bonds. There would then be a direct correlation between the local occupancy of a mixed S/P site and the second source of entropy in these room temperature phases, hydrogen bond disorder.

This disorder of the hydrogen bonds comes in two forms: partial occupation and symmetric distribution. The presence of partially occupied hydrogen bonds occurs only in the structures of $Cs_3(HSO_4)_{2.50}(H_2PO_4)_{0.50}$ and $Cs_3(HSO_4)_{2.25}(H_2PO_4)_{0.75}$, while all but the $CsHSO_4$ and $Cs_6(H_2SO_4)_3(H_{1.5}PO_4)_4$ compounds, have symmetric hydrogen bonds linking some of their tetrahedra. The entropy of either a partially occupied pair of hydrogen bonds or a proton disordered over two sites within one hydrogen bond (per CsH_nXO4 unit) is

$$S_{config} = \frac{(Occupancy * 2) * R * \ln(2)}{(\#\ of\ CsH_n XO_4\ units\ per\ H-bond\ pair)} \qquad (4\text{-}2)$$

where the occupancy of one bond is multiplied by two to give the occupancy of the pair and the occupancy on a disordered proton site is defined as 1/2. The evaluation of Eq. (4-2) will best be done with a specific structure in mind. Moreover, the local ordering of the S/P sites leads to a rather compound specific determination of how to apply Eq. (4-2).

4.4.1 Entropy of $CsHSO_4$ and $Cs_6(H_2SO_4)_3(H_{1.5}PO_4)_4$ ⇒ZERO!

For the $CsHSO_4$ and $Cs_6(H_2SO_4)_3(H_{1.5}PO_4)_4$ compounds, calculating their room temperature entropy is trivial as both compounds have neither mixed S/P sites nor any form of disordered hydrogen bonds, Figures 4.7.

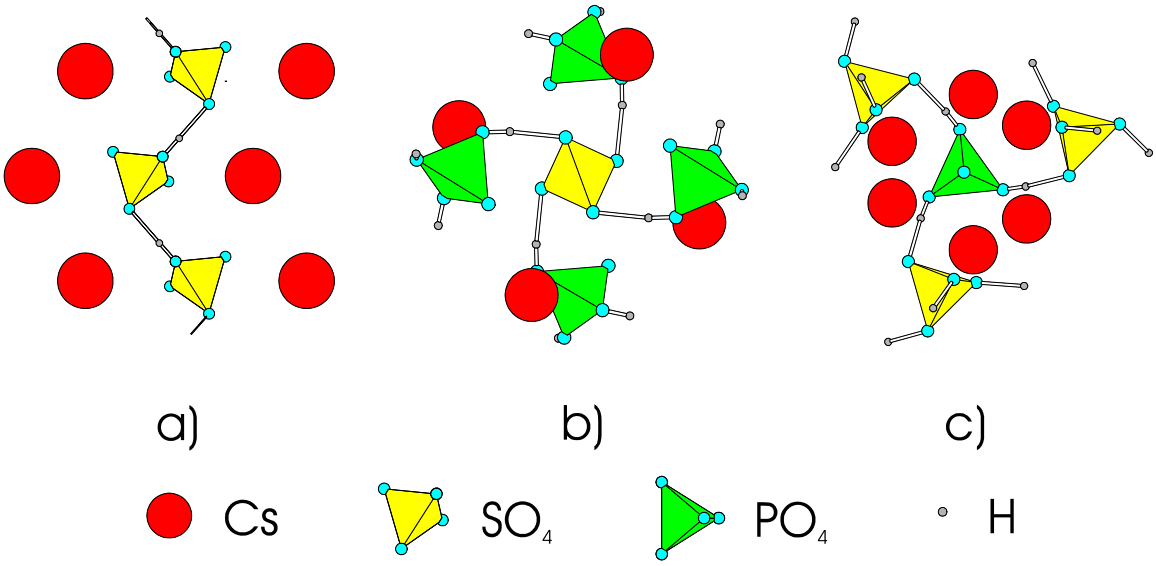

Figure 4.7 Arrangement of the hydrogen-bonded tetrahedra for a) the sulfate chains of $CsHSO_4$ and b) the sulfate and c) phosphate groups of $Cs_6(H_2SO_4)_3(H_{1.5}PO_4)_4$. Asymmetric bonds connect all tetrahedra. Note the peculiar arrangement of the hydrogen bonds in b) and c) where the sulfate and phosphate groups are involved in 4 and 3 hydrogen bonds, respectively.

By definition, $CsHSO_4$ has no mixed S/P sites and as the hydrogen bonds linking the sulfate groups into chains are ordered (Figure 4.7 a), there is only one crystallographic configuration to the room temperature structure. $CsHSO_4$ then has no configurational entropy below the phase transition. The $Cs_6(H_2SO_4)_3(H_{1.5}PO_4)_4$ compound owes its lack of entropy to the fact that it has only one crystallographic sulfate and phosphate group with hydrogen bonds connecting only dislike tetrahedra, Figure 4.7 b and c. There are then no mixed S/P sites and since the hydrogen bonds are between

ordered tetrahedra of a different nature, they are necessarily asymmetric. This structure consequently has only one configuration and zero configurational entropy.

4.4.2 Entropy evaluation for CsH_2PO_4 –the disordered hydrogen bond

Unfortunately, there are no such definitive statements concerning the entropy associated with a symmetric, double-minimum hydrogen bond. This type of bond is found in CsH_2PO_4 where such disordered hydrogen bonds link the tetrahedra into zigzag chains along the *b*-axis, Figure 4.8.

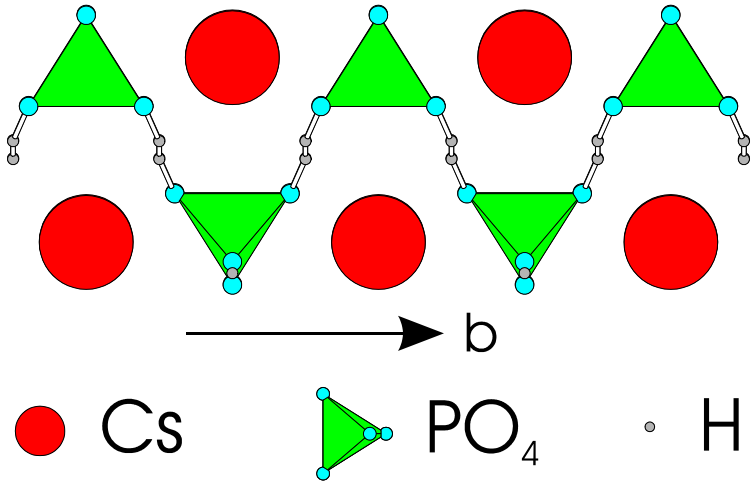

Figure 4.8 Disordered hydrogen bonds in CsH_2PO_4 connect the phosphate groups into zigzag chains along the b-axis[139]. Chains are cross-linked by asymmetric hydrogen bonds, so the disordered chains are pseudo-one-dimensional with respect to ferroelectric behavior.

Classically, a double-minimum potential hydrogen bond will have the proton residing equally in each minimum with a resulting entropy contribution, using the formulation of Eq. (4-2), of (1/2*2)*R* ln(2)/1 = R*ln(2) = 5.76 J/(mol*K), where here the pair refers to the two equivalent proton positions. It turns out that for CsH_2PO_4 this classical value is almost double that found experimentally, the possible cause of which will be discussed here.

Upon cooling, CsH_2PO_4 exhibits a second-order ferroelectric phase transition at 159 K with spontaneous polarization along the *b*-axis (parallel to the symmetric hydrogen bonds) [140]. As well as being connected into zigzag chains by the symmetric hydrogen bonds, each tetrahedra is also hydrogen-bonded by two asymmetric hydrogen bonds, resulting in straight chains running perpendicular to the ferroelectric *b*-axis (see Figure 4.1 c and d). These cross-linking hydrogen bonds have a weak interaction with the disordered protons of the zigzag chains. CsH_2PO_4's ferroelectric transition is therefore most often evaluated using a pseudo-one-dimensional Ising model. The classical Hamiltonian of such a model in an external electric field, E, is

$$\mathcal{H} = -\sum_{i,j}\left(J_{//}\sigma_{i+1,j}\sigma_{i,j} + J_{\perp}\sigma_{i,j+1}\sigma_{i,j} + \mu E\sigma_{i,j} \right) \tag{4-3}$$

where the two possible values of the pseudospin variable, $\sigma = \pm 1$, represent the position of the proton in the double minima potential well and μ is the electric dipole moment of the spins[141]. $J_{//}$ and $J_{\perp}$ are, respectively, the intrachain (from protons along the zigzag chains) and interchain (from protons in the straight chains) interactions acting upon the disordered protons of the zigzag chains. The weak interchain coupling is essential to properly describe the ferroelectric phase transition as the exactly solvable one-dimensional Ising Hamiltonian (which excludes the second term of Eq. 4-3) does not produce a phase transition for any finite temperature[142].

Using experimental data from heat capacity, dielectric, and solid state NMR measurements, the ferroelectric transition of CsH_2PO_4 has been modeled using Hamiltonians identical or very similar to that in Eq. (4-3)[140,143,144]. The ratio of weak interchain to strong intrachain interactions, $J_{\perp} / J_{//}$, is consistently found to be on the order

of 1:100[145]. Such models describe well the critical slowing down of the dielectric relaxation time, as well as the heat capacity jump of and temperature of the transition. However, anomalous behavior in the heat capacity and dielectric measurements were observed significantly above and below the transition ($T_c \pm 60$ K), which cannot be described using Eq. (4-3). This property was universally attributed to abnormally large polarization fluctuations which develop below the ferroelectric transition and continue well into the paraelectric phase. Theoretical discussions of these polarization fluctuations suggest they are due to anisotropic short range correlations, from the interaction of $J_{//}$ and $J_{\perp}$, resulting in local order extending along the symmetrically bonded chains[141]. Such fluctuations would be due to mainly the strong intrachain interaction and should therefore be most evident for temperatures with $kT < J_{//}$ [146]. Indeed, the anomalous behavior of the heat capacity and dielectric constant measurements ends well before the average value of $J_{//} / k \approx$ 275 K.

The other inconsistency with theory based on the Hamiltonian of Eq. (4-3) comes in the total transition entropy. Even including the entropy of the anomalous regions, the measured entropy changes were in the range of 1.05(1)-3.2(1) J/(mol*K), much smaller than the expected value of R*ln(2) = 5.76 J/(mol*K)[143,145]. Although it has not been suggested in the literature, this rather large difference between the theoretical and measured transition entropy would seem (to this author) to be related to the anomalous behavior seen in the heat capacity and dielectric measurements credited to short range order running "along the chain(s) for many fundamental chain lengths."[141] It seems possible that the chains have some small amount of local order even outside the measured anomalous temperature ranges found in the experiments. This is particularly likely as

these anomalous regions were defined by a baseline fit to the heat capacity curves, with the result that the anomalous temperature range and total calculated entropy change were quite dependent on the form of the baseline fit[143]. For temperatures with $J_{//}/kT < 1$, the length scale of any such ordering would be quite small, and yet even an average local order involving only two hydrogen bonds would decrease the entropy of the transition to 1/2*R*ln(2) = 2.88 J/(mol*K), a value much closer to those measured. Such a very short range ordering would be extremely difficult to measure by the heat capacity and dielectric experiments due to the very large temperature and frequency ranges, respectively, necessary to discern the effect.

There is then a dilemma as to the amount of entropy that should be associated with a disordered symmetric hydrogen bond. For CsH_2PO_4, this value would seem to be in the range $3.2 \leq \Delta S \leq R*\ln(2) = 5.76$ J/(mol*K). However, as the superprotonic phase transition occurs nearly 350, 290, and 230 K above the ferroelectric transition, the end of the anomalous regions, and $J_{//}/k$, respectively, a value closer to the full R*ln(2) appears more likely. Hence, the "best guess" value for the entropy of CsH_2PO_4's disordered hydrogen bonds is exactly what one would expect a priori, $S_{Hbonds} = R*\ln(2)$. The last three pages may therefore seem unnecessarily pedantic, but their purpose was to lay the foundation for compound specific arguments on the entropic contribution of other symmetric hydrogen bonds found in the room temperature phases, where the "best guess" value may not be that derived from statistical mechanics. Specifically, the interchain and intrachain interactions should vary significantly from structure to structure, which the above discussion tells us will have a large effect on the behavior of protons in double-mimima potential wells.

For example, the behavior of CsH_2PO_4 near its ferroelectric transition is quite different from that of the related compounds KH_2PO_4, RbH_2PO_4, and $PbHPO_4$ due to the different dimensionality (3-D, 3-D, and more fully 1-D, respectively) of those compounds hydrogen-bonded networks[140,144]. Moreover, for the compounds in question, the disordered hydrogen bonds are almost always situated between the mixed S/P sites. The average structure seen by X-ray diffraction methods could then be a compilation of locally ordered structures distributed at random, depending on only the occupants of the nearby mixed S/P sites. This was exactly the result found from a neutron diffraction measurement taken on $Cs_3(HSO_4)_{2.50}(H_2PO_4)_{0.50}$ at 15 K, where the average structure reported from X-ray diffraction methods at 298 K was resolved into two different, but related, local structures (discussed below in section 4.4.3)[72]. It would then seem that the entropy contribution from a disordered hydrogen bond will have to be evaluated independently for each compound. Generally, the most reasonable conclusion reached for these mixed compounds is that the local occupation of the S/P sites causes an effective ordering of the protons, thereby greatly diminishing or completely negating the entropic contribution from the disordered hydrogen.

4.4.3 Entropy of $Cs_3(HSO_4)_{2.50}(H_2PO_4)_{0.50}$ and $Cs_3(HSO_4)_{2.25}(H_2PO_4)_{0.75}$ – partially occupied hydrogen bonds

The structure of $Cs_3(HSO_4)_{2.50}(H_2PO_4)_{0.50}$ is composed of zigzag chains of hydrogen-bonded tetrahedra and Cs cations arranged almost identically to those in

$CsHSO_4$ but with phosphate groups inserted into every third tetrahedral site of a chain, Figure 4.9. The ensuing mixed tetrahedra have a S:P ratio of 1.

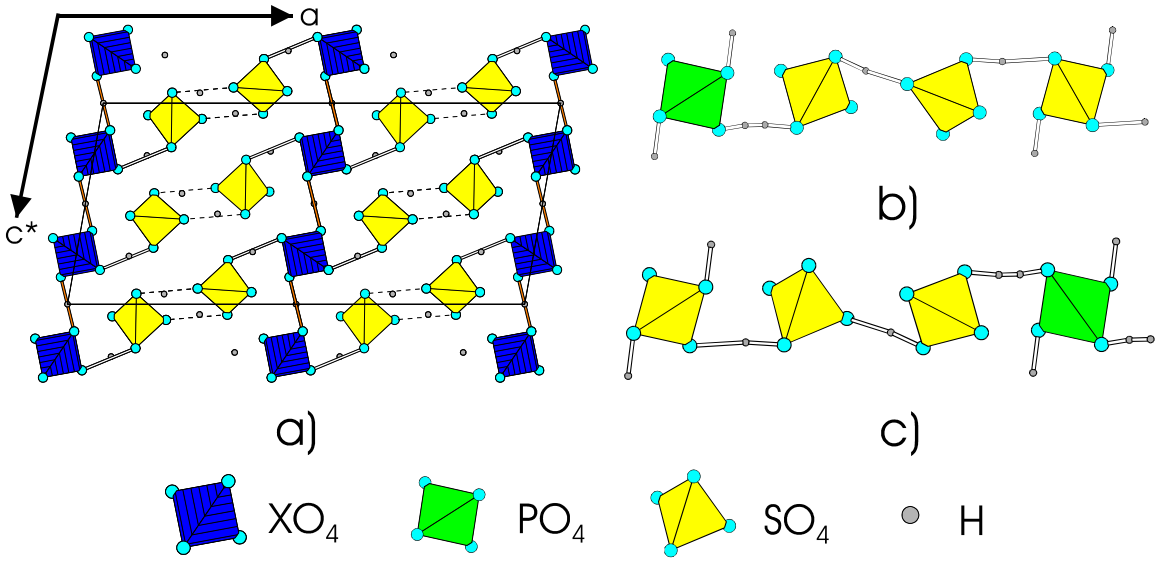

Figure 4.9 Room temperature structure of $Cs_3(HSO_4)_{2.50}(H_2PO_4)_{0.50}$. Averaged structure (from X-ray) view down the b-axis, a), shows the altered zigzag chains of CsHSO4 running in the [10-1] direction while the symmetric hydrogen bonds between the mixed tetrahedra form chains in the [001] direction[32].Two variants (from neutron) of the averaged structure along the zigzag chains, b) and c), showing the effect of local order on hydrogen bonding[72]. The rectangle shows a unit cell and Cs atoms are absent for clarity.

With respect to the evaluation of the entropy of this compound, the addition of phosphates to $CsHSO_4$'s zigzag chains has three effects: the obvious introduction of mixed S/P sites, formation of symmetric hydrogen bonds linking the mixed tetrahedra of neighboring chains, and the creation of a symmetry related pair of partially occupied hydrogen bonds between the adjacent SO_4 groups of the zigzag chains, Figure 4.9 a. The contribution of the mixed sites to the structures entropy can be evaluated by Eq. (4-1), giving $S_{mix} = -(1/3)*R[(1/2*\ln(1/2)+1/2*\ln(1/2)] = (1/3)*0.69*R = 1.92$ J/mol*K, where the factor of 1/3 comes from the fact that there is only one mixed site for every three moles of $CsHXO_4$ unit.

The entropy contribution from the symmetric bonds can be evaluated with much less work than that of CsH_2PO_4 due to very precise diffraction measurements and structure refinements. The structure of $Cs_3(HSO_4)_{2.50}(H_2PO_4)_{0.50}$ has been studied by both single crystal X-ray and neutron diffraction experiments at 298 and 15 K, respectively. In the room temperature X-ray measurement, the symmetric bond between the mixed tetrahedra was thought to be disordered. This assignment was based on the bond's O-O distance of 2.474(9) Å, which is above the lower limit of observed double-minimum symmetric bonds, and its similarity to other disordered hydrogen bonds such as those found in CsH_2PO_4[32]. However, the low temperature neutron experiment found "unsatisfying" thermal displacement parameters in the refinement using a disordered hydrogen bond. Furthermore, the persistence of the center of symmetry at such low temperatures indicates the lack of a ferroelectric transition[72]. The hydrogen of this bond was therefore fixed at the symmetry position, thereby making the symmetric bond ordered with no entropic contribution to the room temperature structure.

This leaves only the entropy of the partially occupied hydrogen bonds to evaluate. Using the structure resolved by X-ray diffraction measurements, Figure 4.9 a, these bonds have proton sites with 1/4 occupancy, so that only half of the SO_4-SO_4 neighbors along the chains are joined by hydrogen bonds[72]. From Eq. (4-2), the entropy per CsH_nXO_4 unit of these partially occupied proton sites is then S_{Hbond} = (1/3)*(1/4*2)*R *ln(2) = 1/6*R*ln(2) = 0.96 J/mol*K, corresponding to only one of these sites being occupied, on average, for every six adjoining tetrahedra down a chain.

From the neutron data, it was possible to resolve the average structure found by the X-ray measurements into two variants that differed in the local order of the mixed

sites, leading to two different hydrogen bonded schemes, Figure 4.9 b) and c). For each of these variants, the central hydrogen bond is 1/2 occupied, so that again on average only one of these hydrogen bonds will exist for every six neighboring tetrahedra. The entropy calculated using this locally ordered model is then the same as that calculated using the averaged structure, $S_{Hbond} = (1/6)*(1/2*2)*R*\ln(2) = 0.96$ J/mol*K. Although the locally ordered (but globablly disordered) model seems to more accurately represent the real structure of $Cs_3(HSO_4)_{2.50}(H_2PO_4)_{0.50}$, the equivalence between the entropy contribution from both models is convenient as the difference between their refinement residuals is very small, and therefore neither structure can be conclusively ruled out.

The $Cs_3(HSO_4)_{2.25}(H_2PO_4)_{0.75}$ compound is assumed to have a nearly identical structure to that of $Cs_3(HSO_4)_{2.50}(H_2PO_4)_{0.50}$ based on the results of X-ray powder diffraction measurements and the stated stoichiometry was taken from the results of electron microprobe experiments (shown in appendix A). This ability to vary the molar ratio of $Cs_3(HSO_4)_{2.50}(H_2PO_4)_{0.50}$ was proposed with the original structural determination due to the observation that the S:P ratio was not fixed by the crystal structure, additional phosphates simply decreasing the S:P ratio of the mixed tetrahedra[132]. For the stoichimetry of this compound, the S:P ratio becomes 1:3. The entropy of mixing is then $S_{mix} = -(1/3)*R[(1/4*\ln(1/4)+3/4*\ln(3/4)] = (1/3)*0.56*R = 1.56$ J/mol*K.

The higher phosphate content will also increase the hydrogen content of the compound with the most logical conclusion being that the proton occupancy of the partially occupied hydrogen bonds increases from 1/4 to 3/8. This results in an entropy, per CsH_nXO4 unit, of $S_{Hbond} = (1/3)*(3/8*2)*R*\ln(2) = 1/4*R*\ln(2) = 1.44$ J/(mol*K). Or, in terms of the locally ordered model, the proton occupancy for each structural

variant increases from 1/2 to 3/4, to which is associated an entropy of S_{Hbond} = (1/6)*(3/4*2)*R*ln(2) = 1/4*R*ln(2) = 1.44 J/(mol*K). Again, the entropy contribution from these partially occupied hydrogen bonds being equivalent for both the average and locally ordered models.

4.4.4 Room Temperature Entropy of $Cs_3(HSO_4)_2(H_2PO_4)$

In this compound every third tetrahedra in the zigzag chains is fully occupied by a phosphate group, Figure 4.10.

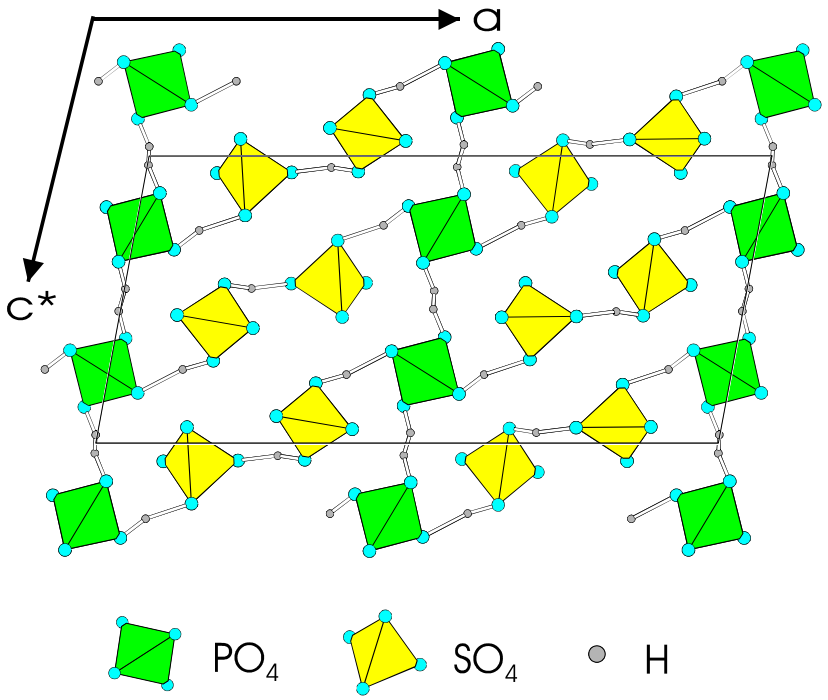

Figure 4.10 Structure for $Cs_3(HSO_4)_2(H_2PO_4)$ with emphasis on the similarity to the structures of $Cs_3(HSO_4)_{2.50}(H_2PO_4)_{0.50}$ and $Cs_3(HSO_4)_{2.25}(H_2PO_4)_{0.75}$. The fully occupied PO_4 site results in ordered hydrogen bonds between all tetrahedra except for the bonds between the phosphate groups where two distinct disordered bonds link the phosphates into chains along [001][30]. Otherwise, the arrangement of anions and cations is nearly identical to the two related compounds. The rectangle shows the unit cell and Cs atoms have been removed for the purpose of clarity.

This compound's only form of disorder in the room temperature phase comes from two crystallographically distinct disordered hydrogen bonds connecting the phosphate groups into chains down the [001] direction. These chains are structurally very similar to those found in CsH_2PO_4, although here the disordered chains should have a very small interchain interaction as they are separated by two sulfate tetrahedra, instead being directly linked to each other as in CsH_2PO_4. The chains should therefore be more one-dimensional than those of CsH_2PO_4 and it would be surprising to find a ferroelectric transition except very close to 0 K. The entropy will therefore be taken to be the classical value, per $CsHXO_4$ unit, which gives an entropy of (1/6)*(1/2*2)*R*ln(4) = (1/3)*R *ln(2) = 1.92 J/mol*K to the room temperature structure.

4.4.5 Room Temperature Entropy of $Cs_5(HSO_4)_3(H_2PO_4)_2$

This compound has a structure that has been described as being composed of alternating layers of $CsHSO_4$ and CsH_2PO_4 like regions due to the checkerboard arrangement of hydrogen bonded chains and Cs rows when view down the c-axis, Figure 4.11 a. A comparison with Figure 4.1 b reveals the similarity of layer I to $CsHSO_4$ when one looks down the zigzag chains of the structures, while Figure 4.1 c shows the anions and cations in CsH_2PO_4 distributed almost identically to layer II except for small differences in the orientation of the tetrahedra and hydrogen bonds. Crystallographically, there are two distinct mixed tetrahedra and three distinct symmetric hydrogen bonds in the structure. The mixed sites, labeled as 1 and 2 in Figure 4.11, have site multiplicities of 4 and 8, respectively. Both mixed tetrahedra have an S:P ratio of 1:2 and the remaining tetrahedral site is solely occupied by SO_4 groups with a multiplicity of 8. There are then 20 tetrahedra in the unit cell with 12 mixed sites of (S,P) occupancy (1/3,2/3). The

entropy of mixing from these sites per $CsHXO_4$ unit is then, S_{mix} = -(12/20)* R*[(1/3)*ln(1/3) + (2/3)*ln(2/3)] = (12/20)*R*[0.366 + 0.270] = 3.175 J/mol*K.

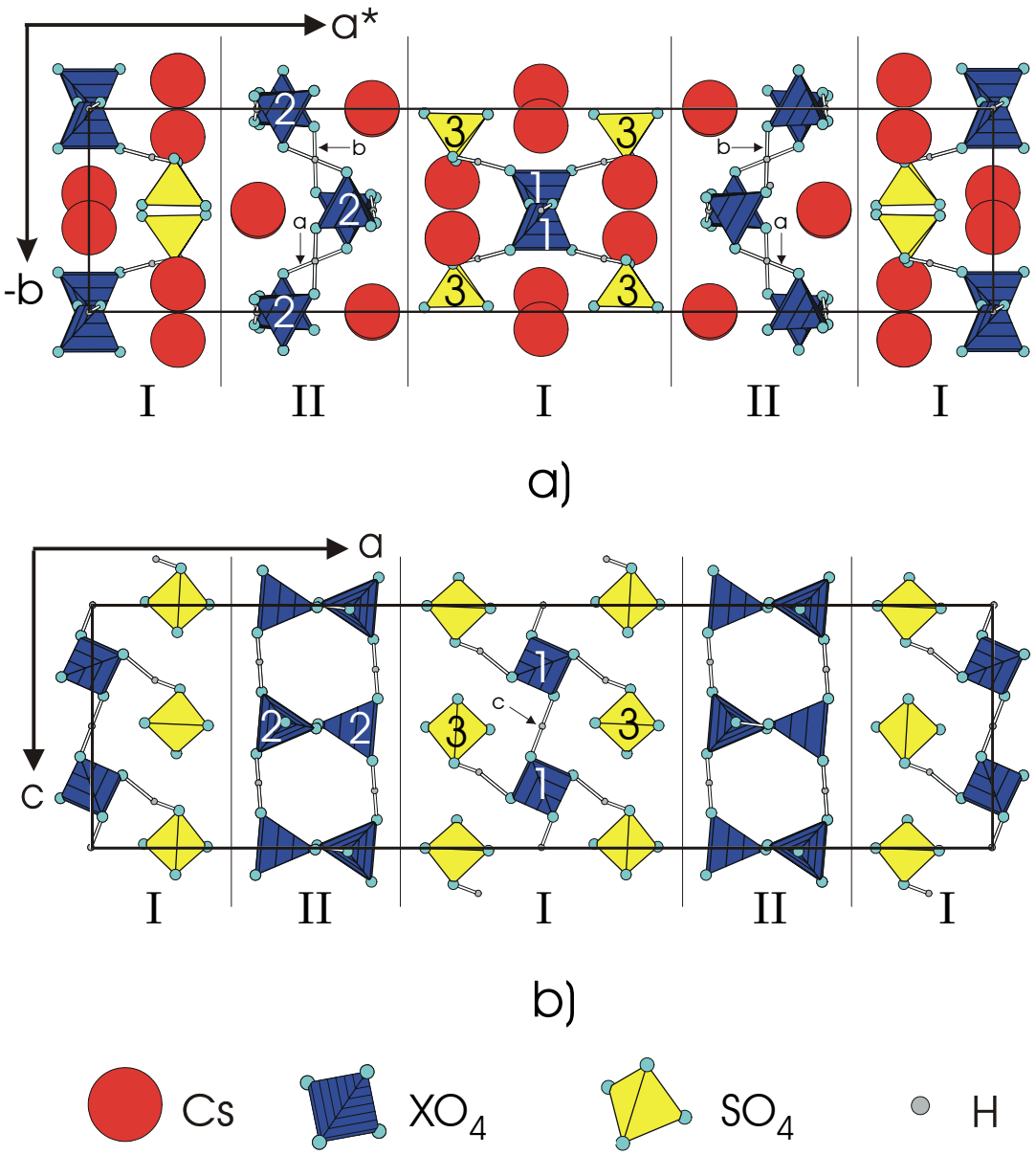

Figure 4.11 Structure of $Cs_5(HSO_4)_3(H_2PO_4)_2$: a) shown to maximize the similarities of the different layers, I and II, to the arrangement of cations and anions in $CsHSO_4$ and CsH_2PO_4 and b) to reveal the disordered hydrogen bonds connecting the mixed tetrahedra into chains along the c-axis[31]. The rectangles illustrate the unit cell and the cesium atoms have been removed in b) to call attention to the disordered chains.

The three distinct symmetric hydrogen bonds are found between the mixed tetrahedra with two of them, label (a) and (b), linking the type 2 tetrahedra of layer II into zigzag chains along the b-axis, Figure 4.11 a. The other symmetric bond, (c), connects the type 1 tetrahedra of layer I into straight chains parallel to the c-axis, Figure 4.11 b. The O-O distances are 2.589(18), 2.483(17), and 2.517(15) Å for bonds (a), (b), and (c), respectively. The first bond, (a), is almost certainly disordered due to its long bond length, large thermal parameters of its oxygen atoms, and bond sum considerations, but the short X-O distances associated with the bond are inconsistent with such a designation. For the (b) and (c) symmetric bonds, it is even more unclear whether the bonds have single or double-minima potential wells. However, on the basis of the low temperature neutron results for $Cs_3(HSO_4)_{2.50}(H_2PO_4)_{0.50}$, it seems likely that all three bonds are ordered on a local scale, but globally disordered. This would explain the intermediate behavior of the bond parameters, as they would pertain to the average structure recorded by the X-ray diffraction measurement.

In describing this local ordering and evaluating the entropy associated with it, there will be one assumption: the oxygen atoms of the sulfate groups in the disordered chains do not act as donor oxygens. This assumption is quite reasonable from considering structures of the two disordered chains. In layer II, each mixed tetrahedral site is bonded by four hydrogen bonds, two disordered and two ordered. From the ordered bonds, each tetrahedra will have one oxygen participate as a donor and one as an acceptor. For a sulfate group thus bonded, its oxygen atoms are much less likely to participate as donor oxygens in the disordered bonds compared to the oxygen atoms of a similarly bonded phosphate group. Such an effect would follow from the difference in p*K* values of

phosphoric and sulfuric acid[138]. The disordered chains of layer I also have four hydrogen bonds per tetrahedra, two of which are disordered and two ordered. However, for these mixed tetrahedra, the oxygen atoms involved in the two asymmetric hydrogen bonds are acceptors. In contrast to the disordered bonds of layer II , a sulfate on such a mixed site *would* desire to have one of its remaining oxygens act as a donor atom. However, the similarly bonded neighboring phosphate groups would be proportionally more hungry for the proton than the sulfate groups. Therefore, the protons in layer I's disordered chains should not reside next to the sulfate groups, resulting in exactly the same local ordering effect, although for a different reason.

It should be mentioned that the assumption used in these arguments (that the oxygen atoms on the sulfate groups involved in disordered hydrogen bonds do not act as donor oxygens) ignores the possibility of two sulfate groups residing next to each other. In such a case, either the hydrogen bond between the sulfate groups would be truly disordered or other local effects would favor one of the oxygen atoms over the other. The local ordering arguments to date would tend to suggest that the later case happens more often and in any case, the two SO_4 groups should be neighbors only $1/3*1/3 = 1/9^{th}$ of the time. It therefore seems reasonable to ignore such configurations when calculating the configurational entropy of this compound's room temperature structure.

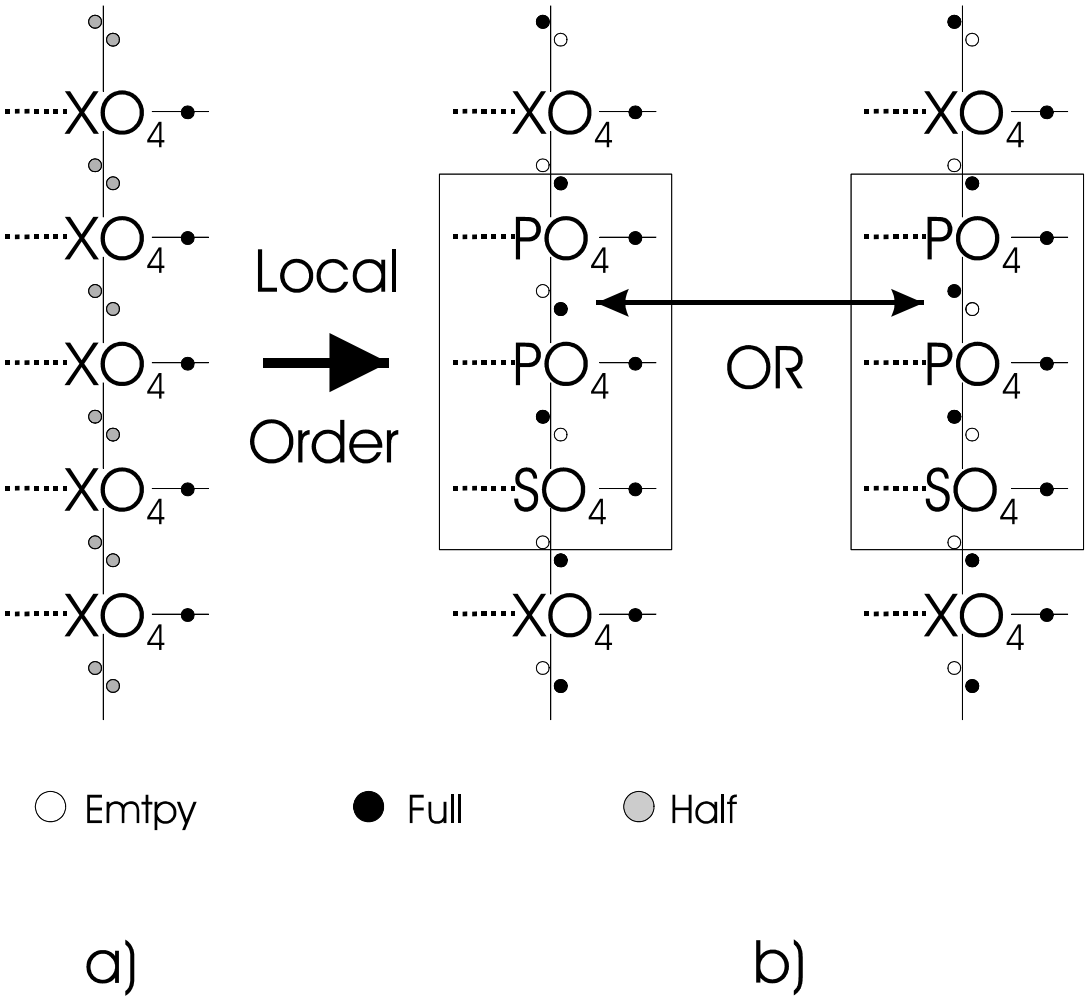

Figure 4.12 Probable effect of local order in the mixed S/P sites on neighboring disordered hydrogen bonds: a) the average structure with disordered hydrogen bonds connecting the mixed tetrahedra and b) the two variants due to the local arrangement of the sulfate and phosphate groups.

With this assumption it becomes easy to evaluate the entropy of the disordered bonds based on the average unit of two phosphates and one sulfate tetrahedra. As the proton sites adjacent the sulfate group will be vacant along the disordered chains, the two disordered bonds near it will become locally ordered, leaving only the hydrogen bond between the phosphates with a choice to the position of its proton, Figure 4.12.

As there are twelve of these mixed S/P sites per twenty tetrahedra in the unit cell, the entropy per mol of $CsHXO_4$ will be $S_{Hbond} = (12/20)*(1/3)*R*\ln(2) = (1/5)*R*\ln(2) =$ 1.15 J/mol*K.

4.4.6 Room Temperature Entropy of $Cs_2(HSO_4)(H_2PO_4)$

$Cs_2(HSO_4)(H_2PO_4)$'s room temperature structure is composed of zigzag chains of tetrahedra cross-linked to neighboring chains to form a planar structure, Figure 4.13 a.

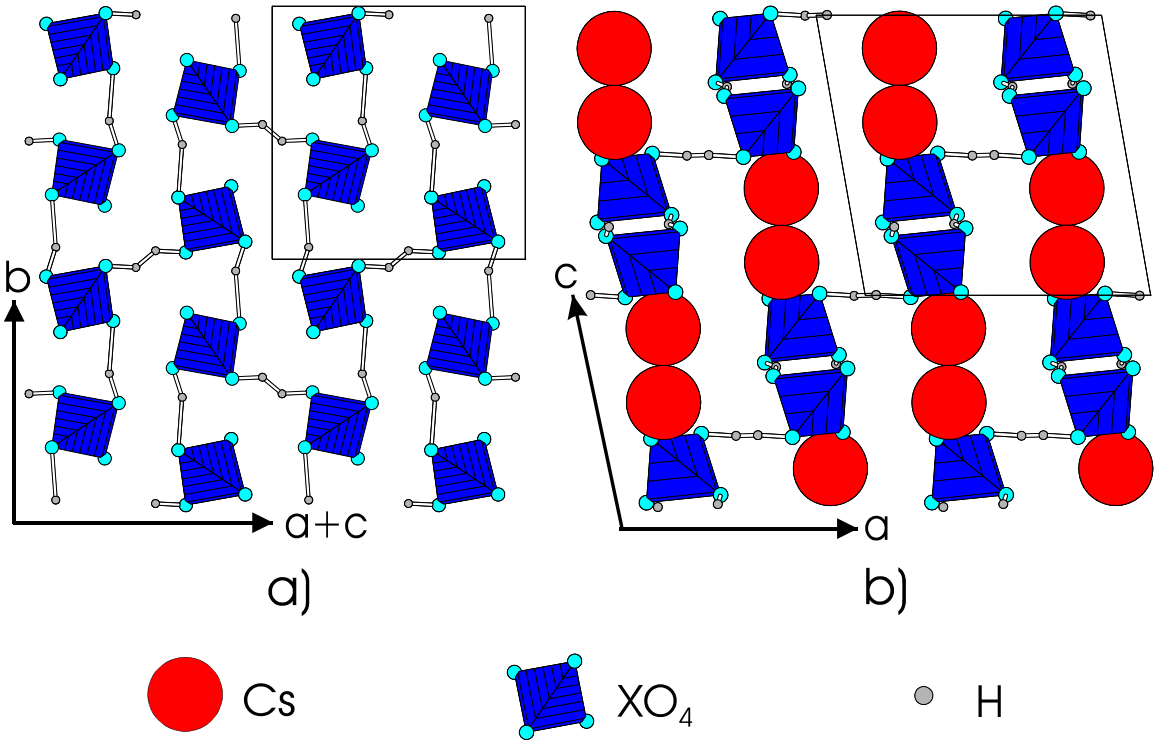

Figure 4.13 Structure of $Cs_2(HSO_4)(H_2PO_4)$ in a) the $\vec{b}\ x\ (\vec{a}+\vec{c})$ plane showing the sheets of XO_4 tetrahedra made of ordered hydrogen bonded chains in the [010] direction being connected by disordered hydrogen bonds in the [101] direction. The planes are also visible when viewed down the b-axis, b), as is the checkerboard arrangement of anion and cation rows. Rectangles represent the unit cell and Cs atoms were omitted in a) for clarity.

A unique property of this phase is that there is only one crystallographic (S,P) site, with a S:P ratio fixed by the stoichiometry of the compound at 1:1. This results in a unique hydrogen-bond network where each tetrahedra is involved in three hydrogen

bonds: two ordered bonds (crystallographically identical) that link the tetrahedra into chains running down [010] and one disordered bond in the [101] direction that connects the chains into sheets in the $\vec{b}\,x\,(\vec{a}+\vec{c})$ plane, Figure 4.13 b). As the X site is evenly occupied by S and P atoms, the entropy of mixing for this compound is the maximum value of Eq. (4-1) S_{mix} = -R*[2*(1/2)*ln(1/2)] = R*ln(2) = 5.76 J/mol*K.

There is some suggestion that the asymmetric hydrogen bond connecting the tetrahedra into chains has a very unusual double-minimum asymmetric potential well with minima of comparable energy. Since there is a lack of symmetry relating the minima, which minimum is occupied would be fundamentally related to the whether the adjoining tetrahedra were PO_4 or SO_4 groups. Any disorder in the proton site should then be related to the disorder on the XO_4 site. Hence, the S/P mixing entropy term is taken to include any disorder associated with this bond. The entropy of the symmetric hydrogen bond can be evaluated as where those of $Cs_5(HSO_4)_3(H_2PO_4)_2$. Since the S:P ratio for the tetrahedra is 1:1 and there is one disordered hydrogen bond per two tetrahedra, there are only two possible local variants to the structure, Figure 4.14. The entropy contribution from the hydrogen bonds is then S_{Hbond} = (1/2)*R*ln(2) = 2.88 J/mol*K.

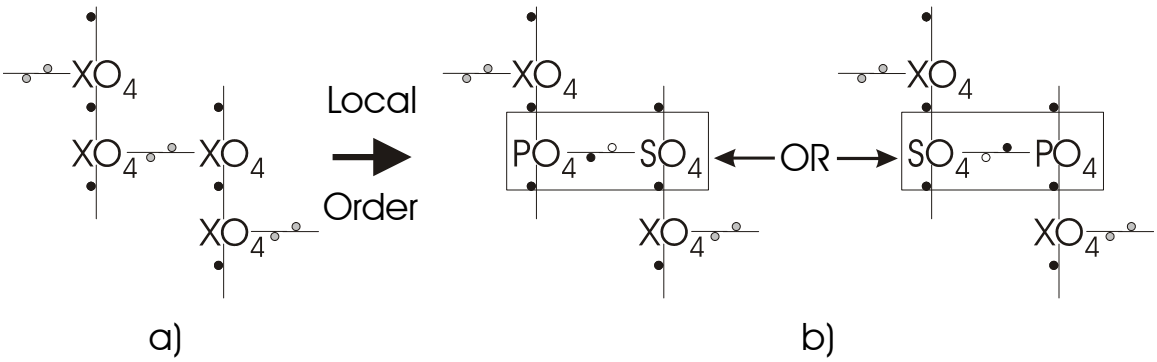

Figure 4.14 Local variants on the structure of $Cs_2(HSO_4)(H_2PO_4)$ with the average structure, a), being resolved into two distinct arrangements of the proton system, b).

4.4.7 Summary of entropy evaluations for the room temperature phases

We have now finished the evaluation of the entropy related with the room temperature phases. For the entropy of mixing, the values expected from statistical mechanics were found acceptable. The evaluation of hydrogen bond disorder produced some adjustments to the expected statistical mechanics' values. These adjustments accounted for the effect of local order (of mixed S/P sites) on the disordered hydrogen bonds. The configurational entropy of each compound's room temperature structure is listed in Table 4.4. These values will be subtracted from the calculated entropies of the high temperature phases to assess the transition entropy for each compound.

Table 4.4 Values for the configurational entropy of the room temperature structures

Compound	S_{mix} (J/mol*K)	S_{Hbond} (J/mol*K)	S_{total} (J/mol*K)
$CsHSO_4$	0	0	0
$Cs_3(HSO_4)_{2.50}(H_2PO_4)_{0.50}$	1.92	0.96 (partial)	2.88
$Cs_3(HSO_4)_{2.25}(H_2PO_4)_{0.75}$	1.56	1.44 (partial)	3.00
$Cs_3(HSO_4)_2(H_2PO_4)$	0	1.92 (disordered)	1.92
$Cs_5(HSO_4)_3(H_2PO_4)_2$	3.18	1.15 (disordered)	4.33
$Cs_2(HSO_4)(H_2PO_4)$	5.76	2.88 (disordered)	8.64
$Cs_6(H_2SO_4)_3(H_{1.5}PO_4)_4$	0	0	0
CsH_2PO_4	0	5.76 (disordered)	5.76

4.5 Entropy Rules for the High Temperature Phases

Having described the sources of configurational entropy in the room temperature structures, we can now proceed to the more satisfyingly general approach for calculating the entropy of the highly dynamic superprotonic phases. However, before describing this work's model, it is appropriate to discuss the only other theoretical approach used in the literature to explain the driving force behind these superprotonic phase transitions.

4.5.1 Plakida's theory of the superprotonic phase transition in $CsHSO_4$

This model focuses only on the "disordering" of the protons in the zigzag chains of $CsHSO_4$ across the superprotonic transition[147]. It is based on Landau's theory of phase transitions, and assigns an order parameter to the proton positions. The basic premise is that in the room temperature structure a second chain of hydrogen-bonded tetrahedra is possible, perpendicular to the existing zigzag chains, but with zero proton occupancy below the phase transition, Figure 4.15. This assumption is arrived at not by actual structural considerations, but more by a general comparison to CsH_2PO_4's structure, in which exactly such an arrangement of cross-linked zigzag chains is found. In this model, the superionic transition results from a disordering of the protons along these two chains, where disorder here refers to the occupancy of the perpendicular chains *and not* any intra-hydrogen bond dynamical disordering[136].

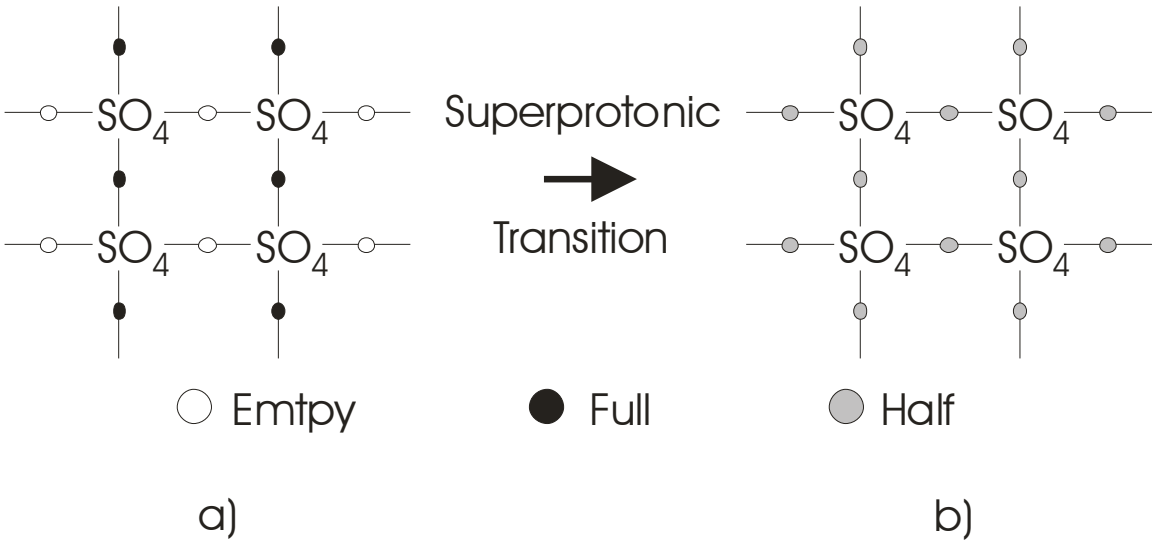

Figure 4.15 Disordering of protons across the superprotonic transition. Below T_c, a), the hydrogen bonds in the zigzag chains are completely occupied and those of cross-linking chains unoccupied. Above the transition, b), the protons are distributed with equal probability.

The values obtained for the model's parameters result in a first-order transition of the Slater type with a jump in the order parameter at T_c. The calculated transition entropy of this model is $\Delta S \approx 0.52*R$, which the author noted was much less than the experimental data of the time, $\Delta S = 1.32*R$[3]. This discrepancy between the calculated and measured ΔS was attributed to the disregard for entropic contributions from other degrees of freedom. In particular, they noted that the rapid reorientations of the tetrahedra had been ignored. A later calculation that incorporated the disorder of the oxygen atoms into the proton positions of this model and arrived at an entropy jump of $\Delta S = 1.1*R$ for the transition, the difference between calculated and observed values again being related to the neglect of additional degrees of freedom[148].

Although it is certainly true that the protons are ordered in the room temperature structure and disordered in the high temperature structure, this model does not seem to adequately describe the whole transition, but only a sub-system within it. Moreover, for

CsH_2PO_4 this model (not including oxygen disorder) does not predict a transition as the protons would be ordered in both the low and high temperature structures. There would then be no entropic benefit to a superprotonic phase transition from a disordering of the protons. This is probably why no attempt was made to apply this theory to the transition of CsH_2PO_4, as well as the fact that the structure of the compound's superprotonic phase was not known at the time.

When this structure was published, the entropy of the transition was attributed completely to the tetrahedral disorder and ignored any possible proton disorder. In this, we might absolve the theorists as the measurement of the day gave $\Delta S = 1.821*R$ for the superprotonic transition of CsH_2PO_4[134]. This value is very close to $R*\ln(6) = 1.792*R$, the entropy associated with the six orientations of the phosphate groups calculated from diffraction measurements. There were then two fairly independent models for the transitions of $CsHSO_4$ and CsH_2PO_4, which stressed the increased entropy of the protons and tetrahedra, respectively.

4.5.2 Ice rules type model for superprotonic transitions

In the early stages of formulating this work's model, discussions with other researchers led to the discovery that the evolving rules governing these calculations were very similar to those used in the evaluation of the residual entropy of ice by Linus Pauling[135]. Based on the observations of Bernal and Fowler, hexagonal ice (ice Ih) is composed of oxygen ions and protons, with each oxygen atom coordinated by the four closest oxygens residing on the corners of a regular tetrahedron. Hydrogen bonds connect the oxygen atoms with O-O and O-H distances of 2.76 and 1.0 Å, respectively. Each

oxygen atom is surrounded by four potential proton sites, the distance between proton sites on the same hydrogen bond being 0.76 Å, Figure 4.16[48].

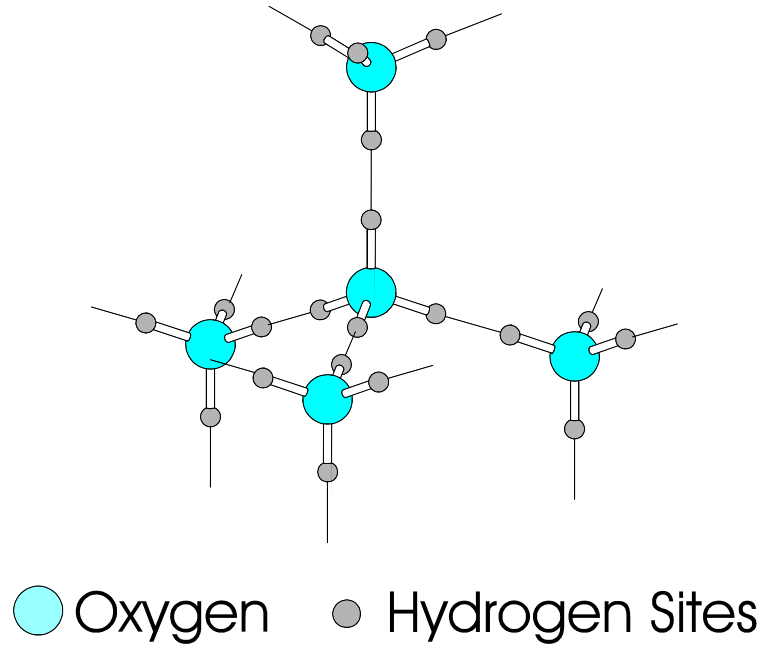

Figure 4.16 Hexagonal ice: each oxygen in tetrahedrally surrounded by four oxygens and four potential proton sites[48].

Bernal and Fowler also concluded that the structures of individual water molecules in ice were not that different from the those in steam and therefore must satisfy two rules[48]:

i) two and only two protons are bonded to each oxygen

ii) one and only one proton is allowed per hydrogen bond.

To these so called ice rules, Pauling added that[135]

iii) the hydrogen bonds must be directed approximately towards two of the four neighboring oxygen atoms

iv) the interaction of non-neighboring water molecules does not energetically favor one possible arrangement of protons with respect to other possible configurations so long as they all satisfy i)-iii).

Using these four rules Pauling estimated the number of configurations for a molecule to be

$$\Omega = \begin{pmatrix} \#\ of\ \ proton \\ configurations \end{pmatrix} * \begin{pmatrix} probability\ a\ proton \\ site\ is\ open \end{pmatrix}^{\begin{pmatrix} \#\ of \\ protons \end{pmatrix}} \qquad (4\text{-}4)$$
$$= \binom{4}{2} * \left(\frac{2}{4}\right)^2 = 6 * \left(\frac{1}{4}\right) = \frac{3}{2}$$

giving ice a residual molar entropy of R*ln(3/2) = 3.37 J/(mol*K), in extremely good agreement with the experimental data[149]. Now these rules were first applied to the relatively static structure of ice, but others found that it equally well explains the increase in entropy of order-disorder transitions in ice polymorphs, clathrate hydrates, and many other water containing compounds such as $SnCl_2 \bullet 2H_2O$, $Cu(HCO_2)_2 \bullet 4H_2O$, and $[H_{31}O_{14}][CdCu_2(CN)_7]$[150-153]. This is in spite of the fact that the compounds vary greatly in both the extent and dimensionality of their hydrogen bonded networks. The application of Pauling's rules to systems with reorientational disorder is then well documented.

The only remaining logical leap is to apply these ice rules to the tetrahedra found in the compounds in question. A literature search showed that this exact step was performed by Slater to describe the ferroelectric transition of KH_2PO_4[154]. This further application of the ice rules would seem trivial, since each oxygen atom in ice is tetrahedrally coordinated by four oxygen atoms and each phosphate in KH_2PO_4 is similarly surrounded by four other phosphate groups. However, in ice the six allowed configurations of the protons are crystallographically identical, whereas in KH_2PO_4 two of the arrangements are different from the other four. The two special configurations

result in a dipole pointing either in the positive or negative c-axis (the preferred axis of the crystal since KH_2PO_4 is tetragonal) while the other four give polarizations in the plane perpendicular to the c-axis.

The two configurations aligned with $\vec{c}$ can therefore have different energies from those perpendicular to $\vec{c}$. This is actually the cause of the spontaneous polarization of the ferroelectric phase, dielectric measurements having shown the c-axis aligned configurations to have a lower energy than the other four. Thus, a crystal should be completely polarized (ordered) at zero temperature and completely random at high temperatures with the configurational entropy difference between the two states equal to R*ln(3/2) as $T \Rightarrow \infty$[154]. It turns out that the measured entropy change for the ferroelectric transition of KH_2PO_4 has an excess entropy when compared to R*ln(3/2). This was recently explained by way of local excitation of phosphate defects (HPO_4^{-2} and H_3PO_4), the formulation of which was given by Takagi in 1948[155]. These defect pairs add significantly to the entropy of both the ferroelectric and paraelectric phases and lead to the 12 % increase in the measured transition entropy compared the ice rules value[156].

The ice rules have then successfully described the entropy changes of both disordered ice-like systems and compounds containing tetrahedral groups. This makes the step of applying them to the disordered tetrahedra of the high temperature phases more like a hop. However, this is certainly the first time they have been applied to the superprotonic phases of solid acids, resulting in a very compelling description of the entropic driving force for these transitions, found lacking in the current literature. The ice rules applied to the compounds under consideration are very similar to those given by Slater for KH_2PO_4, but with the additional complexity that there are now both sulfate and

phosphates in the structure. Besides adding the obvious entropy associated with mixing, calculated with Eq. (4-1), this will also cause the average number of hydrogen atoms per tetrahedron to change from compound to compound. This changes the first ice rule to:

i) only one or two protons will be associated with a tetrahedron (4-5a)

There will therefore be two types of tetrahedra in these disordered phases, differentiated not by their central cation, but by the number of protons bonded to their oxygen atoms. This will add to the entropy of these phases as there will be different possible configurations associated with the ordering of the one and two proton laden tetrahedra. The other rules will remain relatively unchanged:

ii) only one proton per hydrogen bond (4-5b)

iii) hydrogen bonds are directed towards oxygen atoms of neighboring tetrahedra (4-5c)

iv) interactions of non-adjacent tetrahedra do not effect the possible configurations of a tetrahedron and its protons (4-5d)

The reference to the configurations of a tetrahedron in Eq (4-5d) is necessary to include the entropic contribution from the crystallographically identical orientations of the tetrahedra.

With this formulation we can adjust Eq. (4-4) to calculate the entropy of these high temperature phases:

$$\Omega = \begin{pmatrix} \#\ of \\ proton \\ configurations \end{pmatrix} * \begin{pmatrix} probability \\ a\ proton \\ site\ is\ open \end{pmatrix}^{\begin{pmatrix} \#\ of \\ protons \end{pmatrix}} * \begin{pmatrix} \#\ of \\ tetrahderal \\ arrangements \end{pmatrix} * \begin{pmatrix} \#\ of \\ oxygen \\ positions \end{pmatrix} \quad (4\text{-}6)$$

where the first two terms are evaluated exactly as with ice, only here the coordination need not be tetrahedral. The third term arises from the distinguishable arrangements of one and two proton laden tetrahedra. For example, there are three distinguishable arrangements of one HXO_4 and two H_2XO_4 groups, ten distinguishable arrangements of two HXO_4 and three H_2XO_4 groups, and so on. The final term is caused by the librations of the tetrahedra between their possible orientations that result in multiple oxygen positions for the same hydrogen bond direction, hence increasing the number of configurations. With Eq. (4-6) we are now ready to calculate the configurational entropy of the high temperature phases!

4.6 Calculated Transition Entropies for the $CsHSO_4$-CsH_2PO_4 System of Compounds

In this section, the rules developed in section 4.5 will be applied to the high temperature structures found in the cesium sulfate-phosphate compounds. As was previously suggested, the calculation of the high temperature forms using Eq. (4-6) is straight-forward compared to the evaluation of the entropy associated with the room temperature phases. Since the structures of the high temperature forms are either isostructural to or a combination of the superprotonic structures of $CsHSO_4$ and CsH_2PO_4 (see section 4.2.2), we will start with evaluating the configurational entropy of these two structures. It will then be possible to evaluate the entropy of the remaining superprotonic phases by taking the right ratios of the two values.

4.6.1 Entropy calculations for $CsHSO_4$

As was discussed in section 4.2.3, the high temperature structure of $CsHSO_4$ is a body centered tetragonal structure in which each sulfate anion is tetrahedrally surrounded by four other SO_4 groups. This leads to four possible directions for the dynamically disordered hydrogen bonds that connect the tetrahedra. On average, the oxygen atoms of each tetrahedra should be involved in two hydrogen bonds, so that the proton associated each sulfate will have $\binom{4}{1} = 4$ possible positions (i.e., the four hydrogen bond directions), with each position having a $3/4^{th}$ probability of being open. Each tetrahedra should have only one proton, so the number of tetrahedral arrangements equals one. This leaves only the knowledge of the number of tetrahedral orientations necessary for the evaluation of Eq. (4-6). Unfortunately, as was mentioned before, this number is of considerable debate in the literature. The three distinct structures proposed result in either two or four orientations of the tetrahedra, Figure 4.17. There is no definitive reason to prefer one model over the others and so the entropy for both 2 and 4 orientations of the tetrahedra will be calculated.

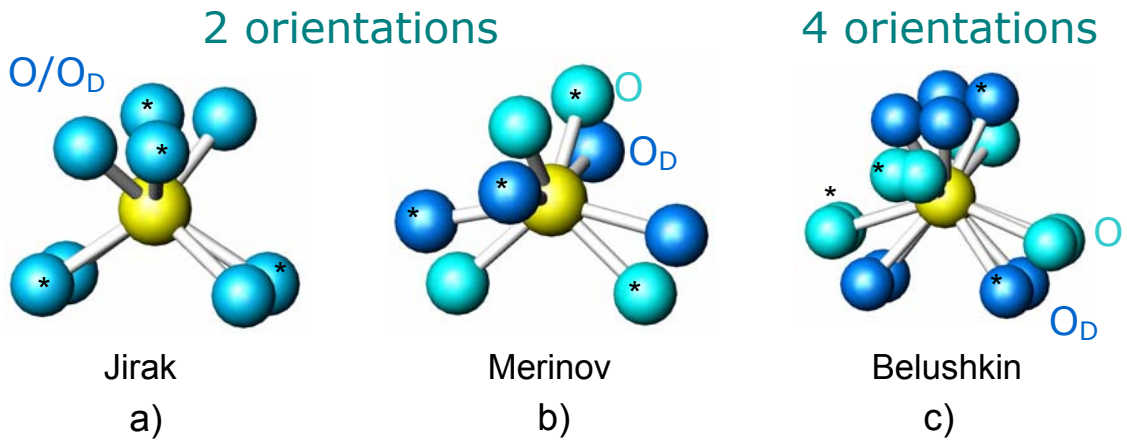

Figure 4.17 Possible configurations of the sulfate tetrahedra in the superprotonic phase: the structures by Jirak-a)[61], Merinov-b)[125], and Belushkin-c)[124] have two, two, and four orientations, respectively, which transform into each other by rotations of 32°, 30°, and 30°, respectively. The * designates one possible arrangement for the oxygen atoms of a tetrahedra.

Since there are only four hydrogen bond directions, the number of tethradedral orientations will equal the number of oxygen positions around each hydrogen bond. Using Eq. (4-6), the average number of configurations for $CsHSO_4$ in its tetragonal phase is therefore

$$\Omega = \begin{pmatrix} \#\ of \\ proton \\ configurations \end{pmatrix} * \begin{pmatrix} probability \\ a\ proton \\ site\ is\ open \end{pmatrix}^{\begin{pmatrix} \#\ of \\ protons \end{pmatrix}} * \begin{pmatrix} \#\ of \\ tetrahderal \\ arrangements \end{pmatrix} * \begin{pmatrix} \#\ of \\ oxygen \\ positions \end{pmatrix} \qquad (4\text{-}7)$$

$$= \begin{pmatrix} 4 \\ 1 \end{pmatrix} * \left(\frac{3}{4}\right)^1 * (1) * (2\ or\ 4) = 6\ or\ 12$$

resulting in an entropy of

$$S_{config} = R*\ln(\Omega) = R*\ln(6\,or\,12) = \begin{cases} 1.79*R \\ 2.48*R \end{cases} = \begin{cases} 14.90 J/mol*K \\ 20.66 J/mol*K \end{cases} \qquad (4\text{-}8)$$

Now, since we are going to use one of these numbers as the entropy associated with the tetragonal phases of the other compounds, we need to pick one or the other. From section 4.2.4, this work measured the transition enthalpy for $CsHSO_4$ as being 15.0 J/mol*K, a value higher than previously reported[3,130]. Trusting in this work' s value and the fact that all other published values are smaller, it seems pretty likely that the 14.90 J/mol*K value (corresponding to two orientations of the tetrahedra) better represents the superprotonic structure of $CsHSO_4$. An entropy of

$$S_{config} = R*\ln(\Omega) = R*\ln(6) = 1.79*R = 14.90 J/mol*K \quad (4\text{-}9)$$

is then the value assigned to the tetragonal phase in these calculations.

4.6.2 Entropy calculations for CsH_2PO_4

The CsCl-like structure of CsH_2PO_4 has the PO_4 anions at the center and Cs cations at the corners of a cube. This arrangement allows hydrogen bonds to extend out the six faces of the cube, Figure 4.18. There will be two protons per tetrahedra resulting in $\binom{6}{2} = 15$ ways of positioning the two protons in the six possible directions of the hydrogen bonds. Two protons per tetrahedra also means that two hydrogen bonds will enter the cube, giving the probability of a direction being open = 4/6 = 2/3. The tetrahedra should all have an average of two protons, so the number of tetrahedral arrangements equals one. And finally, each tetrahedra will have six orientations, a number which is pleasingly not in dispute. Six orientations equates to 24 oxygen positions spread out over the six faces, or 4 oxygen positions per hydrogen bond direction.

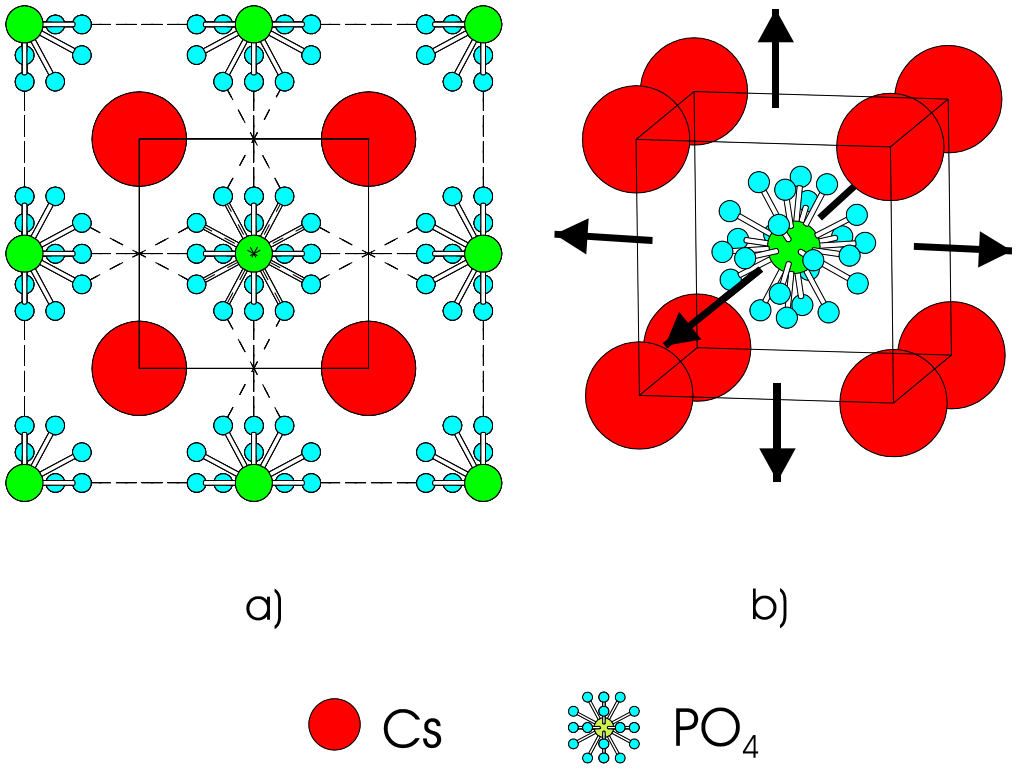

Figure 4.18 Cubic structure of CsH_2PO_4: a) the shortest distance between oxygen atoms of different tetrahedra extends out the faces of the cube, which results in six possible directions for hydrogen bonding, b)[92]. Dashed lines represent disordered hydrogen bonds.

The number of configuration for CsH_2PO_4 in its cubic phase is therefore,

$$\Omega = \begin{pmatrix} \#\ of \\ proton \\ configurations \end{pmatrix} * \begin{pmatrix} probability \\ a\ proton \\ site\ is\ open \end{pmatrix}^{\begin{pmatrix} \#\ of \\ protons \end{pmatrix}} * \begin{pmatrix} \#\ of \\ tetrahderal \\ arrangements \end{pmatrix} * \begin{pmatrix} \#\ of \\ oxygen \\ positions \end{pmatrix} \qquad (4\text{-}10)$$

$$= \begin{pmatrix} 6 \\ 2 \end{pmatrix} * \left(\frac{4}{6}\right)^2 * (1) * (4) = 15 * \left(\frac{4}{9}\right) * 4 = 26.\overline{6}$$

from which comes an entropy of

$$S_{config} = R * \ln(\Omega) = R * \ln(26.\overline{6}) = 3.28 * R = 27.30 J/mol*K \qquad (4\text{-}11)$$

This value is then the amount of entropy associated with CsH_2PO_4's cubic phase. Unlike the tetragonal phase of $CsHSO_4$, however, this value will not be assigned to all the high

temperature cubic phases because of the varying proton content of the phases. For each compound the first, second, and third terms in Eq. (4-6) will need to be evaluated before the entropy of the compounds high temperature phase can be calculated.

4.6.3 Entropy calculations for pure cubic phases

With no further ado, we can now calculate the entropy associated with the high temperature phases of the $Cs_3(HSO_4)_2(H_2PO_4)$, $Cs_5(HSO_4)_3(H_2PO_4)_2$, and $Cs_2(HSO_4)(H_2PO_4)$ compounds. We will need three $CsHXO_4$ units to describe the cubic phase of $Cs_3(HSO_4)_2(H_2PO_4)$, with one two-proton unit and two one-proton units. Eq. (4-6) then gives

$$\Omega = \begin{pmatrix} \#\ of \\ proton \\ configurations \end{pmatrix} * \begin{pmatrix} probability \\ a\ proton \\ site\ is\ open \end{pmatrix}^{\begin{pmatrix} \#\ of \\ protons \end{pmatrix}} * \begin{pmatrix} \#\ of \\ tetrahderal \\ arrangements \end{pmatrix} * \begin{pmatrix} \#\ of \\ oxygen \\ positions \end{pmatrix} \qquad (4\text{-}12)$$

$$= \begin{pmatrix} 6 \\ 2 \end{pmatrix} \begin{pmatrix} 6 \\ 1 \end{pmatrix}^2 * \left(\frac{14}{18}\right)^4 * \left(\frac{3!}{2!1!}\right) * (4) = 2.37x10^3$$

equal to an entropy per $CsHXO_4$ unit of

$$S_{config} = 1/3 * R * \ln(\Omega) = 1/3 * R * \ln(2.37x10^3) = 2.59 * R = 21.54\ J/mol*K \qquad (4\text{-}13)$$

Applying Eq. (4-6) to the $Cs_5(HSO_4)_3(H_2PO_4)_2$ compound results in

$$\Omega = \begin{pmatrix} 6 \\ 2 \end{pmatrix}^2 \begin{pmatrix} 6 \\ 1 \end{pmatrix}^3 * \left(\frac{23}{30}\right)^7 * \left(\frac{5!}{3!2!}\right) * (4) = 3.03x10^5 \qquad (4\text{-}14)$$

giving an entropy per $CsHXO_4$ unit of

$$S_{config} = 1/5 * R * \ln(\Omega) = 1/5 * R * \ln(3.03x10^5) = 2.52 * R = 20.99\ J/mol*K \qquad (4\text{-}15)$$

And finally, the $Cs_2(HSO_4)(H_2PO_4)$ compound has

$$\Omega = \binom{6}{2}\binom{6}{1} * \left(\frac{9}{12}\right)^3 * \left(\frac{2!}{1!1!}\right) * (4) = 3.04x10^2 \quad (4\text{-}16)$$

configurations, which leads to an entropy per $CsHXO_4$ unit of

$$S_{config} = 1/2 * R * \ln(\Omega) = 1/2 * R * \ln(3.04x10^2) = 2.86 * R = 23.76\, J/mol*K \quad (4\text{-}17)$$

This leaves only the entropy of mixing for the sulfate and phosphate tetrahedra to be calculated. Using Eq (4-1) on the compounds gives

$S_{mix}[Cs_3]$ = -R*[(1/3)ln(1/3)+(2/3)ln(2/3)] = 0.64*R = 5.29 J/mol*K

$S_{mix}[Cs_5]$ = -R*[(2/5)ln(2/5)+(3/5)ln(3/5)] = 0.67*R = 5.6 J/mol*K (4-18)

$S_{mix}[Cs_2]$ = -R*[(1/2)ln(1/2)+(1/2)ln(1/2)] = 0.64*R = 5.76 J/mol*K

The total configurational entropies for these three compounds in their cubic structures is

$$\begin{aligned} S_{total}[Cs_3] &= S_{config} + S_{mix} = 21.54 + 5.29 = 26.83\, J/mol*K \\ S_{total}[Cs_5] &= S_{config} + S_{mix} = 20.99 + 5.60 = 26.59\, J/mol*K \\ S_{total}[Cs_2] &= S_{config} + S_{mix} = 23.76 + 5.76 = 29.52\, J/mol*K \end{aligned} \quad (4\text{-}19)$$

4.6.4 Entropy calculations for mixed tetragonal/cubic compounds

To evaluate the configurational entropy of these compounds, we need to know the stoichiometry and mole fractions of the tetragonal and cubic phases. For the tetragonal ($CsHSO_4$-type) phases, the stoichiometry will be assumed that of $CsHSO_4$. This assumption is justified by the observation that the cubic phase is the preferred phase for a wide compositional range, from an S:P ratio of 2:1 to 0:1, Figure 4.3. Therefore, for S:P ratios ~ 2:1, equivalent to H:XO_4 ratios of 1.33:1, the configurational entropy gained by

all tetrahedra being in the cubic phase balances any other entropy and energy bonuses conveyed by the co-existence of the tetragonal and cubic phases.

The conjecture that each tetrahedron in the tetragonal phase has an average of only one proton can also be justified on an atomistic level. Assuming an equilibrium state in which both the tetragonal and cubic phases are present, taking a proton from a two-proton loaded tetrahedra in the cubic phase and moving it to a one-proton tetrahedra in the tetragonal phase results in an entropy loss, the magnitude of which will depend on the average $H:XO_4$ value of each phase. For tetragonal and cubic phases with $H:XO_4$ ratios of 1 and 2, respectively, this entropy loss equals $0.39*k_b$ per proton transferred, Figure 4.19. Of course, there are other entropy and energy terms associated with such a switch. This is obvious from the very fact that there is a tetragonal phase at all. After all, from entropy considerations alone, the cubic phase is preferred over the tetragonal phase for all possible proton loadings.

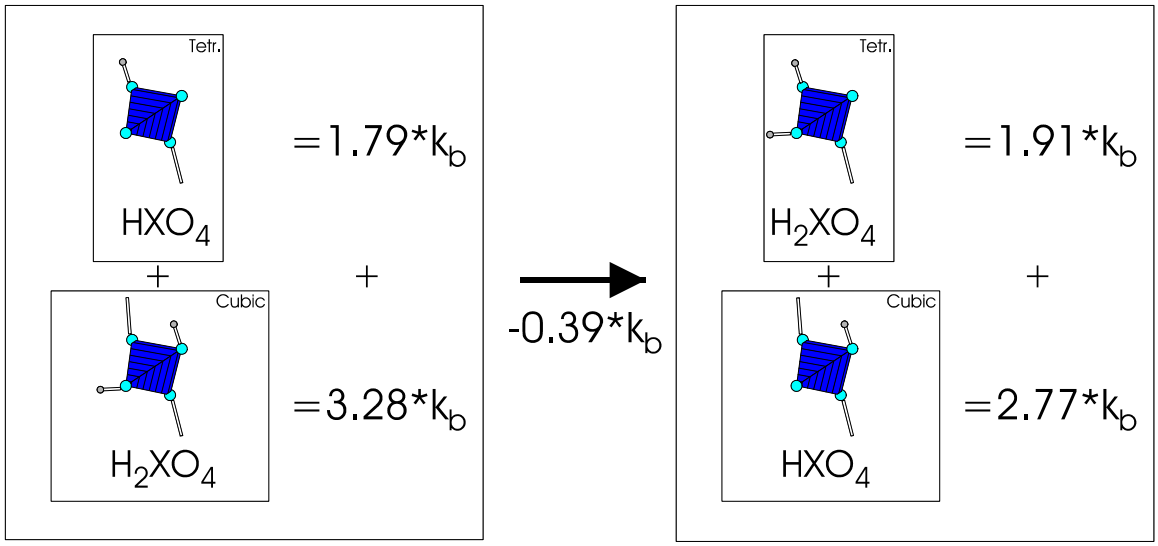

Figure 4.19 The configurational entropy loss due to a proton transfer from the cubic to tetragonal phase. No entropy is gained in making a two-proton from a one-proton tetrahedra in the tetragonal structure, but entropy is lost by reducing a tetrahedra's proton loading from two to one in the cubic structure.

From the above listed arguments, the tetragonal phases are assumed to have an average proton/tetrahedra value extremely close to 1 (i.e., it is pure $CsHSO_4$), while the minimum $H:XO_4$ ratio for the cubic phases should be ~ 1.33:1, thus allowing the evaluation of the high temperature forms that express both structural types.

The requirement that the tetragonal phase be pure $CsHSO_4$ implies that not only do the sulfate and phosphate tetrahedra migrate into different phases, but that they form phase domains on the order of 1000 Å, as evidenced by the diffraction patterns of $Cs_3(HSO_4)_{2.5}(H_2PO_4)_{0.5}$ and $Cs_3(HSO_4)_{2.25}(H_2PO_4)_{0.7}$ which show two distinct structures. This might seem to give the tetrahedra an unreasonably high mobility, but even for the fastest measurement of the transitions, 20 K/min, these transitions took ~ 2 min to complete. From the simple diffusion equation, $x = \sqrt{Dt}$, we can deduce a minimum diffusion coefficient (assuming the tetrahedra to move 1000 Å in 2 min) of $D \cong 1x10^{-12}$ cm^2/s. This value can be compared to that of phosphorous in fused phosphoric acid (i.e., the diffusion constant of PO_4 groups), which at ~25°C is approximately $1x10^{-7}$ cm^2/s[44]. Since our minimum diffusion coefficient is 100,000 times smaller than this measured value, the tetrahedral migration necessary to form a pure $CsHSO_4$ tetragonal phase certainly seems possible on the atomistic level.

To evaluate the entropy of these mixed superprotonic phases we now need only to know the amount of cubic and tetragonal phase present in the compounds at elevated temperatures. The required values were calculated from Rietveld refinements of high temperature diffraction patterns for the two compounds (Appendix A). At 140°C, the ratio of the cubic to tetragonal phase was 44(1):56(1) and 50(1):50(1) for the $Cs_3(HSO_4)_{2.5}(H_2PO_4)_{0.5}$ and $Cs_3(HSO_4)_{2.25}(H_2PO_4)_{0.75}$ compounds, respectively.

Refinements at other temperatures above the onset of the transitions showed that the ratio of cubic to tetragonal phase increased with increasing temperature, agreeing with the cubic phase having the higher entropy of the two phases. The above listed ratios will be used in the entropy calculations for these two compounds because the diffraction patterns at 140°C were the first not to exhibit a monoclinic phase, suggesting the superprotonic transitions had just completed. A temperature of 140°C for the final transition temperature is also in agreement with the values deduced from the conductivity data (Table 4.3).

A cubic to tetragonal ratio of 44(1):56(1) results in the cubic phase of $Cs_3(HSO_4)_{2.5}(H_2PO_4)_{0.5}$ having a S:P ratio of 1.6:1, with a nominal stoichiometry of $Cs_{13}(HSO_4)_8(H_2PO_4)_5$. The number of configurations for such a compound is

$$\Omega = \binom{6}{2}^5 \binom{6}{1}^8 * \left(\frac{60}{78}\right)^{18} * \left(\frac{13!}{8!5!}\right) * (4) = 5.84x10^{13} \quad (4\text{-}20)$$

giving an entropy per $CsHXO_4$ unit of

$$S_{config} = 1/13 * R * \ln(\Omega) = 1/13 * R * \ln(5.84x10^{13}) = 2.44 * R = 20.27\ J/mol*K \quad (4\text{-}21)$$

Using the entropy of the tetragonal phase, 14.9 J/mol*K, and the cubic phase, 20.27 J/mol*K, the calculated entropy of the superprotonic phase of $Cs_3(HSO_4)_{2.5}(H_2PO_4)_{0.5}$ becomes

$$\begin{aligned} S_{config} &= X_{cub} * S_{cub} + X_{tetra} * S_{tetra} = \\ &= 0.44*(20.27) + 0.56*(14.9) = 17.26\ J/mol*K \end{aligned} \quad (4\text{-}22)$$

The entropy of mixing will be likewise weighted and using Eq. (4-1) gives an additional entropy of

$S_{mix}[Cs_3(HSO_4)_{2.5}(H_2PO_4)_{0.5}] = 0.44*S_{mix}(\text{cubic}) + 0.56*S_{mix}(\text{tetra}) =$

= 0.44*(- R*[(5/13)ln(5/13)+(8/13)ln(8/13)]) + 0.56*(0) = (4-23)

= 0.44*(0.67*R) = 2.44 J/mol*K

The total entropy of the high temperature phase of $Cs_3(HSO_4)_{2.5}(H_2PO_4)_{0.5}$ is then

$$S_{total} = S_{config} + S_{mix} = 17.26 + 2.44 = 19.7\ J/mol*K \quad (4\text{-}24)$$

For the $Cs_3(HSO_4)_{2.25}(H_2PO_4)_{0.75}$ compound a 50(1):50(1) cubic to tetragonal ratio leads to the cubic phase having a S:P ratio of 1:1 and a stoichiometry of $Cs_2(HSO_4)(H_2PO_4)$. Therefore, taking the average of the calculated entropies for $CsHSO_4$ and $Cs_2(HSO_4)(H_2PO_4)$,

$$S_{config} = X_{cub}*S_{cub} + X_{tetra}*S_{tetra} = \\ = 0.5*(23.76) + 0.5*(14.9) = 19.33\ J/mol*K \quad (4\text{-}25)$$

gives us the configurational entropy, per $CsHXO_4$ unit, for the high temperature phase of $Cs_3(HSO_4)_{2.25}(H_2PO_4)_{0.75}$. The entropy of mixing for this phase is

$S_{mix}[Cs_3(HSO_4)_{2.5}(H_2PO_4)_{0.5}] = 0.5*S_{mix}(cubic) + 0.5*S_{mix}(tetra) =$

= 0.5*(- R*[(1/2)ln(1/2)+(1/2)ln(1/2)]) + 0.5*(0) = (4-26)

= 0.5*(0.69*R) = 2.88 J/mol*K

Making the total entropy of the high temperature phase of $Cs_3(HSO_4)_{2.25}(H_2PO_4)_{0.75}$ equal to

$$S_{total} = S_{config} + S_{mix} = 19.33 + 2.88 = 22.21\ J/mol*K \quad (4\text{-}27)$$

4.6.5 Entropy calculations for $Cs_6(H_2SO_4)_3(H_{1.5}PO_4)_4$

The only configurational entropy calculation remaining is that for the black sheep of the family, $Cs_6(H_2SO_4)_3(H_{1.5}PO_4)_4$. The high temperature structure for this compound

is presumed to be similar to the other cubic phases based on the high temperature X-ray diffraction pattern (Figure 4.3) and current neutron diffraction experiments which both confirmed a primitive cubic space group. Of course, the Cs:XO_4 ratio does not conform to the 1:1 ratio implied by the CsCl structure. It is therefore assumed that there are Cs vacancies in the $Pm\bar{3}m$ structure. This conjecture is supported by the fact that this phase has a **negative thermal expansion**, which can be most simply explained by Cs cations vibrating more and more into the vacancy sites as temperature increases. If we take the existence of these Cs vacancies as fact, we then must make some changes to the assumptions used in calculating the other cubic phases entropy. First, instead of there being only two types of proton burdened tetrahedra in the cubic phase, i.e., HXO_4 and H_2XO_4, there will now be a third type, H_3XO_4. From the stoichiometry of the compound, we can estimate the ratio of these tetrahedral forms, H_3XO_4:H_2XO_4: HXO_4, will be 1:3:3. Using such a ratio and Eq. (4-6), the configurations for the proton system becomes

$$\Omega = \binom{6}{3}\binom{6}{2}^3\binom{6}{1}^3 * \left(\frac{30}{42}\right)^{12} * \left(\frac{7!}{3!3!1!}\right) * (4) = 1.44x10^8 \quad (4\text{-}28)$$

equating to a configuration entropy of

$$S_{config} = 1/7 * R * \ln(\Omega) = 1/7 * R * \ln(1.44x10^8) = 2.68 * R = 22.31\, J/mol*K \quad (4\text{-}29)$$

The presence of Cs vacancies also changes the entropy of mixing calculation. There will now be two entropy of mixing terms: one for the sulfate/phosphate groups and one for the Cs_{Cs}/V_{Cs} sites. Using the appropriate ratios from the stoichiometry of the compound and Eq. (4-1) these entropy terms are evaluated as

$S_{mix}[XO_4's] = - R*[(3/7)\ln(3/7)+(4/7)\ln(4/7)]) = 0.68*R = 5.68$ J/mol*K (4-30)

$S_{mix}[Cs/V] = - R*[(1/7)\ln(1/7)+(6/7)\ln(6/7)]) = 0.41*R = 3.41$ J/mol*K (4-31)

The final contribution to this phase's entropy comes from positional disorder of the Cs cations, the support for which is again based on this phase's negative thermal expansion. It is postulated that the cations near a vacancy have an extra entropy component, *evaluated in terms of configurational entropy* by allowing these cesium atoms two positions: the lattice sites on which they should reside and dynamic positions halfway between the cesium and vacancy sites. As the Cs:V ratio is 6:1 this can be visualized by the vacancy being placed at the center of a regular octahedron with Cs atoms at the vertices and the dynamic positions lying between the cesiums and the vacancy, Figure 4.20. As the material is heated up, the cesium atoms should jump more frequently to the intermediate position giving the observed negative thermal expansion.

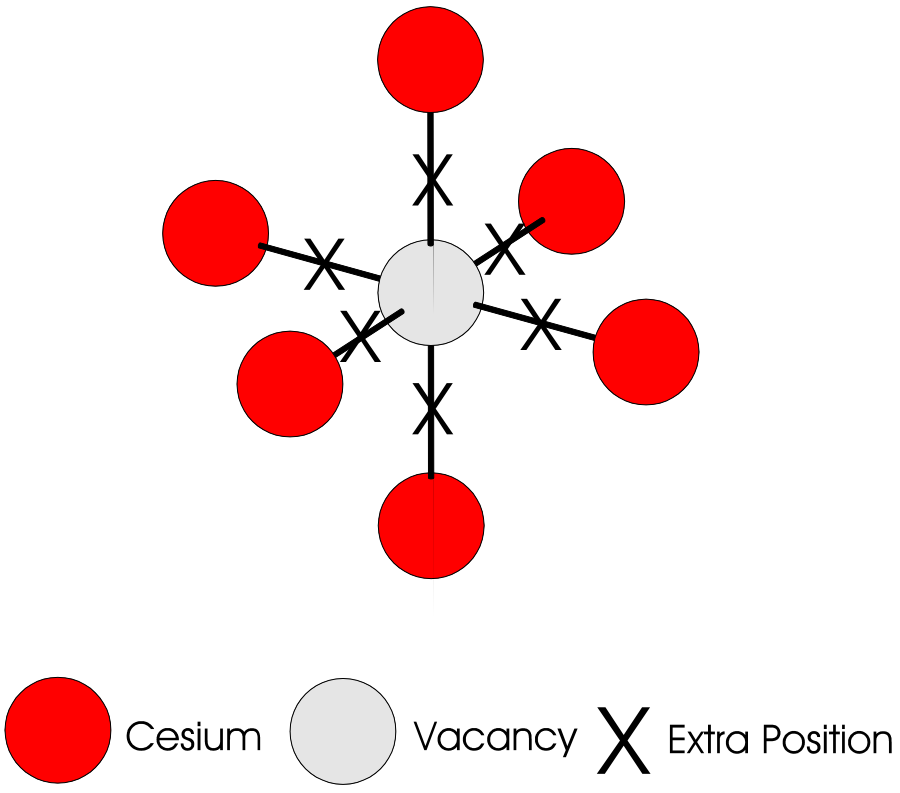

Figure 4.20 Possible source of extra entropy in the cubic phase of $Cs_6(H_2SO_4)_3(H_{1.5}PO_4)_4$: Normal and dynamic position for the cesium atoms due to the presence of vacancies on the cesium lattice.

The entropy of the arrangement shown in Figure 4.19 would increase as the two positions for the cesium atoms became equally occupied at which point each Cs would have an extra entropy of R*ln(2) associated with it. The entropy per $CsHXO_4$ unit would then be

$$S_{config}(Cs/V) = 1/7 * R * \ln(\Omega) = 1/7 * R * \ln(2^6) = 0.59 * R = 4.94\ J/mol*K \quad (4\text{-}32)$$

Again, this is a configurational evaluation of the extra entropy associated with the presence of cesium vacancies, the real entropy possibly being better described as vibrational or translational. The total entropy of this phase is then the sum of Eqs. (4-29), (4-30), (4-31), and (4-32):

$$\begin{aligned} S_{total} &= S_{config} + S_{mix}(XO_4) + S_{mix}(Cs/V) + S_{config}(Cs/V) = \\ &= 22.31 + 5.68 + 3.41 + 4.94 = 36.34\ J/mol*K \end{aligned} \quad (4\text{-}33)$$

4.6.6 Summary of entropy calculations for high temperature phases

Table 4.5 details the calculated entropies for the tetragonal and cubic high temperature phases of these compounds. For $CsHSO_4$, CsH_2PO_4, and the pure cubic compounds, the total entropy of the high temperature phases was calculated using only the ideal entropy of mixing, Eq. (4-1), and applying the adjusted ice rules, Eq. (4-6). The compounds which transform to both tetragonal and cubic phases at elevated temperatures required an additional assumption to calculate their total entropy. This was that the tetragonal phase consists of pure $CsHSO_4$. The entropy of these compounds was then straightforwardly appraised by Eq. (4-1) and Eq. (4-6). Finally, the $Cs_6(H_2SO_4)_3(H_{1.5}PO_4)_4$ compound obligated multiple assumptions, the most central of which was that there exist cesium vacancies in the cubic high temperature phase. This

calculation is quite speculative due to the lack of data concerning this particular high temperature structure and will need further experimental input to become more conclusive.

Table 4.5 Calculated entropies for high temperature phases

Compound	S_{mix} (J/mol*K)	S_{config} (J/mol*K)	S_{total} (J/mol*K)
$CsHSO_4$	0	14.9	14.9
$Cs_3(HSO_4)_{2.50}(H_2PO_4)_{0.50}$	2.44	17.26	19.7
$Cs_3(HSO_4)_{2.25}(H_2PO_4)_{0.75}$	2.88	19.33	22.21
$Cs_3(HSO_4)_2(H_2PO_4)$	5.29	21.54	26.83
$Cs_5(HSO_4)_3(H_2PO_4)_2$	5.6	20.95	26.55
$Cs_2(HSO_4)(H_2PO_4)$	5.76	23.76	29.52
$Cs_6(H_2SO_4)_3(H_{1.5}PO_4)_4$	9.09	27.25	36.34
CsH_2PO_4	0	27.3	27.3

4.6.7 Calculated ΔS_{trans} and comparison with experimental ΔS_{trans}

The calculated transition entropies for these cesium sulfate-phosphate compounds are then simply the values in Table 4.4 subtracted from those of Table 4.5. We can compare these numbers to the measured entropies by dividing the experimental transition enthalpies by the mean of the various transition temperatures listed on Table 4.3. The results of this comparison are shown graphically in Figure 4.21 and listed in Table 4.6. The first thing one should observe when viewing Figure 4.21 is the very satisfactory

agreement between the experimental and calculated transition entropies, which are quite often within error of each other.

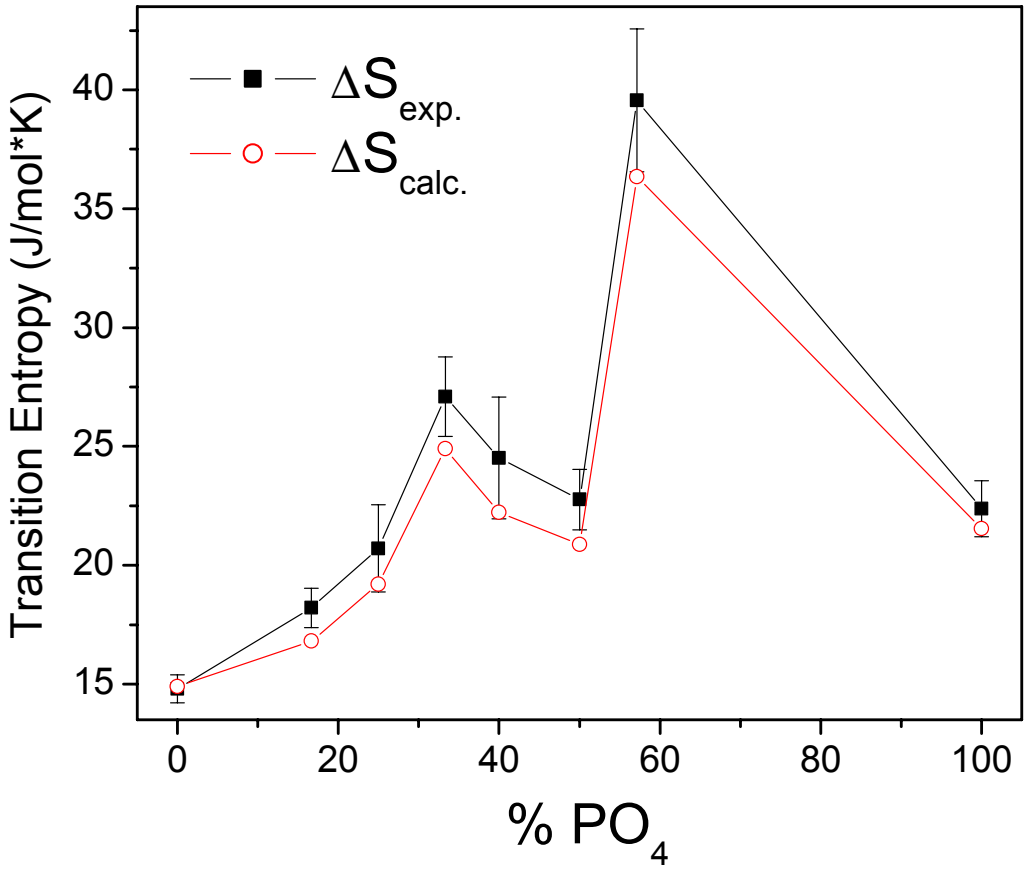

Figure 4.21 Measured versus calculated transition entropies. The shape of the calculated curve closely mimics that of the experimental. Note calculated and experimental values are nearly identical for $CsHSO_4$, for which the subjective evaluation of the room temperature entropy was not necessary.

The sometimes large errors in the experimental entropies are due mainly to the ambiguity in T_c caused by the large range over which some of the compounds transform. From a thermodynamic perspective, one might expect that the onset temperatures, T_{onset}(DSC) and $T_{onset}(\sigma)$, would tend to underestimate ΔH_{trans} because the compound has

not actually reached equilibrium with respect to the high temperature phase until the transition is complete. Conversely, the final temperatures, T_{peak}(DSC) and T_{final}(σ), will tend to overestimate ΔH_{trans} as the room temperature phase stopped being the most energetically favorable phase at T_{onset}. For these reasons, the mean value of the transition temperatures was taken as T_c for each compound, which led to large errors in the experimental entropies for compounds with extend transition temperature ranges.

It is interesting that the calculated and measured transition entropies for $CsHSO_4$ are very similar. This would tend to confirm not only the hypothesis that $CsHSO_4$ has two (rather than four) orientations in its tetragonal phase, but also justify the use of the mean transition temperature for the following reason: this compound had zero entropy in its room temperature structure and therefore the somewhat subjective entropy evaluation of its room temperature phases was avoided. Consequently, the calculated entropy for $CsHSO_4$ should have the least amount of unaccounted for entropy. The nearly perfect match of calculated and experimental values is then very reassuring. The systematically lower values of the calculated, compared to experimental, entropies for the rest of the compounds are probably a combination of the fact that the maximum reasonable amount of entropy was assigned to the room temperature phases and that only the mixing and configurational contributions to the transition entropy were evaluated. Even the calculated entropies for the $Cs_6(H_2SO_4)_3(H_{1.5}PO_4)_4$ compound have the right magnitude, although this result must be taken with a large grain of salt considering the amount of speculation that went into the entropy evaluation of this compound's cubic structure.

Table 4.6 Calculated and experimental transition entropies.

Compound	T_c (mean)- (K)	ΔH_{exp} - (kJ/mol)	$\Delta S_{exp} = \Delta H_{exp} / T_c$ (J/mol*K)	ΔS_{calc} - (J/mol*K)
$CsHSO_4$	419(3)	6.2(2)	14.8(6)	14.90
$Cs_3(HSO_4)_{2.50}(H_2PO_4)_{0.50}$	407(7)	7.4(2)	18.2(8)	16.82
$Cs_3(HSO_4)_{2.25}(H_2PO_4)_{0.75}$	401(11)	8.3(5)	20.7(18)	19.21
$Cs_3(HSO_4)_2(H_2PO_4)$	395(17)	10.7(2)	27.1(17)	24.91
$Cs_5(HSO_4)_3(H_2PO_4)_2$	375(11)	9.2(7)	24.5(26)	22.22
$Cs_2(HSO_4)(H_2PO_4)$	364(12)	8.3(2)	22.8(13)	20.88
$Cs_6(H_2SO_4)_3(H_{1.5}PO_4)_4$	382(14)	15.1(6)	39.6(30)	36.34
CsH_2PO_4	505(4)	11.3(5)	22.4(12)	21.54

Finally, it should be noted that although the investigations into the entropic driving force of these compounds were originally propelled by an apparent correlation between phosphorous content and T_c (see Figure 4.6 a)), the final results deny any such relationship. It was originally thought that the lowering of T_c with rising phosphate percentage indicated that ΔH was remaining relatively constant while ΔS increased with phosphorous content. However, as more data became available, it became clear that this was not in fact the case. With the full data set available to us now, it would seem that although there are undoubtedly very general effects to increasing the phosphorous content, the particulars of the room temperature structures far outweigh any such effects.

This conclusion is quite evident in Figure 4.6 d), a plot of molar H-bond energy versus $\%PO_4$, where one might have guessed a priori that the energy associated with the hydrogen bonds would increase fairly linearly with phosphate, and therefore hydrogen, content. In fact, starting with just the end members $CsHSO_4$ and CsH_2PO_4, such a linear relationship would have seemed justified as the hydrogen bond energy (per mole

$CsHXO_4$) of CsH_2PO_4 is almost twice that of $CsHSO_4$. The intermediate compounds, however, fall far from the line connecting the two end members and it can only be said very generally that increasing phosphate/hydrogen content correlates to higher molar hydrogen bond energies.

It is then even more pleasing that Pauling's ice rules, adjusted to properly describe the superprotonic phases of these cesium sulfate-phosphate compounds, produce transition entropies that compare very well with the measured values. Since these rules combine the positional disorder of the proton system with the rotational disorder of the tetrahedra, it should be applicable to any transition that involves a disordering of a hydrogen-bonded network via disorder of the hydrogen carriers. This has already been shown to be true in compounds where the hydrogen-bonded network is composed of water molecules and would now appear to be true for systems containing hydrogen-bonded tetrahedra.

4.6.8 Application of the adjusted ice rules to other superprotonic transitions

There are other compounds for which these adjusted ice rules should apply. First and foremost are the compounds $CsHSeO_4$ and CsH_2AsO_4, which have superprotonic transitions at (T_{onset}) 128 and 165°C, respectively[157,158]. The compounds are also isostructural to $CsHSO_4$ and CsH_2PO_4, respectively, in their superprotonic phases[46,159]. $CsHSeO_4$ has no configurational entropy below its transition as it is isostructural to $CsHSO_4$'s room temperature phase[160]. The CsH_2AsO_4 compound, however, is not isostructural to its phosphate cousin, but has a tetragonal structure at room temperatures[161]. The tetrahedra of CsH_2AsO_4 have all four oxygen atoms involved in

hydrogen bonds, similar to CsH_2PO_4, but here *all bonds are disordered*, so that CsH_2AsO_4 will have an entropy of 2*R*ln(2) associated with its room temperature structure. Using the calculated configurational entropy of the superprotonic tetragonal and cubic phases (Eqs. (4-9) and (4-11), respectively), the transition entropies can then be calculated. The resulting entropies match up very well with the measured values, Table 4.7. Having successfully applied these ice rules to the $CsHSO_4$-CsH_2PO_4 system and to the end members $CsHSeO_4$ and CsH_2AsO_4, one would expect that they should apply equally well to any mixed Cs-S-Se-P-As compounds. Some of these mixed compounds have already been synthesized, such as $Cs_4(SeO_4)(HSeO_4)_2(H_3PO_4)$, $Cs_3(HSeO_4)_2(H_2PO_4)$, and $Cs_5(HSeO_4)_3(H_2PO_4)_2$, $(NH_4)_2(HSO_4)(H_2AsO_4)$, however their properties have not been reported[162,163].

Table 4.7 Application of ice rules to other solid acid supeprotonic phase transitions

Compound	T_c-mean (K)	$S_{calc} - RT$ (J/mol*K)	$S_{calc} - HT$ (J/mol*K)	ΔS_{calc} (J/mol*K)	$\Delta S_{exp}=\Delta H_{exp}/T_c$ (J/mol*K)	ref
$CsHSeO_4$	140	0	14.90	14.90	16.0(5)	157 164
CsH_2AsO_4	186	11.53	27.30	15.77	17.4(6)	158
$K_3H(SeO_4)_2$	121	5.76	13.38	7.62	7.8(3)	165 101
$CsHPO_3H$	140	0	30.67	30.67	30.1(11)	166
$RbHSeO_4$	182	2.88	?	?	23.9(4)	167
NH_4HSeO_4	157	2.88 + 9?	?	?	15.1(5)	167

Until now, only compounds with Cs cations have been examined, but this theory places no limitation on the type or number of cations present. The prevalence for Cs cations is directly linked with the cation size effect discussed in Chapter 3, in that superprotonic transitions are more often found in compounds with large cations. These

ice rules should then also be applicable to the superprotonic transitions of $MHXO_4$ compounds (where M = Li, Na, K, NH_4, Rb, Tl, Cs; X = S, Se, P, As). These compounds could have varying $M:XO_4$ ratios, mixed cations, or both, such as $(NH_4)_4H_2(SeO_4)_3$, $Cs_{0.9}Rb_{0.1}HSO_4$, and $Rb_4LiH_3(SeO_4)_4$, respectively, all of which have reported superprotonic transitions (without, unfortunately, the transition enthalpies or entropies)[168, 97,169]. And, of course, the intersection of these two sets, compounds with mixed anions and mixed cations, will be equally susceptible to having these ice rules applied to any uncovered superprotonic phase transitions.

Also, the disordered network of hydrogen bonds need not be three-dimensional, as with all the previous examples, for these rules to apply. The class of compounds $M_3H(XO_4)_2$ (M= Na, K, NH_4, Rb, Cs: X = S, Se) exhibits superprotonic phase transitions where the proton transport occurs within planes[170]. The compounds are pseudo-trigonal in their room temperature phases and most of them transform into a trigonal phase at elevated temperatures[100]. For the compounds with such transitions, these ice rules should reproduce the measured transition enthalpies quite well, as can be seen for the $K_3H(SeO_4)_2$ compound in Table 4.6.

Finally, these ice rules also appear valid for compounds with alternative anion chemistries, such as $CsHPO_3H$, where one of the tetrahedral oxygens has been replaced by a hydrogen atom. This compound exhibits a superprotonic phases transition at 137°C, transforming into the same cubic CsCl like structure as the mixed cesium sulfate phosphates[166]. Adjusting the ice like rules developed here for the dissimilarity of the tetrahedra's coordinating ions will cause two changes. First, no hydrogen bonds can be formed to the tetrahedral hydrogens. The tetrahedral hydrogen then effectively acts as an

OH group and the probablility of a direction being open will be 4/6 rather than the normal 5/6 for a hydrogen to tetrahedron ratio of 1:1. Second, there will be three distinguishable configurations of the two possible acceptor oxygen atoms and the tetrahedral hydrogen for every configuration of the proton/donor oxygen system. This will cause an extra factor of three. The number of configurations for this compound in its cubic phase is then

$$\Omega = \binom{6}{1} * \underline{\left(\frac{4}{6}\right)^{1}} * (1) * (4) * \underline{(3)} = 48 \qquad (4\text{-}32)$$

which results in a calculated enthalpy very close to the measure value, Table 4.6.

This exposition of applications serves to prove the flexibility of these ice rules; a flexibility that allows for a certain amount of prediction concerning poorly characterized compounds or entirely new systems. For example, the high temperature structures of $RbHSeO_4$ and NH_4HSeO_4 are not well determined and so an evaluation of their entropy is not possible[87,91]. However, the measured transition entropies of 24 and 15 J/mol*K for $RbHSeO_4$ and NH_4HSeO_4, respectively, and these ice rules indicate that the high temperature phase cannot be the tetragonal phase of $CsHSO_4$[167]. These compounds are isostructural to each other in their room temperature phase with one disordered hydrogen bond per two tetrahedra (S = 1/2*Rln(2) = 2.88 J/mol*K)[171]. The ammonium compound also has orientational disorder associated with the SeO_4 and NH_4 ions, which most probably accounts for the difference in transition entropies between the two compounds[102]. There is then a considerable amount of entropy incorporated into the room temperatures of these compounds and yet the transition entropies are both above the calculated 14.9 J/mol*K maximal transition entropy for the tetragonal phase of $CsHSO_4$.

It is also possible that entirely new systems of compounds with superprotonic transitions will be discovered, systems with perhaps mixed M^{+2} and M^{+1}cations or including various other anion groups (i.e., SiO_4, ClO_4, PO_3F, SiF_6, COF_3, etc.). It would be very nice to estimate the probability of an order-disorder transition in such new compounds so as to narrow the focus of experiments to those compounds most likely to exhibit superprotonic conduction. After all, the entire purpose of this work is to better understand what causes superprotonic phases to exist and to then apply that to making materials more suited for application.

With this purpose in mind, it is suggested that a hypothetical transition temperature could be derived from an observed correlation between the transition ΔV and ΔH, and liberal use of these ice rules in estimating a transition entropy. For the $CsHSO_4$-CsH_2PO_4 compounds, the correlation between transition enthalpy and volume is quite clear, Figure 4.22. Since the variation of the data is so small, it seems possible that if one estimated a transition volume from the predicted room and high temperature structures, it would be possible to derive a fairly accurate transition enthalpy. Also, using the predicted structures and these ice-like rules, a likely entropy could also be obtained. Taking the ratio of these two values would then give an approximate transition temperature, hopefully telling the investigator whether a compound was worth investigating or not. In other systems, a similar relationship could be calculated from existing data, or perhaps extrapolated from structurally and chemically related compounds. This process could save a vast amount of experimental time as synthesis of even these water soluble compounds was not trivial.

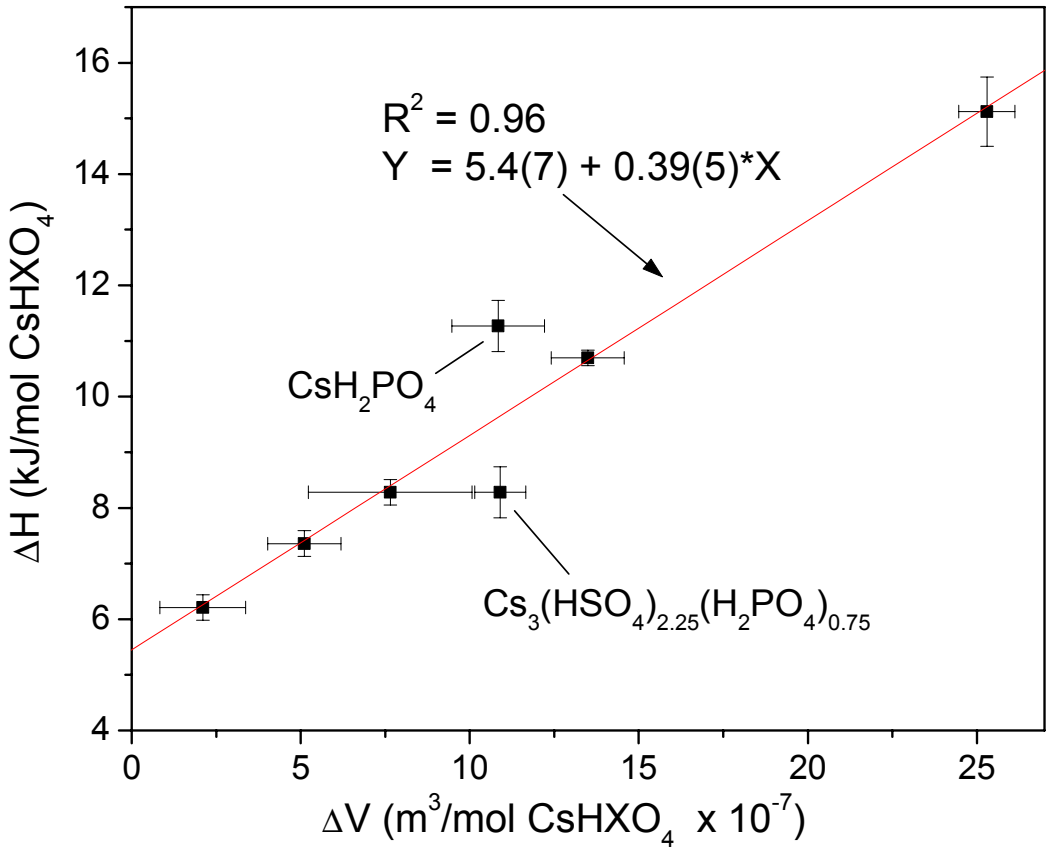

Figure 4.22 Transition volume versus enthalpy. The apparent correlation between the two values suggests the possibility of estimating a transition enthalpy from a predicted volume change.

It would be interesting to add the transition enthalpies and volumes of the other known superprotonic conductors to Figure 4.22. Alas, even though the room and high temperature structures have been measured for most of the known superprotonic compounds, accurate thermal expansion coefficients are almost universally lacking. Since the difference between the temperature at which the room and high temperature structures are measured is usually in the hundreds of degrees, the expansion (or contraction) of the phases with temperature would greatly effect the transition volumes. If and when more accurate transition volumes become available, it will be very interesting to see if the

linear trend seen in Figure 4.22 holds for all the known superprotonic conductors, or if different structural and chemical families of compounds require their own categorization.

Chapter 5. Superprotonic Phase Transition of $CsHSO_4$: A Molecular Dynamics Simulation Study with New MSXX Force Field

5.1 Introduction

This molecular dynamics (MD) study of the superprotonic phase transition of $CsHSO_4$ was undertaken with two aims: to determine whether the transition could be simulated without allowing proton migration and to develop a procedure for creating MD force fields (FF) applicable to other solid acids. The first objective was motivated by the desire to know whether proton hopping or tetrahedra reorientations are the essential ingredient in stimulating a transition from the ordered room temperature structure to the highly disordered superprotonic phase. The latter goal comes from the desire to greatly speed up the search for new superprotonic compounds with properties ideal for application. It was hoped that a simple process could be developed to predict superprotonic phase transitions of, as yet unknown, compounds without first synthesizing the material, which can take untold time in the laboratory.

Success in simulating the transition of $CsHSO_4$ gave sufficient confidence in the new FF that the effects of changing various FF parameters on the transition were investigated. The adjusted parameters included the charge distribution of the oxygen atoms, hydrogen bond strength and torsional barrier height. In each case, a single parameter was changed and the simulations re-run with all other FF and simulation

variables held constant. Thus, the superprotonic phase transition of $CsHSO_4$ was probed in a manner not possible by experimental methods.

The results of this chapter will then compliment those of the experimental chapters (3 and 4) in that all three chapters aim to better our understanding of which parameters favor superprotonic transitions. In particular, this chapter gives atomistic information (you can even watch them if you like!) not available from physical measurements. Also, the success of this chapter's FF in simulating the superprotonic transition of $CsHSO_4$ suggests that the same procedure could be employed to generate FF's for other cations and anions. Combining these FF could then give us a powerful tool for predicting novel superprotonic conducting solid acids.

5.2 Characterization of $CsHSO_4$

Although both the structures and superprotonic phase transition of $CsHSO_4$ have been described multiple times in this text, for the sake of this chapter's completeness, the compound's important characteristics will be detailed below.

5.2.1 Crystal structures of $CsHSO_4$

The actual room temperature phase of $CsHSO_4$, especially when it is obtained from a mixture of equimolar Cs_2SO_4 and H_2SO_4 in aqueous solution, is $CsHSO_4$-III (phase III) not $CsHSO_4$-II (phase II) that has been described throughout the text. That is, there are three phases in the crystal of $CsHSO_4$ in the temperature range from 123 to 420 K[84,172]:

$$\text{phase III}\,(P2_1/c) \xrightarrow{330\text{-}370\,K} \text{phase II}\,(P2_1/c) \xrightarrow{410\text{-}415\,K} \text{phase I}\,(I4_1/amd)$$

Whereas the II-to-I phase transition is quite reversible, the III-to-II phase transition depends on the amount of the absorbed water in the sample. A water-free powder sample ("dry" sample) remains at phase II on cooling down to 123 K. Only a water-saturated sample ("wet" sample) becomes the initial phase III on cooling[84]. Moreover, if $CsHSO_4$ is deuterated to more that 30-40 %, only phases II and I are present in the temperature range of 123-420 K[172].

Thus, in the present work, we assumed that the room temperature phase of "dry" $CsHSO_4$ is the phase II rather than phase III and focused only on the II-to-I phase transition. Phase II is monoclinic (space group $P2_1/c$) as determined by single crystal X-ray diffraction at 298 K[173], Figure 5.1 a. The lattice parameters are a=7.781(2) Å, b=8.147(2) Å, c=7.722(2) Å, and β=110.78° . The hydrogen bonds configure so as to form zigzag chains along the [001] direction (c-direction) and the O-H· · · O bonds are fully ordered with <(O-H· · · O) = 174(6)° , d(O-H) = 0.94(4) Å, d(H· · · O) = 1.70(4) Å, and d(O· · · O) = 2.636(5) Å.

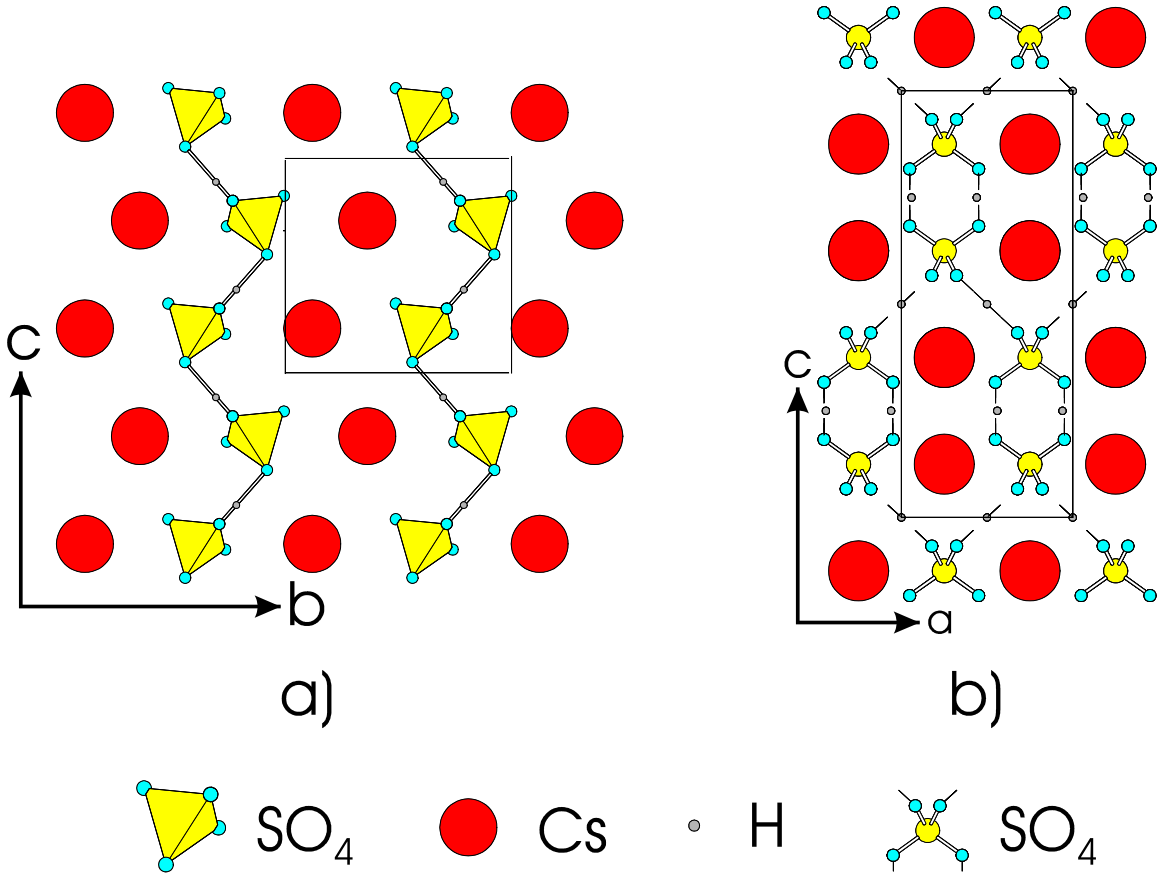

Figure 5.1 Crystal structure of $CsHSO_4$: a) monoclinic phase II [26]and b) tetragonal phase I as proposed by Jirak[61]. In b), each oxygen position has half occupancy and the hydrogen atoms are placed in the middle of the disordered hydrogen bonds (dashed lines).

The high temperaturephase (phase I) is tetragonal (space group $I4_1/amd$), Figure 5.1 b. There is considerable disorder in the orientation of the hydrogensulfate (HSO_4) groups (HSO_4 libration) in this phase[102], with some debate as to the actual number and/or direction of the orientations possible for each tetrahedron. The multiple orientations for each tetrahedron are a result of the high symmetry of this phase and each tetrahedron's need to conform to this symmetry. As the sulfur is centrally located in a tetrahedron, the exact position of the oxygen atoms will then determine how many orientations are necessary to achieve the desired tetragonal symmetry. The disagreement in the literature

about the number and/or direction of the orientations for each tetrahedron is then equivalent to the proposed positions of the oxygen atoms, which were determined by diffraction experiments, Figure 5.2. According to Jirak, who performed a powder neutron diffraction study on $CsHSO_4$ at a temperature slightly above 414 K, each tetrahedron adopts one of two orientations and the phase has lattice constants of a = 5.718(3) Å and c = 14.232(9) Å[61]. The structure proposed by Jirak is shown in Figure 5.1 b. The structure put forward by Merinov from an single crystal X-ray diffraction study of $CsDSO_4$ at 430 K has lattice constants of a=5.729(9) Å and c=14.21(1) Å with two orientations for each tetrahedron[125]. A high-resolution neutron powder diffraction study by Belushkin, on $CsDSO_4$ at 448 K, gave lattice parameters of a=5.74147(9) Å and c=14.31508(26) Å with four orientations for each tetrahedron[124].

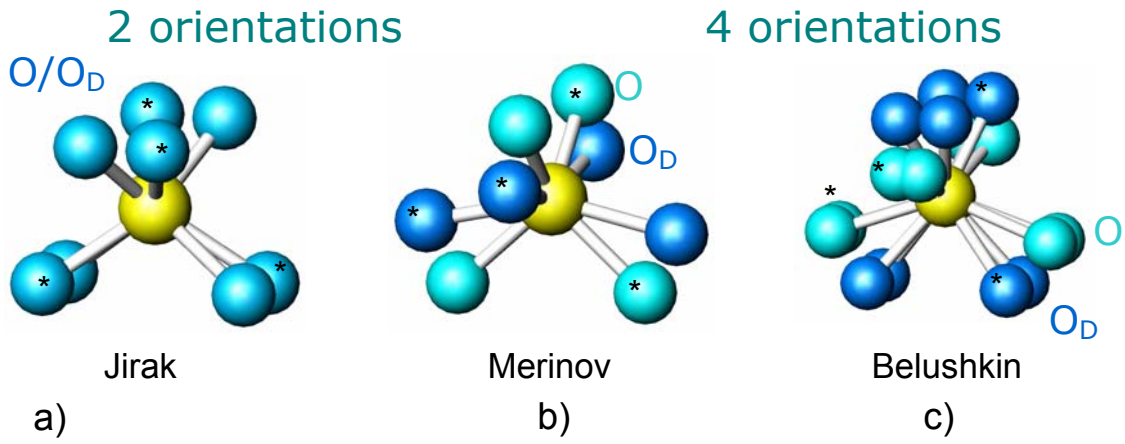

Figure 5.2 Possible configurations of the sulfate tetrahedra in the superprotonic phase: the structures by Jirak-a)[61], Merinov-b)[125], and Belushkin-c)[124] have two, two, and four orientations, respectively, which transform into each other by rotations of 32°, 30°, and 30°, respectively. The * designates one possible arrangement for the oxygen atoms of a tetrahedra.

5.2.2 Nature of the superprotonic transition of $CsHSO_4$

Regardless of which structure you pick for $CsHSO_4$ phase I, the basic nature of the phase transition and mechanism of proton conduction remains the same. The transition is of first order from the ordered, low symmetry phase to the disordered high symmetry phase[124]. The increase in entropy due to this disorder is the energetic driving force for the transition. The reorientations of the tetrahedra are then both energetically and symmetrically required for this transition. As the protonic conductivity is a direct result of these tetrahedral reorientations, the superprotonic conductivity of phase I is a by product of the ideal structure[2]. Across the transition, the protonic conductivity increases by 3-4 orders of magnitude from 10^{-6} Ω^{-1} cm^{-1} (phase II) to 10^{-3}-10^{-2} Ω^{-1} cm^{-1} (phase I)[4].

That the main contribution to the enhanced conductivity of phase I stems from the mobility of protons is confirmed by both H^+ NMR measurements and quasi-elastic neutron scattering (QNS) experiments on phase I of $CsHSO_4$. Both methods found a proton diffusion constant, D_H, equal to ~ $1x10^{-7}$ cm^2/s at temperatures above 414 K[6]. Rf-microwave dielectric measurements have confirmed that the sulfate tetrahedra are undergoing fast reorientations (10^{12}Hz) while proton transfer occurs more slowly (10^9Hz)[174].

The proton transfer process in phase I is therefore thought to consist of two steps: the creation of hydrogen bonds between previously isolated tetrahedra by HSO_4 rotations and the translation of protons between the two equilibrium sites in the newly created O-H· · · O bond resulting in an H_2SO_4 defect[35]. The "doubly protonated" H_2SO_4 defect may propagate rather fast by phonon-assisted tunneling or classical hopping of protons between the two minima in the O-H· · · O bonds along the H-bonded chains[6]. With

libration of the HSO_4 groups the weak link H-acceptor disordered hydrogen bond is broken, while the strong link H-donor is preserved. On account of rapid rotation of the sulfate groups, the proton samples all possible crystallographic positions; with translation of the proton along a newly formed two-minimum hydrogen bond occurring once in about a hundred rotations of the tetrahedra. Thus, migration of protons is effected both by their jumping between positions on the hydrogen bond and by rotation of HSO_4 groups. Such a process is called a Grotthuss type mechanism proton conduction[39].

5.3 MD Simulation of Superprotonic Transition of $CsHSO_4$

5.3.1 Overview

The II-to-I superprotonic phase transition of $CsHSO_4$ was simulated by the molecular dynamics (MD) as temperature was increased from 298 K to 723 K in 25 K steps. The force field for these MD simulations treated the hydrogen as bonded exclusively to a single oxygen atom (donor oxygen, O_D), with hydrogen bonds extending to nearby oxygen atoms (acceptor oxygen, O_A). Proton diffusion (i.e., proton jumps) between oxygen atoms cannot occur with this kind of force field. Thus, the contribution of proton jumps to the phase transition was removed and only the effects of the orientation disorder of HSO_4 groups were considered.

5.3.2 Calculation details: Force fields

The functional forms and parameters of the force field (FF) used in the simulation are given in Tables 5.1 and 5.2. This FF is based on Dreiding FF [175]. The off-diagonal

van der Waals (vdW) parameters (Cs-O, Cs-S, Cs-H, S-O, S-H, and O-H) are determined by the standard combination rules[175]. No nonbonding interaction is considered for 1,2-pairs (bonded atoms) and 1,3-pairs (atoms bonded to a common atom), because it is considered that their electrostatic and vdW interactions are included in their bond- and angle-interactions.

Table 5.1 Force field[a] for $CsHSO_4$.

$E = E^{nonbond} + E^{valence}$
$E^{nonbond} = E^{coulomb} + E^{vdW} + E^{H-bond}$
$E^{valence} = E^{bond}_{SO} + E^{angle}_{OSO} + E^{RR}_{OSO} + E^{\theta\theta}_{SOOO} + E^{torsion}_{OSOH}$
$E^{coulomb}_{ij}(R) = C_0 \frac{q_i q_j}{\varepsilon R_{ij}}$
$E^{vdW}_{ij}(R) = D_0 \left\{ \left[\left(\frac{6}{\varsigma - 6} \right) e^{\varsigma \left(1 - \frac{R}{R_0} \right)} \right] - \left[\left(\frac{\varsigma}{\varsigma - 6} \right) \left(\frac{R_0}{R} \right)^6 \right] \right\}$
$E^{H-bond}_{O-O}(R) = D_0 \left\{ 5 \left(\frac{R_0}{R} \right)^{12} - 6 \left(\frac{R_0}{R} \right)^{10} \right\}$
$E^{bond}_{SO}(R) = \frac{1}{2} K_R (R - R_0)^2$
$E^{angle}_{OSO}(\theta) = E^{angle}_{SOH}(\theta) = \frac{1}{2} \frac{K_\theta}{\sin^2 \theta_0} (\cos\theta - \cos\theta_0)^2$
$E^{RR}_{OSO}(R_1, R_2) = K_{RR}(R_1 - R_0)(R_2 - R_0)$
$E^{\theta\theta}_{SOOO}(\theta_1, \theta_2) = \frac{K_{\theta\theta}}{\sin\theta_{0_1} \sin\theta_{0_2}} (\cos\theta_1 - \cos\theta_{0_1})(\cos\theta_2 - \cos\theta_{0_2})$
$E^{torsion}_{OSOH}(\varphi) = \frac{1}{2} K_\varphi [1 + \cos(2\varphi)]$

[a]The constants in $E^{Coulomb}$ are the dielectric constant (ε) and $C_0 = 332.0637$ (the unit conversion factor when atomic charges q_i's are in electron units (|e|), the distance R is in Å, and $E_{Coulomb}$ is in kcal/mol).

Table 5.2 Force field parameters for $CsHSO_4$.[a]

E^{vdW}	Cs	R_o[b]	4.1741[i]	D_o[c]	0.37[i]	ζ	18[i]
	S	R_o[b]	4.03[h]	D_o[c]	0.344[h]	ζ	12.0[h]
	O	R_o	3.4046[h]	D_o[c]	0.0957[h]	ζ	13.483[h]
	H	R_o	3.195[h]	D_o[c]	0.0001[h]	ζ	12.0[h]
E^{bond}	S-O_D	R_o[b]	1.6925[i]	K_b[d]	700.0[h]		
	S-O_A	R_o[b]	1.499[i]	K_b[d]	700.0[h]		
	O_H-H	R_o[b]	0.988[i]	K_b[d]	700.0[h]		
E^{angle}	O_A-S-O_D	θ_o[e]	105.933[i]	K_θ[f]	350.0[h]		
	O_A-S-O_A	θ_o[e]	115.2[i]	K_θ[f]	350.0[h]		
	S-O_D-H	θ_o[e]	109[i]	K_θ[f]	350.0[h]		
E^{RR}	O_A-S-O_A	$R_o(O_A)$[b]	1.4856[i]	$R_o(O_A)$[b]	1.4856[i]	K_{RR}[d]	102.0[h]
E^{RR}	O_A-S-O_D	$R_o(O_A)$[b]	1.4856[i]	$R_o(O_D)$[b]	1.65[i]	K_{RR}[d]	102.0[h]
$E^{\theta\theta}$	S-O_A-O_A-O_A	$\theta_o(O_A,O_A)$[e]	112.8[i]	$K_{\theta\theta}$[f,g]	72.5[h]		
	S-O_A-O_A-O_D	$\theta_o(O_A,O_D)$[e]	105.933[i]	$K_{\theta\theta}$[f,g]	72.5[h]		
	S-O_A-O_D-O_A	$\theta_o(O_A,O_A)$[e]	112.8[i]	$\theta_o(O_A,O_D)$[e]	105.933[i]	$K_{\theta\theta}$[f,g]	72.5[h]
$E^{torsion}$	O_A-S-O_D-H	Symmetry	C_3	φ(min.)	60°	K_φ[c]	2.1669[j]
E^{Hbond}	$O_D\cdots O_A$	R_o[b]	3.0004[k]	D_o[c]	0.2366[k]		

[a]For functional forms, see Table 1.
[b]In Å. [c]In kcal/mol. [d]In kcal/mol/Å^2. [e]In degrees. [f]In kcal/mol/rad^2.
[g]In the current version of Polygraf (version 3.30), the divisor for angle-angle cross term $E^{\theta\theta}$ is written as $E^{\theta\theta}$ $(\cos\theta_1 - \cos\theta_{10})(\cos\theta_2 - \cos\theta_{20})$ where $E^{\theta\theta} = K_{\theta\theta}/ \sin\theta_{0_1} \sin\theta_{0_2} =$ 81.5625 where $K_{\theta\theta} = 72.5$. In Cerius 2 the input is in terms of $K_{\theta\theta}$[176].
[h]From Dreiding FF[175].
[i]Adjusted to reproduce a $CsHSO_4$ monomer ab initio structure, binding energy and frequencies.
[j]Adjusted to reproduce ab initio barrier height (in kcal/mol) for HSO_4^- ion in a dielectric medium with a relative dielectric constant of 10.
[k]Adjusted to fit ab initio O-O distance and binding energy of an H_2SO_4- H_2SO_4 dimer.

Dreiding FF values were adjusted by fitting the parameters to three separate ab initio calculations at the B3LYP/LACVP** level [177-181] [182] (set denotes basis sets of 6-31G** for H/O/S and LACVP for Cs) using *Jaguar* software[183]. The first calculation was on a gas-phase $CsHSO_4$ monomer, the second on a gas-phase $(H_2SO_4)_2$ dimer, and the third calculation on an HSO_4^- ion in a dielectric medium of relative dielectric constant 10 (Figure 5.3 a), b, and c), respectively). Adjustments to the Dreiding FF values were made so that each chemical species would duplicate the results of the QM calculations after a FF minimization to lowest potential energy. All FF energy minimizations were carried out with the Newton-Raphson method on *Cerius2* software[176]. A more detailed explanation of how these QM calculations were used in altering the Dreiding FF values is given below.

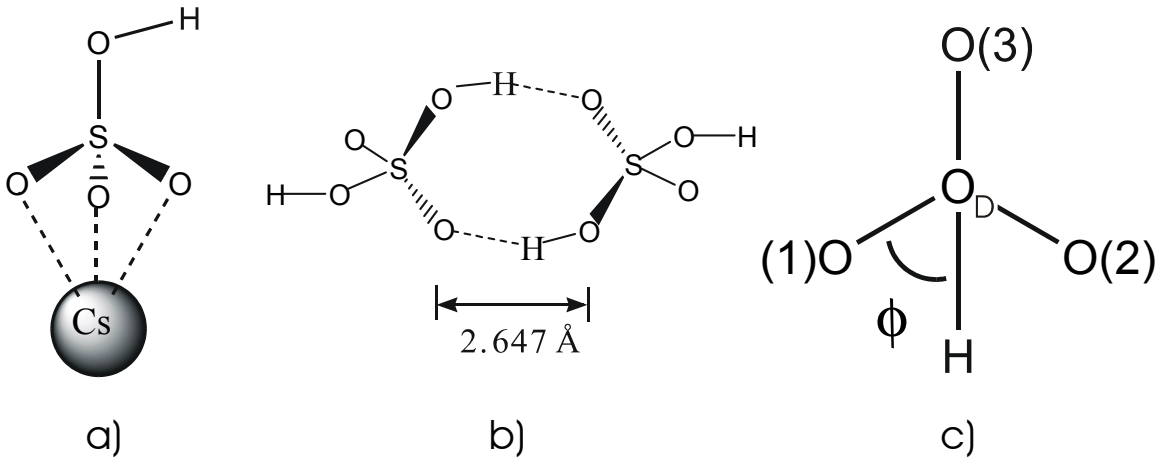

Figure 5.3 Structures used to adjust the Dreiding FF parameters: (a) $CsHSO_4$ monomer, (b)$(H_2SO_4)_2$ dimer, and (c) HSO_4^- ion projected down S-O(H) bond. $CsHSO_4$ monomer used to adjust Cs vdW and all HSO_4^- FF parameters except for the hydrogen bond and O-S-O-H torsional terms which were adjusted with b) and c), respectively.

I. $CsHSO_4$ gas phase monomer:

All cesium (Cs) vdW parameters and FF values for HSO_4^-, *except for torsional and hydrogen bond values*, were varied to reproduce a $CsHSO_4$ monomer derived from the ab initio calculation on gas-phase $CsHSO_4$. Both the initial and final structures of this calculation had the Cs near the three fold axis of symmetry of the tetrahedral face opposite the hydrogen bonded oxygen, Figure 5.3 a). Cesium vdW parameters were fit to the average Cs-O distance for the three non-hydrogen bonded oxygens, the binding energy of the $Cs^+ + HSO_4^-$ ions, and the symmetric stretch frequency of $CsHSO_4$ monomer. FF values for S, O, and H in HSO_4^-, *except for torsional and hydrogen bond parameters*, were adjusted from Dreiding FF values to fit the ab initio structure (bond lengths and angles) and frequencies of the HSO_4^- ion. This was a rather straightforward process, with the added complexity of having two different types of oxygen atoms in the FF: donor oxygens, O_D and acceptor oxygens, O_A. Such a segregation of the oxygen atoms was a direct result of fixing the H atoms to particular oxygens.

Charges for all atoms were derived from the electrostatic-potential-fitted (ESP) charges of the $CsHSO_4$ monomer ab initio calculation[184-186]. The charges taken directly from the ab initio calculation are shown in Table 5.3 along with the final adjusted charges used in these simulations. Adjustment to the charges involved only the Cs and O atoms; the final charges for S and H atoms being identical to those of the QM calculation. The atomic charge for all Cs atoms was fixed at its formal charge +1.0|*e*|. An increase in negative charge to balance the increased positive charge on the Cs atoms (+0.072|*e*|) was distributed evenly over all oxygen atoms (i.e., -0.018|*e*| on each oxygen). The adjusted charges of the O(1) and O(2) oxygen atoms (now, -0.648|*e*| and -0.654|*e*|, respectively)

were then averaged together giving the final charges of these atoms (-0.651|*e*| each). This arrangement of oxygen charges was picked not only to conform with the ab initio values, but also as such a distribution of charges seemed likely for the oxygen atoms of a tetrahedron in phase II $CsHSO_4$. In this phase, asymmetric hydrogen bonds connect the SO_4 tetrahedra into infinite chains and therefore every tetrahedron has a donor and acceptor oxygen, and two oxygen atoms not involved in hydrogen bonds[26].

Table 5.3 ESP charges for $CsHSO_4$: from the *ab initio* QM calculation on the CsHSO4 monomer [B3LYP/LACVP**] and the final set used in the simulations.

Environment	q_{Cs}(|e|)	q_S (|e|)	$q_{O(1)}$ (|e|)	$q_{O(2)}$ (|e|)	$q_{O(3)}$ (|e|)	q_{OD} (|e|)	q_H (|e|)
Gas-phase	0.928	1.045	-0.630	-0.636	-0.588	-0.523	0.404
Simulation	**1.0**	**1.045**	**-0.651**	**-0.651**	**-0.606**	**-0.541**	**0.404**

There are then essentially three types of oxygen atoms in this force field when both an oxygen's FF type and charge are considered: non-hydrogen-bonded, donor and acceptor oxygen atoms. The non-hydrogen-bonded atoms, O(1) and O(2), have O_A FF parameters and a charge of –0.651|e|, while oxygen acceptor atoms, O(3), have O_A FF parameters but a charge (–0.606|e|). Oxygen donor atoms, O_D, have there own FF parameters (O_D values) and charge (–0.541|e|). This division of the oxygens represents the fact that the S-O bonds are not equivalent in the HSO^{4-} ion. The addition of a hydrogen makes the S-O(H) bond rather like a single bond, whereas the S-O(1),O(2),O(3) bonds behave more like multiple bonds with an average bond order of one and two thirds. The O(3) atom was picked as the acceptor oxygen for the simple reason that its charge

was smaller than that of O(1) and O(2). This fact agreed with the premise that an acceptor should have an average bond order less than one and two thirds, but more than one, and so have a charge in between that of O_D and the non-hydrogen bonded O(1) and O(2) oxygens.

II. $(H_2SO_4)_2$ gas phase dimer:

The ab initio calculation on the gas-phase $(H_2SO_4)_2$ dimer was used to adjust the Dreiding FF values of the hydrogen bond to those found in Table 5.2. Using the previously optimized FF parameters for S, O, and H, the hydrogen bond R_o and D_o values were varied to reproduce the ab initio O-O distance (2.647 Å) and binding energy (-18.569 kcal/mole) of the $(H_2SO_4)_2$ dimer calculation. The charges for all atoms were set to the ESP charges of the QM calculation *without adjustment*. This means that the FF parameters for S, O and H atoms were those previously determined for the charges in Table 5.3, but the charges used were not those found in the table. Also, each H_2SO_4 group had two O_D FF type oxygen atoms instead of just one, as was used in the $CsHSO_4$ monomer minimization. Hence, there was some distortion of the bond lengths and angles of the H_2SO_4 tetrahedra from the QM structure when the dimer was minimized using the adjusted FF. However, ignoring this distortion, the hydrogen bond R_o and D_o values were adjusted until the FF minimized O-O distance and binding energy of the $(H_2SO_4)_2$ dimer matched those of the QM calculation.

III. HSO_4^- ion in dielectric medium:

The third QM calculation, on an HSO_4^- ion in a dielectric medium with dielectric constant of 10, was used to adjust the hydrogen torsional barrier height. This adjustment

actually involved a series of QM calculations where the O(1)-S-O_D-H torsional angle was fixed from 60° to 0°, by steps of 7.5°, while the rest of the HSO_4^- ion was allowed to relax. The initial input for these calculations was the optimized structure of the $CsHSO_4$ monomer with the Cs atom removed and the O(1)-S-O_D-H torsional angle fixed at 60°. The result of the 60° calculation was then used as the input for the 52.5° calculation and so on until the O(1)-S-O_D-H torsional angle was optimized at 0°. The QM barrier height was taken to be the difference between the minimum and maximum of the resulting potential energy curve, Figure 5.4 a. Symmetry considerations allow the potential energy curve to be plotted over a full 360° even though calculations were only performed from 0° to 60°.

The potential energy difference between the minimum (~ 52.5°) and maximum (at 0°) of this curve is 1.6 kcal/mol. Analysis of impedance measurements on $CsHSO_4$ in phase II show the dielectric constant not to vary much from 10^3. The calculations were therefore run with a dielectric constant of 10 to simulate the environment the HSO_4^- ion would encounter while changing its torsional angle. In the optimized structures, the oxygen atoms nearest the hydrogen had charges similar to O(1) and O(2), while the oxygen farthest from the hydrogen had a charge similar to O(3). The barrier height of the FF was therefore adjusted so that the HSO_4^- ion, minimized with a fixed O(1)-S-O_D-H torsional angle between 0° and 60°, had an energy difference between the minimum and maximum of 1.6 kcal/mol. This procedure caused an asymmetry in the FF barrier height due to the difference in the fixed oxygen charges, Figure 5.4 b.

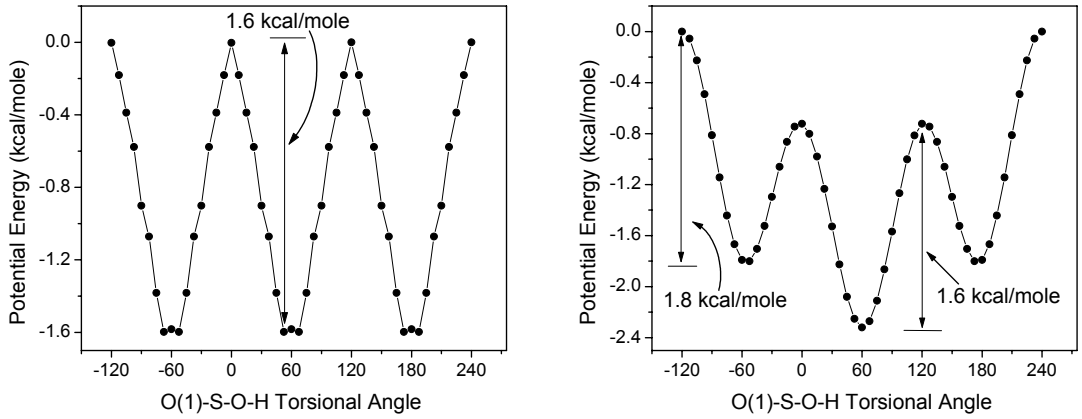

a) b)

Figure 5.4 Potential energy curves for an $HSO4^-$ ion with fixed O(1)-S-O_D-H torsional angles: a) optimized by QM and b) minimized with the adjusted FF.

Finally, it should be mentioned again that in this force field, the hydrogen was treated as exclusively bonded to an oxygen atom with hydrogen bonds to other oxygen atoms. Proton diffusion (or jumps) from one oxygen atom to another cannot occur with this kind of force field. This FF does not correctly describe a proton in either $CsHSO_4$ phase II or I, since in both phases individual protons migrate through the material (requiring proton jumps between tetrahedra)[35]. However, by employing such a constraint, we can separate out the contribution of proton transfer (diffusion or jump) to the superprotonic phase transition.

5.3.3 Calculation Details: Simulations

The structure of the phase II of $CsHSO_4$ was optimized with the Newton-Raphson method with a periodic boundary condition. A $2\times2\times2$ supercell including 32 $CsHSO_4$ units was treated as a unit cell and a series of MD simulations were carried out at various temperatures from 298 K to 723 K in 25 K steps. At each temperature, the Nosé-Hoover

(NPT) Rahman-Parrinello MD simulations[187,188] were carried out at 1 atm for 300 ps with a time step of 1 fs. Properties (potential energy, lattice constants, $HSO4^-$ orientation, etc.) were calculated, after a 150 ps equilibration, from the average over the final 150 ps. This same process was used on the secondary simulations where a particular parameter was varied to quantify its effect on the phase transition. All the simulations were carried out using the *Cerius2* software[176].

5.4 Results

5.4.1 Phase II at Room Temperature: Calculation vs. Experiment

The average structural parameters (density and cell parameters) obtained from the MD simulation at 298 K are within a few percents from the experimental values, Table 5.4. Also, the atomic coordinates are almost all within error of the published values, Table 5.5. This adjusted Dreiding FF has then well reproduced phase II $CsHSO_4$ on both the global (unit cell) and atomistic scale, which is very encouraging since the method which developed it was quite general (i.e., did not use any phase II structure specific information).

Table 5.4 Phase II at room temperature: calculation versus experiment.

Parameter	MD at 298 K	Experiment-X-ray[a]	Experiment-Neutron[b]	Error vs X-ray
density (g/cm^3)	3.35(3)	3.338(3)	3.3429(1)	0.36%
a (Å)	7.93(5)	7.781(2)	7.78013(9)	1.91%
b (Å)	8.11(5)	8.147(2)	8.13916(2)	0.45%
c (Å)	7.74(5)	7.722(2)	7.72187(9)	0.26%

α (°)	90.0(6)	90	90	0%
β (°)	113.7(7)	110.775(13)	110.8720(4)	2.6%
γ (°)	90.0(6)	90	90	0%

[a]From single-crystal X-ray diffraction on $CsHSO_4$ at 298K[26].

[b]From the high-resolution neutron powder diffraction study of $CsDSO_4$ at 300 K[124].

Table 5.5 Atomic positions for MD simulation at 298 K.

Atom	MD at 298 K			Experiment at 293 K[a]			Deviation
	x/a	y/b	z/c	x/a	y/b	z/c	$\left(\frac{\Delta x^2+\Delta y^2+\Delta z^2}{3}\right)^{1/2}$
Cs	0.22(2)	0.12(2)	0.22(2)	0.21551(4)	0.12907(3)	0.20605(4)	0.009
S	0.75(2)	0.11(2)	0.27(2)	0.75214(14)	0.12727(12)	0.27996(14)	0.012
O_D	0.60(3)	0.20(3)	0.09(3)	0.5890(5)	0.2207(5)	0.1312(6)	0.025
$O_A(2)$	0.65(3)	0.03(4)	0.37(3)	0.6647(5)	0.0700(4)	0.4079(5)	0.035
O(3)	0.87(4)	0.24(2)	0.88(3)	0.8947(5)	0.2536(4)	0.8594(5)	0.021
O(4)	0.83(4)	1.00(4)	0.20(4)	0.8062(6)	0.9960(4)	0.1867(5)	0.017
H	0.66(4)	0.25(3)	0.02(2)	0.625(8)	0.295(6)	0.057(7)	0.040

[a]From single crystal X-ray diffraction on $CsHSO_4$ at 298K[26].

Looking at Table 5.5, it can be seen that the largest differences between the experimental and calculated atomic positions (i.e., the deviations) occur for the atoms

which crystallographically participate in the hydrogen bonds (O_D, O_A, and H). This can be attributed predominantly to the high "thermal vibrations" of the hydrogen atom, which was observed to vary its position quite dramatically. However, it was also observed that the non-donor oxygen atoms moved appreciably and in fact even rotated, with a 3-fold like symmetry, around the S-O_D bond. This motion was significantly activated even at 298 K and became more so with temperature. Not surprisingly, these motions had a particularly dramatic effect on the hydrogen bond parameters, Table 5.6. It was difficult to get these average values without either (1) influencing the results of the measurement or (2) including the effects of atomic motions other than normal thermal vibrations. Nevertheless, the listed values should reasonably well describe the average values involved in the hydrogen bonds from which it is clear that they deviate significantly from the average values determined by X-ray diffraction. This is particularly interesting for the O-O distance as the FF was adjusted to a value of 2.647 Å, very similar to the experimental value.

Table 5.6 Hydrogen bond comparison between MD and experiment in phase II

	MD at 298 K	Experiment-X-ray[a]	Experiment-Neutron[b]	Error (%) vs. X-ray
r(O_D-H) (Å)	0.99 ±0.07	0.94 ±0.04	0.983 ±0.005	5
r(H···O_A) (Å)	2.03 ±0.4	1.70 ±0.04	1.667 ±0.008	28
r(O_D···O_A) (Å)	2.77 ±0.16	2.636 ±0.005	2.633 ±0.005	11
<(O_DHO_A) (°)	130 ±24	174 ±6	166.6 ±0.6	25

[a]From single crystal X-ray diffraction on $CsHSO_4$ at 298K[26].

[b]From the high-resolution neutron powder diffraction study of $CsDSO_4$ at 300 K[124].

The simulation results also deviate from the measured values for the bond lengths and angles of the HSO_4 groups, Figure 5.7. However, in this case the simulation values are very close to those with which the FF was optimized. These deviations are then more a result of the procedure by which the FF was developed and than an artifact of the simulations themselves.

Table 5.7 HSO_4 group arrangement: QM and FF calculations versus MD and experimental values in phase II

	Optimized CsHSO4 Monomer	FF Min. $CsHSO_4$ Monomer	MD (at 298 K)	Experiment-X-ray[a] (at 298 K)	Experiment-Neutron[b] (at 300 K)
r(S-O) (Å)	1.488, 1.487	1.484, 1.484	1.48(3), 1.48(3)	1.438(3), 1.433(3)	1.430(5), 1.435(9)
r(S-O_D) (Å)	1.650	1.650	1.65(3)	1.573(4)	1.589(8)
r(S-O_A) (Å)	1.479	1.487	1.49(3)	1.461(3)	1.472(5)
<(SO_DH) (°)	105.9	105.9	106(3)	114.7(4)	110.6(6)
<(OSO_D) (°)	107.3, 106.6, 103.9	107.0, 105.3, 105.3	105(2), 104(2), 104(2)	107.4(2), 106.6(2), 101.5(2)	107.5(5), 106.9(4), 101.9(5)
<(OSO) (°)	113.5, 113.1, 111.8	113.0, 113.0, 112.3	114(2), 114(2), 114(2)	113.6(2), 113.5(2), 113.1(2)	114.2(6), 113.4(5), 111.9(5)
<OSOH	53.1	60.6	60(15)	42.2(4), 79.7(3)	47.3(7), 75.6(7)
r($\overline{Cs-O_{nn}}$)(Å)	3.218	3.217	3.16(27)	3.220(4)	3.218(6)

[a]From single crystal X-ray diffraction on $CsHSO_4$ at 298K[26].

[b]From the high-resolution neutron powder diffraction study of $CsDSO_4$ at 300 K[124].

In conclusion, it can be said that these MD simulations have done a very good job in reproducing the overall structure of phase II $CsHSO_4$, in spite of the fact that the hydrogen bonds parameters and internal structure of the tetrahedra deviate significantly from experimental values.

5.4.2 Phase Transition: Cell Parameters

The average cell parameters, *a*, *b*, *c*, α, β, and γ were plotted as a function of temperature in Figure 5.5. At 598 K, the cell parameters, *a*, *b*, *c*, and β, show dramatic changes. These parameters are expected to change if the symmetry of the cell is to increase from monoclinic to tetragonal. The exact nature of the changes is determined by relating the cell vectors of the monoclinic phase ($\vec{a}_m$, $\vec{b}_m$ and $\vec{c}_m$) to those of the tetragonal phase ($\vec{a}_t$, $\vec{b}_t$ and $\vec{c}_t$) as follows[125]:

$$\vec{a}_t = \frac{1}{2}\left(\vec{a}_m + \vec{b}_m\right), \quad \vec{b}_t = \frac{1}{2}\left(\vec{a}_m - \vec{b}_m\right), \quad \vec{c}_t = \vec{a}_m + 2\vec{c}_m \tag{5-1}$$

Using this relation, we can compare the lattice parameters of the supercell at 623K to the experimental values of phase I $CsHSO_4$, Table 5.8, where *a, b, c* of the supercell have been divided by two to give $\vec{a}_m$, $\vec{b}_m$ and $\vec{c}_m$, respectively. There is a good agreement between the transformed lattice parameters of the simulation and the published values. Thus, Figure 5.5 indicates the phase transition from the monoclinic phase II to the tetragonal phase I $CsHSO_4$ between 573 K and 623 K. Moreover, the atom positions of the Cs and S atoms, transformed with Eq. 5-1, are extremely close to the measured values for the tetragonal phase, Table 5.9.

Note that the average internal structure of the HSO_4 groups remains basically unchanged from that of the simulations at 298 K. It would then seem possible to predict superprotonic phase transitions without reproducing the specifics of the tetrahedral groups below or above the transition. This fact makes the search for new superprotonic solid acids via computer simulations seem quite feasible.

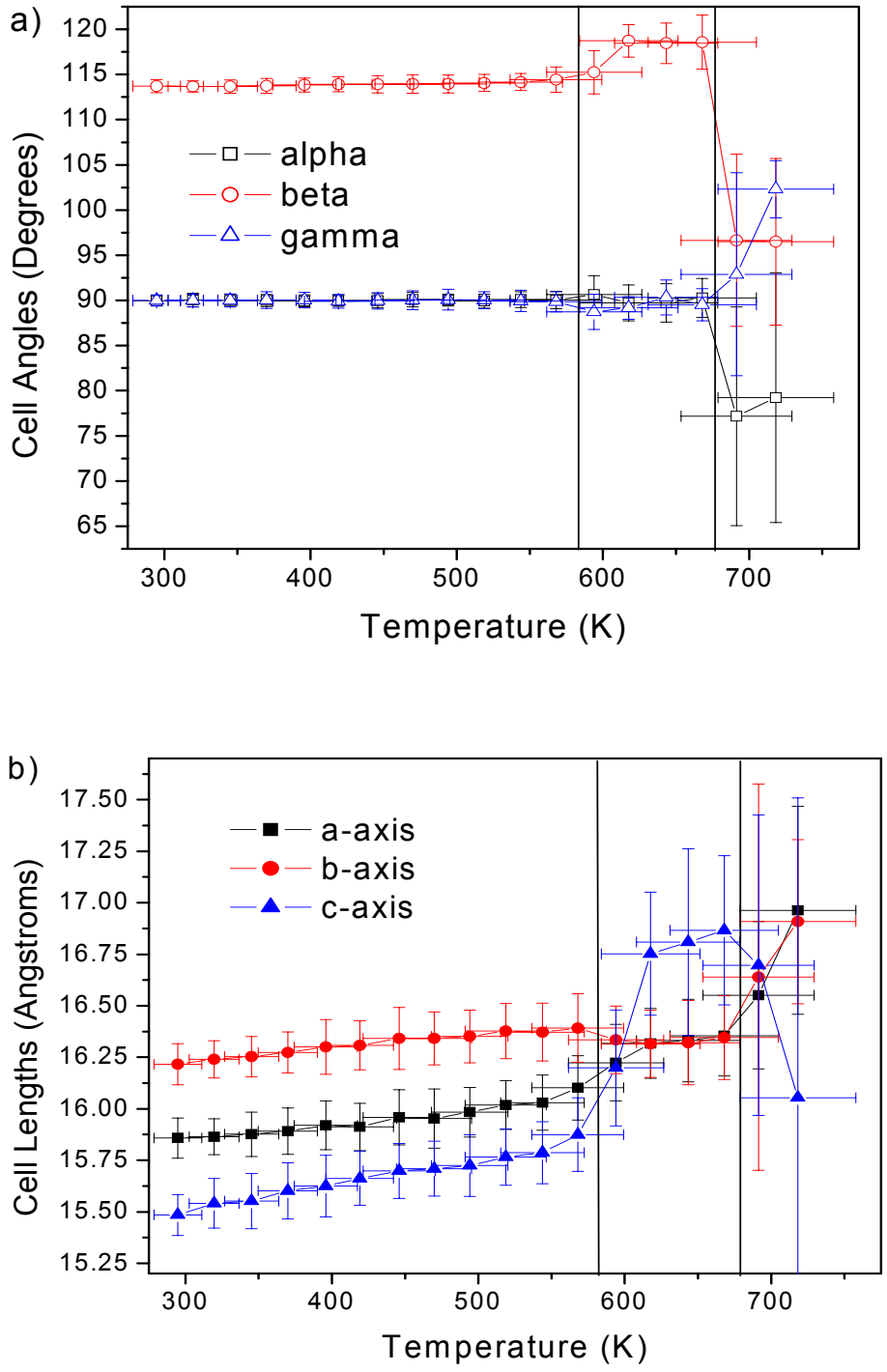

Figure 5.5 Cell parameters as a function of temperature (MD simulations): average values calculated from the final 150 picoseconds of each 300 ps simulation. Lines indicate the two transitions at 598 and 698 K.

Table 5.8 MD vs. experimental parameters for tetragonal phase I $CsHSO_4$

Parameter	MD (at 623 K)	Experiment-Neutron[a] (at 414 K)	Experiment-Neutron[b] (at 430K)	Experiment-Neutron[c] (at 448K)
density (g/cm^3)	3.13(5)	3.282(6)	3.27(2)	3.2366(2)
a (Å)	5.77(17)	5.718(3)	5.729(9)	5.74147(9)
b (Å)	5.77(17)	5.718(3)	5.729(9)	5.74147(9)
c (Å)	14.66(54)	14.232(9)	14.21(1)	14.31508(26)
α (°)	90(2)	90	90	90
β (°)	90(2)	90	90	90
γ (°)	90(1)	90	90	90
r(S-O) (Å)	1.65(4), 1.49(4), 1.48(4), 1.48(4)	4 x 1.48(2)	2 x 1.46(5), 2 x 1.48(7)	2 x 1.504(10), 2 x 1.570(5)
<(OSO) (°)	114(4), 114(4), 114(4), 104(3), 104(3), 104(3)	2 x 111.9(8), 4 x 108.3(9)	125.5(9), 95.5(8), 2 x 116.8(8), 2 x 98.2(10),	112.5(3), 112.5(3) 108.9(3), 108.9(2) 107.2(2), 107.1(4)
$r(O_D\text{-}O_A)$ (Å)	2.9(3)	8 x 2.79(4)	4 x 2.84(6)	16 x 2.59(1), 8 x 2.806(18)
r($\overline{Cs-O_{nn}}$) (Å)	3.17(34)	3.17(2)	3.18(4)	3.248(7)

[a]From the neutron powder diffraction study of $CsHSO_4$ at 414 K[61].

[b]From the neutron powder diffraction study of $CsDSO_4$ at 430 K[125].

[c]From the high-resolution neutron powder diffraction study of $CsDSO_4$ at 448 K[124].

Table 5.9 MD vs. experimental atomic positions for Cs and S in phase I $CsHSO_4$

	MD at 623 K			Experiments above 414 K[a]			Deviation
	x/a	y/b	z/c	x/a	y/b	z/c	$((\Delta x^2+\Delta y^2+\Delta z^2)/3)^{1/2}$
Cs	0.501(16)	0.249(9)	0.124(17)	0.5	0.25	0.125	0.0010
S	0.002(11)	0.749(7)	0.125(6)	0	0.75	0.125	0.0015

[a]From X-ray and neutron diffraction studies of $CsHSO_4$ above 414 K[61,124,125].

5.4.3 Phase transition: Volume and energy change across T_{sp}

The average potential energy and volume of the unit cell is shown as a function of temperature in Figure 5.6. Both graphs display a jump in their values at 598 K and again at 698 K. From the arguments of the previous sections, we can clearly associate the first discontinuity with the transition of $CHSO_4$ to its superprotonic phase. The second discontinuity would appear to be melting as it involves a large volume change. A least squares fit to the data in the ranges 298-573 K and 598-673 K allows for a comparison between the simulation and experimental values of the volume and enthalpy changes across the phase II→I, Table 5.10

The MD values for the volume and enthalpy change of the transition as well as the stability range of the superpronic phase (T_m-T_{sp}) are in very good agreement with the reported values. The transition temperature, however, is almost 200 K higher than that measured experimentally. This is the first large discrepancy with the experimental data, but is not particularly distressing as it most likely represents some of unrealistic

limitations placed on the system by the simulations. The parameters effecting the phase transition temperature are investigated in more depth in section 5.5.

Table 5.10 MD vs. experiment: Characteristic values of the superprotonic phase transition in $CsHSO_4$.

	T_{sp} (K)	$\Delta(volume)_{sp}$ (%)	$\Delta(enthalpy)_s$ (kcal/mol)	T_m (K)	Stability Range- (T_m-T_{sp}) (K)
MD results	598	1.7	1.6	673 K	75
experiment	414(1)	0.9-1.9	1.43(12)	485(2) K	71(3)
reference	3,85	61,109 109,109a	85,189	59,130	3,85 59,130

[a] Calculated from structural data. Note thermal expansion coefficient for phase II CsHSO4 given in [109]is incorrect when compared to the printed data: listed as 0.056 cm3/deg, but a direct calculation gives 0.035 cm3/deg.

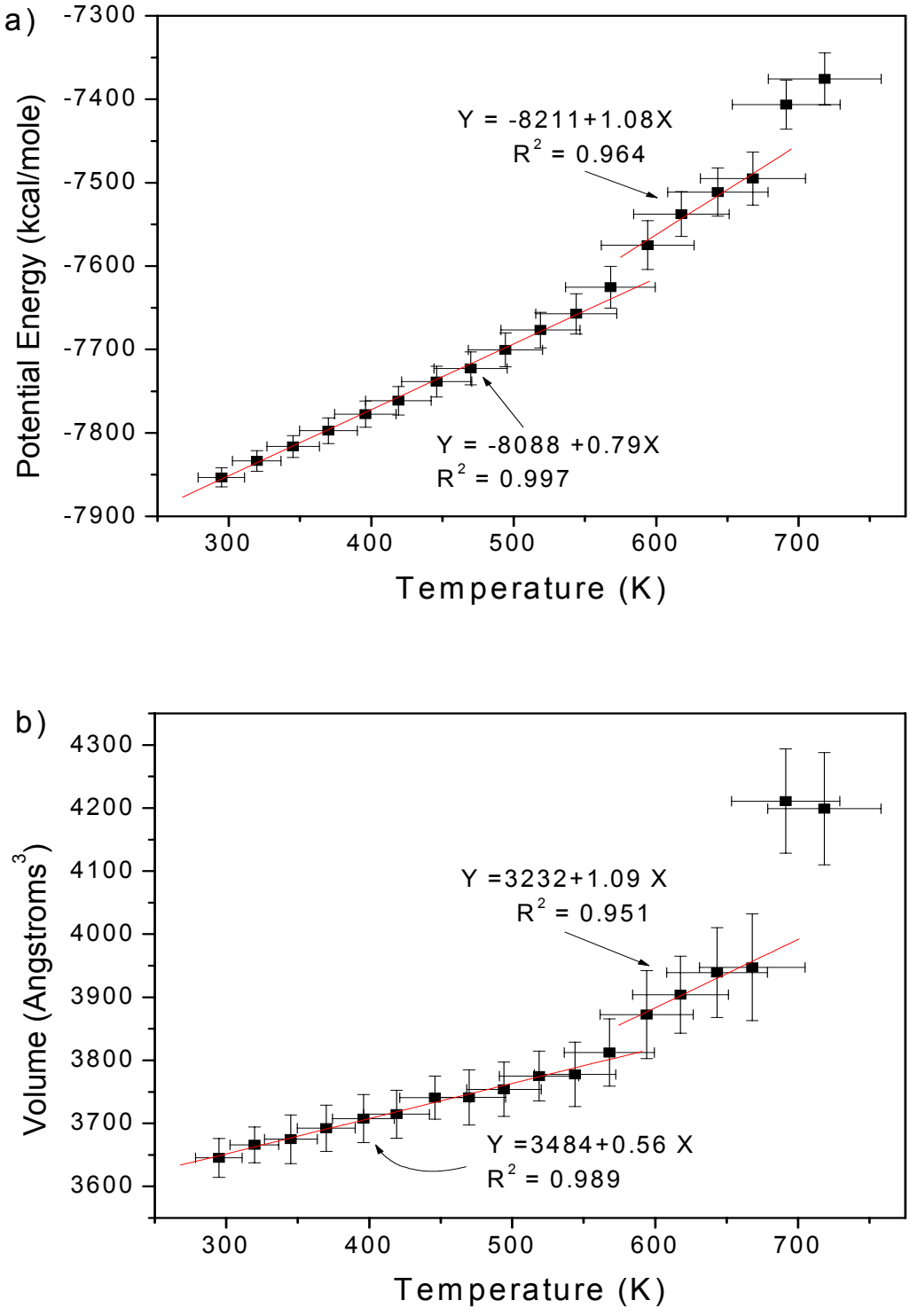

Figure 5.6 Potential energy, a), and volume, b), as a function of temperature from MD simulations: 298 K to 723 K.

5.4.4 Phase transition: X-ray diffraction

Perhaps the most direct and convincing way to determine if the MD simulations have correctly predicted the superprotonic transition of $CsHSO_4$ is to look at the diffraction patterns calculated from the MD structures below and above the transition. Thus, the time-averaged X-ray powder diffraction (XPD) pattern for each tempeture was calculated using the instantaneous structure at each 0.1 ps of the final 150 ps and averaging the 1500 XPD patterns generated using the *Cerius2* program[176]. For comparison, the XPD patterns of the experimentally determined crystal structures of phase II, Figure 5.7 a, and phase I, Figure 5.7 d, were also calculated. It is clear that the patterns below 598 K are characteristic of phase II, Figures 5.7 b and c, while the patterns above 598 K are characteristic of phase I, Figures 5.7 e. This is quite conclusive evidence that the II $\rightarrow$I phase transition was obtained during the simulation. A X-ray diffraction pattern from the MD simulation at 723 K was also generated, Figure 5.7 f. It shows significantly less structure than the other patterns and reinforces the idea that the second phase transition is associated with melting.

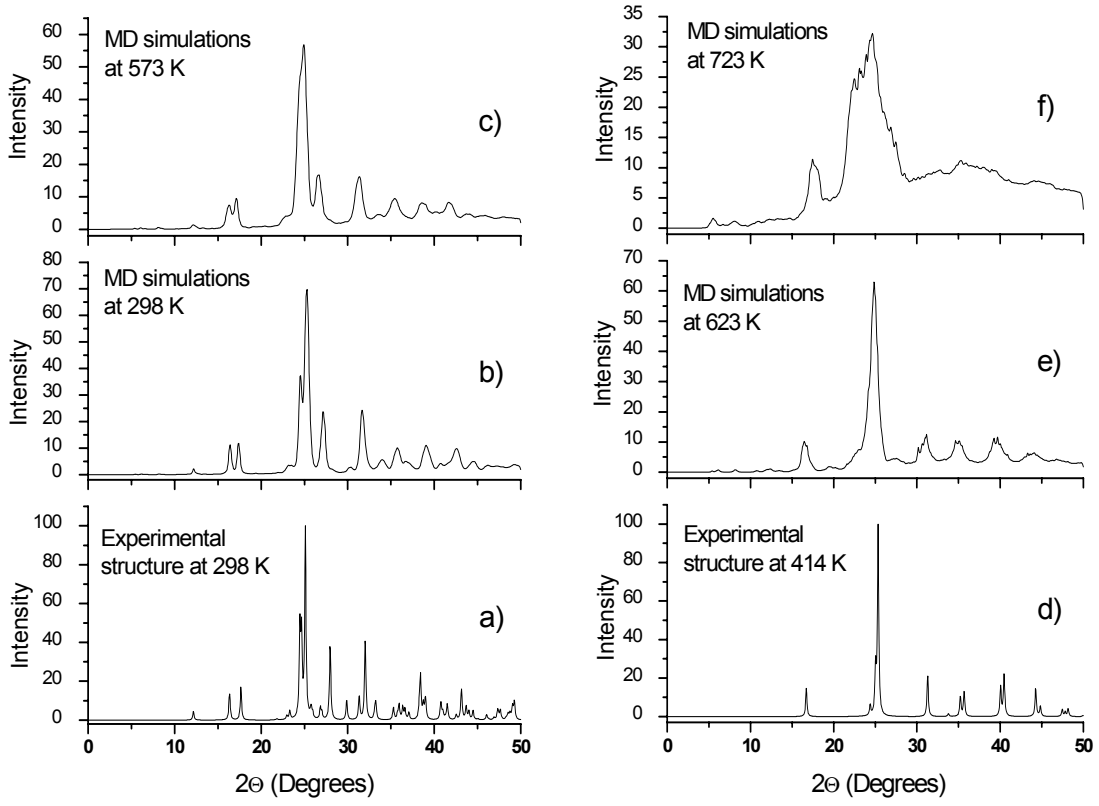

Figure 5.7 Calculated X-ray powder diffraction patterns. (a) Phase II $CsHSO_4$ calculated from the experimental structure[26]. (b) and (c) Phase II calculated from MD simulations at 298 K and 573 K, respectively. (d) Phase I $CsHSO_4$ calculated from Jirak's experimental structure[61]. (e) Phase I calculated from MD simulations at 623 K. (d) X-ray diffraction pattern calculated from MD simulations at 723 K, above the 2nd (melting) transition.

5.4.5 Vibrational spectrum of Phase I $CsHSO_4$

It is quite apparent from sections 5.4.1 to 5.4.4 that the time averaged structures of both phase II and phase I $CsHSO_4$ have been well duplicated by these MD simulations. To determine whether the dynamics these phases were equally well reproduced, the IR spectra of the simulations at 298 and 623 K were calculated using the *Cerius2* software[176], Figure 5.8 a and b. These graphs were created by taking the average of 30 IR

spectra, calculated every 5 ps from 150 to 300 ps. The comparison with experimental data is favorable for both phases of $CsHSO_4$, Figure 5.8 c) and d).

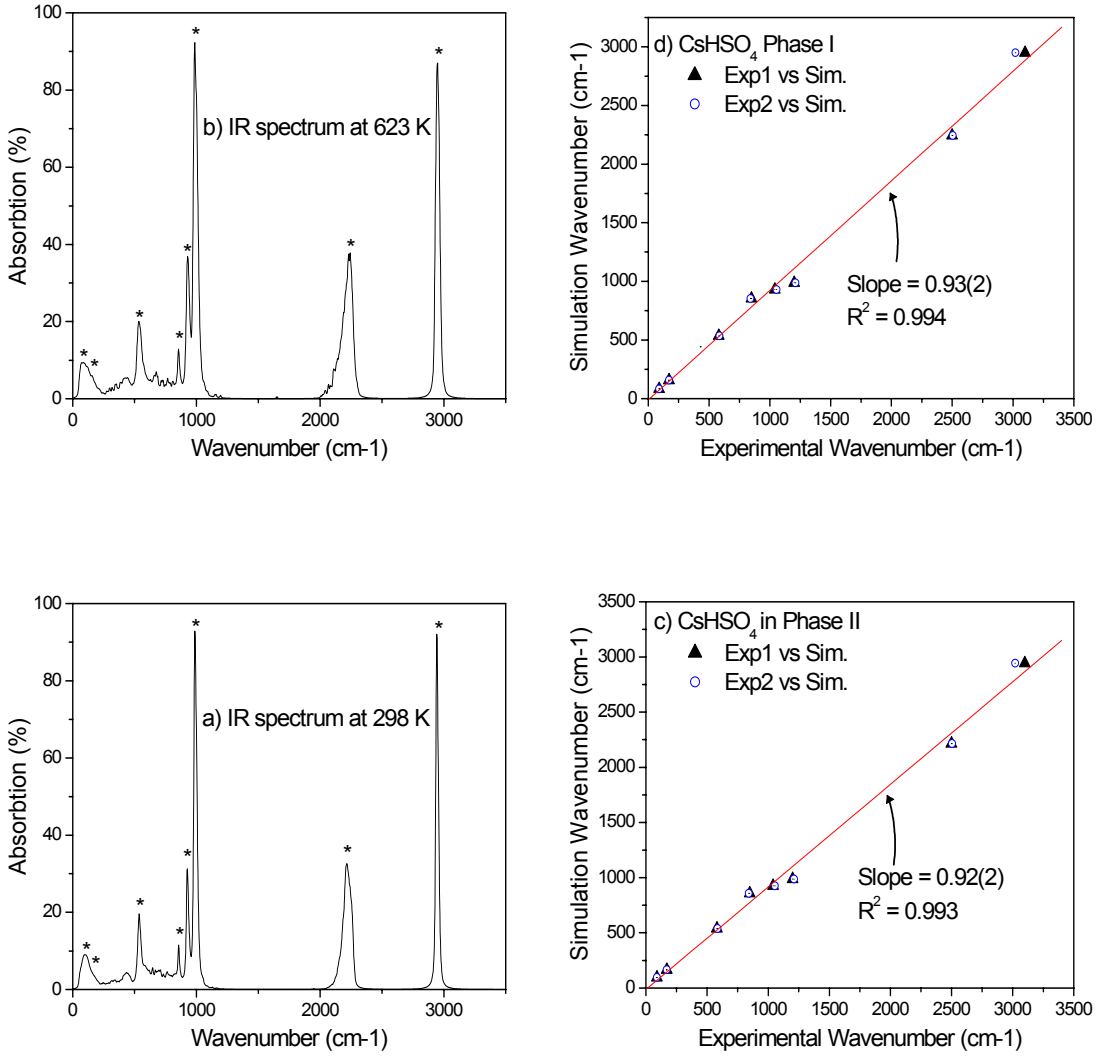

Figure 5.8 Calculated IR spectra for MD simulations: for phase II and I of $CsHSO_4$, a) and b), respectively. Peaks with strongest absorption are marked with an asterix and the frequencies at the peak maximums are compared to those of the strongest peaks found by infrared spectroscopy on polycrystalline $CsHSO_4$ [107,190]. In both phase II, c), and phase I, d), the simulation and experimental peak positions are very similar (for perfect match $\Rightarrow$ slope = 1). A plot of experiment 1 versus experiment 2 (not shown) results in a slope of 0.98(1), $R^2 = 0.999$, as the measured IR spectra changes little over the phase II-I transition.

The overall vibrational behavior of the simulations therefore closely mimics reality. However, as the IR spectra for phase II and I are very similar (for the experiments and simulations alike), further analysis of the simulation data is required to discover if the dynamics of the two phases do indeed change across the phase transition as expected: i.e., from oscillations around a fixed structure to librations/reorientations in a disordered phase.

5.4.6 Orientation of the HSO_4 groups

To confirm that the simulations contain the observed change from a static to dynamic structure across the superprotonic phase transition, the orientation of the HSO_4^- ions in the simulations was examined. In phase II, the tetrahedra have only one crystallographically distinct orientation, whereas the HSO_4^- groups accommodate the higher symmetry of phase I by librating between different orientations [84]. The orientation of a tetrahedron was defined as the vector between its S and O_D atoms. If the simulations correctly predicted these two phases, one would expect a particular tetrahedron to have only one general orientation for all temperatures below 598 K, but that its S-O_D vector would begin to change direction significantly for T > 598 K. With this in mind, the vector pointing from the S85 to O86 atom was measured every 0.1 ps from 150-300 ps at each temperature step. This particular vector was chosen because it belongs to one of the eight central tetrahedra not directly effected by the boundary conditions of the supercell and should therefore librate (or not) the most freely. The orientation of this vector was

mapped onto a polar coordinate system with a particular direction (x,y,z) determining a pair of angels (θ , ϕ) using the standard equations:

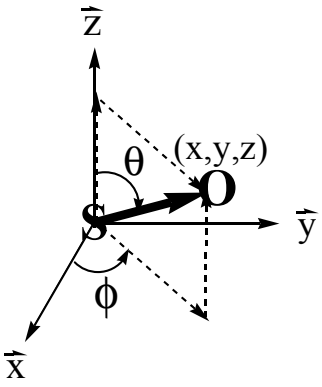

Laboratory (fixed) frame

$$\theta = a\cos\left(\frac{z}{\sqrt{x^2+y^2+z^2}}\right)$$

$$\text{and} \quad \begin{cases} \phi = a\cos\left(\dfrac{x}{\sqrt{x^2+y^2}}\right) & \text{if} \quad y > 0 \\ \phi = 2\pi - a\cos\left(\dfrac{x}{\sqrt{x^2+y^2}}\right) & \text{if} \quad y < 0 \end{cases}$$

These pairs of angles were then used to create the density maps shown in Figures 5.9 and 5.10, where each contour line represents a tenth of the maximum density of the plot. In Figure 5.9 a, b, and c) it is clear that the S85-O86 vector had only one orientation while in phase II (298-573 K). Immediately above the transition, however, this vector began reorienting between four different directions, Figure 5.9 c). A plot of all orientations taken by the four S-O vectors of the S85 tetrahedron from 598-673 K, Figure 5.9 e), shows the same four basic orientations, agreeing with the expectation that the oxygen atoms swap positions in the superprotonic phase[124]. As stated before, this type of dynamical behavior is essential to the phase II to I transition of $CsHSO_4$ and it therefore seems that these simulations have correctly predicted the dynamics as well as the structure of phase I. Above the second transition at 698 K, the S85-O86 vector appears to orient randomly, Figure 5.9 f), consistent with this phase's designation as a liquid.

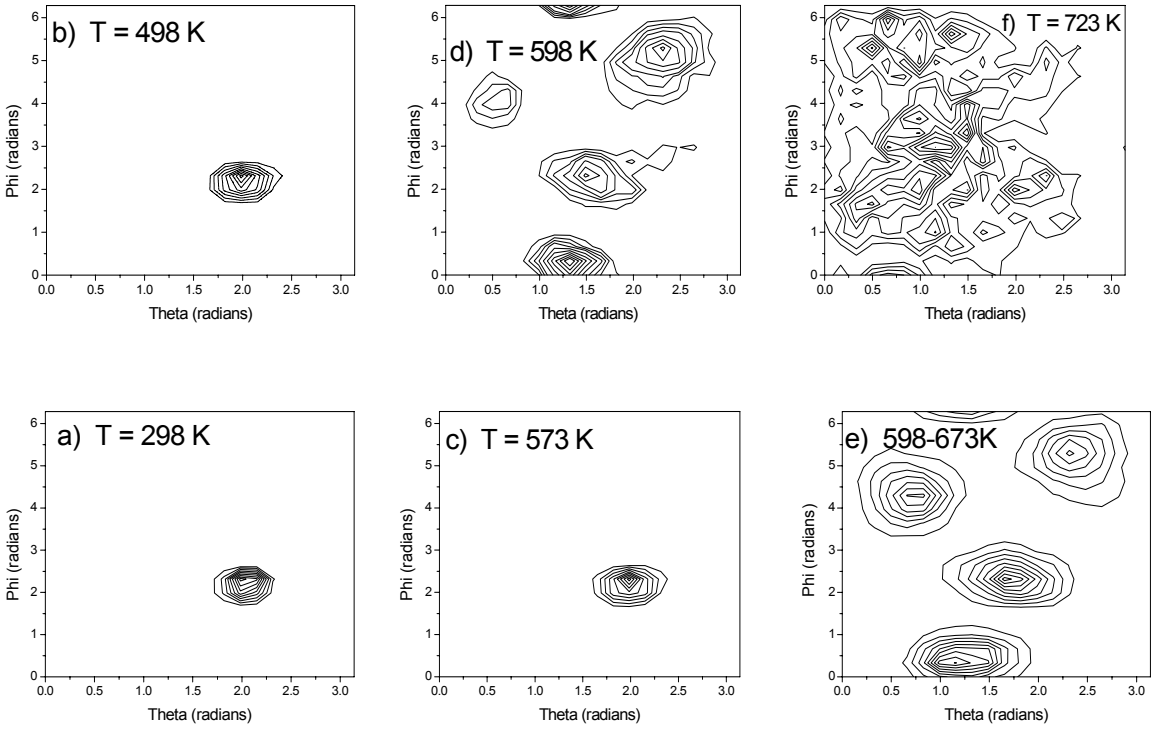

Figure 5.9 Probability distribution functions for the S-O vectors: a), b), c), d), and f) were created using only the orientations of the S85-O86 (donor oxygen) at 298, 498, 573, 598, and 723 K, respectively, e) is a combination of the orientations for *all four* S-O vectors of the S85 tetrahedron in the temperature range 598-673 K (phase I). The directions of the S-O vectors were converted into the polar coordinates (θ, ϕ) and then mapped onto the 2-D (θ, ϕ) space. A probability distribution function was created by dividing up the full ranges of each variable ($0 \leq \theta < \pi$, $0 \leq \phi < 2\pi$) into a 20x20 matrix and assigning each (θ, ϕ) pair to a particular cell.

A direct comparison of Figure 5.9 d) and f) shows a small but significant difference in the positions of their respective peaks. To examine this discrepancy, the data from 598 to 698 K was combined separately for each oxygen of the S85 tetrahedra. It was found that the three oxygens not bonded to the hydrogen (i.e., $O_A(1)$, O(2), O(3)) had peaks positions that were indistiguishable from each other, while the donor oxygen had peak positions very similar to those shown in Figure 5.9 d. This subtle difference in peak positions is therefore an artifact of the FF which differentiated between donor

oxygens and all other oxygen atoms, as is evident in the O-S-O angles of the tetrahedra (Table 5.7 and 5.8).

By plotting the orientations of the S-O vectors *for all tetrahedra in the simulations*, another trait of the high temperature phase of $CsHSO_4$ is duplicated. Although there is only one *crystallographically* distinct sulphate tetrahedra in phase I, the symmetry of the phase is such that the tetrahedra can be grouped into two types when the S-O vectors are mapped onto the (θ, ϕ) plane. These two types of tetrahedra can be seen in Figure 5.1 b, where layers of "up" and "down" pointing tetrahedra are arranged perpendicular to the c-axis. A density map for *all* the orientations of *all* the S-O vectors in phase I should then have eight distinct directions (4 "up" and 4 "down"). Indeed, when all S-O vectors in the supercell are used to create a density map, eight general directions are evident in the 598-673 K simulations (temperature range of phase I), Figure 5.10.

Again, the "up" and "down" tetrahedra and their corresponding orientations are not crystallographically distinct and do not refer to the librations necessary to satisfy the symmetry of phase I. The actual number and direction of the libration orientations are in dispute, Table 5.11. We can compare these directions with those of the experimental structures after properly adjusting the coordinate system of these structures to that of the laboratory frame of the simulations. Such a comparison does not, unfortunately, significantly favor one structure over another as all three have orientations distributed around those found in the simulation. It does, however, confirm that the orientations of

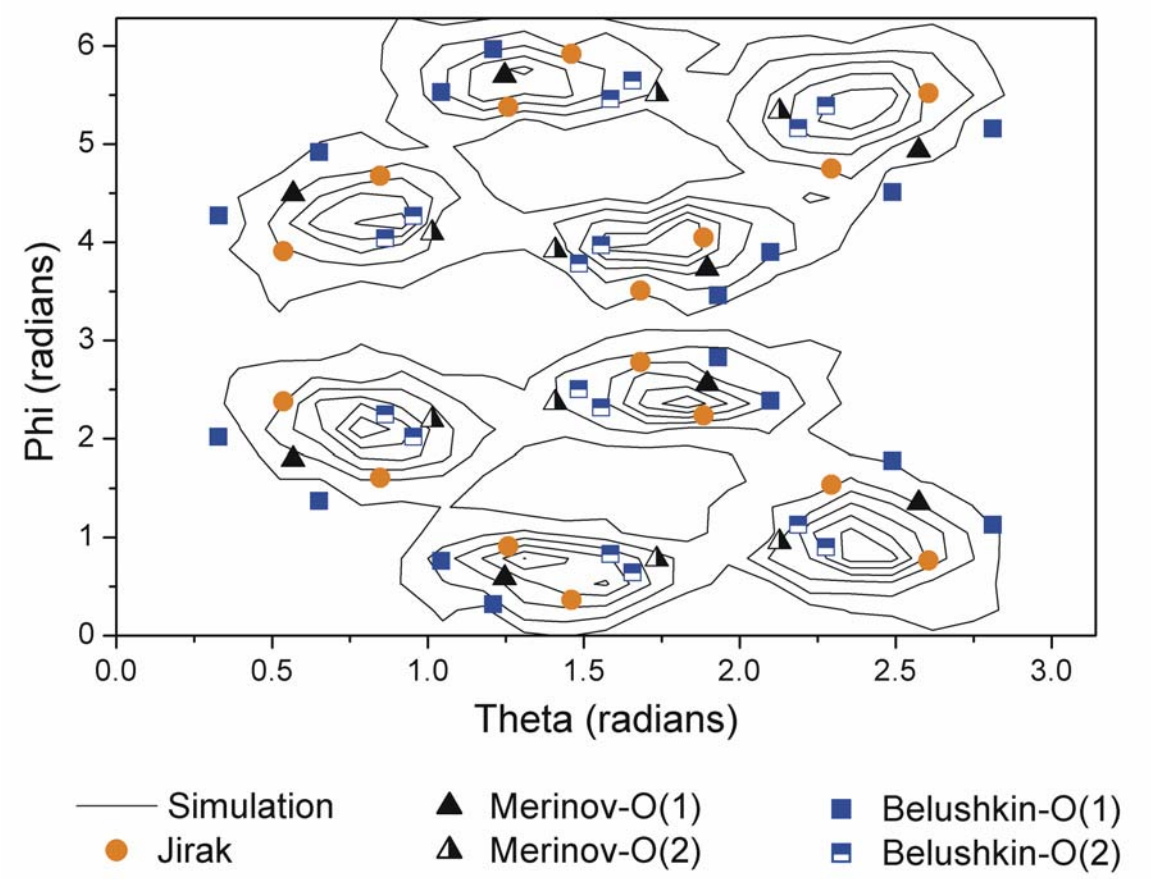

Figure 5.10 Probability distribution functions for all S-O vectors in phase I (from 598-673 K simulations). The eight distinct directions correspond fairly well to S-O directions derived from the published structures.

the tetrahedra in the simulations are consistent with those determined experimentally. The density map also helps to explain the difficulty of determining the exact position of the oxygen atoms in phase I as the large deviation of each orientation in Figure 5.10 suggests an equally disperse electron density around the corresponding oxygen.

Quantitatively, the deviation of the orientations was evaluated by measuring the FWHM of the eight positions and calculating the average, resulting in an average of 27(3)° and 39(7)° for θ and ϕ, respectively. The statistically larger average FWHM in the ϕ direction is most easily explained by librations of the oxygen atoms. To compare

this result with the published structures, the average angular difference between the experimentally determined libration directions (in the simulation frame) was calculated, Table 5.11. The librations inherent to the structures of both Jirak and Belushkin result in a larger angular difference in the ϕ compared to θ direction, in agreement with the simulation results. The librations proposed by Merinov, however, result in a larger angular difference for the θ direction.

Table 5.11 Proposed librations in $CsHSO_4$ phase I compared to simulation results

Source	# of librations	Average $\Delta\theta$ between librations	Average $\Delta\phi$ between librations	$\Delta\phi - \Delta\theta$	ref
Merinov	2	27	17	-10	[125]
Jirak	2	17	38	21	[61]
Belushkin	4	20	24	4	[124]
Simulation	N/A	27(3)	39(7)	12(10)	

5.4.7 Reorientation of the HSO_4 groups

The *degree* to which the 32 HSO_4^- ions reoriented in the simulation was also evaluated. As it was necessary to know not just how much the tetrahedra were reorienting, but also the type of reorientation (e.g., oscillation, libration, rotation), the tetrahedra were examined by two methods. First, reference orientations for the tetrahedra were defined as their orientation at 150 ps into each temperature step. Then the amount each tetrahedra changed these reference orientations was measured. Second, the average angular change per picosecond of these orientations was calculated for each temperature

equilibration. Both these methods continued to define the orientation of an HSO_4^- ion by the vector pointing from its S to O_D atoms and measured this vector, for all 32 tetrahedra, from 150-300 ps in 1 ps steps, Figure 5.11.

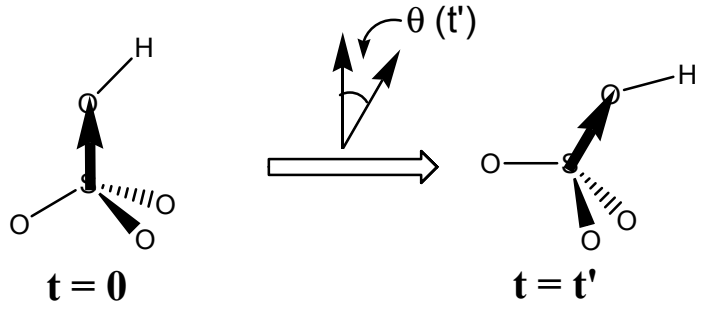

a) b)

Figure 5.11 Orientation/reorientation of an HSO_4^- ion defined by its S-O_D vector: a) an $HSO4^-$ ion has the vector pointing from its S to O_D atom initially aligned vertically; b) after a time t′, the HSO_4^- ion has changed its orientation and the S to O_D vector now forms an angle θ(t′) with the vertical.

To measure the extent to which each tetrahedra changed its orientation with respect to the reference S-O_D vector (at 150 ps), the cosines of the angles formed by the reference vector and the S-O_D vectors at 151-300 ps (by 1 ps steps) were calculated. At each temperature the average cosine value and its standard deviation were then computed from the cosine values of all 32 tetrahedra to determine the overall variance of the HSO_4^- ions' orientation with increasing temperature, Figure 5.12 a. Looking at Figure 5.12 a, we see a gradual decrease in the average cosine value as it approaches the transition temperature of 598 K and a drop across the transition (from 0.76 to 0.48 at 573 and 598 K, respectively), indicating that the $HSO4^-$ groups are reorienting to a far greater degree above the transition.

In fact, the data is misleading as an analysis of the average cosine value per picosecond reveals that the tetrahedra reorient significantly away from the reference direction at 573 K, but do not completely "forget" their original orientation, Figure 5.12 b. This behavior is consistent with a large oscillation or libration around a central direction. However, from the previous section (Figure 5.9) we know that the simulation tetrahedra do not librate in phase II (298-573 K) and so the form of Figure 5.12 b should represent oscillations.

Above the superprotonic transition, the average cosine value steadily drops toward zero, Figure 5.12 c): where zero represents a total randomization of the tetrahedral orientations with respect to the reference directions. In fact, at 623 K the average cosine value reaches zero by the end of the simulation, Figure 5.12 d). One can then expect that the autocorrelation plot at 598 K, Figure 5.12 c), and all like it above 573 K, would approach zero with a significantly long equilibration time. This is consistent with the description of near "free rotation" of the tetrahedra in phase I and the melt[190].

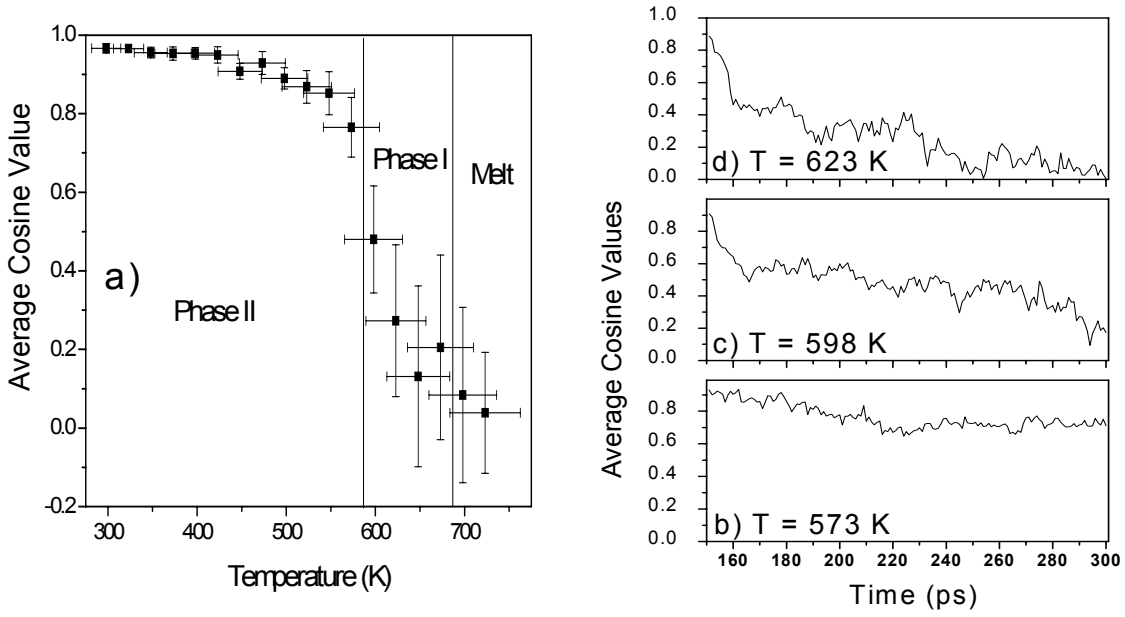

Figure 5.12 Autocorrelation functions for all 32 tetrahedra evaluated using their average cosine values between the reference orientations (at 150 ps) and subsequent orientations: a) average cosine value versus temperature; b), c), d) average cosine value at 573, 598, and 623 K, respectively, versus time. Note the decrease in the average cosine value across the phase II to I transition in a) and the fact that the average cosine values continue to decrease above the transition, c) and d), whereas they equilibrate around 0.73 below the transition, b).

To quantitatively describe the extent to which the sulfate tetrahedra were reorienting in the simulations, the average angular change per picosecond for the S-O_D vectors were calculated for each temperature. This calculation involved measuring the angular change between a HSO_4^- ion's S-O_D vector with respect to its orientation 1 ps before (Figure 5.11 , $t' = 1$ ps). Similar to the previous method, the angular velocities for all 32 tetrahedra were then averaged at each temperature, Figure 5.13. Looking at the results of this calculation, it is apparent that although the tetrahedra increase their angular velocities at the phase II to I transition, this increase is not a large one. This again emphasizes that the two phases are fairly similar in their overall vibrational spectra,

observed by IR and Raman spectroscopy [190], and that the manner in which they reorient is the cause of the phases' dramatically different properties (i.e., superprotonic conductivity of phase I).

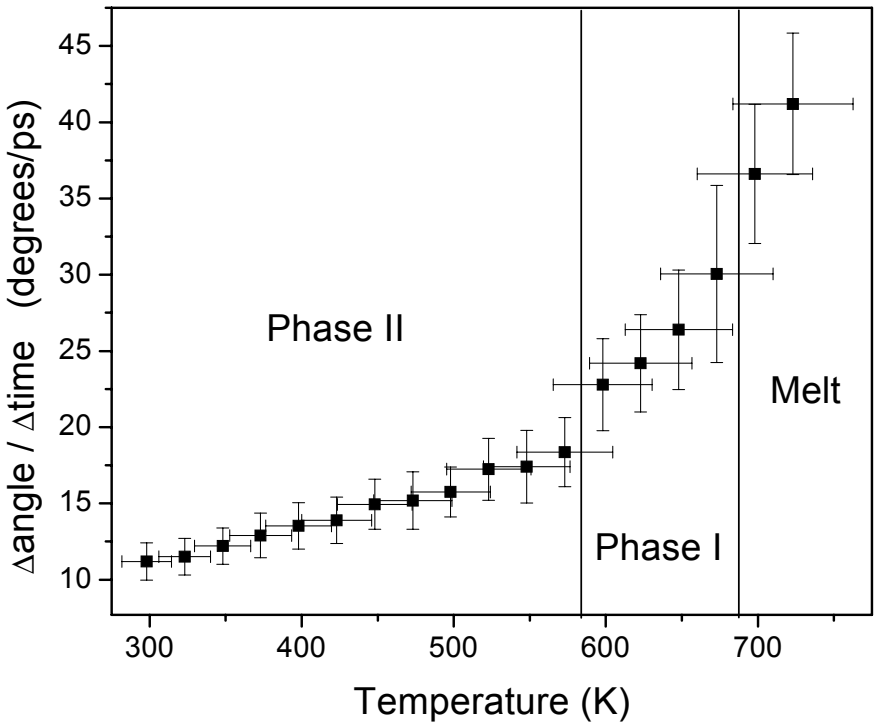

Figure 5.13 Average angular velocity of all 32 S-O_D vectors versus temperature. Note that the jump in this value at the phase II-I transition is only ~ 25 %. Therefore the dramatic increase in protonic conductivity across the transition (10,000-100,000 %) is due to a change in the *nature* of the reorientations (e.g., oscillation to libration/rotation) rather than the *degree* of the reorientations.

5.5 Parameters Effecting the Phase Transition Temperature

As the previous results have described, these simulations have duplicated extremely well the characteristics of $CsHSO_4$ in its room and high temperature phases

including the necessary changes at the phase transition. However, the one property in which the simulation results and experimental observations are glaringly at odds is the phase transition temperature itself: 598 K versus 414 K, respectively. This contradiction between very good and very poor agreement with experimental values suggests that in general the force field parameters correctly define the interatomic interactions of $CsHSO_4$ in both phase-II and I, but that some particular force field parameters have a large retarding effect on the phase transition temperature. Of course, it is a distinct possibility that the decision to prohibit proton hopping is responsible for the high transition temperature. Proton hops between oxygen atoms in phase II $CsHSO_4$ would necessarily require breaking of crystallographic hydrogen bonds and/or rotations of the sulphate groups. Both these actions would tend to destabilize the fixed structure of phase-II when compared to the dynamically disorder phase-I, where the breaking of hydrogen bonds and tetrahedral rotations are a must. Therefore, fixing the protons to their respective donor oxygens will favor phase-II over phase-I, possibly to the tune of 175 degrees K. However, as one of the purposes of these simulations was to determine if indeed the superprotonic transition was possible without proton hopping (YES!), we must look for other parameters effect the transition temperature.

A priori, one would suspect that parameters delaying the onset of the superprotonic transition would include any that tend to favor a fixed over dynamic structure, order versus disorder, low versus high symmetry; that is to say, parameters that inhibit the "free" reorientation of the sulphate groups. One would hence tend to ignore the parameters that deal with the internal atomic interactions of the HSO_4^- ions and focus on the parameters that govern the HSO_4^- to HSO_4^- and HSO_4^- to Cs^+ interactions. Such

parameters as the atomic charges, hydrogen bond strength, and hydrogen torsional barrier height. Hence, the effect of these three areas on the transition temperture were evaluated by re-running the MD simulations after the parameters effecting one (and only one) of these three areas were changed, with all other FF parameters *identical* to that found in Table 5.2.

Before exploring the results of the above experiments, it should be mentioned that the effect of increasing the equilibration time was also investigated as this overarching parameter effects all simulation runs. This investigation consisted of doubling the soak time of each temperature step from 300 to 600 ps and re-running the original simulations. Analysis of this series of simulations revealed the transition temperatures for both the phase-II to I and phase-I to melt transitions to decrease by 25 K (one temperature step). Hence, the equilibriation time does indeed have an effect on the temperature at which the phase transition appears (as expected) and therefore it is possible the original set of FF parameters would give a transition just above 414 K with a sufficiently long soak time. This statement applies equaly well to the following simulation runs and in particular to those with “transition zones” in which the simulations results do not conform to any of the experimentally observed phases, as the timescale of most laboratory experiments are in seconds if not minutes or hours. However, since it is not resonable to perform simulations such as these with equilibration times much over 300 ps, a better understanding of the FF parameters effecting the presence and temperature of phase transitions is necessary. Of course, identifying the parameters that have the largest effect on a phase transition also gives very useful insight into underpinings of the transition itself.

5.5.1 Oxygen charge distribution

As the dominant binding energy of ionic solids comes from their Coulombic potential energy[191], the atomic charges were expected to have a large effect on the MD simulations. Indeed, by far the largest change to the superprotonic phase transition temperature (from 598 to 423 K, Figure 5.14) resulted from setting all the oxygens charges to – 0.612 |e|, equal to the average of the four charges in Table 5.3. This egalitarian distribution of the oxygen charges favors the superprotonic phase where all oxygens are identical over time and should therefore have an equivalent *average* charge.

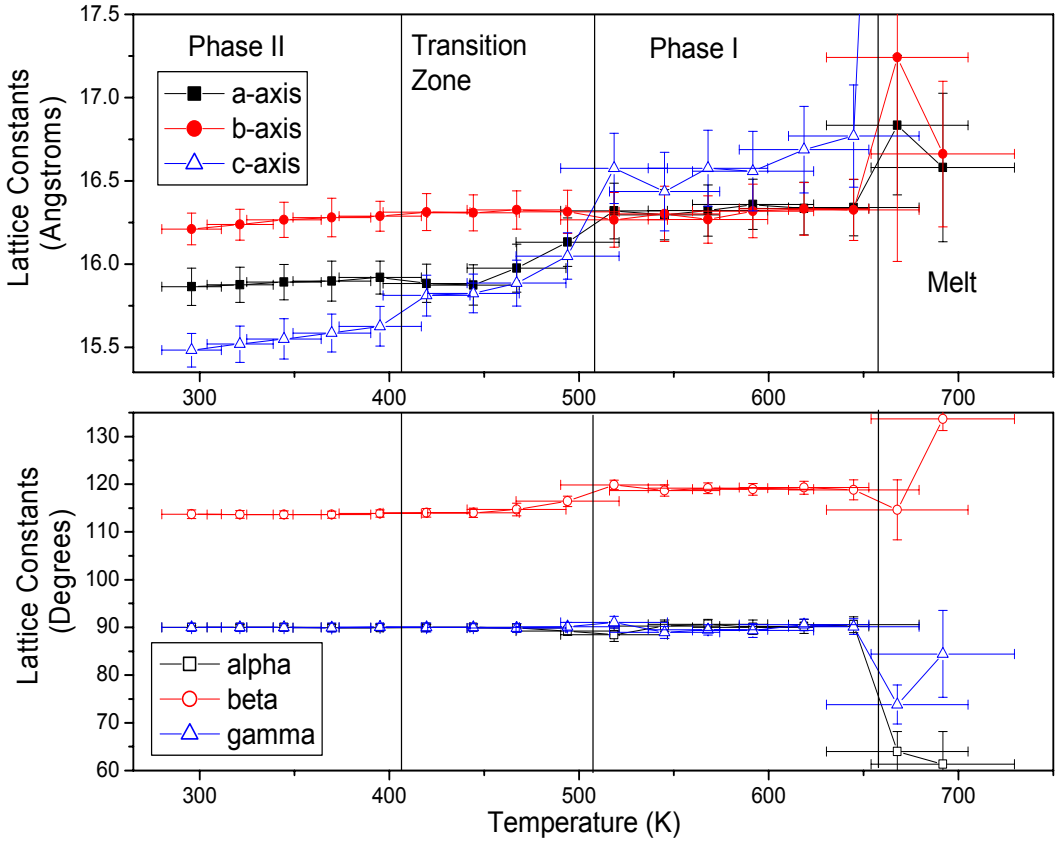

a)

Figure 5.14 (See figure caption on next page.)

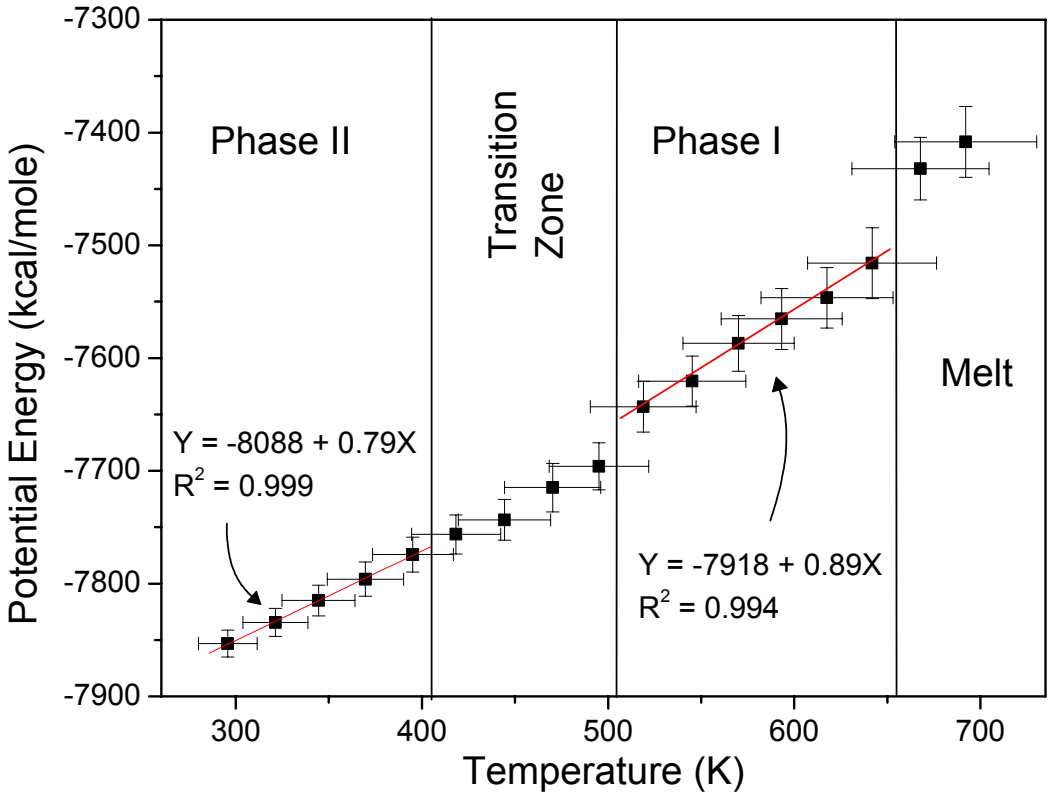

b)

Figure 5.14 Results of equal oxygen charge MD simulations: a) plot of lattice constants versus temperature reveals only the c-axis lattice constant to change significantly from 398 to 423 K and that lattice parameters do not achieve the values respective of phase I until 523 K; b) graph of potential energy versus temperature shows little change until 523 K and then again at 673 K.

From Figure 5.14 a, b, and the analysis of section 3.2, it is clear that the transition from phase II to phase I begins at 423 K. A close inspection of Figure 5.13 a shows that only the c-axis lattice constant changes significantly from 398 to 423 K. This increase in the c-axis is consistant with a straightening of the zigzag chains of hydrogen bonded sulphate groups. A careful analysis of all possible radial distribution functions confirmed

such a straightening. The transition to phase I then begins at 423 K, but is not completed until 523 K; at which temperature |c| > |a| = |b| corresponding to phase I. To confirm such an analysis, the X-ray diffraction patterns were calculated at 398, 423, and 523 K, Figure 5.15. The simulation patterns at 398 and 423 agree with that calculated from the experimental data on phase II[26], while the pattern at 523 K matches up with the XPD pattern calculated using the measured structure of phase I[61].

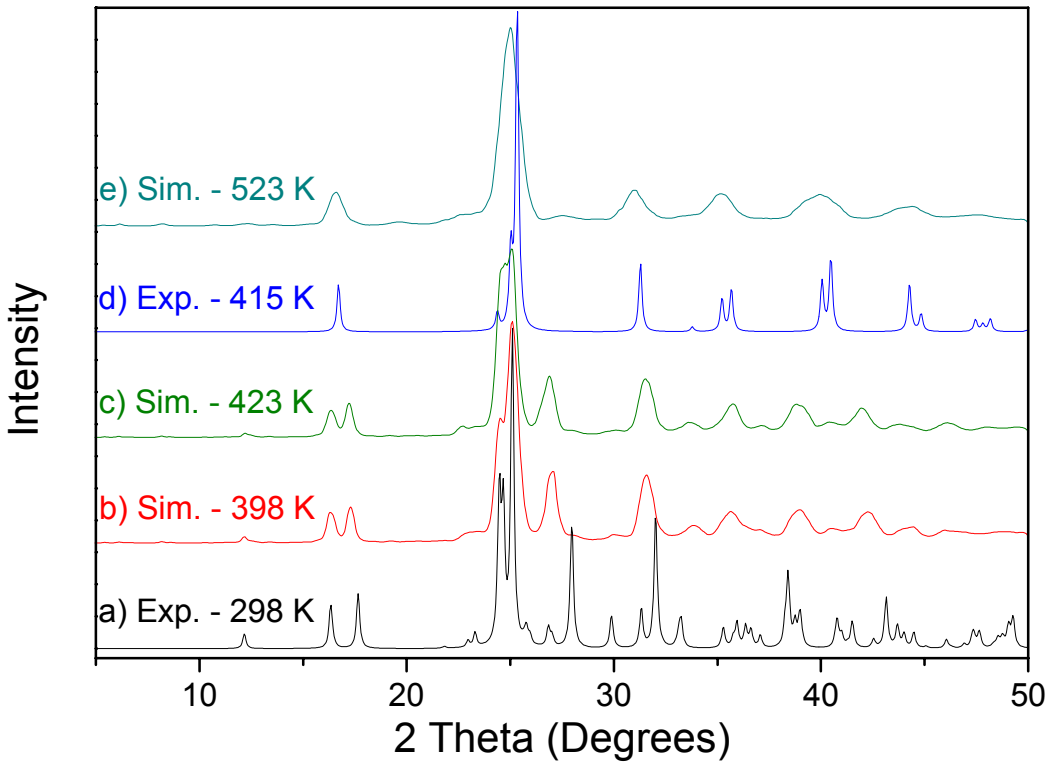

Figure 5.15 Calculated X-ray diffraction patterns for equal oxygen charge MD simulations: a) from structure determined by single crystal X-ray diffraction at 298 K, b) from simulation results at 398 K, c) from simulation results at 423 K, d) calculated from structure determined by powder X-ray diffraction at 415 K, e) from simulation results at 523 K. Comparison of patterns in a), b), and c) show the simulations at 398 and 423 K to be in phase II $CsHSO_4$. Whereas, the diffraction pattern at 523 K matches the phase I pattern calculated from experiment, e) and d), respectively.

Giving all the oxygen atoms equivalent charges then caused the onset temperature of the transition to drop by 175 degrees, to the first MD simulation above the reported transition temperature of 414 K. Although making all the oxygen charges equivalent is not realistic, a force field that allowed for continually changing charges on the oxygens based on their environment would be expected to give similar results. Such a force field is currently under development at Caltech in the Goddard Simulations Group and these simulations will be run again with this force field to judge the veracity of the previous statement. This new force field can also allow the hydrogen atoms to hop between oxygens which, combined with the continual re-evalutation of oxygen charges, should give very realistic MD simulations, the results of which will make for an interesting comparison with this study.

5.5.2 Hydrogen Bond Strength

To evaluate the effect of hydrogen bond strength on the superprotonic transition, it was first necessary to define the strength of a hydrogen bond in these simulations. The strength of a hydrogen bond usually refers to the energy required to disociate the O_D-H···O_A complex which is highly correlate to the O_D-O_A distance: the smaller the donor to acceptor distance, the greater this disociation energy and vice versa[14,21]. Hence to increase/decrease the hydrogen bond strength should require shortening/lengthening the equilibrium O_D—O_A distances in the simulations. However, for the purpose of a direct comparison between the original and subsequent simulations, changing these distances was not ideal. So, the hydrogen bond strength was defined as the binding energy of the H_2SO_4 dimer used to determine the hydrogen bond parameters found in Table 5.2. Using

the same force field energy minimization techniques as described in section 5.3.2, the hydrogen bond parameters (R_O and D_O) were adjusted to either increasing or decreasing this binding energy, *while maintaining* the same equilibrium O_D—O_A distance of 2.647 Å. Unfortunately, such a definition did not allow for a significant decrease in the hydrogen bond strength (due to competition with electrostatic energy) to merit re-running the simulations. However, an increase in the hydrogen strength was possible and the simulations were re-run with a 150% and 200% increase in the afore mentioned binding energy; i.e., 1½ and 2 times the original hydrogen bond strength, Figures 5.16.

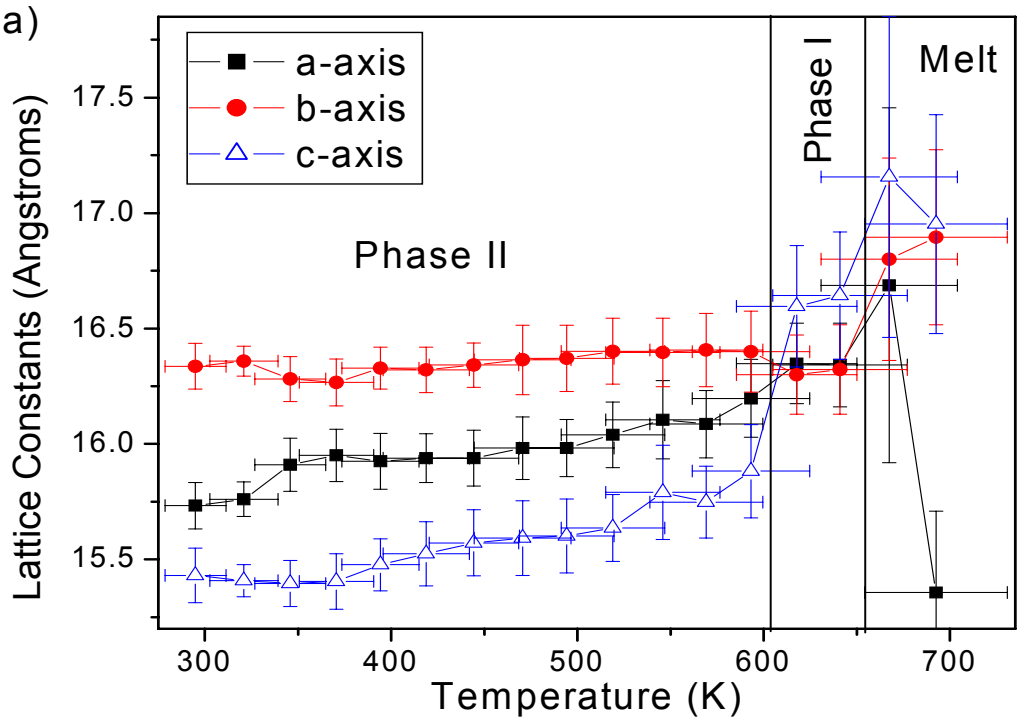

Figure 5.16 (See figure caption on following page.)

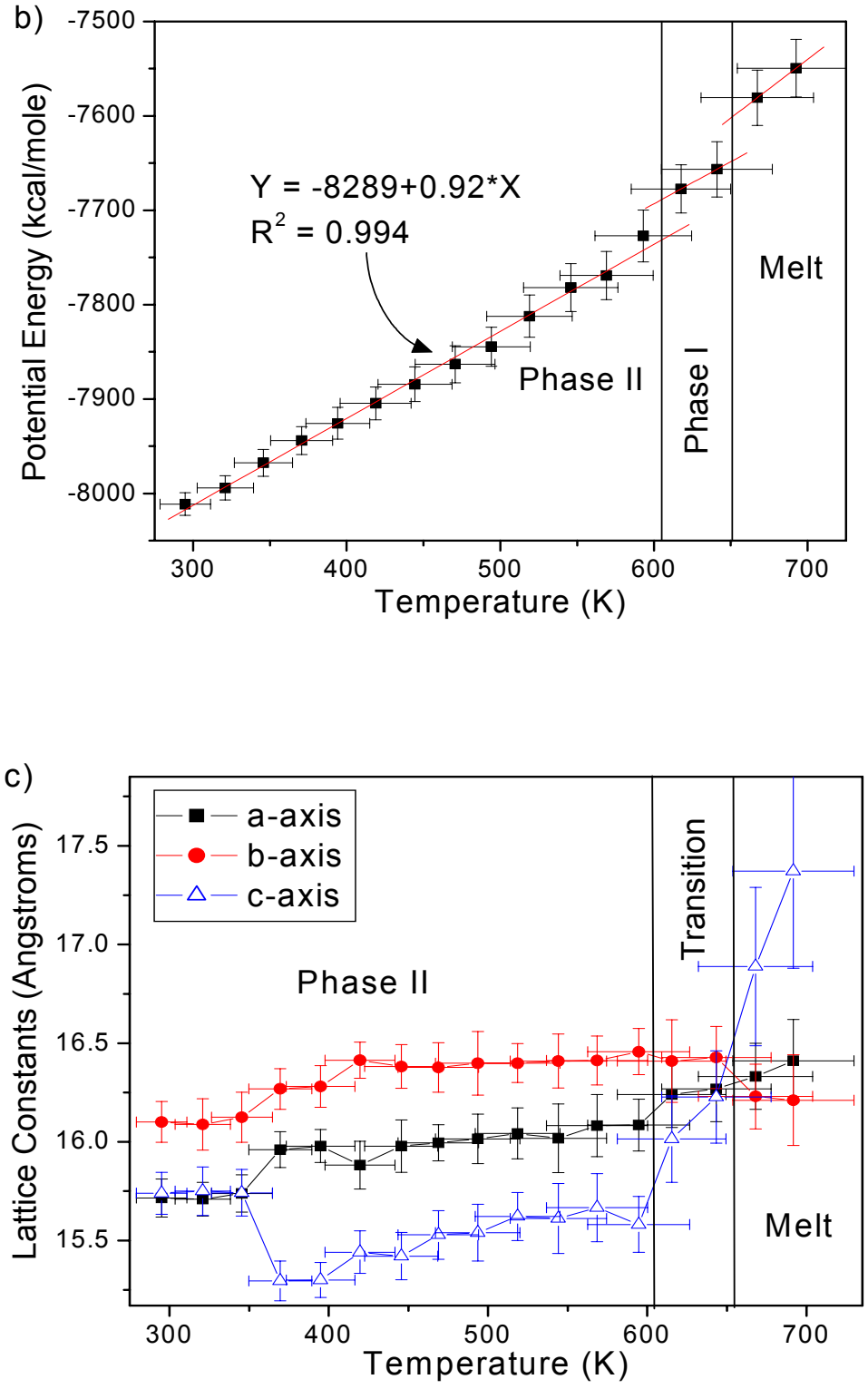

Figure 5.16 (See figure caption on next page.)

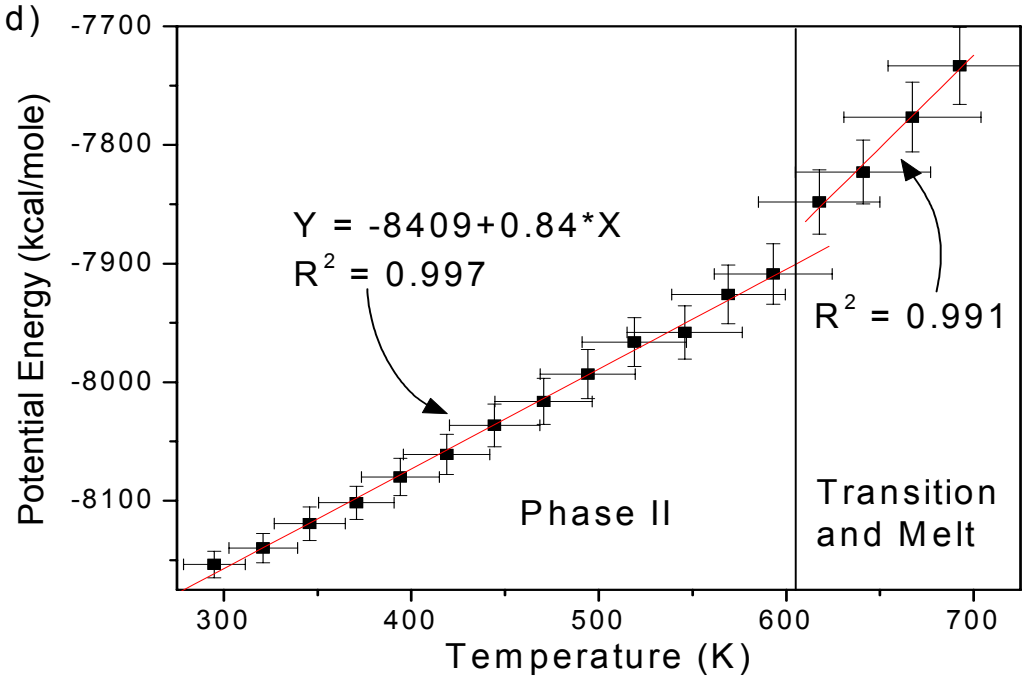

Figure 5.16 Simulation results with the binding energy of the hydrogen bonds increased by 150 percent, a) and b), and by 200 percent, c) and d). Note the low temperature transitions in the 323 to 373 K regions of a) and c) and the fact that overall, potential energy of the simulations decreases by around 150 kcal/mole as the hydrogen bond strength increases from 1 (see Figure 5.6) to 1.5 to 2 times that of the original simulation.

In agreement with previous arguments, the 50 and 100 percent increase in the hydrogen bond strength favored the fixed structure of phase II over the disordered phase I and delayed the transition by 25 K. Thermal experiments show the superprotonic transition of $CsHSO_4$ to be 3-5 degrees higher than that of $CsDSO_4$, which has been attributed to an increase in the O_D-O_A distance and subsequent decrease in bond strength when deuterium is swapped for hydrogen[2]. This experimental result would seem to concur with the above delays in the transition temperature. However, as there is no statistical difference between the O_D-O_A distances of the two compounds[26], it is

impossible to say whether the measured 3-5 degree shift is due to an increase in hydrogen bond strength or, perhaps, the higher mobility of the proton versus deuterium atom.

The increase in hydrogen bond strength also had an effect on the phase I to melt transition. For the simulation with a 50 percent increase in hydrogen bond energy, this effect was to lower the transition by 25 K. Even more dramatically, the simulation with hydrogen bond strength doubled never achieved phase I, but transformed continuously from phase II through a phase I like region to the melt. A possible explanation for this behavior involves the stronger hydrogen bonds limiting the "free rotations" of the tetrahedra in phase I and the melt, but as the melt also has translational entropy, it becomes more energetically stable compared to phase I. Creating autocorrelation functions for these two simulations, as was done for the original simulation in section 5.4.7, it is apparent that as the hydrogen bond strength increases, the degree of tetrahedral reorientation decreases significantly only in phase I and the melt, Figure 5.17.

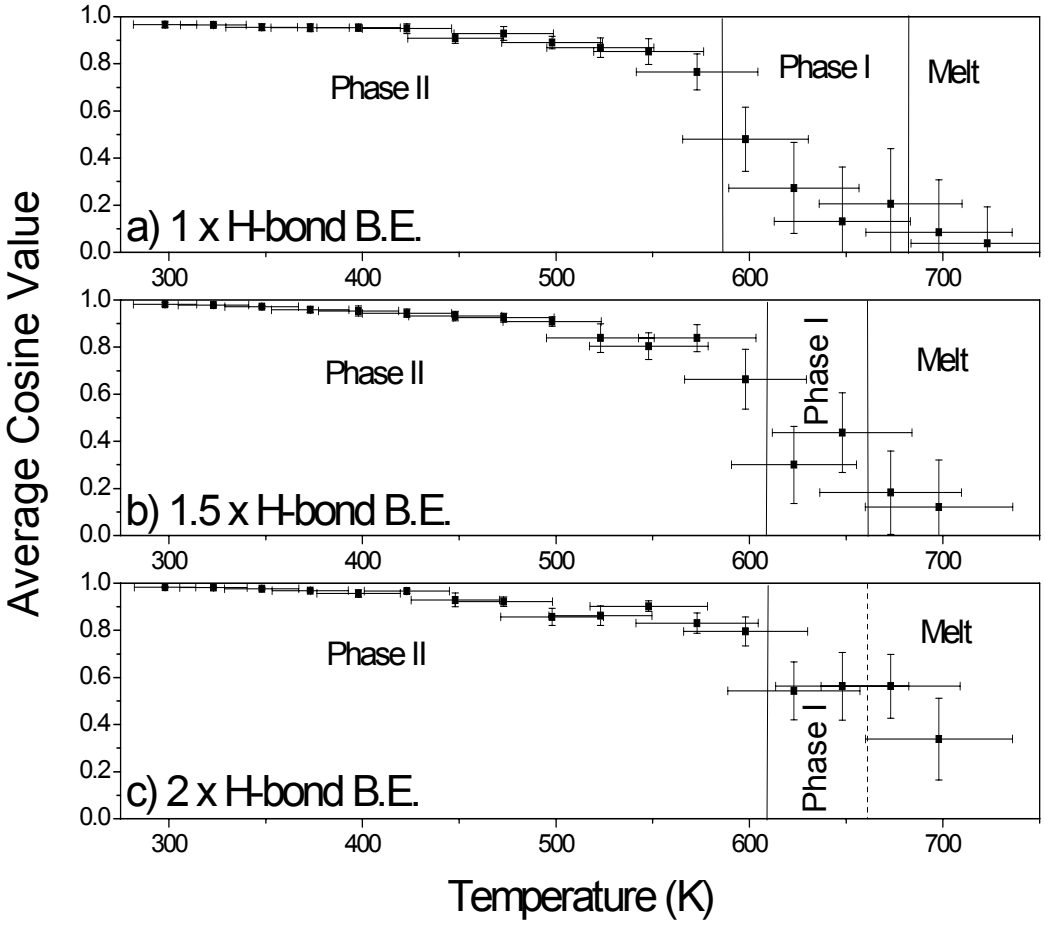

Figure 5.17 Autocorrelation functions for a) original simulation and simulations with b) 50 and c) 100 % increase in hydrogen bond strength. The average of the cosine values in phase two increases from 0.27 to 0.37 to 0.55 going from a) to b) to c). Similarly, in the melt this average value is 0.06, 0.15, and 0.45 for a), b), c), respectively. In contrast, the averages of the cosine values in phase II are within error for all three simulations: 0.91, 0.90, 0.92 for a), b), and c), respectively.

Although there is no way to experimentally confirm this conclusion, the related compound CsH_2PO_4 does exhibit properties that collaborate this rotation limited theory. This compound has all oxygens involved in strong hydrogen bonds with O_D-O_A distances of either 2.54 or 2.47 Å, which connect the phosphate tetrahedra into planes[28]. As both these hydrogen bonds are shorter than those found in phase II $CsHSO_4$, this compound

should have significantly more than twice the amount of energy invovled in hydrogen bonds than $CsHSO_4$. At 505 K, CsH_2PO_4 has a superprotonic phase transition to a cubic phase which is stable in a water saturated environment, but under ambient conditions quickly decomposes to form $Cs_2H_2P_2O_7$[92]. *If* the differences in the phase transitions of $CsHSO_4$ and CsH_2PO_4 are *mainly* due to the difference in the total hydrogen bond energies of the two compounds (see section 4.2.4, Figure 4.6 d) , then the stronger and twice as plentiful hydrogen bonds in CsH_2PO_4 are responsible for a 90 K delay in the superprotonic transition and the instability of the superprotonic phase versus a second, more entropic, state (in this case decomposition). Of course, as the two compounds are neither isostructural below nor above their superprotonic transitions, phosphates have been swapped for sulfates, and two strong hydrogen bonds have replaced one medium strength bond, that is a very big if. Nevertheless, since the overall arrangement of atoms in the two compounds is quite similar (both have zigzag chains of hydrogen bonded tetrahedra, but those chains are cross-linked in CsH_2PO_4) and because of the chemical similarity of phosphorus and sulfur (the S-O and P-O bond valence contributions are nearly identical), this analogy does not seem too far-fechted[31].

Another interesting feature of these simulations with increased hydrogen bond energies, is the low temperature changes in their lattice constants which are suggestive of the phase III to II transition of $CsHSO_4$ (Figure 5.16 a and c, between 298 and 423 K). These changes occur at 348 and 373 K with cell volume changes of -0.7 and -1 percent, for the 1.5 and 2 times hydrogen bond strength simulations, respectively. Experimentally, the phase III to II transition occurs around 330 K with an accompaning volume decrease of ~ 1 percent[109]. The enthalpy change of the transition is small, ~ 0.12-

0.24 kcal/mol[130] (which equates to ~1-2 kcal/mole for the supercell), and therefore the lack of transition in the potential energy plots (Figure 5.16 b and d) further encourages associating these changes with a phase III-II like transition.

Perhaps most importantly, the real phase III-II transition involves a lengthening of the hydrogen bonds: the O_D-O_A distances are 2.54(1) and 2.636(5) Å for phase III and II, respectively[26,109]. From experimental data, these two O_D-O_A distances can be related to hydrogen bond energies of approxiamately 11 and 7.5 kcal/mole, respectively[21]. The hydrogen bonds in phase III $CsHSO_4$ should therefore have around 1 ½ times more energy associate with its hydrogen bonds than phase II. Hence, the low temperature transitions of these two simulations are probably due to the energetic stabilization of phase III versus II as the hydrogen bond stength is increased. Indeed, for the force field with 1 ½ times the original hydrogen bond energy, the low temperature transition occurs at the first simulation step above 330 K. Whereas for the force field with twice the hydrogen bond energies of the original simulation, the phase III to II like transition occurs 25 K later at 373 K, consistent with increasing hydrogen bond strength stabilizing phase III over phase II.

However, the average X-ray diffraction patterns show little change before and after these transitions, Figure 5.18. Although this would seem to disprove the above arguments, the fact that the equilibrium O_D-O_A distance remained at 2.647 Å in both simulations pretty much rules out the atoms actually arranging themselves in a phase III structure as this would require O_D-O_A distances of around 2.5 Å. Instead, the transition seems to consist of a relaxation of the phase II structure, which was held fairly fixed

before the transition. This change can be seen in the X-ray diffraction patterns in the loss of some of the smaller peaks and general broadening of the peaks across the transition.

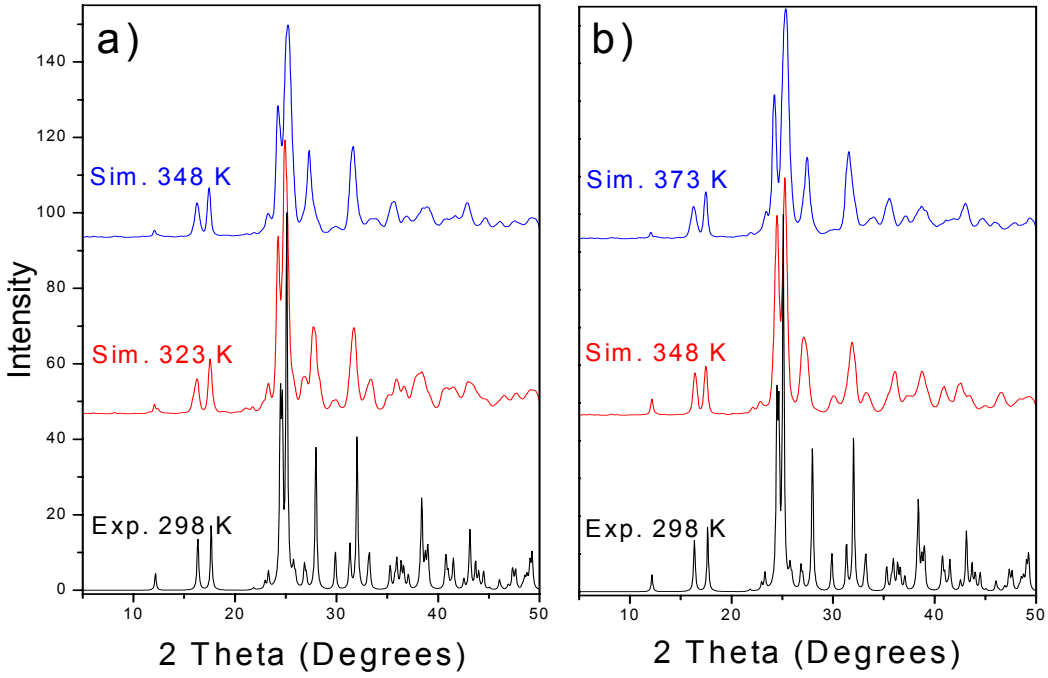

Figure 5.18 X-ray diffraction patterns for simulations with increased hydrogen bond strength below and above the low temperature transitions: simulation with 1.5 times, a), and 2 times, b), the hydrogen bond energy of the original simulations.

Further proof that these transitions are similar to the phase III to II transition come from Raman and infrared experiments. These vibrational measurements point to a substantial increase in sulphate tetrahedra rearrangements across the phase III to II transition[190]. By calculating the number of reorientations (rotations involving all four oxygens of a tetrahedra) and 3-fold rotations of the simulation tetrahedra at each temperature, it is clear that the *number of 3-fold rotations* increases significantly above

the two transitions, Figure 5.19. At the same time, the number of reorientations of the tetrahedra remains essentially zero, which explains how the simulations could increase their vibrational disorder without this increase showing up in the autocorrelation functions of Figure 5.17.

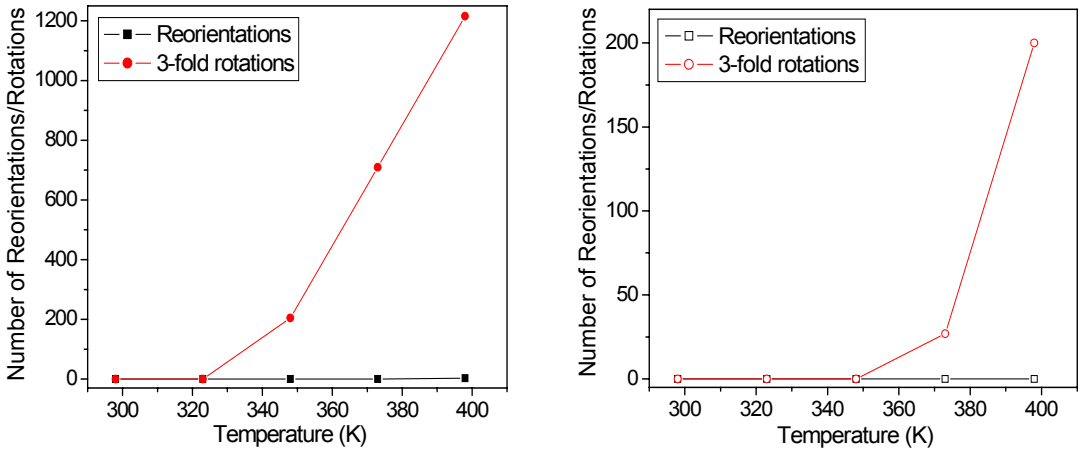

a) b)

Figure 5.19 Rearrangements of the sulphate tetrahedra across the low temperature transitions of the simulations with increased hydrogen bond strength: a) 1.5 and b) 2 times the original hydrogen bond energies. Note the jump in 3-fold rotations at precisely the same temperatures the lattice constants changed in Figure MM a) and c), while the number of reorientations remains at or very near zero.

Not only are these results quite convincing evidence that these low temperature phase transtitions mimic the phase III to II transition of $CsHSO_4$, they also suggest that the measured increase in orientational disorder of the suphate groups across the transition is due to 3-fold rotations and not cyclic dimers as proposed in the literature[190]. Particularly as the published structures disagree with the presence of cyclic dimers in phase II[26,124]. It is encouraging that the total number of 3-fold rotations in the 2 times simulation is much less than that of the 1.5 times simulation, as one would expect the

strong hydrogen bonds to hamper such rearrangements. These increased hydrogen bond strength simulations are therefore in very good agreement with both the experimental data and a priori knowledge concerning the hampering effect of increased hydrogen bond strength on superprotonic phase transitions like that found in $CsHSO_4$.

5.5.3 Torsional barrier height

One would expect the effect of decreasing the hydrogen torsional barrier height to be an increase in mobility of the hydrogens, leading to an increase in their ability to break and reform hydrogen bonds. Consequently, the HSO_4^- ions themselves would be more free to vibrate, librate, and rotate. This greater vibrational character of the sulfate tetrahedra should make phase I more energetically favorable when compared to phase II. Hence, the transition to phase I should happen at a temperature lower than 598 K for a simulation with a smaller hydrogen torsional barrier height than the original. To test such assumptions, the value of the hydrogen torsion barrier was divided by ten, from 2.1699 to 0.21699 kcal/mole, and the simulations re-run with no other changes to the original FF. Analysis of these simulations show that the phase II to I transition was indeed encouraged by the lowered torsional barrier, beginning at 473 K and finishing at 523 K, 75 degrees lower than the original simulations, Figure 5.20.

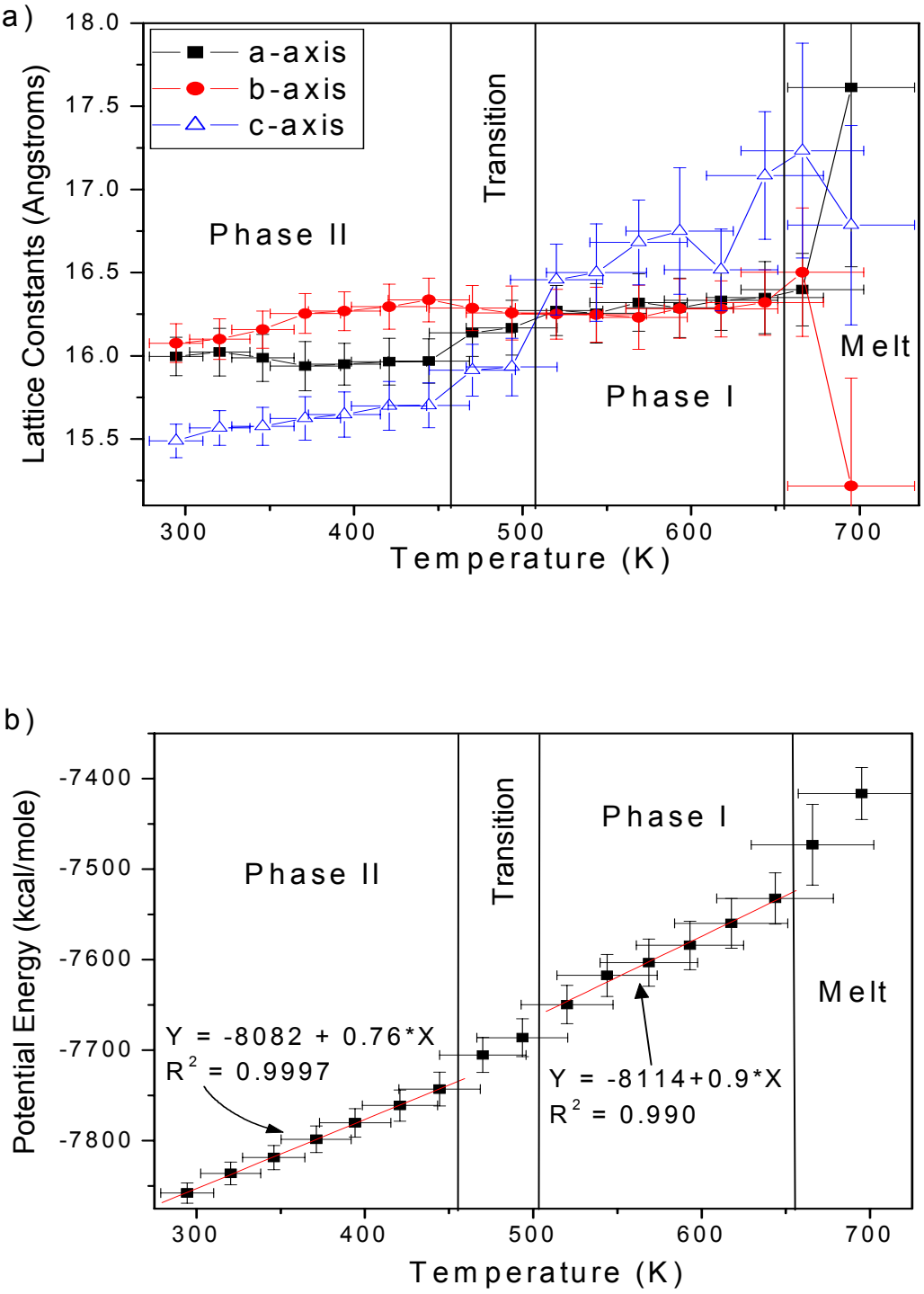

Figure 5.20 Results of simulations with lowered torsional barrier: a) cell lengths and b) potential energy versus temperature. Simulations undergo the superprotonic phase transition from 473-523 K and melt at 673 K.

Although this simulation's values for the potential energy in phase II are virtually identical to the corresponding values of the original simulation, the transition enthalpy change (measured at 523 K) was 5.5 kJ/mol, which is only 83 % of the original value. Therefore, decreasing the torsional barrier height did energetically favor phase I over phase II. The transition to the melt was also decreased by 25 K compared to the original melt temperature. Just as the lowered torsional barrier favored the dynamic phase I over the static phase II, the increased mobility of the HSO_4^- ions will favor the isotropic melt over the dynamically disordered phase I, hence the lowering of the melt temperature.

X-ray diffraction patterns of the simulations at low temperatures show the atoms to remain basically in phase II until 473 K. The low temperature changes in the lattice parameters are then probably due to phase changes similar to the ones found in the simulations with increased hydrogen bond strength (i.e., a relaxing of the atoms into a more energetically stable structure nearly identical to phase II). This is not unexpected as arbitrarily changing a parameter of the force field is bound to have effects in all temperature regions as was seen in the hydrogen bond strength simulations.

The effect of increasing the hydrogen torsional barrier was explored by setting the barrier height to 10 times the original value, from 2.1669 to 21.669 kcal/mole. The simulations were then re-run with no other changes to the original FF parameters. Following the arguments that a smaller barrier height lowers the superprotonic phase transition, one might expect a bigger barrier height to raise the transition temperature. The results of the simulation, however, are more complicated than that as the transition starts at 523 K, but does not finish until 648 K, Figure 5.21. The onset temperature is

therefore 75 K lower, while the final arrival in phase I is 50 K higher than 598 K value of the original simulations.

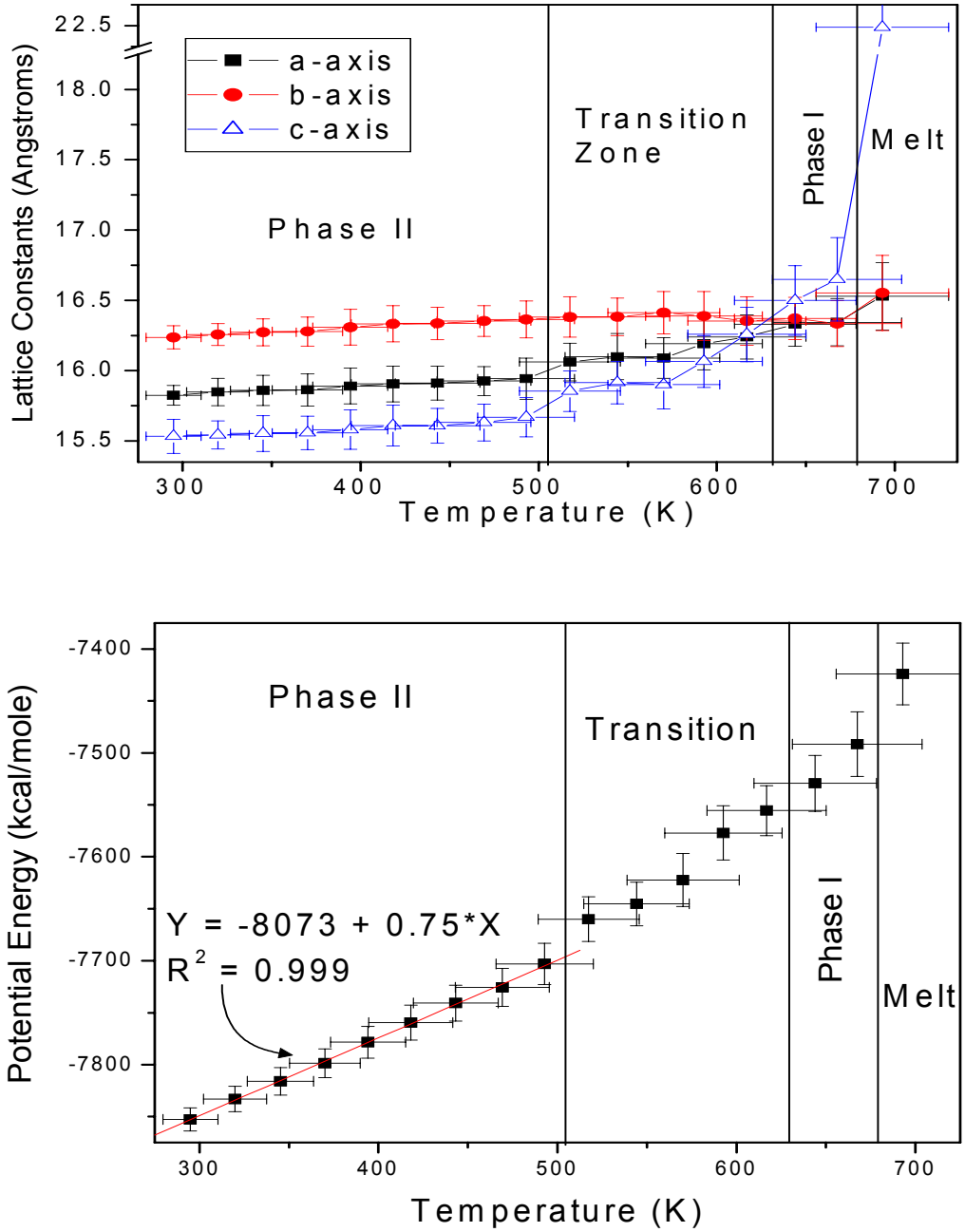

Figure 5.21 Results for simulations with torsional barrier 10 times value in original FF: a) cell lengths and b) potential energy versus temperature. The superprotonic transition begins at 523 and ends at 648 K, while melting ocurrs at 698 K.

These two effects would appear to be in contradiction. The lower onset temperature suggests the higher torsional barrier to have energetically favored phase I over phase II. Whereas the higher arrival temperature implies a greater degree of thermal energy is required to transition to phase I. As with the lower barrier height simulations, the potential energy values of this simulation in phase II are almost identical to those of the original simulation. Energetically then, phase II should be very similar for the three simulation runs with 1, 1/10 and 10 times the barrier height value of 2.1669 kcal/mole. Measuring the enthalpy change for the current simulation gives 1.8 kJ/mole (at 648 K), a value that is 114 % of the original. Therefore, increasing the barrier by 10 times increased the transition enthalpy by 0.2 kcal/mole while decreasing the barrier by 10 times decreased the transition enthalpy by 0.3 kcal/mole. Although the values of 1.8, 1.6, and 1.3 certainly within the error of each other, the almost linear decrease in ΔH as the torsional barrier height is lowered strongly points to the stabilizing effect of a highly mobile hydrogen on phase I. The explanation for the lowered onset temperature of the superprotonic transition in the simulations with the largest torsional barrier should then lie in the effect of this barrier on phase II and not phase I.

The lower onset temperature is most simply explained by a destabilization of phase II due to a conflict between increasing tetrahedral vibrations and the rigidity imposed on the hydrogen by the high torsional barrier. An autocorrelation function for these simulations (Figure 5.22) shows a small but significant amount of tetrahedral reorientations in phase II. The hydrogen bonds in phase II will become more and more distorted as these reorientations increase because of the hydrogen atoms' reduced ability to cross the torsional barrier. The lower onset temperature is then possibly the result of a

compromise between the energy required to rearrange the atoms and the hydrogen bond energy regained in the process.

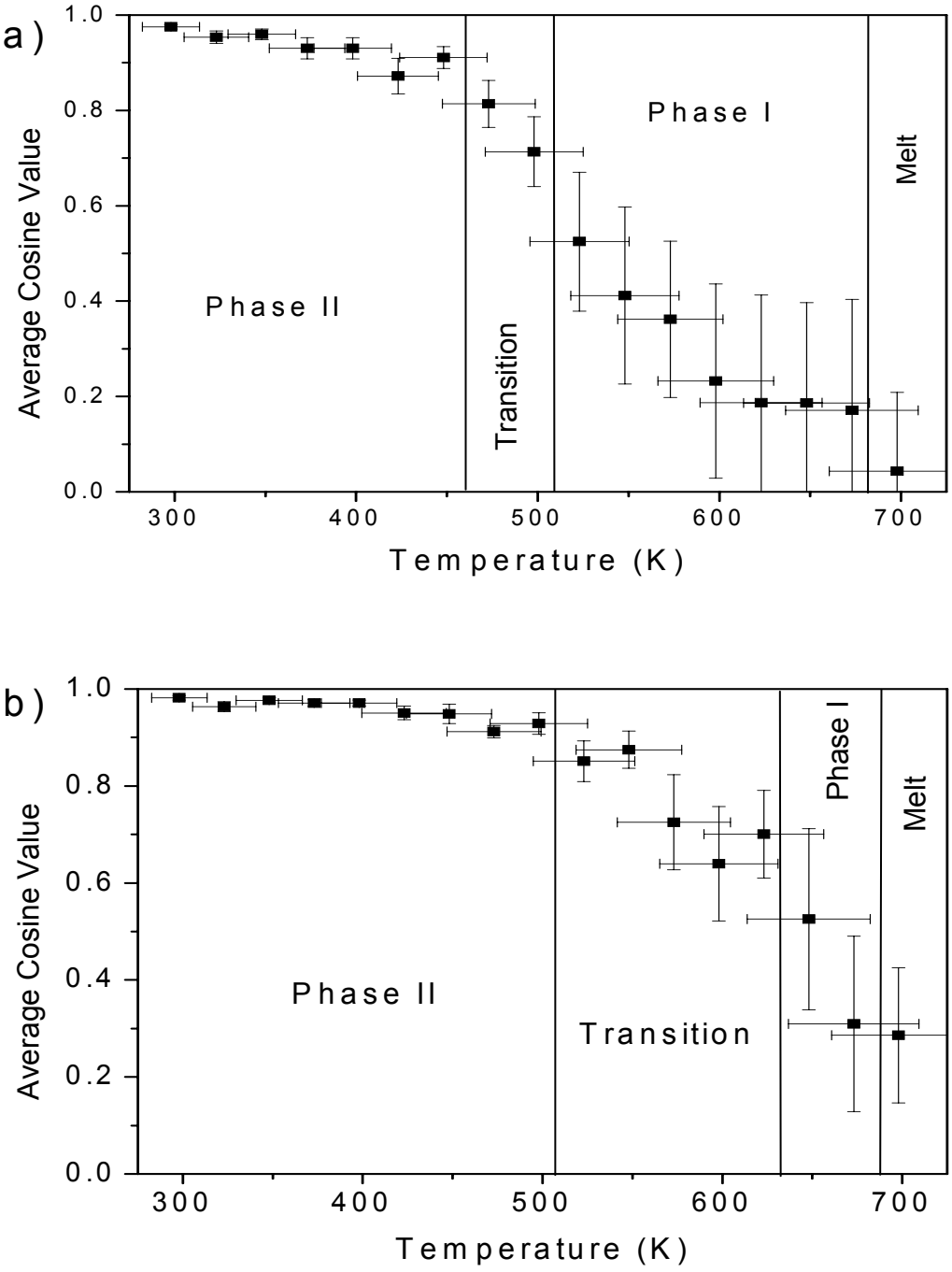

Figure 5.22 Autocorrelation functions for simulations with a) decreased and b) increased torsional barrier heights. The values are lower in a) and higher in b) when compared to the original simulations Figure 5.12 a).

A comparison of the two autocorrelation functions for the lower and higher torsional barrier simulations reveals the average cosine values of the lower barrier runs to be consistently smaller than those of the higher barrier runs at all temperatures. This systematic difference equates to a higher degree of tetrahedral reorientations for the lower versus higher barrier simulations, as expected. The change with temperature of the average cosine values above the onset transition is also quite different for the two simulations; with a rapid fall versus a gradual decrease for the low versus high barrier runs, respectively. This result agrees with the previous arguments as the low and high torsional barriers should increase/decrease the rotational ability of the sulfate groups generated by the structural changes.

5.6 Summary and Conclusions

The superprotonic phase transition (phase II → phase I; 414 K) of $CsHSO_4$ was simulated by 300 ps molecular dynamics as temperature increased from 298 K to 723 K in 25 K-step. A Dreiding based force field was used in the simulation. The initial force field parameters of S, O, and H were set to Dreiding default values, which were then adjusted to reproduce the quantum mechanically derived structure and frequencies of a gas-phase $CsHSO_4$ monomer. Cesium vdW parameters were modified to duplicate the quantum mechanical bonding energy, average Cs—O distance and symmetric-stretch frequency of the monomer. Hydrogen bond parameters were adjusted to reproduce the ab initio O_D-O_A distance and binding energy of a gas-phase $(H_2SO_4)_2$ dimer. The hydrogen

torsional barrier height of the HSO_4^- groups was fit to a series of ab initio calculations on a HSO_4^- ion in a dielectric medium of relative dielectric constant 10, where each calculation fixed the O(1)-S-O_D-H torsional angle and let the remaining structure relax to lowest energy.

Such a process for adjusting the Dreiding FF parameters was picked not only for its simplicity, but also because it could potentially be used to derive the FF for any other MH_nXO_4 compound (M = Cs, Rb, NH4, K, Na, Li; X = S, Se, P, As). By analysis of simulations similar to those presented here, one might then be able to explain why only $CsHSO_4$, $CsHSeO_4$, CsH_2AsO_4 and $RbHSeO_4$ exhibit stable superprotonic phase transitions under ambient pressures[85]. An FF that combined the parameters of the different cations and anions might also predict which new mixed compounds will have superprotonic phase transitions.

In this force field, the hydrogen was treated as bonded exclusively to a single oxygen atom (proton donor), with hydrogen bonds extending to other nearby oxygen atoms (proton acceptors). Proton diffusion (i.e., proton jumps) between oxygen atoms cannot occur with this kind of force field. Nevertheless, this series of simulations showed a clear phase transition during the 300 ps simulation at 598 K. Evidence of the phase transition was present in the change of: lattice parameters, X-ray powder diffraction patterns, enthalpy and volume of the cell as well as the direction and degree of reorientation of the HSO_4 groups. The orientations of HSO_4 groups were dramatically randomized and the hydrogen bonds re-distributed above the transition temperature, in agreement with other experimental and theoretical results that attribute the dramatic increase of the proton conductivity to the nearly free rotation of the tetrahedra[173,192].

These results show that proton diffusion is not essential to the existence of a superprotonic phase transition, and that rotational disorder of HSO_4 groups is a sufficient condition to predict the presence of such transitions.

The importance of the hydrogen torsional barrier height, hydrogen bond strength, and oxygen charge distribution to the transition temperature was probed by changing one of these parameters and re-running the series of simulations. The results of these secondary simulations are in agreement with a priori arguments that any parameter inhibiting the rotations of the HSO_4 groups will increase the temperature of the transition and vice versa. Of particular interest were the results of the simulations run with all oxygen electrostatic charges equivalent, where the transition temperature dropped from 598 to 423 K, immediately above the experimental value of 414 K[3]. This was expected as the even charge distribution should favor the more symmetric and highly dynamic phase I compared to the relatively fixed, monoclinic structure of phase II. As the transition temperature changed so much with this variable, it will be interesting to compare these results to those of future simulations which will use a reactive force field that constantly adjusts the oxygen charges. Such a force field will also allow for proton migration between the tetrahedra, the results of which could be compared to these results to evaluate the effect of fixing the protons to a particular oxygen atom (as was done in this work) on the transition temperature.

In conclusion, these simulations have convincingly reproduced both the structural and dynamic properties of $CsHSO_4$'s superprotonic phase transition using a FF derived from Dreiding default values. A sufficiently general approach was utilized to adjust the

FF parameters so as to be applicable to other systems, suggesting that similar force field calculations can be used to “discover” new superprotonic conducting compounds.

Chapter 6. Conclusions

The present work attempted to uncover the structural and chemical parameters that favor superprotonic phase transitions over melting or decomposition in the $MHXO_4$, MH_2ZO_4, and mixed $MHXO_4$-MH_2ZO_4 classes of compounds (X=S, Se; Z=P, As; M=Li, Na, K, NH_4, Rb, Cs) and to thereby gain some ability to "engineer" the properties of solid acids for applications. Three separate investigations were carried out.

First, the cation size effect on superprotonic phase transitions similar to that of $CsHSO_4$ was studied. Preliminary investigations attempted to create new, mixed cation solid acids from the Cs/K, Cs/Na, Cs/Li systems and thereby vary the average cation size. This work resulted in two new compounds pertinent to the question of the cation size effect: $Cs_2Na(HSO_4)_3$ and $CsNa_2(HSO_4)_3$. Comparing the defining distances of these two compounds as well as the other known $MHSO_4$ compounds, the <M-X> distance surfaced as the likely critical crystal-chemical measure of whether a compound has a superprotonic phase transition or not. This was in contrast to the predominant theory that the <S-S> distance was the critical parameter [39]. However, it could not be ruled out that these results were due to structural differences between the compounds, in particular as the structures of $Cs_2Na(HSO_4)_3$ and $CsNa_2(HSO_4)_3$ were quite unique.

Therefore an investigation into the $M_2(HSO_4)(H_2PO_4)$ family of compounds was undertaken as these compounds are isostructural for M = Cs, Rb, NH_4, K. In this system only the Cs compound was found to have a superprotonic phase transition, so that the cation size effect was conclusively confirmed. The <M-X> distance was once again the most salient crystal-chemical measure in predicting the superprotonic phase transition.

The importance of this distance was explained in terms of bigger M-O and X-O distances giving "floppier" MO_x polyhedra and XO_4 tetrahedra, respectively, thereby lowering the barriers to tetrahedral reorientations, which are inherent to superprotonic phase transitions. One then has an a priori measure of a (known or unknown) compound's likelihood for undergoing a superprotonic phase transition.

Second, the entropic driving force behind superprotonic phase transitions was probed by investigations into the $CsHSO_4$-CsH_2PO_4 family of compounds. Three new compounds were synthesized for this study: $Cs_2(HSO_4)(H_2PO_4)$, $Cs_3(HSO_4)_{2.25}(H_2PO_4)_{0.75}$, and $Cs_6(H2SO_4)_3(H_{1.5}PO_4)_2$. All the known mixed cesium sulfate-phosphate compounds were synthesized and their properties, particularly those involving their superprotonic phase transitions, were carefully analyzed. Detailed analysis of these properties revealed that the transition enthalpy and volume change were closely related.

The (configurational) entropy of the transitions was then modeled using two sets of rules: one for the room temperature structures and one for the superprotonic structures. The low temperature rules used statistical mechanics, adjusted to account for the probable local ordering of protons near mixed S/P sites, to evaluate the entropy of the disordered hydrogen bonds (symmetric and partial occupancy disorder) and mixed sulfate/phosphate tetrahedra found in the room temperature structures. The set of rules used to calculate the entropy of the superprotonic structures was based on Pauling's approach to the residual entropy of ice [135]. His rules were adjusted to describe the highly dynamic tetrahedra and disordered hydrogen bonds of the superprotonic structures, which resulted in the following equation for evaluating the configurational entropy

$$\Omega = \begin{pmatrix} \#\ of \\ proton \\ configurations \end{pmatrix} * \begin{pmatrix} probability \\ a\ proton \\ site\ is\ open \end{pmatrix}^{\begin{pmatrix} \#\ of \\ protons \end{pmatrix}} * \begin{pmatrix} \#\ of \\ tetrahderal \\ arrangements \end{pmatrix} * \begin{pmatrix} \#\ of \\ oxygen \\ positions \end{pmatrix}$$

Applying this equation to the superprotonic structures of the mixed cesium sulfate-phosphate compounds allowed for the evaluation of the configurational entropy change across their transitions. These values were found to be in excellent agreement with the experimental data. The above equation was then applied to other solid acids with known superprotonic transitions but different room/high temperature structures and was found to give results that matched well the published data. It would then seem possible to predict a potential compound's transition entropy from predicted room and high temperature structures. Since the transition volume change and enthalpy were closely related, it should also be possible to estimate a transition enthalpy from the same predicted structures. There is then the possibility of calculating a transition temperature for a desired, but as yet unsynthesized, compound and thereby deducing if it is likely to transform before decomposition or melting.

Third, the superprotonic phase transition of $CsHSO_4$ was simulated by molecular dynamics. The phase transition was successfully simulated and analysis of the data showed both the structural and dynamic behavior of the superprotonic phase of $CsHSO_4$ to have been reproduced. The importance of oxygen charge distribution, hydrogen bond energy and the torsional barrier height was investigated through a series of secondary simulations. Analysis of these simulations confirmed the a priori assumption that superprotonic phase transitions are facilitated by the easy reorientations of the tetrahedra

and vice versa. Also, since this force field did not allow proton migration, it can be said definitively that proton hopping is not essential to superprotonic phase transitions.

The approach used to generate the FF of the simulations adjusted Dreiding default values (where available) to reproduce three ab initio calculations. The S,O, H, and Cs vdW force field parameters were adjusted to reproduce the quantum mechanically derived structure, binding energy and frequencies of a gas-phase $CsHSO_4$ monomer. Hydrogen bond parameters were tuned to reproduce the ab initio O_D-O_A distance and binding energy of a gas-phase $(H_2SO_4)_2$ dimer. And finally, the hydrogen torsional barrier height of the HSO_4^- groups was fit to a series of ab initio calculations on a HSO_4^- ion in a dielectric medium of relative dielectric constant 10.

Such a process for adjusting the Dreiding FF parameters was picked not only for its simplicity, but also because it could potentially be used to derive the FF for any other MH_nXO_4 compound (M = Cs, Rb, NH4, K, Na, Li; X = S, Se, P, As). It should then be possible to develop a general FF that could be used to "discover" novel superprotonic solid acids.

All three approaches were therefore successful in furthering the knowledge of which structural and chemical features favor superprotonic phase transitions, and as such, should be useful to future research on these compounds.

Appendix: Compendium of Experimental Data

In the interest of time and space, many of the measurements performed on the compounds found in this work were alluded to but not explicitly shown. Those results are shown here, in the order that they were discussed in the text.

A.1 Chapter 3

A.1.1 β-$CsHSO_4$-III

The structures for α, β, γ-$CsHSO_4$-III are nearly identical, and as much more attention was given to β-$CsHSO_4$-III, only its structure will be shown in this appendix. The SCXD data collection was taken on a crystal from a 80:20 $CsHSO_4$:$NaHSO_4$ aqueous solution. The crystal structure is shown in Figure A.1, the atomic coordinates in Table A.1, anisotropic thermal parameters in Table A.2, and the data collection parameters in Table A.3. The compound has a formula of $(CsHSO_4)_3$ and crystallizes in space group $P2_1/m$. The final residuals, based on 4032 independent reflections, were wR(F2) = 0.2314 and R(F) = 0.0566. The data were weighted as described in Table A.3 and refinements were preformed against F^2 values. Note the disorder of the protons in the hydrogen bonds, which motivated the DSC experiment looking for an ordering of the protons at low temperatures.

Table A.1 Atomic coordinates and equivalent displacement parameters ($Å^2$) for β-$CsHSO_4$-III. $U_{eq} = (1/3)Tr(U^{ij})$.

Atom	x/a	y/b	z/c	U_{eq}
Cs1	0.2888(2)	0.25	0.66095(10)	0.0313(4)
Cs2	0.28799(18)	-0.75	0.99514(9)	0.0250(4)

Cs3	0.7127(2)	-0.25	0.67268(9)	0.0309(5)
S4	0.2466(7)	-0.25	0.8177(4)	0.0242(10)
S5	0.7552(9)	0.25	0.5168(3)	0.0272(11)
S6	0.7534(6)	0.25	0.8496(4)	0.0251(11)
O1	0.392(2)	-0.25	0.7744(12)	0.040(4)
O2	0.606(2)	0.25	0.5624(11)	0.042(5)
O3	0.608(3)	0.25	0.8978(13)	0.044(5)
O4	0.702(3)	0.25	0.7602(10)	0.038(4)
O5	0.121(2)	-0.460(2)	0.7893(9)	0.047(3)
O6	0.702(3)	0.25	0.4287(10)	0.039(4)
O7	0.308(2)	-0.25	0.9056(11)	0.040(4)
O8	0.8779(15)	0.455(2)	0.8777(7)	0.032(3)
O9	0.869(3)	0.454(3)	0.5405(12)	0.052(4)
H2	0.04(3)	-0.45(4)	0.850(12)	0.05
H3	0.90(8)	0.52(12)	0.55(4)	0.05

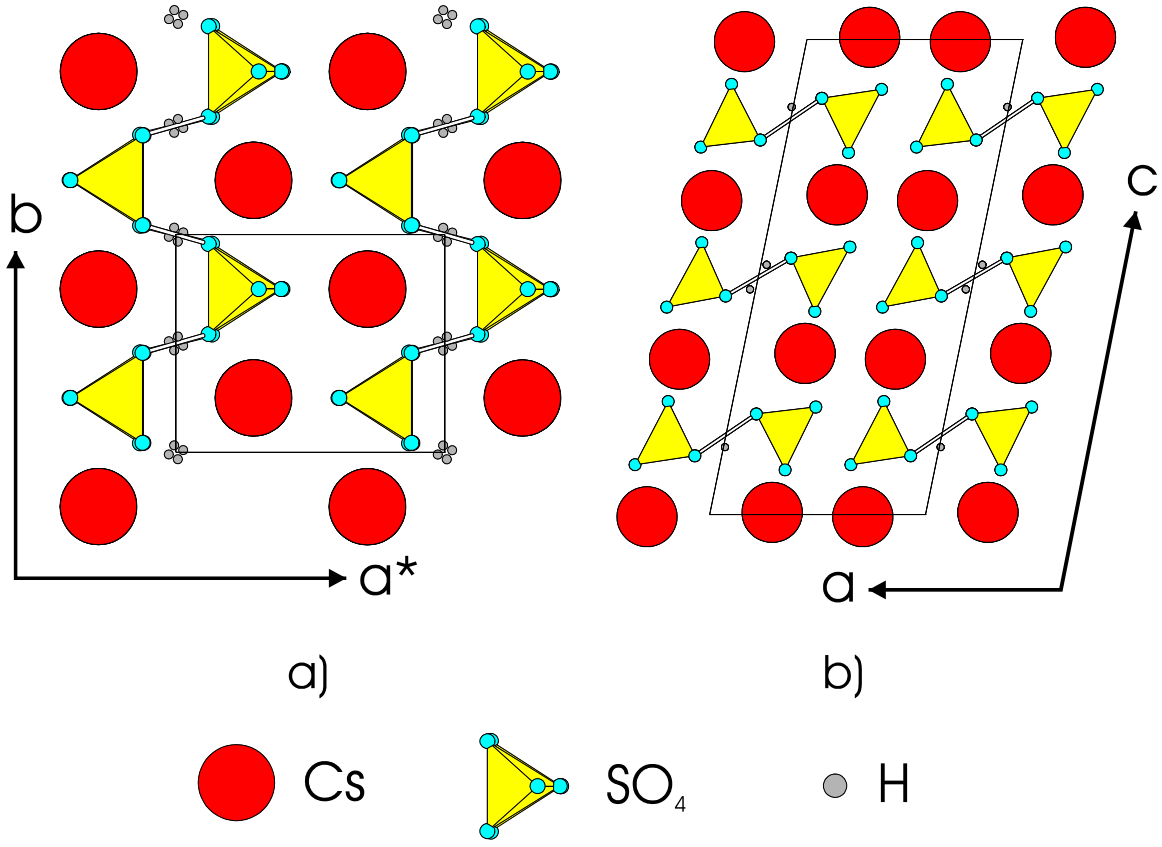

Figure A.1 Crystal structure of β-$CsHSO_4$-III: a) down the [001] and b) down the [010] directions. Note the disordered hydrogen bonds connecting the tetrahedra into zigzag chains along the [010] direction. Parallelepipeds represent unit cells.

Table A.2 Anisotropic Thermal parameters ($Å^2$) for β-$CsHSO_4$-III.

Atom	U_{11}	U_{22}	U_{33}	U_{23}	U_{13}	U_{12}
Cs1	0.0269(7)	0.0343(8)	0.0329(8)	0	0.0068(6)	0
Cs2	0.0249(7)	0.0227(6)	0.0278(7)	0	0.0061(5)	0
Cs3	0.0290(7)	0.0330(8)	0.0317(8)	0	0.0084(6)	0
S4	0.017(2)	0.025(2)	0.032(3)	0	0.0081(19)	0
S5	0.041(3)	0.033(3)	0.009(2)	0	0.0075(19)	0
S6	0.012(2)	0.031(3)	0.033(3)	0	0.0057(19)	0
O1	0.033(8)	0.043(10)	0.053(11)	0	0.029(8)	0
O2	0.024(7)	0.065(13)	0.043(10)	0	0.019(7)	0
O3	0.038(9)	0.034(9)	0.064(13)	0	0.021(9)	0
O4	0.064(12)	0.029(8)	0.020(7)	0	0.008(8)	0
O5	0.062(8)	0.028(6)	0.061(8)	-0.013(6)	0.033(7)	-0.013(6)
O6	0.050(10)	0.037(9)	0.023(8)	0	-0.008(7)	0
O7	0.021(7)	0.065(13)	0.030(8)	0	0.000(6)	0
O8	0.032(5)	0.034(6)	0.031(5)	-0.017(5)	0.007(4)	-0.015(5)
O9	0.053(9)	0.058(11)	0.050(8)	-0.023(8)	0.022(6)	-0.026(7)

Table A.3 Data collection specifics for β-$CsHSO_4$-III, $(CsHSO_4)_3$

#----------	CHEMICAL	INFORMATION
_chemical_formula_	$(CsHSO_4)_3$	
_chemical_formula_weight	689.88	
#----------	UNIT CELL	INFORMATION
_cell_length_a (Å)	7.329(5)	
_cell_length_b (Å)	5.829(4)	
_cell_length_c (Å)	16.525(13)	
_cell_angle_alpha (°)	90	
_cell_angle_beta (°)	101.55(3)	
_cell_angle_gamma (°)	90	
_cell_volume ($Å^3$)	691.7(9)	
_cell_formula_units_Z	1	
_cell_measurement_temperature (K)	293(2)	
#----------	CRYSTAL	INFORMATION
_exptl_crystal_density_diffrn (g/cm^3)	2.785	
_exptl_crystal_density_method	'not	measured'
_exptl_crystal_F_000	536	
_exptl_absorpt_coefficient_mu	5.442	
_exptl_absorpt_correction_type	none	
#----------	DATA	COLLECTION
_diffrn_radiation_wavelength (Å)	0.7107	

_diffrn_radiation_type	MoK\a	
_diffrn_reflns_number	4032	
_diffrn_reflns_limit_h_min	0	
_diffrn_reflns_limit_h_max	10	
_diffrn_reflns_limit_k_min	-8	
_diffrn_reflns_limit_k_max	8	
_diffrn_reflns_limit_l_min	-23	
_diffrn_reflns_limit_l_max	22	
_diffrn_reflns_theta_min	1.26	
_diffrn_reflns_theta_max	29.99	
_diffrn_reflns_theta_full	29.99	
_diffrn_measured_fraction_theta_max		
	1	
_diffrn_measured_fraction_theta_full		
	1	
_reflns_number_total	2204	
_reflns_number_gt	906	
_reflns_threshold_expression	>2sigma(I)	
#----------	COMPUTER	PROGRAMS
_computing_structure_refinement	'SHELXL-97	(Sheldrick,
#----------	REFINEMENT	INFORMATION
_refine_ls_structure_factor_coef	Fsqd	
_refine_ls_matrix_type	full	
_refine_ls_weighting_scheme	calc	
_refine_ls_weighting_details		
	'calc	w=1/[\s^2^(Fo^2^)+(0.0781P)^2^+15.6726P]
_refine_ls_hydrogen_treatment	mixed	
_refine_ls_extinction_method	SHELXL	
_refine_ls_extinction_expression		
	Fc^*^=kFc[1+0.001xFc^2^\l^3^/sin(2\q)]^-1/4^	
_refine_ls_extinction_coef	0.0148(17)	
_refine_ls_number_reflns	2204	
_refine_ls_number_parameters	107	
_refine_ls_number_restraints	0	
_refine_ls_R_factor_gt	0.0566	
_refine_ls_wR_factor_ref	0.2314	
_refine_ls_goodness_of_fit_ref	1.135	
_refine_ls_restrained_S_all	1.135	
_refine_ls_shift/su_max	0.487	
_refine_diff_density_max	1.583	
_refine_diff_density_min	-1.181	

The NMR experiments on this compound revealed the presence of Na cations best in the H^+ NMR measurements where the proton signal was split into two peaks compared to the references one, Figure A.2. The main peak was also shift ~ 1 ppm between the two plots.

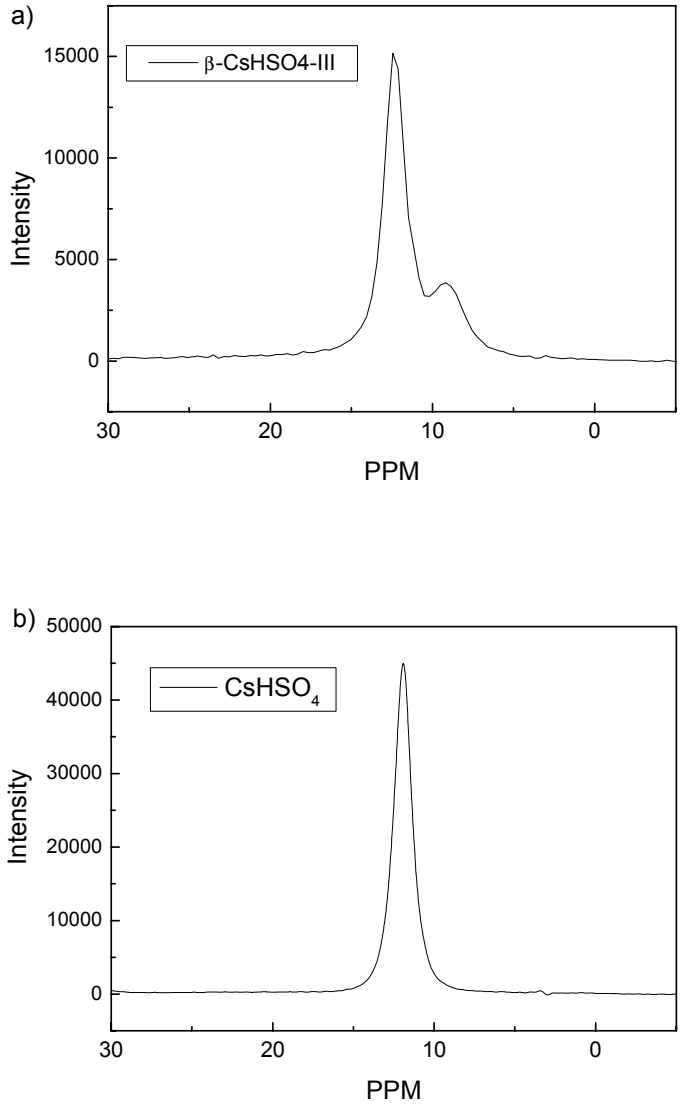

Figure A.2 H^+ NMR measurements on a) β-$CsHSO_4$-III and b) true $CsHSO_4$-III. The two peaks in a) versus one in b) as well as the ppm shift in the main peaks is attributed to the trace incorporation of Na cations into the structure of $CsHSO_4$-III. Both measurements taken on a Bruker DSX 500 MHz NMR spectrometer using the MAS technique with spin rates of 12 kHz. Each measurement is a combination of 8 scans with a D_1 of 1000s.

A.1.2 $Cs_2Li_3H(SO_4)_3*H_2O$

The compound $Cs_2Li_3H(SO_4)_3*H_2O$ is orthorhombic, crystallizing in space group $Pbn2_1$, with lattice parameters a = 12.945(3), b = 19.881(4), c = 5.111(1) Å, as determined by SCXD. The unit cell has four formula units and a volume of 1315.41(30) $Å^3$. The crystal structure is shown in Figure A.3, the atomic coordinates in Table A.4, anisotropic thermal parameters in Table A.5, and data collection parameters in A.6.

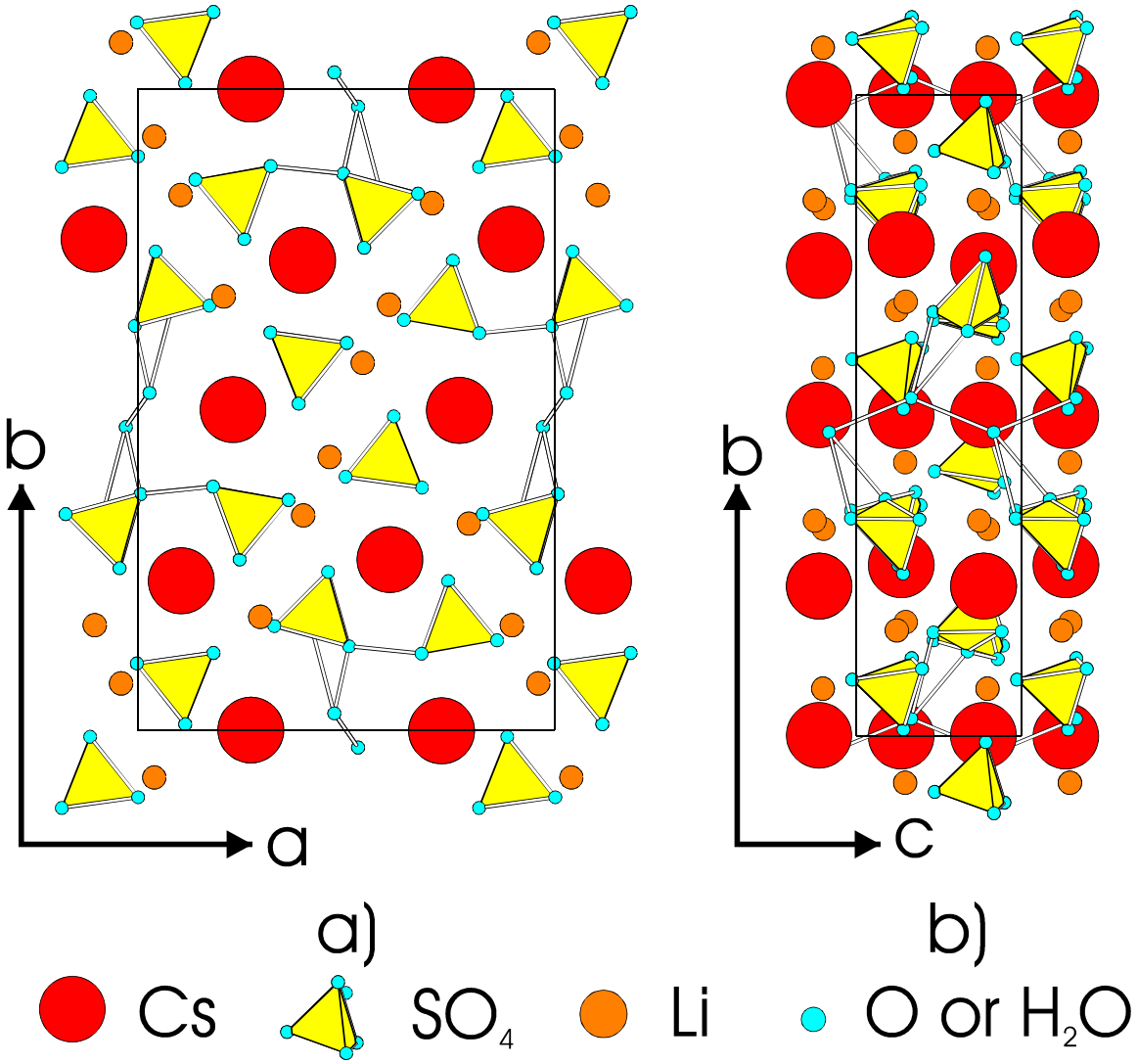

Figure A.3 Structure of $Cs_2Li_3H(SO_4)_3*H_2O$ projected down a) the c-axis and b) the a-axis. The hydrogen atoms were not found in this structure and therefore the water molecules appear as isolated oxygens. Rectangles show the unit cell.

Table A.4 Atomic coordinates and equivalent displacement parameters ($Å^2$) for $Cs_2Li_3H(SO_4)_3*H_2O$. $U_{eq} = (1/3)Tr(U^{ij})$.

Atom	x/a	y/b	z/c	U_{eq}
Cs1	0.60461(5)	0.26657(3)	0.2722(3)	0.02334(18)
Cs2	0.77140(5)	0.49948(3)	0.2711(5)	0.03029(19)
S3	0.59253(16)	0.41951(11)	0.7661(13)	0.0156(4)
S4	0.42422(18)	0.17708(12)	-0.2276(15)	0.0219(5)
S5	0.76667(16)	0.16184(11)	0.7684(13)	0.0182(5)
O1	0.4570(6)	0.2465(4)	-0.228(5)	0.0290(18)
O2	0.7444(7)	0.2333(4)	0.779(5)	0.040(3)
O3	0.6139(8)	0.4904(4)	0.797(7)	0.057(5)
O4	0.8613(7)	0.1407(4)	0.8853(16)	0.0220(17)
O5	0.7778(7)	0.1488(5)	0.4684(18)	0.029(2)
O6	0.5050(10)	0.1298(7)	-0.129(7)	0.02(2)
O7	0.6813(8)	0.3781(5)	0.8306(18)	0.036(3)
O8	0.4158(7)	0.1608(6)	-0.5363(16)	0.033(2)
O9	0.5750(7)	0.4126(5)	0.4742(17)	0.0263(19)
O10	0.3270(8)	0.1617(6)	-0.1201(18)	0.031(2)
O11	0.4986(8)	0.3961(5)	0.8925(17)	0.027(2)
O12	0.6816(7)	0.1187(5)	0.8586(17)	0.030(2)
OH2	0.4702(11)	0.0273(7)	-0.709(8)	0.095(6)
Li1	0.4591(12)	0.4267(8)	0.239(4)	0.014(4)
Li2	0.8958(15)	0.1640(9)	0.302(5)	0.020(4)
Li3	0.7944(14)	0.3232(9)	0.778(11)	0.029(4)

Table A.5 Anisotropic Thermal parameters ($Å^2$) for $Cs_2Li_3H(SO_4)_3*H_2O$.

Atom	U_{11}	U_{22}	U_{33}	U_{23}	U_{13}	U_{12}
Cs1	0.0221(3)	0.0271(3)	0.0208(3)	0.0001(8)	0.0001(7)	-0.0002(2)
Cs2	0.0269(3)	0.0304(3)	0.0336(3)	-0.0012(10)	0.0000(10)	-0.0044(2)
S3	0.0105(9)	0.0145(9)	0.0218(10)	0.006(3)	0.008(2)	0.0009(7)
S4	0.0135(9)	0.0176(10)	0.0345(12)	0.006(3)	0.009(3)	0.0005(8)
S5	0.0120(9)	0.0167(10)	0.0259(11)	-0.014(3)	-0.003(2)	0.0028(8)
O1	0.029(4)	0.017(3)	0.041(4)	0.011(9)	0.002(9)	-0.001(3)
O2	0.032(4)	0.022(4)	0.065(7)	0.026(8)	0.007(10)	0.002(4)
O3	0.022(4)	0.015(4)	0.134(14)	-0.010(13)	-0.003(13)	-0.002(3)
O4	0.019(4)	0.024(4)	0.023(4)	-0.006(3)	-0.011(3)	0.011(4)
O5	0.024(5)	0.041(6)	0.022(4)	-0.005(4)	-0.002(4)	0.006(4)
O6	0.019(5)	0.035(7)	0.00(7)	0.043(18)	0.023(16)	0.005(5)
O7	0.030(5)	0.042(5)	0.034(7)	-0.007(4)	-0.004(4)	0.022(5)
O8	0.024(5)	0.063(7)	0.011(4)	0.004(4)	0.001(3)	0.000(5)
O9	0.017(4)	0.040(5)	0.022(4)	-0.005(4)	-0.002(3)	-0.002(4)

O10	0.021(4)	0.043(6)	0.029(4)	-0.006(4)	0.002(4)	-0.003(4)
O11	0.026(5)	0.034(5)	0.023(4)	-0.013(4)	0.006(3)	-0.015(4)
O12	0.018(4)	0.035(5)	0.036(5)	0.013(4)	0.005(3)	0.004(4)
OH2	0.055(8)	0.040(6)	0.189(18)	0.023(17)	0.026(18)	0.001(6)

Table A.6 Data collection specifics for $Cs_2Li_3H(SO_4)_3*H_2O$

#----------	CHEMICAL INFORMATION
_chemical_formula_	$Cs_2Li_2H(SO_4)*H_2O$
_chemical_formula_weight	593.84
#----------	UNIT CELL INFORMATION
_cell_length_a	12.95(3)
_cell_length_b	19.881(4)
_cell_length_c	5.1110(10)
_cell_angle_alpha	90
_cell_angle_beta	90
_cell_angle_gamma	90
_cell_volume	1315(3)
_cell_formula_units_Z	4
_cell_measurement_temperature	293(2)
#----------	CRYSTAL INFORMATION
_exptl_crystal_density_diffrn	2.999
_exptl_crystal_density_method	'not measured'
_exptl_crystal_F_000	1096
_exptl_absorpt_coefficient_mu	6.078
_exptl_absorpt_correction_type	none
#----------	DATA COLLECTION
_diffrn_radiation_wavelength	0.71073
_diffrn_radiation_type	MoK\a
_diffrn_reflns_number	5717
_diffrn_reflns_limit_h_min	0
_diffrn_reflns_limit_h_max	18
_diffrn_reflns_limit_k_min	-10
_diffrn_reflns_limit_k_max	27
_diffrn_reflns_limit_l_min	-7
_diffrn_reflns_limit_l_max	7
_diffrn_reflns_theta_min	1.88
_diffrn_reflns_theta_max	30
_diffrn_reflns_theta_full	30
	1

	1
_reflns_number_total	3833
_reflns_number_gt	2858
_reflns_threshold_expression	>2sigma(I)
#----------	COMPUTER PROGRAMS USED
_computing_structure_refinement	'SHELXL-97
#----------	REFINEMENT INFORMATION
_refine_ls_structure_factor_coef	Fsqd
_refine_ls_matrix_type	full
_refine_ls_weighting_scheme	calc
_refine_ls_weighting_details	w=1/[\s^2^(Fo^2^)+(0.0787P)^2^+11.8743P] where P=(Fo^2^+2Fc^2^)/3'
_refine_ls_hydrogen_treatment	mixed
_refine_ls_extinction_method	SHELXL
_refine_ls_extinction_coef	0.0026(4)
_refine_ls_number_reflns	3833
_refine_ls_number_parameters	176
_refine_ls_number_restraints	1
_refine_ls_R_factor_gt	0.0628
_refine_ls_wR_factor_ref	0.1737
_refine_ls_goodness_of_fit_ref	1.166
_refine_ls_restrained_S_all	1.166
_refine_ls_shift/su_max	9.983
_refine_ls_abs_structure_Flack	0
_refine_diff_density_max	4.104
_refine_diff_density_min	-2.833

This compound did not exhibit a superprotonic phase transition before decomposition/dehydration at ~ 105°C, which was deduced from TGA, DSC, and conductivity data, Figures A.4 and A.5.

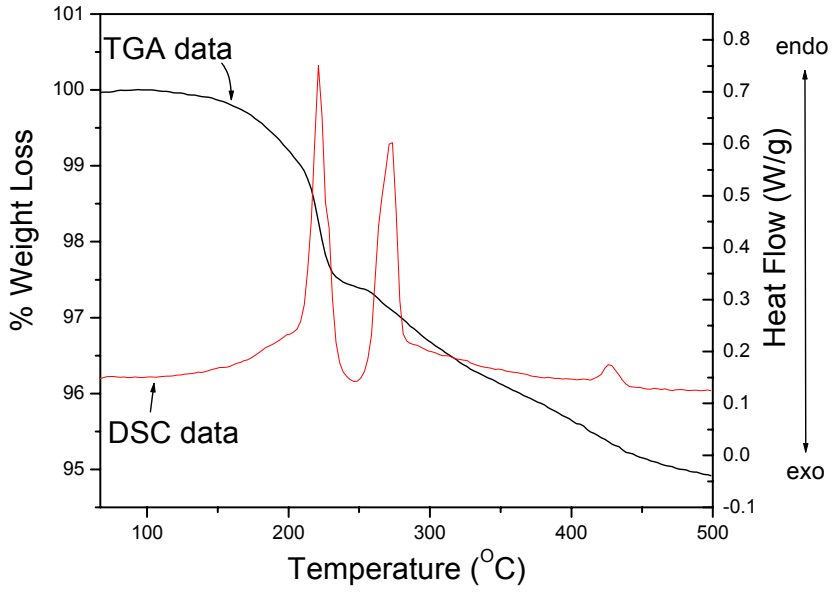

Figure A.4 TGA and DSC data for $Cs_2Li_3H(SO_4)_3*H_2O$. No superprotonic phase transition is evident before the onset of decomposition/dehydration at ~ 105°C. Both measurements taken under flowing N_2 with heating rates of 5°C/min.

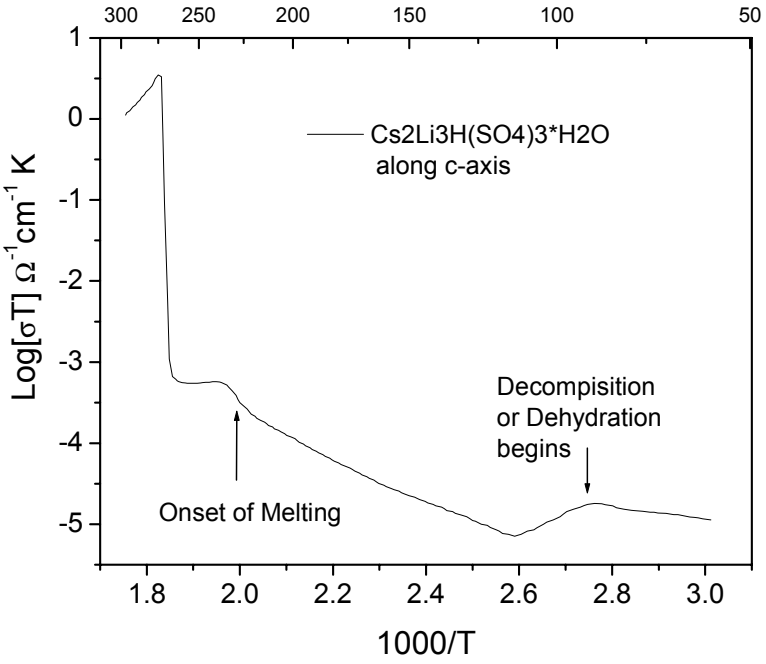

Figure A.5 Conductivity of $Cs_2Li_3H(SO_4)_3*H_2O$. Measurement taken on a single crystal sample parallel to the c-axis under ambient air atmosphere at a heating rate of 0.5°C/min.

A.2 Chapter 4

A.2.1 Causes for discrepancies in experimental data between published values and those reported in Chapter 4

It was mentioned in the text that there are some discrepancies between the published values and those presented in Chapter 4, with particular emphasis on the transition enthalpies. Some probable reasons for this were already expressed, but here we will go into more detail. First, these differences are probably due mostly to the quality and quantity of the samples as well as the measurement techniques used in those measurements. For many of the mixed compounds, the samples measured were reported to have liquid filled voids or be part of a powder mixture of different phases[30,32,133]. Moreover, many of these compound are **extremely** hard to grow as large single crystals, and so very small crystals would have to be identified from a multiple of phases, limiting the number and type of measurements possible[27,31]. These limits to the quality and quantity of the desired compound can only have had an adverse effect on the measurement of the transition enthalpy.

By far the most time-consuming and laborious part of this work was preparing adequate amounts of the mixed compounds with a high level of phase purity.
For the end members, $CsHSO_4$ and CsH_2PO_4, high-quality large single crystals are not difficult to grow. The minor discrepancy between the published and this work's ΔH for $CsHSO_4$ (5.5 vs. 6.2(2) kJ/mol $CsHXO_4$, respectively) may simply be to statistical error or differences in measurement techniques. However, during this work it was found that $CsHSO_4$ samples from mixed cation solutions had reproducibly lower transition

enthalpies even though their lattice constants (measured by SCXD techniques) were nearly identical to published values. For example, from mixed Cs/K or Cs/Na solutions the average ΔH for seven different measurements was 5.2(5) kJ/mol, with a low of 4.5 and high of 5.5 kJ/mol, Table A.7. These values are to be compared to the average of 6.2(2) kJ/mol measured on samples grown from solutions containing only Cs cations. This suggests that the purity of the initial reagents has a significant effect on enthalpy of the transition. The effect of trace impurities also showed up in other properties of these samples. To avoid any such obfuscating effects, only ultrahigh purity reagents were used in making the compounds of this study.

Table A.7 Variation of the transition enthalpy for $CsHSO_4$ from pure and mixed cation solutions.

	T_{onset}(Na/K) (°C)	ΔH(Na/K) (kJ/mol)	Tonset(Cs) (°C)	ΔH (kJ/mol) (kJ/mol)
Exp 1	142.8	4.5	140.9	6.0007
Exp 2	142.5	5.5	141.2	6.2491
Exp 3	143.5	5.1	140.5	6.2376
Exp 4	143.5	5.2	140.5	6.8241
Exp 5	139	5.3	143.5	6.0881
Exp 6	140.2	5.5	143.8	6.0858
Exp 7	138.8	5.0	141.6	37.4854
Average	141.5(19)	5.2(5)	141.9(16)	6.2(2)

A.2.2 $CsHSO_4$

Powder X-ray diffraction patterns from which the thermal expansions of the room temperature and high temperature phase of $CsHSO_4$ were calculated are shown in Figure A.6 and the results of the Rietveld analysis on these patterns in Table A.8

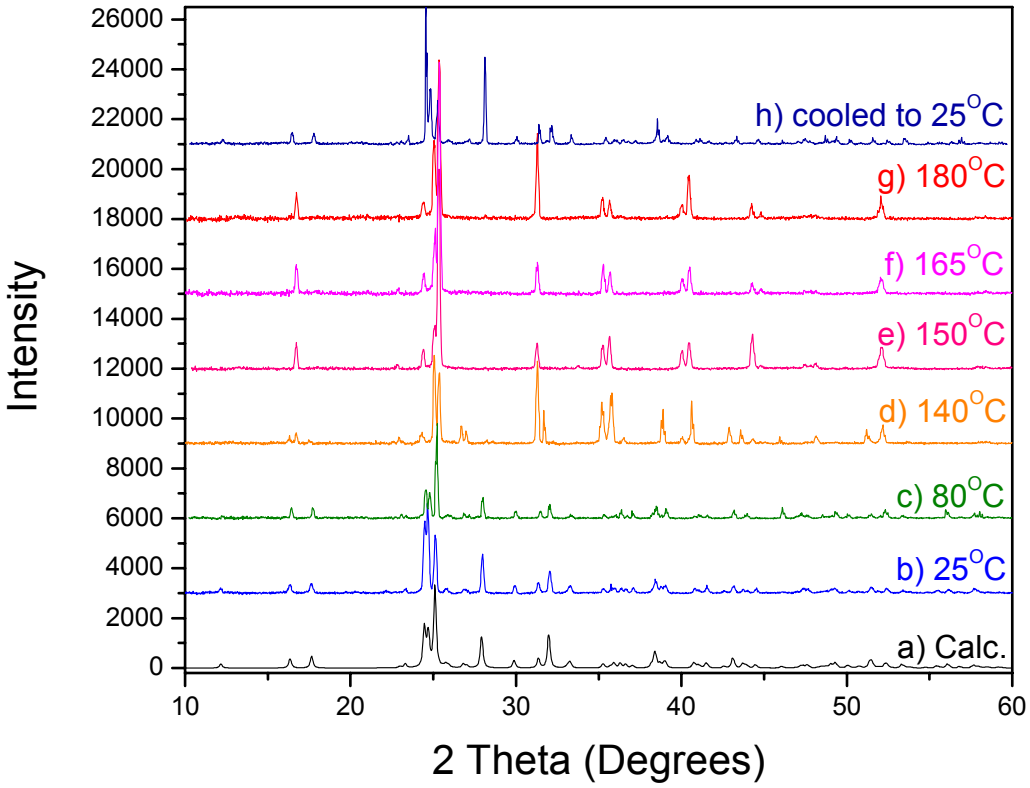

Figure A.6 PXD patterns of $CsHSO_4$ taken at various temperatures (as shown). Data taken in ambient atmosphere with a 3 second scan rate and 0.02° 2θ scan step.

Table A.8 Results of Rietveld Analysis on $CsHSO_4$ PXD patterns taken at various temperatures.

phase	Temp (°C)	% phase	Rp	Rwp	a (Å)	b (Å)	c (Å)	Beta (°)	Volume Per CsHXO4
mono	25(1)	100	11.1	15.46	7.772	8.133	7.715	110.84	113.93(5)
mono	80(2)	100	9.44	13.77	7.811	8.156	7.729	110.972	114.94(5)
mono	140(2)	35.5(2)	14.03	22.29	7.881	8.16	7.743	111.32	116.0(2)
tetra	140(2)	64.5(3)			5.712	5.712	14.199	90	115.8(1)
tetra	150(3)	100	5.66	8.26	5.725	5.725	14.225	90	116.56(4)
tetra	165(3)	100	6.43	8.44	5.7277	5.7277	14.233	90	116.73(4)
tetra	180(3)	100	8.33	12.74	5.73	5.73	14.262	90	117.06(6)

A.2.3 $Cs_3(HSO_4)_{2.50}(H_2PO_4)_{0.50}$

Powder X-ray diffraction patterns from which the thermal expansions of the room temperature and high temperature forms of $Cs_3(HSO_4)_{2.50}(H_2PO_4)_{0.50}$ were calculated are shown in Figure A.7 and the results of the Rietveld analysis on these patterns in Table A.9

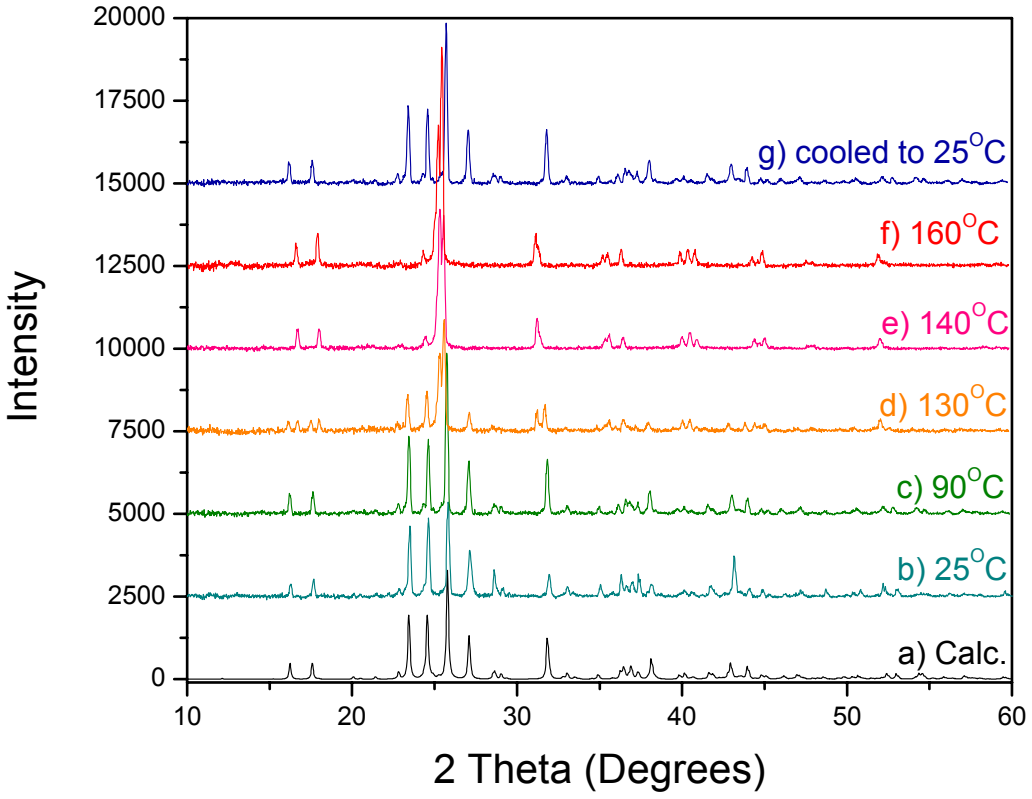

Figure A.7 PXD patterns of $Cs_3(HSO_4)_{2.50}(H_2PO_4)_{0.50}$ taken at various temperatures (as shown). Data taken in ambient atmosphere with a 3 second scan rate and 0.02° 2θ scan step.

Table A.9 Results of Rietveld Analysis on $Cs_3(HSO_4)_{2.50}(H_2PO_4)_{0.50}$ PXD patterns taken at various temperatures.

phase	% phase	Temp (°C)	Rp	Rwp	a (Å)	b (Å)	c (Å)	Beta (°)	Volume Per CsHXO4
mono	100	25(1)	7.66	12.13	19.930(3)	7.862	8.996	100.16	115.62(6)
mono	100	90(2)	4.41	5.72	19.991(1)	7.902	9.011	100.038	116.81(3)
mono	49(1)	130(3)	5.27	6.63	20.046(3)	7.933	9.01	100.028	117.58(5)
cubic	12(1)	130(3)			4.932(1)	4.932	4.932	90	119.97(7)
tetra	39(1)	130(3)			5.732(1)	5.732	14.167	90	116.37(9)
Cubic	44(1)	140(3)	3.89	4.88	4.9345(5)	4.9345	4.9345	90	120.15(4)
tetra	56(1)	140(3)			5.7359(5)	5.7359	14.178	90	116.62(3)
Cubic	58(1)	160(3)	5.29	6.63	4.9423(5)	4.9423	4.9423	90	120.72(4)
tetra	42(0.5)	160(3)			5.7411(6)	5.7411	14.211	90	117.10(4)

A.2.4 $Cs_3(HSO_4)_{2.25}(H_2PO_4)_{0.75}$

Microprobe data supplying the stoichiometry of the compound are given Table A.10. Data taken at a beam voltage and current of 15 kV and 25 mA, respectively, on a pressed powder sample. Standards were pressed powder pellets of $CsHSO_4$ and CsH_2PO_4. Visible beam damage occurred while taking data, which is probably responsible for th low totals. Powder X-ray diffraction patterns from which the thermal expansions of the room temperature and high temperature forms of $Cs_3(HSO_4)_{2.50}(H_2PO_4)_{0.50}$ were calculated are shown in Figure A.8 and the results of the Rietveld analysis on these patterns in Table A.11

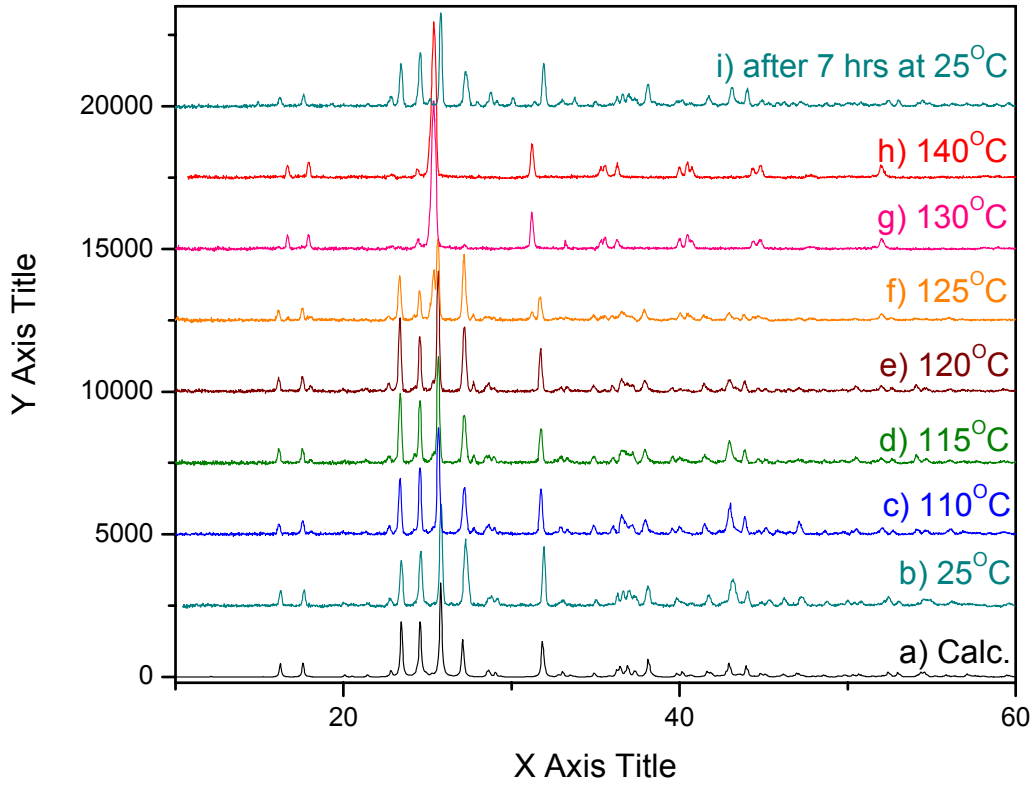

Figure A.8 PXD patterns of $Cs_3(HSO_4)_{2.25}(H_2PO_4)_{0.75}$ taken at various temperatures (as shown). Data taken in ambient atmosphere with a 3 second scan rate and 0.02° 2θ scan step.

Table A.10 Microprobe data on $Cs_3(HSO_4)_{2.25}(H_2PO_4)_{0.75}$.

	Cs	S	P	Sum
Exp 1	56.311	10.615	3.496	70.422
Exp 1	57.679	10.584	3.813	72.075
Exp 1	57.083	10.913	3.589	71.584
Exp 1	57.051	10.617	3.848	71.517
Exp 1	55.809	10.195	3.515	69.519
Exp 1	57.078	10.798	3.662	71.538
Exp 1	55.283	10.475	3.594	69.353
Exp 1	57.025	10.888	3.498	71.41
Exp 1	57.485	10.686	3.397	71.568
Exp 1	56.896	10.55	3.203	70.649
Exp 1	59.042	10.805	3.453	73.301
Average	56.977	10.648	3.552	71.176
SDeV	0.986	0.207	0.183	1.169205

Table A.11 Results of Rietveld Analysis on $Cs_3(HSO_4)_{2.50}(H_2PO_4)_{0.50}$ PXD patterns taken at various temperatures.

phase	% phase	Temp (°C)	Rp	Rwp	a (Å)	b (Å)	c (Å)	Beta (°)	Volume Per CsHXO4
mono	100	25(1)	7.87	11.17	19.913	7.853	8.999	100.132	115.44(5)
mono	100	110(2)	6.46	8.92	19.975	7.912	9.021	100.031	116.99(4)
mono	90(1)	115(2)	6.12	8.35	19.98	7.9175	9.02	100.063	117.08(4)
cubic	8(1)	115(2)			4.93	4.93	4.93	90	119.82(1)
tetra	2(1)	115(2)			5.424	5.424	17.535	90	129.0(8)
mono	93(1)	120(2)	7.15	11.6	19.978	7.9186	9.025	100.04	117.16(5)
cubic	6(1)	120(2)			4.91	4.91	4.91	90	118.4(4)
tetra	1(1)	120(2)			5.415	5.415	17.733	90	120.0(9)
mono	77(1)	125(2)	7.58	11.52	19.982	7.926	9.025	100.038	117.29(7)
cubic	5(1)	125(2)			4.907	4.907	4.907	90	118.2(1)
tetra	18(1)	125(2)			5.715	5.715	14.224	90	116.14(9)
mono	7(1)	130(2)	5.36	8.65	19.9552	8.002	9.03	99.65	118.5(1)
cubic	46(1)	130(2)			4.9519	4.9519	4.9519	90	121.43(4)
tetra	47(1)	130(2)			5.7359	5.7359	14.173	90	116.57(4)
cubic	50	140(3)	4.38	5.59	4.9522	4.9522	4.9522	90	121.4492
tetra	50	140(3)			5.7362	5.7362	14.183	90	116.6693

A.2.5 $Cs_3(HSO_4)_2(H_2PO_4)$

Powder X-ray diffraction patterns from which the thermal expansions of the room temperature and high temperature forms of $Cs_3(HSO_4)_2(H_2PO_4)$ were calculated are shown in Figure A.9 and the results of the Rietveld analysis on these patterns in Table A.12.

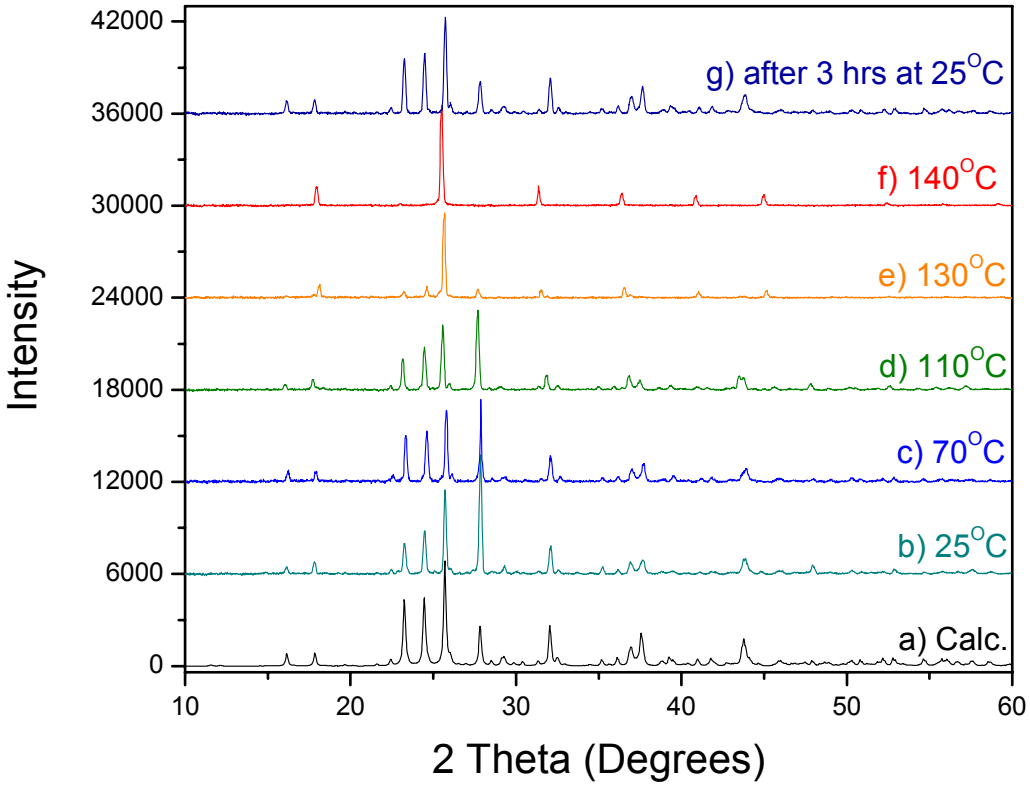

Figure A.9 PXD patterns of $Cs_3(HSO_4)_2(H_2PO_4)$ taken at various temperatures (as shown). Data taken in ambient atmosphere with a 3 second scan rate and 0.02° 2θ scan step.

Table A.12 Results of Rietveld Analysis on $Cs_3(HSO_4)(H_2PO_4)$ PXD patterns taken at various temperatures.

phase	Temp (°C)	% phase	Rp	Rwp	a (Å)	b (Å)	c (Å)	Beta (°)	Volume Per CsHXO4
mono	25(1)	100	11.45	19.47	19.527	7.871	9.162	100.51	115.38(9)
mono	70(1)	100	5.78	7.42	19.603	7.9	9.167	100.309	116.39(3)
mono	110(2)	100	9.84	16.41	19.627	7.93	9.172	100.165	117.10(8)
mono	130(2)	71(2)	7.45	10.3	19.689	7.93	9.159	99.94	117.38(6)
cubic	130(2)	29(1)			4.9304	4.9304	4.9304	90	119.85(3)
cubic	140(2)	100	4.93	6.43	4.9336	4.9336	4.9336	90	120.09(3)

A.2.6 $Cs_5(HSO_4)_3(H_2PO_4)_2$

Powder X-ray diffraction patterns from which the hysteresis of the reverse transition and lattice parameter for the high temperature phase of $Cs_5(HSO_4)_3(H_2PO_4)_2$ were calculated are shown in Figure A.10 and the results of the Rietveld analysis on these patterns in Table A.13.

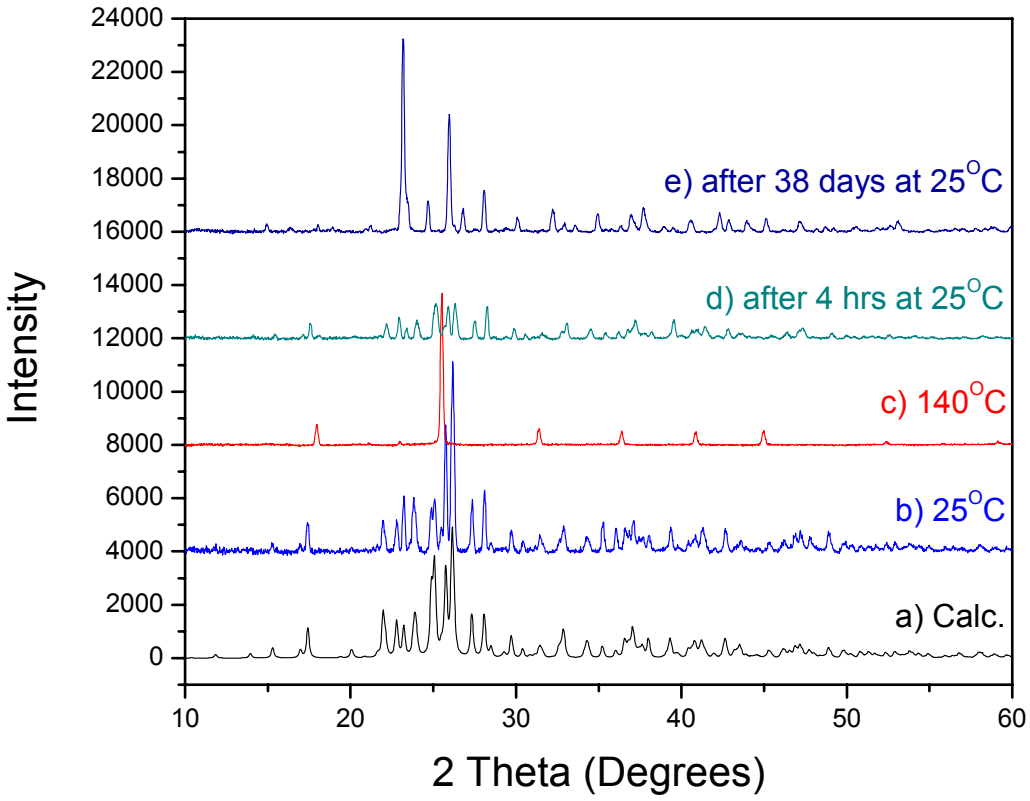

Figure A.10 PXD patterns of $Cs_5(HSO_4)_3(H_2PO_4)_2$ taken at various temperatures (as shown). Data taken in ambient atmosphere with a 3 second scan rate and 0.02° 2θ scan step.

Table A.13 Results of Rietveld Analysis on $Cs_5(HSO_4)_3(H_2PO_4)_2$ PXD pattern in cubic high temperature phase.

phase	Temp (°C)	% phase	Rp	Rwp	a	Beta	Volume/CsHXO4
cubic	140(2)	100	5.89	7.46	4.9378	90	120.39(3)

A.2.7 $Cs_2(HSO_4)(H_2PO_4)$

Powder X-ray diffraction patterns from which the thermal expansions of the room temperature and high temperature forms of $Cs_2(HSO_4)(H_2PO_4)$ were calculated are shown in Figure A.11 and the results of the Rietveld analysis on these patterns in Table A.14. The hysteresis of the reverse transitions was also estimated from the after heating patterns.

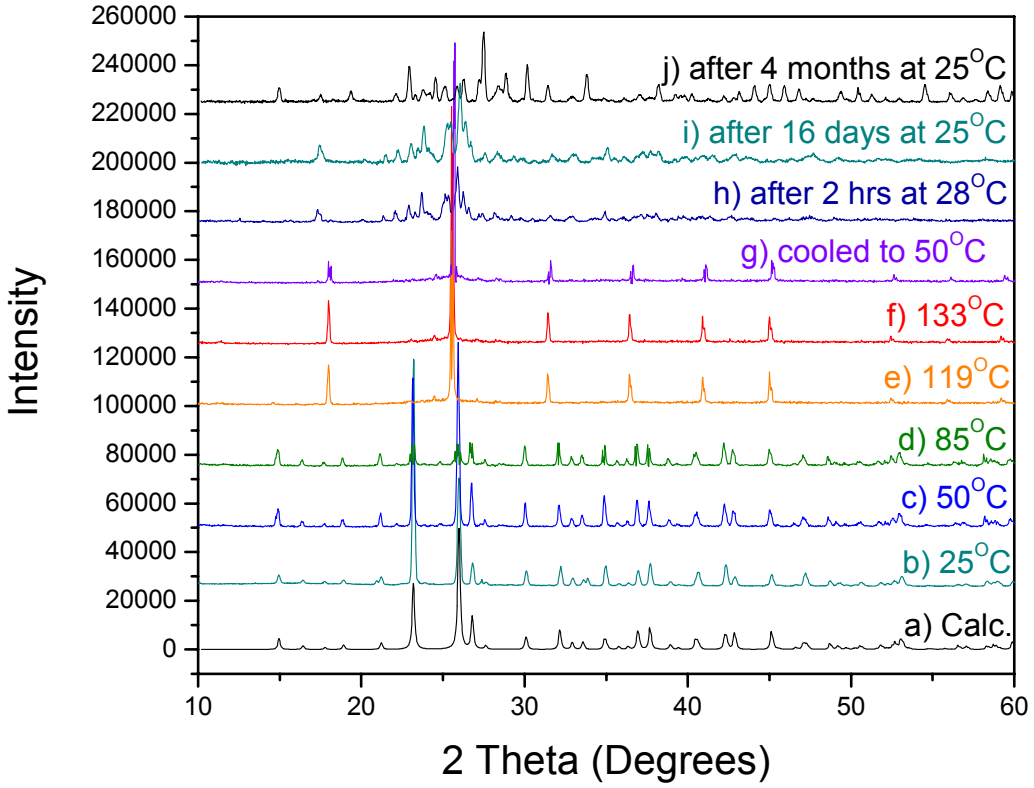

Figure A.11 PXD patterns of $Cs_2(HSO_4)(H_2PO_4)$ taken at various temperatures (as shown). Data taken in ambient atmosphere with a 3 second scan rate and 0.02° 2θ scan step.

Table A.14 Results of Rietveld Analysis on $Cs_2(HSO_4)(H_2PO_4)$ PXD patterns taken at various temperatures.

phase	Temp (°C)	% phase	Rp	Rwp	a (Å)	b (Å)	c (Å)	Beta (°)	Volume Per CsHXO4
mono	25(1)	100	3.48	8.55	7.856	7.732	7.827	99.92	117.1(2)
mono	25(1)	100	6.61	9.36	7.8196	7.704	7.796	99.892	115.67(2)
mono	40(3)	100	18.58	23.82	7.86	7.743	7.838	99.907	117.47(5)
mono	50(3)	100	19	24.18	7.864	7.745	7.845	99.91	117.67(5)
mono	85(4)	100	45.13	54.79	7.884	7.774	7.845	99.8	118.4(6)
cubic	119(5)	100	25.75	34.24	4.9291	4.9291	4.9291	90	119.76(3)
cubic	133(5)	100	25.38	34.21	4.9349	4.9349	4.9349	90	120.18(3)
cubic	50(1)	100	30.59	64.87	4.9186	4.9186	4.9186	90	118.99(3)

A.2.8 $Cs_6(H2SO_4)_3(H_{1.5}PO_4)_4$

Powder X-ray diffraction patterns from which the thermal expansions of the room temperature and high temperature forms of $Cs_6(H2SO_4)_3(H_{1.5}PO_4)_4$ were calculated are shown in Figure A.12 and the results of the Rietveld analysis on these patterns in Table A.15. The hysteresis of the reverse transitions was also estimated from the after heating patterns.

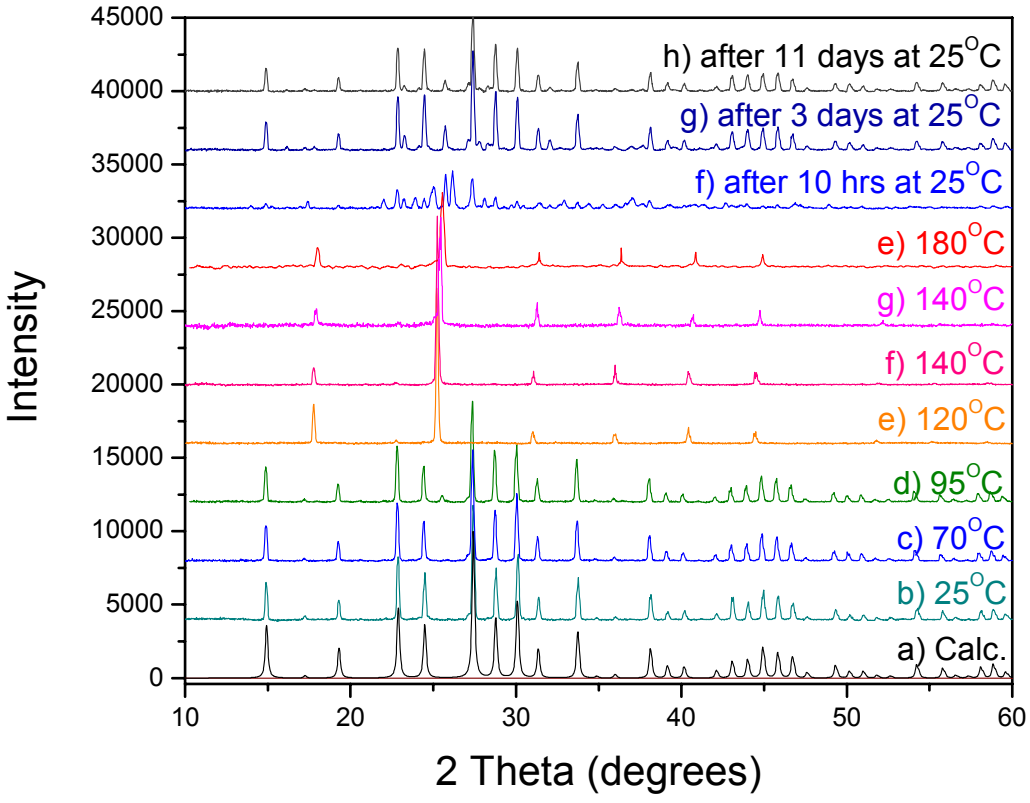

Figure A.12 PXD patterns of $Cs_6(H2SO_4)_3(H_{1.5}PO_4)_4$ taken at various temperatures (as shown). Data taken in ambient atmosphere with a 3 second scan rate and 0.02° 2θ scan step.

Table A.15 Results of Rietveld Analysis on $Cs_6(H2SO_4)_3(H_{1.5}PO_4)_4$ PXD patterns taken at various temperatures.

phase	Temp (°C)	% phase	Rp	Rwp	a (Å)	b (Å)	c (Å)	Beta (°)	Volume Per CsHXO4
cubic I	25(1)	100	1.64	3	14.5388	14.5388	14.5388	90	116.4(1)
cubic I	25(1)	100	8.49	11.36	14.541	14.541	14.541	90	116.46(2)
cubic I	70(2)	100	8.46	11.53	14.573	14.573	14.573	90	117.23(2)
cubic I	95(2)	100	8.58	11.62	14.582	14.582	14.582	90	117.45(5)
cubic P	120(3)	100	5.88	7.12	4.9908	4.9908	4.9908	90	124.31(3)
cubic P	140(3)	100	5.05	6.56	4.9844	4.9844	4.9844	90	123.83(30)
cubic P	160(3)	100	5.98	8.08	4.9631	4.9631	4.9631	90	122.25(7)
cubic P	180(3)	100	5.98	7.83	4.952	4.952	4.952	90	121.4(1)

The structure of this compound was described in the text. Its atomic coordinates are given in Table A.16, anisotropic thermal parameters in Table A.17, and data collection parameters in A.18. The final residuals, based on 2719 independent reflections, were wR(F2) = 0.0339 and R(F) = 0.0164. The data were weighted as described Table A.3 and refinements were preformed against F^2 values.

Table A.16 Atomic coordinates and equivalent displacement parameters ($Å^2$) for $Cs_6(H2SO_4)_3(H_{1.5}PO_4)_4$. $U_{eq} = (1/3)Tr(U^{ij})$.

Atom	x/a	y/b	z/c	U_{eq}
Cs1	0.75	0.84924(2)	1	0.02458(12)
P2	0.74779(6)	0.74779(6)	0.74779(6)	0.0193(3)
S3	0.75	1.125	1	0.0201(3)
O1	0.7014(2)	0.8384(2)	0.7815(2)	0.0245(7)
O2	0.6722(2)	1.1833(2)	1.02869(19)	0.0275(7)
O3	0.6891(2)	0.6891(2)	0.6891(2)	0.0291(13)
H4	0.645(4)	0.840(4)	0.794(3)	0.04

Table A.17 Anisotropic Thermal parameters ($Å^2$) for $Cs_6(H2SO_4)_3(H_{1.5}PO_4)_4$.

Atom	U_{11}	U_{22}	U_{33}	U_{23}	U_{13}
Cs1	0.0259(2)	0.0273(2)	0.0205(2)	0	0.00116(19)
P2	0.0193(3)	0.0193(3)	0.0193(3)	-0.0009(5)	-0.0009(5)
S3	0.0168(5)	0.0268(9)	0.0168(5)	0	0
O1	0.0218(14)	0.0196(14)	0.0322(17)	-0.0010(12)	0.0009(13)
O2	0.0224(16)	0.0367(17)	0.0233(17)	-0.0040(13)	-0.0037(11)
O3	0.0291(13)	0.0291(13)	0.0291(13)	-0.0035(13)	-0.0035(13)

Table A.18 Data collection specifics for $Cs_6(H2SO_4)_3(H_{1.5}PO_4)_4$

#----------	CHEMICAL INFORMATION
_chemical_formula_	$Cs_6(H2SO_4)_3(H_{1.5}PO_4)_4$
_chemical_formula_weight	459.87
#----------	UNIT CELL INFORMATION
_cell_length_a	14.539(6)
_cell_length_b	14.539(6)
_cell_length_c	14.539(6)
_cell_angle_alpha	90
_cell_angle_beta	90
_cell_angle_gamma	90
_cell_volume	3073(2)
_cell_formula_units_Z	16
_cell_measurement_temperature	293(2)
#----------	CRYSTAL INFORMATION
_exptl_crystal_size_max	0.4
_exptl_crystal_size_mid	0.3
_exptl_crystal_size_min	0.3
_exptl_crystal_density_diffrn	3.976
_exptl_crystal_density_method	'not
_exptl_crystal_F_000	3328
_exptl_absorpt_coefficient_mu	9.977
_exptl_absorpt_correction_type	none
#----------	DATA COLLECTION INFORMATION
_diffrn_radiation_wavelength	0.71073
_diffrn_radiation_type	MoK\a

_diffrn_reflns_number	2719
_diffrn_reflns_limit_h_min	0
_diffrn_reflns_limit_h_max	15
_diffrn_reflns_limit_k_min	-4
_diffrn_reflns_limit_k_max	15
_diffrn_reflns_limit_l_min	-4
_diffrn_reflns_limit_l_max	15
_diffrn_reflns_theta_min	3.43
_diffrn_reflns_theta_max	29.98
_diffrn_reflns_theta_full	29.98
_diffrn_measured_fraction_theta_max	0.755
_diffrn_measured_fraction_theta_full	0.755
_reflns_number_total	483
_reflns_number_gt	466
_reflns_threshold_expression	>2sigma(I)
#----------	COMPUTER PROGRAMS USED
_computing_structure_refinement	'SHELXL-97
#----------	REFINEMENT INFORMATION
_refine_ls_structure_factor_coef	Fsqd
_refine_ls_matrix_type	full
_refine_ls_weighting_scheme	calc
_refine_ls_weighting_details	'calc
	w=1/[\s^2^(Fo^2^)+(0.0138P)^2^+1.8917P] where P=(Fo^2^+2Fc^2^)/3'
_refine_ls_hydrogen_treatment	mixed
_refine_ls_extinction_method	SHELXL
_refine_ls_extinction_expression	
	Fc^*^=kFc[1+0.001xFc^2^\l^3^/sin(2\q)]^-1/4^
_refine_ls_extinction_coef	0.00160(8)
_refine_ls_number_reflns	483
_refine_ls_number_parameters	36
_refine_ls_number_restraints	0
_refine_ls_R_factor_gt	0.0164
_refine_ls_wR_factor_ref	0.0339
_refine_ls_goodness_of_fit_ref	1.167
_refine_ls_restrained_S_all	1.167
_refine_ls_shift/su_max	0.001
_refine_ls_abs_structure_Flack	-0.03(4)
_refine_diff_density_max	0.415
_refine_diff_density_min	-0.41

Bibliography

1. Bacon, G. E. & Pease, R. S. (1955). *Prof. Roy. Soc. A.*, **230**, 359-381.

2. Baranov, A. I. (1987). *Izvestiya Akademii Nauk SSSR. Seriya Fizicheskaya*, **51**, 2146-2155.

3. Komukae, M., Osaka, T., Makita, Y., Itoh, K. & Nakamura, E. (1981). *J. Phys. Soc. Jpn.*, **50**, 3187-3188.

4. Baranov, A. I., Shuvalov, L. A. & Shchagina, N. M. (1982). *JETP Lett.* **36**, 459-462.

5. Haile, S. M. (1995). *Private Comm.*, 4,7.

6. Blinc, R., Dolinsek, J., Lahajnar, G., Zupancic, I., Shuvalov, L. A. & Baranov, A. I. (1984). *Phys. Stat. Sol. b*, **123**, 83-87.

7. Shchepetil'nikov, B. V., Baranov, A. I., Shuvalov, L. A. & Dolbinina, V. A. (1990). *Sov. Phys. Solid State* , **32**, 142-147.

8. Munch, W., Kreuer, K. D., Traub, U. & Maier, J. (1995). *Solid State Ionics*, **77**, 10-14.

9. Baranov, A. I., Merinov, A. V., Tregubchenko, A. V., Khiznichenko, V. P., Shuvalov, L. A. & Schagina, N. M. (1989). *Solid State Ionics*, **36**, 279-282.

10. Shewmon, P. *Diffusion in Solids*; The Minerals, Metals, & Materials Society: Warrendale, Pennsylvania, 1989.

11. Hummel, R. E. *Electronic Properties of Materials* ; Springer-Verlag: New York, 1985.

12. Tuller, H. L. *Ceramic Materials for Electronics*; Marcell Dekker, Inc.: New York, 1986.

13. Huntington, H. B., Shirn, G. A. & Wajda, E. S. (1955). *Physical Review*, **99**, 1085-1091.

14. Schuster, P. ; Zundel, G.; Sandorfy, C. *The Hydrogen Bond* ; North-Holland Publishing Company: Amsterdam, 1976.

15. Levine, I. N. *Physical Chemistry*; McGraw-Hill Book Company: New York, 1988.

16. Allen, L. C. (1975). *J. Am. Chem. Soc.*, **97**, 6921.

17. Ichikawa, M. (1978). *Acta Cryst.* **B34**, 2074-2080.

18. Haile, S. M. (1995). *Private Comm.*, 4,7.

19. Scheiner, S. (1981). *J. Am. Chem. Soc.*, **103**, 315-320.

20. Brown, I. D. (1976). *Acta. Cryst. A*, **32**, 24-31.

21. Lippincott, E. R. & Schroeder, R. (1955). *J. Chem. Phys.*, **23**, 1099-1106.

22. Wells, A. F. *Structural Inorganic Chemistry*; Clarendon Press: Oxford, 1975.

23. Noda, Y., Uchiyama, S., Kafuku, K., Kasatani, H. & Terauchi, H. (1990). *J. Phys. Soc. Jpn.*, **59**, 2804-2810.

24. Payan, F. & Haser, R. (1976). *Acta Cryst. B*, **32**, 1875-1879.

25. Chisholm, C. R. I., Cowan, L. A. & Haile, S. M. (2001). *Chem. Mater.* **13**, 2574-2583.

26. Chisholm, C. R. I. & Haile, S. M. (2000). *Mater Res Bull*, **35**, 999-1005. Structure of CsHSO4-II.

27. Chisholm, C. R. I. & Haile, S. M. (1999). *Acta. Cryst. B*, **55**, 937-946.

28. Matsunaga, H., Itoh, K. & Nakamura, E. (1980). *J. Phys. Soc. Jpn.*, **48**, 2011-2014.

29. Nelmes, R. J. & Tun, Z. (1987). *Ferroelectrics*, **71**, 125-141.

30. Haile, S. M. , Kreuer, K.-D. & Maier, J. (1995). *Acta Cryst.* **B51**, 680-687.

31. Haile, S. M. & Calkins, P. M. (1998). *J. Solid State Chem.*, **140**, 251-265.

32. Haile, S. M. , Calkins, P. M. & Boysen, D. (1998). *J. Solid State Chem.*, **139**, 373-387.

33. Goodenough, J. B. (1990). *NATO ASI Ser.B*, **217**, 195.

34. Latimer, W. M. & Rodebush, W. H. (1920). *J. Am. Chem. Soc.*, **42**, 1419-1433.

35. Kreuer, K.-D. (1996). *Chem. Mater.* **8**, 610-641.

36. Kreuer, K.-D. (1988). *J. Mol. Struct.*, **177**, 265-276.

37. Colomban, P. *Proton Conductors*
Solids, Membranes and Gels - Materials and Devices; Cambridge University Press: Cambridge, 1992.

38. Kreuer, K.-D., Rabenau, A. & Weppner, W. (1982). *Angew. Chem. Int. Ed. Engl.*, **21**, 208-209.

39. Kreuer, K. D., Dippel, Th., Hainovshy, N. G. & Maier, J. (1992). *Ber. Bunsenges. Phys. Chem.* **96**, 1736-1742.

40. van Grotthuss, C. J. T. (1806). *Annales De Chimie* , **58**, 54-74.

41. Chung, S. H. , Bajue, S. & Greenbaum, S. G. (2000). *J. Chem. Phys.*, **112**, 8515-8521.

42. Dippel, Th. & Kreuer, K. D. (1991). *Solid State Ionics*, **46**, 3-9.

43. Batamack, P. & Fraissard, J. (1997). *Catal. Lett.*, **49**, 129-136.

44. Dippel, Th. & Kreuer, K. D. (1993). *Solid State Ionics*, **61**, 41-46.

45. Potier, A. & Rousselet, D. (1973). *Journal De Chimie Physique*, **70**, 873.

46. Baranov, A. I., Khiznichenko, V. P. & Shuvalov, L. A. (1989). *Ferroelectrics*, **100**, 135-141.

47. Lechner, R. E. (2001). *Solid State Ionics*, **145**, 167-177.

48. Bernal, J. D. & Fowler, R. H. (1933). *J. of Chem. Phys.*, **1**, 515-548.

49. Hobbs, P. V. *Ice Physics*; Clarendon Press: Oxford, 1974.

50. Hubmann, M. (1979). *Z. Physik*, **B32**, 127-141.

51. Aslanov, L. A., Kudryavtsev, I. K. & Bezuglyi, B. A. (1993). *Russian Journal of Inorganic Chemistry*, **38**, 1077-1097.

52. Murphy, E. J. (1964). *J. Appl. Phys.*, **35**, 2609-2614.

53. O'Keeffe, M. & Perrino, C. T. (1967). *J. Phys. Chem. Solids*, **28**, 211-218.

54. Pollock, J. M. & Sharan, M. (1969). *J. Chem. Phys.*, **51**, 3604-3607.

55. Meyer, G. M. , Nelmes R. J. & Tibballs, J. E. (1982). *Journal of Physics C*, **15**, 59-75.

56. Endo, S., Chino, T., Tsuboi, S. & Koto, K. (1989). *Nature*, **340**, 452-455.

57. Sharon, M. & Kalia, K. (1977). *J. Solid State Chem.*, **21**, 171-183.

58. Goto, A., Hondoh, T. & Mae, S. (1990). *J. Chem. Phys.*, **93**, 1412-1417.

59. Pham-Thi, M. , Colomban, Ph., Novak, A. & Blinc, R. (1985). *Solid State*

Commun., **55**, 265-270.

60. Belushkin, A. V., Carlile, C. J. & Shuvalov, L. A. (1992). *J. Phys.: Condens. Matter* , **4**, 389-398.

61. Jirak, Z., Dlouha, M., Vratislav, S., Balagurov, A. M., Beskrovnyi, A. I., Gordelii, V. I., Datt, I. D. & Shuvalov, L. A. (1987). *Phys. Stat. Sol. A*, **100**, K117-122.

62. Sinitsyn, V. V., Ponyatovskii, E. G., Baranov, A. I., Tregubcheko, A. V. & Shuvalov, L. A. (1991). *Sov. Phys. JETP*, **73**, 386-393.

63. Chisholm, C. R. I. & Haile, S. M. (2000). *Solid State Ionics*, **136**, 229-241.

64. Sheldrick, G. M.; Kruger, C.; Goddard, R. *Crystallographic Computing 3*; Oxford University Press: Oxford, 1985.

65. Sheldrick, G. M.; Flack , H. D.; Parkanyi, L.; Simon, K. *Crystallographic Computing 6*; Oxford University Press: Oxford, 1993.

66. Dowty, E. *ATOMS* Shape Software: 521 Hidden Valley Rd, Kingsport, TN 27663, USA, 1999.

67. Hunter, B. A. (1997). *IUCR Powder Diffraction*, **22**, 21.

68. Yoshitaka, B. *Micro-Powd* [Micro-Powd Version 2.3A]. Materials Data, Inc.: 1995.

69. *Jade* [Jade, Jade+ Version 2.1]. Materials Data, Inc.: 1994.

70. Squires, G. L. *INTRODUCTION TO THE THEORY OF THERMAL NEUTRON SCATTERING*; Dover Publications, Inc.: Mineola, New York, 1996.

71. Skold, K.; Price, D. L. *Methods of Experimental Physics*; Academic Press, Inc.: Olrando, Florida, 1986.

72. Haile, S. M. & Klooster, W. T. (1999). *Acta. Cryst.*, **B55**, 285-296.

73. Armstrong, J. T. (1995). *Microbeam Anal.*, **4**, 177-200.

74. Abraham, R. J.; Fisher, J.; Loftus, P. *INTRODUCTION TO NMR SPECTROSCOPY*; John Wiley & Sons: Chichester, 1988.

75. Yesinowski, J. & Eckert, H. (1987). *J. Am. Chem. Soc.*, **109**.

76. Boukamp, B. B. *EQUIVCRT* University of Twente: The Netherlands, 1988.

77. Haile, S. M. Massachusetts Institute of Technology, Boston, 1992.

78. Macdonald, R. J. *Impedance Spectroscopy*; John Wiley & Sons: New York, 1987.

79. Buchanan, R. C. *Ceramic Materials for Electronics*; Marcel Dekker, Inc.: New York, 1986.

80. Warburg (1899). *Ann. Phys. Chem.*, **67**, 493-499.

81. Poole, C. P., Farach, H. A. & Creswick, R. J. (1987). *Ferroelectrics*, **71**, 143-148.

82. Calve, N. L. , Pasquier, B., Romain, F. & Taffin, A. (1994). *J. of Raman Spectroscopy*, **25**, 387-394.

83. Shannon, R. D. (1976). *Acta Cryst.* **A** , 751-767.

84. Belushkin, A. V., Natkaniec, I., Pakida, N. M., Shuvalov, L. A. & Wasicki, J. (1987). *J. Phys. C: Solid State Phys.*, **20**, 671-687.

85. Friesel, M., Baranowski, B. & Lundén, A. (1989). *Solid State Ionics*, **35**, 85-89.

86. Sinitsyn, V. V., Ponyatovskii, E. G., Baranov, A. I., Shuvalov, L. A. & Bobrova, N. I. (1988). *Sov. Phys. Solid State*, **30**, 1636-1638.

87. Tsukamoto, T., Komukae, M., Suzuki, S., Futama, H. & Makita, Y. (1983). *J. Phys. Soc. Jpn* , **52**, 3966-3973.

88. Makarova, I. P., Muradyan, L. A., Rider, E. E., Sarin, V. A., Alexandrova, I. P. & Simonov, V. I. (1990). *Ferroelectricss*, **107**, 281-286.

89. Baranov, A. I., Ponyatovskii, E. G., Sinitsyn, V. V., Fedosyuk, R. M. & Shuvalov, L. A. (1985). *Sov. Phys. Crystallogr.*, **30**, 653-654.

90. Moskvich, Yu. N., Sukhovshii, A. A. & Rozanov, O. V. (1984). *Sov. Phys. Solid State*, **26**, 21-25.

91. Onodera, A., Rozycki, A. & Denoyer, F. (1988). *Ferroelectrics Letters*, **9**, 77-82.

92. Preisinger, A., Mereiter, K. & Bronowska, W. (1994). *Mater. Sci. Forum*, **166-169**, 511-516.

93. Nirsha, B. M., Gudinitsa, E. N., Fakeev, A. A., Efremov, V. A., Zhadanov, B. V. & Olikova, V. A. (1982). *Russian Journal of Inorganic Chemistry*, **27**, 770-772.

94. Tahoon, K. K., Abosehly, A. M., Abdel-Kader, M. M., El-Sharkawy, A. A. & El-Mansi, F. M. (1994). *Acta Phys. Pol., A*, **86**, 349-354.

95. Guseinov, R. M., Gadzhiev, S. M. & Prisyazhnyi, V. D. (1994). *Russian Journal of Electrochemistry*, **30**, 1150-1152.

96. Vasil'ev, V. G., Markov, V. S., Utkina, O. N. & Shulyatikov, B. V. (1975). *Zh. Neorg. Khim.*, **20**, 2875-2881.

97. Merinov, BV. , Jones, D., Roziere, J. & Mhiri, T. (1996). *Solid State Ionics*, **91**, 323-330.

98. Mhiri, T. & Daoud, A. (1994). *J. Alloys Compd.*, **205**, 21-25.

99. Mhiri, T. & Colomban, Ph. (1991). *Solid State Ionics*, **44** , 235-243.

100. Pawlowski, A., Pawlaczyk, Cz. & Hilczer, B. (1990). *Solid State Ionics*, **44**, 17-19.

101. Al-Kassab, A., Liesegang, J. & James, B. (1993). *Structural Chemistry*, **4**, 19-22.

102. Colomban, P. & Badot, J. C. (1992). *J. Phys. Condens. Matter*, **4**.

103. Raimbault, G., Romain, R. & Lautie, A. (1992). *J. Raman. Spectr.*, **23**, 147-154.

104. Tritt-Goc, J., Pislewski, N., Hoffman, S. K. & Augustyniak, M. (1993). *Phys. Stat. Sol. b*, **176**, K13-K16.

105. Mhiri, T. & Colomban, Ph. (1989). *Solid State Ionics*, **35**, 99-103.

106. Mhiri, T. & Daoud, A. (1991). *Solid State Ionics*, **44**.

107. Varma, V., Rangavittal, N. & Rao, C. N. R. (1993). *J. Solid State Chem.*, **106**, 164-173.

108. Cullity, B. D.; Stock, S. R. *ELEMENTS OF X-RAY DIFFRACTION*; Prentice Hall: Upper Saddle River, NJ, 2001.

109. Lipkowski, J., Baranowski, B. & Lunden, A. (1993). *Polish J. Chem.*, **67**, 1867-1876.

110. Chisholm, C. R. I. & Haile, S. M. (2001). *Solid State Ionics*, **145**, 179-184.

111. Chisholm, C. R. I., Cowan, L. A. & Haile, S. M. (2001). *Chem. Mater.*, **13**, 2909-2912.

112. Baranowski, B. & Lipkowski, J. (1995). *J. Solid State Chem.*, **117**, 412-413.

113. Stasyuk, I. V. & Pavlenko, N. (1998). *J. Phys.: Condens. Matter* , **10**, 7079-7090.

114. Kemnitz, E. & Werner, C. (1995). *Z. Anorg. Allg. Chem.*, **621**, 675-678.

115. Sonneveld, E. J. & Visser, J. W. (1979). *Acta. Cryst.*, **B35**, 1975-1977.

116. Nelmes, R. J. (1971). *Acta. Cryst.*, **B27**, 272-281.

117. Itoh, K. O. H. & Kuragaki, S. (1995). *J. Phys. Soc. Jpn.* **64**, 479-484.

118. Ashmore, J. P. & Petch, H. E. (1975). *Can. J. Phys.* **53**, 2694-2702.

119. Averbuch-Pouchot, M. T. (1981). *Mat. Res. Bull.* **16**, 407-411.

120. Stiewe, A., Sonntag, R., Troyanov, S. I., Hansen, T. & Kemnitz, E. (2000). *J. of Solid State Chemistry*, **149**, 9-15.

121. Averbuch-Pouchot, M. T. & Durif, A. (1980). *Mat. Res. Bull.*, **15**, 427-430.

122. Sinitsyn, V. V. & Baranov, A. I. (1996). *Russian Journal of Electrochemistry*, **32**, 427-431.

123. Schaffer, J. P.; Saxena, A.; Antolovich, S. D.; Sanders, T. H.; Warner, S. B. *The Science and Design of Engineering Materials*; Irwin: Chicago, 1995.

124. Belushkin, A. V., David, W. I. F., Ibberson, R. M. & Shuvalov, L. A. (1991). *Acta Cryst.* **B47**, 161-166.

125. Merinov, B. V., Baranov, A. I., Shuvalov, L. A. & Maksimov, B. A. (1987). *Kristallografiya*, **32**, 86-92.

126. Sharma, J. C., Shanker, J. & Goyal, S. C. (1977). *J. Phys. Chem. Solids*, **38**, 327-328.

127. Haile, S. M., Lentz, G., Kreuer, K.-D. & Maier, J. (1995). *Solid State Ionics*, **77**, 128-134.

128. Brown, I. D. & Altermatt, D. (1985). *Acta. Cryst.* **B41**, 244-247.

129. Boysen, D., Haile, S. M., Liu, H. J. & Secco, R. A. (in the press). *Chem. Mater.*.

130. Baranowski, B., Friesel, M. & Lundén, A. (1989). *Physica A*, **156**, 353-363.

131. Boysen, D. & Haile, S. (in the press). *Chem. Mater.*.

132. Haile, S. M., Calkins, P. M. & Boysen, D. (1997). *Solid State Ionics*, **97**, 145-151.

133. Calkins, P. M. University of Washington, Seattle, 1996.

134. Metcalfe, B. & Clark, J. B. (1978). *Thermochim. Acta*, **24**, 149-153.

135. Pauling, L. (1935). *J. Am. Chem. Soc.*, **57**, 2680-2684.

136. Plakida, N. M. (1986). *Phys. Stat. Sol.* **b**, 133-139.

137. Romain, F. & Novak, A. (1991). *J. Mol. Struct.*, 69-74.

138. Kossiakoff, A. & Harker, D. (1938). *J. Am. Chem. Soc.*, **60**, 2047-2055.

139. Nelmes, R. J. & Choudhary, R. N. P. (1978). *Solid State Commun.*, **26**, 823-826.

140. Blinc, R., Zeks, B., Levstik, A., Filipic, C., Slak, J., Burgar, M., Zupancic, I., Shuvalov, L. A. & Baranov, A. I. (1979). *Phys. Rev. Lett.*, **43**, 231-234.

141. Scalapino, D. J. & Imry, I. (1975). *Physical Review B*, **11**, 2042-2048.

142. Baxter, J. R. *Exactly Solved Models in Statistical Mechanics*; Academic Press: London, 1982.

143. Kanda, E., Masahito Y., Tsutom Y. & Tadao, F. (1982). *J. Phs. C: Solid State Phys.*, **15**, 6823-6831.

144. Kanda, E., Tamaki, A. & Fujimura, T. (1982). *J. Phys. C: Solid State Phys.* **15**, 3401-3410.

145. Imai, K. (1983). *J. Phys. Soc. Jpn.*, **52**, 3960-3965.

146. Zumer, S. (1980). *Physical Review B*, **21**, 1298-1303.

147. Plakida, N. M. (1985). *JETP Lett.*, **41**, 114-116.

148. Dzhavadov, N. A. & Rustamov, K. A. (1992). *Phys. Stat. Sol. b*, **170**, 67-77.

149. Giauque, W. E. & Ashley, J. W. (1933). *Phys. Rev.* **43**, 81-82.

150. Suga, H., Matsuo, T. & Yamamuro, O. (1992). *Pure and Appl. Chem.*, **64**, 17-26.

151. Matsuo, T., Oguni, M., Suga, H., Seki, S. & Nagle, J. F. (1972). *Bull. Chem. Soc. Jpn.*, **47**, 57.

152. Matsuo, T., Kume, Y., Suga, H. & Seki, S. (1976). *J. Phys. Chem. Solids*, **37**, 499.

153. Okishiro, K., Yamamuro, O., Matsuo, T., Nishikiori, S. & Iwamoto, T. (1996). *J. Phys. Chem.* **100**, 18546-18549.

154. Slater, J. C. (1941). *J. Chem. Phys.*, **9**, 16-33.

155. Takagi, Y. (1948). *J. Phys. Soc. Japan*, **3**, 271-272.

156. Matsuo, T., Yamamuro, O., Oguni, M. & Saga, H. (1996). *J. Therm. Anal.*, **46**, 1167-1176.

157. Yokota, S., Takanohashi, N., Osaka, T. & Makita, Y. (1982). *J. Phys. Soc. Jpn.*, **51**, 199-202.

158. Hart, S., Richter, P. W. & Clark, J. B. (1981). *J. Solid State Chem.*, **37**, 302-307.

159. Zakharov, M. A., Troyanov, S. I. & Kemnitz, E. (2001). *Z. Kristallogr.* **216**, 172-175.

160. Baran, J. & Lis, T. (1987). *Acta. Cryst. C*, **43**, 811-813.

161. Hay, W. J. & Nelmes, R. J. (1981). *Journal of Physics C* , **14**, 1043-1052.

162. Troyanov, S. I., Morozov, I. V., Rybakov, V. B., Stiewe, A. & Kemnitz, E. (1998). *J. Solid State Chem.*, **141**, 317-322.

163. Boubia, M., Averbuch-Pouchot, M. T. & Durif, A. (1985). *Acta. Cryst. C.*, **41**, 1562-1564.

164. Hilczer, B. , Pawlaczyk, C. & Salman, F. E. (1988). *Ferroelectrics*, **81**, 193-196.

165. Yokata, S., Makita, Y. & Takagi, Y. (1982). *J. Phys. Soc. Jpn.*, **51**, 1461-1468.

166. Chisholm, C. R. I., Merle, R. B., Boysen, D. & Haile, S. M. (2002). *Chem. Mater.*

167. Poprawski (1988). *Solid State Commun.*, **67**, 629-631.

168. Hilczer, B. , Polomska, M. & Pawlowski, A. (1999). *Solid State Ionics*, **125**, 163-169.

169. Fajdiga-Bulat, A. M., Lahajnar, G., Dolinsek, J., Slak, J., Lozar, B., Zalar, B., Shuvalov, L. A. & Blinc, R. (1995). *Solid State Ionics*, **77**.

170. Baranov, A. I., Tregubchenko, A. V., Shuvalov, L. A. & Shchagina, N. M. (1987). *Sov. Phys. Solid State*, **29**, 1448-1449.

171. Makarova, I. P. (1993). *Acta. Cryst. B*, **49**, 11-18.

172. Balagurov, A. M., Belushkin, A. V., Dutt, I. D., Natkaniec, I., Plakida, N. M., Savenko, B. N., Shuvalov, L. A. & Wasicki, J. (1985). *Ferroelectrics*, **63**.

173. Zetterström, P., Belushkin, A. V., McGreevy, R. L. & Shuvalov, L. A. (1999). *Solid State Ionics*, **116**, 321-329.

174. Badot, J. C. & Colomban, Ph. (1989). *Solid State Ionics*, **35**, 143-149.

175. Mayo, S. L. , Olafson, B. D. & Goddard III, W. A. (1990). *J. Phys. Chem.*, **94**, 8897-8909.

176. *Cerius2 4.0* Molecular Simulations Inc..

177. Slater, J. C. *Quantum Theory of Molecules and Solids. Vol 4. The Self-Consistent Field for Molecules and Solids*; McGraw-Hill: New York, 1974.

178. Becke, A. D. (1988). *Phys. Rev. A*, **38**, 3098-3100.

179. Vosko, S. H., Wilk, L. & Nusair, M. (1980). *Can. J. Phys.*, **58**, 1200-1211.

180. Lee, C. T., Yang, W. T. & Parr, R. G. (1988). *Phys. Rev. B*, **37**, 785-789.

181. Miehlich, B., Savin, A., Stoll, H. & Preuss, H. (1989). *Chem. Phys. Lett.* **157**, 200-206.

182. Hay, P. J. & Wadt, W. R. (1985). *J. Chem. Phys.* **82**, 299-.

183. *Jaguar V.3.5* Schrodinger, Inc..

184. Chirlian, L. E. & Francl, M. M. (1990). *J. Comput. Chem.*, **8**, 894-907.

185. Woods, R. J., Khalil, M., Pell, W., Moffat, S. H. & Smith Jr., V. H. (1990). *J. Comput. Chem.*, **11**, 297-310.

186. Breneman, C. M. & Wiberg, K. B. (1990). *J. Comput. Chem.*, **11**, 361-373.

187. Nose, S. (1984). *Mol. Phys.*, **52**, 255.

188. Hoover, W. G. (1985). *Phys. Rev. A*, **31**, 1695.

189. Boysen, D. A., Chisholm, C. R. I., Haile, S. M. & Narayanan, S. R. (2000). *Journal of the Elecrochemical Society*, **147**, 3610-3613.

190. Pham-Thi, M., Colomban, Ph., Novak, A. & Blinc, R. (1987). *J. Raman Spectroscopy*, **18**, 185-194.

191. Pauling, L. *The Nature of the Chemical Bond*; Cornell University Press: Ithica, New York, 1960.

192. Munch, W., Kreuer, K. D., Traub U. & Maier J. (1996). *J. Mol. Struct.*, **381**, 1-8.